

**ANALYSIS AND NUMERICAL SIMULATION OF STRAIN  
LOCALIZATION IN INELASTIC SOLIDS UNDER FULLY  
COUPLED THERMOMECHANICAL AND  
POROPLASTIC CONDITIONS**

by

**F. ARMERO**

University of California at Berkeley  
Structural Engineering, Mechanics, and Materials  
Department of Civil and Environmental Engineering  
713 Davis Hall, Berkeley, CA 94720  
Phone: (510)-643 0813 FAX: (510)-643 8928  
e-mail: armero@ce.berkeley.edu

**Final Report**

August 2000

Research supported by the ONR under grant  
no. N00014-96-1-0818 with UC Berkeley

The Office of Naval Research  
Ship Structures & Systems Division  
Computational Mechanics Program  
Dr. Luise Couchman, Program Director  
ONR 334  
Ballston Center Tower One  
800 North Quincy Street  
Arlington VA 22217-5660

**DISTRIBUTION STATEMENT A**  
Approved for Public Release  
Distribution Unlimited

DMC QUALITY INSPECTED 4

20000821 045

## Table of Contents

|  |    |
|--|----|
| <b>Abstract</b>  | 1  |
| <b>Key words</b>   | 1  |
| 1. Motivation and Goals  | 2  |
| 2. Research Accomplishments  | 4  |
| 3. Impact of the Research. Relevance to the Navy   | 7  |
| 4. Future Work and Extensions  | 8  |
| 5. Outline of the Rest the Report  | 9  |
| 5.1. Appendix I: Large scale modeling of localized dissipative mechanisms in a local continuum       | 9  |
| 5.2. Appendix II: Analysis of strong discontinuities under fully coupled thermomechanical conditions | 10 |
| 5.3. Appendix III: Analysis of strong discontinuities in poroplasticity                              | 11 |
| 5.4. Appendix IV: An ALE finite element method for finite strain plasticity                          | 11 |
| <b>Publications under ONR support</b>  | 12 |
| <b>Invited Lectures, Conference Contributions, Organized Symposia and Edited Special Issues</b>      | 16 |

|  |    |
|--|----|
| <b>APPENDIX I. Large-Scale Modeling of Localized Dissipative Mechanisms in a Local Continuum</b> | 20 |
| I.1. Introduction  | 21 |
| I.2. The Large-Scale Problem   | 24 |
| I.3. Characterization of Localized Dissipative Mechanisms in the Local Continuum                 | 26 |
| I.3.1. The kinematics of strong discontinuities  | 26 |
| I.3.2. The localized dissipation   | 29 |
| I.3.3. The localized constitutive relations  | 30 |
| I.3.3.1. Model example: a rigid (visco)plastic slip model  | 33 |
| I.4. The Construction of the Local Continuum Formulation   | 34 |
| I.4.1. The final governing equations   | 34 |
| I.4.2. Large-scale regularization of rate-dependent models                                       | 36 |

|        |  |    |
|--------|--|----|
| I.4.3. | The finite element implementation . . . . .                          | 38 |
| I.5.   | The Extension to the Finite Deformation Range . . . . .              | 40 |
| I.5.1. | The finite kinematics of strong discontinuities . . . . .            | 40 |
| I.5.2. | Localized dissipative mechanisms in the finite deformation range . . | 42 |
| I.5.3. | The governing equations and their finite element implementation .    | 44 |
| I.6.   | Representative Numerical Simulations . . . . .                       | 45 |
| I.6.1. | 1D wave propagation problem in a softening viscoplastic shear layer  | 45 |
| I.6.2. | The plane strain tension test . . . . .                              | 51 |
| I.7.   | Conclusions . . . . .  | 53 |

## **APPENDIX II. Analysis of Strong Discontinuities under Fully Coupled Thermomechanical Conditions . . . . .**

|           |   |     |
|-----------|---|-----|
| II.1.     | Introduction . . . . .  | 60  |
| II.2.     | A Spectral Analysis of the Linearized Problem . . . . .                                   | 62  |
| II.2.1.   | Problem definition . . . . .  | 62  |
| II.2.2.   | Linearized stability analysis . . . . .   | 65  |
| II.2.3.   | Investigation of the ill-posedness . . . . .  | 67  |
| II.2.4.   | Evaluation of the mesh-size dependence of the finite element solutions                    | 69  |
| II.3.     | An Analysis of Wave Propagation in A Localized Thermo-ElastoPlastic Shear Layer . . . . . | 73  |
| II.3.1.   | Problem description . . . . .   | 74  |
| II.3.2.   | Exact solution for a localized softening model . . . . .                                  | 75  |
| II.3.3.   | Parametric study . . . . .  | 78  |
| II.3.3.1. | Nondimensional parameters . . . . .   | 78  |
| II.3.3.2. | Properties of the solution . . . . .  | 79  |
| II.4.     | An Analysis of the Approximation of Strong Discontinuities . . . . .                      | 83  |
| II.4.1.   | An approximate solution for $h > 0$ : analytic results . . . . .                          | 84  |
| II.4.2.   | Properties of the solution . . . . .  | 88  |
| II.4.3.   | Representative finite element simulations . . . . .                                       | 91  |
| II.5.     | Extensions to General Multi Dimensional Problems . . . . .                                | 94  |
| II.5.1.   | The continuum model . . . . .   | 94  |
| II.5.2.   | Strong discontinuities in thermoplastic media . . . . .                                   | 95  |
| II.5.3.   | The finite element implementation . . . . .   | 97  |
| II.5.4.   | Representative numerical simulations . . . . .  | 100 |
| II.5.4.1. | Plane strain tension test . . . . .   | 102 |

|   |     |
|---|-----|
| II.5.4.2. Rigid block pushed against a thermoplastic foundation . . . . . | 104 |
| II.6. Concluding Remarks . . . . .  | 109 |

## **APPENDIX III. Analysis of Strong Discontinuities in Coupled Poroplasticity . . . . .**

|  |     |
|--|-----|
| III.1. Introduction . . . . .  | 113 |
| III.2. A Characterization of Discontinuous Solutions in Porous Media . . . . .         | 115 |
| III.2.1. The large-scale mechanical problem . . . . .                                  | 115 |
| III.2.2. The kinematics of strong discontinuities . . . . .                            | 116 |
| III.2.3. The characterization of the fluid flow . . . . .                              | 118 |
| III.3. Localized Dissipative Mechanisms in Coupled Poro-Elastoplastic Solids . . . . . | 121 |
| III.3.1. The continuum poro-elastoplastic model . . . . .                              | 121 |
| III.3.2. The localized dissipative mechanism . . . . .                                 | 124 |
| III.4. Model Problem: a Dilatant Shear Layer . . . . .                                 | 126 |
| III.4.1. The poro-elastoplastic model . . . . .  | 127 |
| III.4.2. An enhanced finite element formulation . . . . .                              | 129 |
| III.5. Representative Numerical Simulations . . . . .                                  | 134 |
| III.5.1. The undrained shear test . . . . .  | 135 |
| III.5.2. The drained shear test . . . . .  | 138 |
| III.6. Concluding Remarks . . . . .  | 141 |

## **APPENDIX IV. An ALE Finite Element Method for Finite Strain Plasticity . . . . .**

|  |     |
|--|-----|
| IV.1. Introduction . . . . .                               | 145 |
| IV.2. Continuum Equations of the ALE Formulation . . . . . | 146 |
| IV.2.1. ALE kinematics . . . . .                           | 147 |
| IV.2.2. Material derivative . . . . .                      | 148 |
| IV.2.3. The balance laws . . . . .                         | 150 |
| IV.2.4. Boundary conditions . . . . .                      | 151 |
| IV.2.5. Weak formulation . . . . .                         | 152 |
| IV.2.6. Multiplicative plasticity . . . . .                | 153 |

|   |     |
|---|-----|
| IV.3. A Staggered Approach to the ALE Problem . . . . .                       | 155 |
| IV.3.1. The discrete equations . . . . .                                      | 155 |
| IV.3.2. The global approach . . . . .   | 155 |
| IV.3.3. Mesh distortion measures . . . . .                                    | 156 |
| IV.3.4. Mesh smoothing (determination of $\chi$ ) . . . . .                   | 157 |
| IV.4. An Advection Method Based on Particle Tracking . . . . .                | 158 |
| IV.4.1. Plastic variable advection . . . . .                                  | 158 |
| IV.4.2. The pure advection equation . . . . .                                 | 158 |
| IV.4.3. Numerical particle tracking . . . . .                                 | 160 |
| IV.4.4. Additional practical considerations . . . . .                         | 161 |
| IV.5. Representative Numerical Simulations . . . . .                          | 163 |
| IV.5.1. Patch test . . . . .  | 163 |
| IV.5.2. Indentation of an elastic block . . . . .                             | 165 |
| IV.5.3. Necking of a circular bar . . . . .                                   | 168 |
| IV.5.4. Plane strain tension test . . . . .                                   | 169 |
| IV.5.5. Indentation of an elastoplastic block . . . . .                       | 171 |
| IV.5.6. Impact of a circular bar . . . . .                                    | 171 |
| IV.6. Concluding Remarks . . . . .  | 180 |
| App. IV.1. Constitutive Models . . . . .                                      | 180 |
| App. IV.2. Numerical Implementation of Three Dimensional Elasticity . . . . . | 181 |
| IV.2.1. Preliminaries . . . . .   | 182 |
| IV.2.2. Linearizations . . . . .  | 182 |
| IV.2.2.1. Linear Momentum . . . . .   | 183 |
| IV.2.2.2. Constitutive Equation for Pressure . . . . .                        | 183 |
| IV.2.2.3. Compatibility Equation for Theta . . . . .                          | 183 |
| IV.2.3. Augmented Lagrangian modifications . . . . .                          | 184 |

**ANALYSIS AND NUMERICAL SIMULATION OF STRAIN  
LOCALIZATION IN INELASTIC SOLIDS UNDER FULLY  
COUPLED THERMOMECHANICAL AND  
POROPLASTIC CONDITIONS**

by

**F. ARMERO**

Structural Engineering, Mechanics, and Materials  
Department of Civil and Environmental Engineering  
University of California, Berkeley CA 94720

**Final Report**

August 2000

Research supported by the ONR under grant  
no. N00014-96-1-0818 with UC Berkeley

**Abstract**

We present in this report a summary of the research supported by the ONR during the period June 1 1996 to May 31 2000 on the analysis and numerical simulation of strain localization in inelastic solids. Special attention is given to the analysis of failure under coupled thermo- and poro- plastic conditions, as well as the consideration of coupled plastic damage in solids. The highly non-smooth solutions of interest involve discontinuous displacement fields, the so-called strong discontinuities, requiring the formulation of a new framework for their inclusion in the local continuum and the development of enhanced finite element techniques that incorporate the associated singular strain fields to capture the localized dissipative mechanisms characteristic of the failure of solids in a physically correct and efficient manner. Both Lagrangian and arbitrary Lagrangian-Eulerian finite element techniques have been developed. The resulting models and numerical methods have been studied and evaluated in detail through rigorous mathematical analyses and a number of numerical simulations. Additional tools, like the formulation of new enhanced strain finite elements for finite deformation problems and new globally convergent closest-point projection integrators for elastoplasticity, have been developed as needed in the solution of the highly nonlinear problems of interest in this work.

**KEY WORDS:** strong discontinuities, strain localization, failure, elastoplasticity and damage, coupled thermoplasticity and poroplasticity, enhanced strain finite elements, ALE methods, closest-point projection schemes.

## 1. Motivation and Goals

The complete characterization of the damage and failure in solids is not only of the main theoretical importance, but also of the major interest for its numerous practical applications. Typical examples are the analysis of industrial processes in metal forming, crash worthiness studies, and the simulation of the failure of large structural systems. The failure of most materials is often characterized by a concentration of strains along narrow bands. Characteristic examples are shear bands in metals, geological materials, and localization bands of cracking in brittle materials like concrete, among others. The small scale associated to these bands, compared to the overall response of the solid or structure, is to be noted.

Previous theoretical analyses of local rate-independent plasticity models in the local continuum have shown the existence of discontinuous solutions, thus replicating the above observed phenomena in a large scale. These solutions involve a discontinuous displacement field with the associated strains being bounded measures (e.g. a Dirac delta function). They are referred to as strong discontinuities. In general, the multi-scale nature of the problem is reflected by these complex non-smooth solutions, with small regions (regions of zero measure in the limit case of discontinuous solutions) where the dissipative effects are concentrated. The correct numerical resolution of such discontinuities proves then to be a crucial requirement for large-scale simulations of the failure of solids and becomes the key characteristic of the approach considered in this project. More specifically, the research developed in this project addresses the theoretical and numerical aspects of strain localization in inelastic solids under fully coupled conditions, under both coupled thermo-mechanical conditions (typical of the deformation of metals) and of coupled poroplastic conditions (typical of the deformation of soils and saturated porous media, in general).

The first goal of this project is the derivation of the precise mathematical conditions controlling the formation and propagation of strong discontinuities in solids. This discontinuities are characterized by a discontinuous displacement field, in contrast with the classical approach based on (*weak*) discontinuities of the strains. To that purpose, a complete thermodynamically consistent, multi-scale framework of this phenomenon has been developed to incorporate the effects of the localized dissipative mechanism causing the failure of the material in the local continuum modeling the large-scale response of the solid or structure. As indicated above, the cases of coupled thermo- and poro- plasticity as well as the consideration of damage are of the main interest in this project. The characterization of the strong discontinuities in these conditions is to be accompanied by a complete analysis of the resulting boundary-value problems identifying their well-posedness (in the sense of Hadamard, with a continuous dependence of the data in particular), in contrast with the pathologies observed in models of the local continuum incorporating (continuum) strain softening.

The second goal of this project is the development of new finite element methods

for the fully nonlinear regime that incorporate enhanced discontinuity-capturing interpolations. The new methods must avoid the aforementioned pathologies of the numerical solutions based on a local continuum with strain softening, namely, the non-physical dependence of the computed solutions on the mesh size. Furthermore, the new methods must be able to resolve these highly oriented solutions, characterized by surfaces of discontinuity, independently of the mesh alignment. These properties are to be obtained in unstructured spatial discretizations of the domains under consideration. In addition, the new methods must be computationally efficient showing a local structure, in the sense that the final solution of the large-scale problem involves the nodal unknowns in a typical finite element solution only (e.g., nodal displacements and nodal temperatures in the context of thermoplasticity). In other words, computational efficiency requires that the unknowns introduced to model the localized dissipative mechanisms of interest are eliminated locally at the element level.

All these research objectives identified in the original proposal have been fulfilled in this project. Furthermore, the difficulties associated with the modeling and numerical solution of this highly nonlinear, non-smooth problems required the development of additional tools of analysis. In particular, and at the numerical level, we can quote the need of improved finite elements for finite deformation problems and of improved integration algorithms of the nonlinear equations of inelasticity (plasticity and damage, in general). In the first case, the need of finite element formulations that avoid volumetric and shear locking while being stable (in the sense that they avoid hourgassing) in the fully nonlinear finite deformation range has motivated the developments of new mixed/enhanced finite element formulations, including complete mathematical analyses of the new and existing methods in the general context of finite strain elastoplasticity. Concerning the need of improved local integrators in elastoplasticity, the limited global convergence properties of existing return mapping algorithms (the so-called closest-point projection method) has motivated us to develop a full analysis of the mathematical structure of the resulting discrete equations, again in the general context of finite strain elastoplasticity. This analysis identified new and improved, globally convergent schemes for the local integration of the plastic and damage models employed in this project.

The large strains associated to the localized solutions of interest in this work lead to highly distorted finite elements, preventing the successful numerical solution of the problem. As identified in the original proposal, it is of the main interest to develop then non-Lagrangian techniques that accommodate these distortions. In this way, we have developed a new arbitrary Lagrangian Eulerian (ALE) finite element formulation for finite deformation elastoplasticity that accomplishes effectively these objectives. The consideration of multiplicative finite strain plasticity in a fully implicit context has been our main interest in our developments. In this context, the proposed method involves an efficient advection of the internal plastic variables thanks to the direct consideration of the material remap in contrast with existing formulations based usually on rate forms of the

governing equations. The use of this newly developed method in problems involving strain localization and failure has shown to lead to an improvement over existing Lagrangian methods.

The need for additional tools does not reduce to computational considerations, but also to developments more theoretical in nature. In this way, the analysis of the failure in saturated porous media required the development of the proper framework to account for the different effects of the plasticity and fluid flow. Similarly, the analysis of the coupling between damage and plasticity in materials required the development of the proper framework for its study. To these purposes, we have also considered in this project: 1) the development of a new framework of poroplasticity at finite strains based on a multiplicative decomposition of the deformation gradient and an additive decomposition of the fluid content in elastic and plastic parts, and 2) the formulation of a new framework for coupled damage plastic models based on a kinematic decomposition of the strains in elastic, plastic and damage strains, in contrast with existing models based only on elastic and plastic strains with the damage effects introduced elsewhere. In the case of the developments in poroplasticity, the right consideration of the inelastic effects associated to the fluid flow in the saturated porous media has led to the correct identification of the singular fields at failure in these models. Finally, the newly developed coupled damage plastic framework has allowed the physically motivated modeling of these effects in a modular structure very convenient for its numerical implementation. Applications considered so far include the study of coupled plastic damage in porous metals, with additional applications being currently under consideration.

## 2. Research Accomplishments

We present in this section a summary of the research accomplishments obtained in this project, addressing the objectives identified in the previous section. Complete references to the publications where they appeared are included (see list in page 12 of this report).

1. The formulation of a thermodynamically based framework to model localized dissipative mechanisms in inelastic solids [10, 15, 27, 28, 31, 33]:

1.1 Identification of the proper localized laws along the limit discontinuous solutions (the so-called strong discontinuities) in a multiscale framework by which the localized effects at failure of the small scales are introduced in the large-scale problem of a inelastic local continuum. Applications developed:

1.1.1 Infinitesimal and finite strain elastoplasticity, including localized viscous models. [10, 27]

1.1.2 Infinitesimal and finite deformation anisotropic damage models. [15, 28, 31]

- 1.1.3** Fully saturated porous media and coupled thermomechanical models (see Items 3 and 4 below, respectively).
  - 1.2** Finite element implementation through the formulation of local enhancements of general mixed finite elements with the singular strain fields characteristic of the discontinuous solutions of interest.
- 
- 2.** Complete mathematical analyses of the localized models resulting of the framework developed in the previous item and the proposed finite element methods [11, 25]:
    - 2.1** Exact closed-form solution of the wave propagation in a localized bar exhibiting a softening relation along a strong discontinuity.
    - 2.2** Full analytic characterization of the properties of the finite element approximations in this one dimensional dynamic setting.
  - 3.** The characterization of localized dissipative mechanisms under coupled thermomechanical conditions [3, 22]:
    - 3.1** Linearized spectral analyses identifying the instabilities and ill-posedness in continuum models with strain and thermal softening.
    - 3.2** Full analytic characterization of the exact solutions of wave propagation in a localized softening shear layer, involving strong discontinuities under fully coupled thermomechanical conditions.
    - 3.3** Full analytic characterization of the approximations properties of enhanced finite elements in this one dimensional thermomechanical context with strong discontinuities.
    - 3.4** Characterization of strong discontinuities in thermoplasticity and their resolution through enhanced strain finite element methods in general multi dimensional problems.
  - 4.** The analysis of the failure in coupled elastoplastic models of saturated porous media [8, 9, 14, 23, 24]:
    - 4.1** Formulation of a new finite deformation framework of coupled poroplasticity, incorporating the inelastic effects of the fluid flow through an additive decomposition of the fluid content and a multiplicative decomposition of the deformation gradient. [9, 24]
    - 4.2** Finite element implementation of this framework, including the formulation and analysis of staggered time-stepping algorithms for its efficient numerical solution. [9, 24]

- 4.3** Characterization of strong discontinuities in this fully coupled context, including the formulation of enhanced strain finite element methods for their numerical resolution. [8, 14, 23]
- 4.4** Finite element methods incorporating the limit discontinuous solutions.
- 5.** The formulation of ALE finite element techniques to accommodate the large mesh distortions that appear when resolving localized failures [4, 16, 17]:
  - 5.1** Separate interpolation and resolution of the material and mesh motions.
  - 5.2** Staggered implementation incorporating the finite strain multiplicative models of interest.
  - 5.3** Advection of internal plastic variables step based on particle tracking through mesh graphs.
  - 5.4** Mesh motion resolves the high distortion of localization bands.
  - 5.5** The consideration of both quasi-static and dynamic problems.
- 6.** The development of new enhanced finite element methods for finite deformation problems in elastoplasticity [7, 12, 26, 29, 30, 32]:
  - 6.1** Analytic characterization of the locking and stability properties of different finite element formulations in the finite deformation range.
  - 6.2** Formulation of new enhanced/mixed finite elements, exhibiting a locking-free response in both incompressibility and bending dominated problems.
  - 6.3** Stabilized enhanced finite elements for finite deformation problems.
- 7.** The formulation of new globally convergent closest-point projection algorithms (CPPM) for the integration of the constitutive equations of elastoplasticity [1, 2, 13, 18, 19]:
  - 7.1** Full characterization of the variational structure behind the closest-point projection equations in elastoplasticity: primal, dual and augmented Lagrangian formulations.
  - 7.2** Formulation of improved integration algorithms: globally convergent and locally (asymptotically) quadratic.
- 8.** The formulation of a general framework for the formulation of coupled plastic-damage models [5, 6, 20, 21]:

- 8.1** The framework is based on the kinematic decomposition of the strains in elastic, damage and plastic strains, with the coupled plastic damage evolution equations arising in a fully thermodynamically consistent context.
- 8.2** Two main advantages associated to the use of the damage strains:
  - 8.2.1** Direct physical characterization of the damage mechanism in the material's response (e.g., cracks, void nucleation and distortion, etc.).
  - 8.2.2** Modular structure of the resulting model very well-suited for its numerical integration (separate CPPM schemes for the plastic and damage parts).
- 8.3** The applications developed include the modeling of coupled plastic damage in porous metals.

Additional details on some of the results in Items 1, 3, 4 and 5 can be found in Appendices I to IV of this report. See Section 5 for an outline.

### **3. Impact of the Research. Relevance to the Navy**

We believe that the research developed in this project has led to important advances in the understanding of non-smooth inelastic processes in solids and their numerical modeling. This includes a complete rigorous characterization of the strain localization in solids under coupled thermomechanical and poroplastic conditions. Furthermore, new computational techniques have been developed for the numerical simulation of discontinuous solutions in solids. The results obtained in this project improve the modeling and computational capabilities of existing techniques, especially in the failure analysis of the large-scale structural systems of interest to the Navy. In this way, we have interacted with both the Computational Mechanics and the Solid Mechanics Programs of the ONR.

These results have been presented in a number of refereed publications as well as in many conference contributions and invited lectures. A complete list of the publications prepared in this project is presented in page 12 of this report, and in page 16 for the transitions of the research funded by this ONR project.

Recognition to the research developed in this project has come in different forms. In particular, we can quote the many invitations received by the P.I. to present these findings in national and international conferences, including keynote lectures and addresses in major national and international meetings (like in the World Congress on Computational Mechanics held in Buenos Aires, Argentina, in June 1998, and the European Congress on Computational Mechanics held in Munich, Germany, in September 1999, among others). During the period of performance of this project, the P.I., Francisco Armero, was awarded a NSF CAREER Award in June 1997, and the Juan C. Simo Award and Medal in June 1999.

given by SEMNI (the Spanish Society of Numerical Methods in Engineering) every three years to "a young investigator in recognition of his/her scientific career". Furthermore, he received the Best Paper in Engineering Computations in June 1997 for the paper [12] co-authored with the postdoctoral fellow Dr. S. Glaser.

We would like to mention also the strong educational component of the research developed in this project. In this context, two graduate students have been supported during their doctoral studies: Mr. Edward Love (PhD August 2000) and Mr. Jaegyun Park (PhD expected May 2001). Their respective PhD dissertations include many of the major results in this project. Additional collaborators include visiting postdoctoral fellows and visiting professors.

#### 4. Future Work and Extensions

The models, analyses and numerical methods developed in this project are currently being extended to additional situations. In particular, we note our current efforts to include the thermomechanical effects identified along the strong discontinuities in the newly developed ALE finite element methods, as well as the analysis at failure of the constitutive models developed under the newly proposed framework for coupled plastic damage, including extensions to the finite deformation range.

Our main plans for future work in this area are to develop new adaptive finite element methods based on the enhanced finite elements developed in this project that incorporate within the element interpolations the singular strain fields associated to the discontinuous solutions in the displacement field. The adaptive process will lead gradually to the resolution of these discontinuities by the mesh itself, allowing their separation to model the final fracture and fragmentation of the solid. One of the advantages of the proposed approach, in front of many existing approaches in the literature, is that the propagation of the discontinuities (cracks or localized patterns, in general) occur at the element interiors, independent of the alignment of the finite elements. The subsequent adaptive process can then be based solely on accuracy considerations when resolving these highly non-smooth deformation fields, without the need to provide a myriad of propagation paths to these discontinuities through special mesh alignments. This key feature of the proposed methods motivates a complete theoretical analysis of the a posteriori error estimation in these conditions. To this purpose, residual type error estimators carrying the information of the solution to be resolved (namely, its directionality) will be carried out. These analyses will be developed first in the context of linear elastic problems with embedded cohesive surfaces, taking full advantage of the enhanced strain structure of the proposed finite element methods. In fact, the high-performance observed in the continuum enhanced finite elements developed in this project motivates a complete a posteriori error analysis of this general class of finite element methods. More specifically, the good performance of these

elements in configurations with high aspect ratios, due to the lack of shear-locking that these elements exhibit, makes them very appropriate for anisotropic remeshing strategies, like the ones needed to resolve the highly directional solutions of interest in this work involving cohesive surfaces.

These plans are being supported by a continuing grant from the Computational Mechanics Programs of the ONR, with starting date of June 1, 2000. This continued support is gratefully acknowledged. We believe that the combination of all these results will lead to powerful novel computational tools, with the sound theoretical basis necessary for the analysis of the complex practical problems of interest to the Navy.

## 5. Outline of the Rest the Report

After presenting a complete list of the publications prepared under the support of the ONR and the invited lectures, conference contributions, organized symposia and edited special issues by the P.I. on the research concerning this project, we present in different appendices a summary of the technical results obtained in this grant. More specifically, we present the following four appendices:

- I. Large scale modeling of localized dissipative mechanisms in a local continuum.
- II. Analysis of strong discontinuities under fully coupled thermomechanical conditions.
- III. Analysis of strong discontinuities in poroplasticity.
- IV. An ALE finite element method for finite strain plasticity

As summarized in the following sections, these appendices describe the main results related to the main objectives of the project as identified in the original proposal. No discussion is made of a number of additional important results obtained in this project, including the formulation of coupled damage plastic models and their numerical integration, finite strain multiplicative poroplasticity and its numerical integration, enhanced finite element methods for finite deformation problems, and the development of globally convergent closest-point projection algorithms for elastoplasticity. We refer to the different publications presenting these results as indicated in previous sections.

### 5.1. Appendix I: Large scale modeling of localized dissipative mechanisms in a local continuum

This appendix presents a general framework for the formulation of constitutive models that incorporate a localized dissipative mechanism. The formalism of strong discontinuities is employed, allowing for the decoupling of the constitutive characterization of the

continuum and localized responses of the material. A procedure for incorporating the localized small scale effects of the material response in the large scale problem characterized by the standard local continuum is described in detail. The resulting large scale model is able to capture objectively the localized dissipation observed in localized failures of solids and structures. A localized viscous slip model is presented as a model example. The finite element implementation of the proposed formulation arises naturally as a local element enhancement of the finite element interpolations, with no regularization of the discontinuities. The above considerations are formulated first in the infinitesimal range, and then extended to the finite strain regime. Furthermore, it is shown that the proposed framework allows the development of effective finite element methods capturing in the large scale the localized dissipation observed in the failure of rate-dependent materials, avoiding the resolution of small length scales associated to the localization bands in these regularized models. Several representative numerical simulations are presented to illustrate these ideas.

## 5.2. Appendix II: Analysis of strong discontinuities under fully coupled thermomechanical conditions

This appendix begins with a study of the characteristics of failure of an one-dimensional shear layer with thermomechanical softening behavior. The linearized spectral analysis of the problem involving a local continuum with strain softening is presented first. More specifically, the stability and well-posedness of the resulting boundary value problem is analyzed, identifying the ill-posedness of the local continuum model under certain conditions, most notably, in the inviscid strain-softening case. The lack of an internal length scale associated to the strain localization is concluded. The implications of this analysis for the finite element simulations in the form of pathological mesh-size dependent solutions are also investigated. Next, it is shown that the incorporation of a localized dissipative mechanism in the form of a strong discontinuity avoids the ill-posedness of the original continuum problem. This is done by obtaining the closed-form solutions of the dynamic problem under investigation, showing the uniqueness and continuous dependence of the solution on the data. An analysis of the finite element solutions incorporating the effects of these discontinuous solutions is also included. This analysis reveals, in particular, the effects of thermal softening and its interaction with spatial discretization of the problem. To verify the conclusions drawn from these analyses, finite element simulations are presented and discussed. Finally, extensions to general multi dimensional problems are discussed. An analysis of strong discontinuities is presented in the context of coupled thermoplasticity, characterizing the singular strain and dissipation fields associated with the localized plastic flow along the discontinuities. The implementation of these effects in the context of enhanced finite element methods is discussed. Several representative numerical simulations are presented to illustrate the performance of the proposed methodology.

### 5.3. Appendix III: Analysis of strong discontinuities in poroplasticity

We present in this appendix an analysis of strong discontinuities in fully saturated porous media in the infinitesimal range. In particular, we describe the incorporation of the local effects of surfaces of discontinuity in the displacement field, and thus the singular distributions of the associated strains, from a local constitutive level to the large scale problem characterizing the quasi-static equilibrium of the solid. The characterization of the flow of the fluid through the porous space is accomplished in this context by means of a localized (singular) distribution of the fluid content, that is, involving a regular fluid mass distribution per unit volume and a fluid mass per unit area of the discontinuity surfaces in the small scale of the material. This framework is shown to be consistent with a local continuum model of coupled poroplasticity, with the localized fluid content arising from the dilatancy associated with the strong discontinuities. More generally, complete stress-displacement-fluid content relations are obtained along the discontinuities, thus identifying the localized dissipative mechanisms characteristic of localized failures of porous materials. The proposed framework also involves the coupled equation of conservation of fluid mass and seepage through the porous solid via Darcy's law, and considers a continuous pressure field with discontinuous gradients, thus leading to discontinuous fluid flow vectors across the strong discontinuities. All these developments are then examined in detail for the model problem of a saturated shear layer of a dilatant material. In particular, enhanced finite element methods are developed for this particular problem. The finite elements accommodate the localized fields described above at the element level. Several representative numerical simulations are presented to illustrate the performance of the proposed methods.

### 5.4. Appendix IV: An ALE finite element method for finite strain plasticity

This appendix presents an implicit Arbitrary Lagrangian-Eulerian (ALE) finite element formulation for solid mechanics. The interest in this work lies in the consideration of finite strain elastoplasticity based on a multiplicative decomposition of the deformation gradient in an elastic and plastic part, and the use of an hyperelastic relation for the stresses in terms of the elastic part. This situation is to be contrasted with typical ALE treatments found in the literature based on rate (hypoelastic) forms of the governing equations. In contrast with more classical approaches, the ALE approach presented herein considers the direct use and interpolation of the material motion with respect to the reference mesh. This aspect leads to a considerable simplification of the numerical resolution of the advection of the plastic internal variables. In fact, this advection is accomplished through a simple particle tracking scheme based on the connectivity graph of the reference mesh, avoiding the use of more complex strategies for the solution of the pure advection equation. These ideas are implemented in an efficient staggered framework, involving a Lagrangian step, a material remap, and the aforementioned advection of the plastic internal variables. Representative numerical simulations are presented to assess the performance of the proposed formulation. Both quasi-static and fully dynamic problems are considered.

## **Publications under ONR support**

### **1. REFEREED PUBLICATIONS**

#### **1.1. Articles in archival journals**

- [1] Armero, F. and Pérez-Foguet, A. [2000], "On the Formulation of Closest-Point Projection Algorithms in Elastoplasticity. Part I: The Variational Structure," submitted to *International Journal of Numerical Methods in Engineering*.
- [2] Pérez-Foguet, A. and Armero, F. [2000], "On the Formulation of Closest-Point Projection Algorithms in Elastoplasticity. Part II: Globally Convergent Schemes," submitted to *International Journal of Numerical Methods in Engineering*.
- [3] Armero, F. and Park, J.G. [1999] "An Analysis of Wave Propagation in a Softening Shear Layer under Fully Coupled Thermo-Mechanical Conditions," to be submitted to *International Journal of Solids and Structures* (see Appendix II of this report).
- [4] Armero, F. and Love, E. [2000] "An Arbitrary Eulerian-Lagrangian (ALE) Finite Element Method for Finite Strain Elastoplasticity," to be submitted to *International Journal of Numerical Methods in Engineering* (see Appendix IV of this report).
- [5] Armero, F. and Oller, S. [1999], "A General Framework for Continuum Damage Models. Part II: Integration Algorithms, with Applications to the Numerical Simulation of Porous Metals," *International Journal of Solids and Structures*, in press.
- [6] Armero, F. and Oller, S. [1999], "A General Framework for Continuum Damage Models. Part I: Infinitesimal Plastic Damage Models in Stress Space," *International Journal of Solids and Structures*, in press.
- [7] Armero, F. [2000], "On the Locking and Stability of Finite Elements in Finite Deformation Plane Strain Problems," *Computers & Structures*, 75, 261-290.
- [8] Armero, F. and Callari, C. [1999], "An Analysis of Strong Discontinuities in a Saturated Poro-Plastic Solid," *Int. J. Numerical Methods in Engineering*, 46, 1673-1698.
- [9] Armero, F. [1999], "Formulation and Finite Element Implementation of a Multiplicative Model of Coupled Poro-Plasticity at Finite Strains under Fully Saturated Conditions," *Computer Methods in Applied Mechanics and Engineering*, 171, 205-241.
- [10] Armero, F. [1999], "Large-Scale Modeling of Localized Dissipative Mechanisms in a Local Continuum: Applications to the Numerical Simulation of Strain Localization in Rate-Dependent Inelastic Models," *Mechanics of Cohesive-Frictional Materials*, 4, 101-132.

- [11] Armero, F. [1999], "On the Characterization of Localized Solutions in Inelastic Solids: An Analysis of Wave Propagation in a Softening Bar," submitted to *Computer Methods in Applied Mechanics and Engineering*.
- [12] Glaser, S. and Armero, F. [1997], "On the Formulation of Enhanced Strain Finite Elements in Finite Deformations," *Engineering Computations*, 14, 759-791.

## 1.2. Conference proceedings

- [13] Perez-Foguet, A. and Armero, F. [2000] "Globally Convergent Closest-Point Projection Algorithms in Elastoplasticity," European Congress on Computational Methods in Applied Sciences and Engineering, ECCOMAS 2000, Barcelona, Spain, September 2000.
- [14] Armero, F. and Callari, C. [1998] "Strong Discontinuities in Fully Saturated Porous Media," Computational Mechanics, Proc. IV WCCM, ed by S. Idelsohn, E. Onate and E. Dvorkin, Buenos Aires, 1998.
- [15] Armero, F. [1997] "Localized Anisotropic Damage of Brittle Materials," Proc. Computational Plasticity Conf., COMPLAS V, ed. by D.R.J Owen, E. Onate and E. Hinton, Barcelona, 1997.

## 2. NON-REFEREED PUBLICATIONS

### 2.1. Technical reports

- [16] Love, E. [2000] *Arbitrary Lagrangian-Eulerian Finite Element Methods in Finite Strain Plasticity*, PhD Dissertation, UC Berkeley, August 2000.
- [17] Armero, F. and Love, E. [2000] "An Arbitrary Eulerian-Lagrangian (ALE) Finite Element Method for Finite Strain Elastoplasticity," UCB-SEMM Report no. 2000/04 (to be submitted to *International Journal of Numerical Methods in Engineering*, see list above).
- [18] Armero, F. and Pérez-Foguet, A. [2000], "On the Formulation of Closest-Point Projection Algorithms in Elastoplasticity. Part I: The Variational Structure," UCB Report no. UCB/SEMM-2000/01, UC Berkeley (submitted to *International Journal of Numerical Methods in Engineering*, see list above).
- [19] Pérez-Foguet, A. and Armero, F. [2000], "On the Formulation of Closest-Point Projection Algorithms in Elastoplasticity. Part II: Globally Convergent Schemes," UCB Report no. UCB/SEMM-2000/02, UC Berkeley (submitted to *International Journal of Numerical Methods in Engineering*, see list above).

- [20] Armero, F. and Oller, S. [1999], "A General Framework for Continuum Damage Models. Part II: Integration Algorithms, with Applications to the Numerical Simulation of Porous Metals," UCB Report no. UCB/SEMM-99/09, University of California at Berkeley. (revised version accepted in *International Journal of Solids and Structures*, see list above).
- [21] Armero, F. and Oller, S. [1999], "A General Framework for Continuum Damage Models. Part I: Infinitesimal Plastic Damage Models in Stress Space," UCB Report no. UCB/SEMM-99/07, University of California at Berkeley. (revised version accepted in *International Journal of Solids and Structures*, see list above).
- [22] Armero, F. and Park, J.G. [1998] "An Analysis of Wave Propagation in a Softening Shear Layer: the Thermo-Mechanical Case," Report no. UCB/SEMM 98/12, University of California at Berkeley.
- [23] Armero, F. and Callari, C. [1998], "An Analysis of Strong Discontinuities in a Saturated Poro-Plastic Solid," Report Report no. UCB/SEMM-98/11, University of California at Berkeley (revised version appeared in *International Journal for Numerical Methods in Engineering*, see list above).
- [24] Armero, F. [1998], "Formulation and Finite Element Implementation of a Multiplicative Model of Coupled Poro-Plasticity at Finite Strains under Fully Saturated Conditions," Report no. UCB/SEMM 98/05, University of California at Berkeley (revised version appeared in *Computer Methods in Applied Mechanics and Engineering*, see list above).
- [25] Armero, F. [1997], "On the Characterization of Localized Solutions in Inelastic Solids: An Analysis of Wave Propagation in a Softening Bar," Report no. UCB/SEMM 97/18, University of California at Berkeley (revised version to appear in *Computer Methods in Applied Mechanics and Engineering*, see list above).
- [26] Armero, F. [1997] "Additional Results on the Modal Analysis of Finite Elements for Finite Deformation Problems: Classical and Stabilized Formulations," Report no. UCB/SEMM 97/15, University of California at Berkeley.
- [27] Armero, F. [1997], "Large-Scale Modeling of Localized Dissipative Mechanisms in a Local Continuum: Applications to the Numerical Simulation of Strain Localization in Rate-Dependent Inelastic Models," Report no. UCB/SEMM 97/12, University of California at Berkeley (revised version appeared in *Mechanics of Cohesive-Frictional Materials*, see list above).
- [28] Armero, F. [1997], "Formulation and Numerical Analysis of an Anisotropic Damage Model with a Localized Dissipative Mechanism," Report no. UCB/SEMM 97/11, University of California at Berkeley.
- [29] Armero, F. [1996] "A Modal Analysis of Finite Deformation Enhanced Strain Finite

- Elements," Report no. UCB/SEMM 96/03, University of California at Berkeley.
- [30] Glaser, S. and Armero, F. [1995] "Recent Developments in the Formulation of Assumed Enhanced Strain Finite Elements for Finite Deformation Problems," Report no. UCB/SEMM 95/13, University of California at Berkeley.

## 2.2. Conference proceedings

- [31] Armero, F. and Li, S. [1998] "Numerical Simulation of Anisotropic Damage at Finite Strains," Proc. 12th ASCE Eng. Mech. Conf., La Jolla, CA, May 1998.
- [32] Armero, F. and Glaser, S. [1996] "Enhanced Strain Finite Element Methods for Finite Deformation Problems," Proc. of III Congress of SEMMI, Zaragoza, Spain.
- [33] Armero, F. and Garikipati, K. [1996], "An Analysis of Strong-Discontinuities in Inelastic Solids with Applications to the Finite Element Simulation of Strain Localization Problems," Proc. ASCE Engineering Mechanics Conf., Fort Lauderdale, 1996.

**Invited Lectures, Conference Contributions,**  
**Organized Symposia and Edited Special Issues**

(Based on the research supported by the ONR)

**1. Invited papers and other conference contributions**

1. "A New Framework for the Development of Damage Models at Large Strains," invited contribution, European Conference on Computational Mechanics ECCM'99, Munich, Germany, September 1999.
2. "A General Framework for Damage Theories and its Application to the Numerical Simulation of Failure," invited contribution, V US National Congress on Computational Mechanics, Boulder CO, August 1999.
3. "Formulation and Numerical Simulation of Anisotropic Damage at Finite Strains," invited contribution, keynote, IV World Congress on Computational Mechanics, Buenos Aires, Argentina, June 29-July 2, 1998.
4. "Strong Discontinuities in Fully Saturated Porous Media," invited contribution, IV World Congress on Computational Mechanics, Buenos Aires, Argentina, June 29-July 2, 1998.
5. "On the Stability of Finite Element Formulations in Finite Deformation Elastoplasticity," invited contribution, IV World Congress on Computational Mechanics, Buenos Aires, Argentina, June 29-July 2, 1998.
6. "Numerical Simulation of Anisotropic Damage at Finite Strains," invited contribution, 12<sup>th</sup> ASCE Engineering Mechanics Conference, La Jolla, May 18-20, 1998.
7. "Analysis and Numerical Simulation of Discontinuous Solutions in Inelastic Solids under Dynamic Conditions," invited contribution, 1997 ASME International Mechanical Engineering Congress and Exposition, Dallas, November 16-21, 1997.
8. "On the Analysis of Strain Localization in Inelastic Solids," Keynote Address, XVIII Latin-American Conference of Computational Methods in Engineering (XVIII CIL-AMCE), Brasilia, Brasil, October 27-29 1997.
9. "Some Results on the Formulation of Enhanced Strain Finite Elements for Finite Deformation Elastoplastic Problems," invited plenary lecture, Euromech Colloquium 371, Bad Herrenalb, Germany, September 17-19 1997.
10. "Formulation and Numerical Analysis of a Coupled Model of the Fluid Flow in a Nonlinear Porous Solid," invited contribution, 4<sup>th</sup> US National Congress on Computational Mechanics, San Francisco CA, August 6-8 1997.

11. "Formulation and Numerical Simulation of a Localized Mixed Mode Damage Model" 4<sup>th</sup> US National Congress on Computational Mechanics, San Francisco CA, August 6-8 1997.
12. "On the Theoretical and Numerical Characterization of Discontinuous Solutions in Inelastic Solids," invited contribution, McNU'97, Joint Summer Meeting of ASCE/ASME/SES, Northwestern University, June 29 to July 2 1997.
13. "Localized Anisotropic Damage of Brittle Materials," invited contribution, *Fifth Int. Computational Plasticity Conf., COMPLAS V*, Barcelona, Spain, March 17-20 1997.
14. "Enhanced Strain Finite Element Methods for Finite Deformation Problems," *III Congress of SEMMI*, Zaragoza, Spain, June 3-6 1996.
15. "An Analysis of Strong-Discontinuities in Inelastic Solids with Applications to the Finite Element Simulation of Strain Localization Problems," invited contribution, *ASCE Engineering Mechanics Conf.*, Fort Lauderdale, May 19-22 1996.

## 2. Invited lectures, seminars.

1. "On the Locking and Stability of Finite Elements," invited lecture, Applied Mathematics Seminar, Universitat Politecnica de Catalunya, Barcelona, Spain, July 5, 1999.
2. "Numerical Analysis of Strain Localization Problems," invited lecture, Computational Mechanics Seminar, Universidad de Buenos Aires, Argentina, June 5, 1997.
3. "Formulation and Numerical Analysis of Continuum Models Exhibiting a Localized Damage Mechanism," invited lecture, Civil Engineering Seminar, Universidad Nacional de Tucuman, Tucuman, Argentina, June 3, 1997.
4. "On the Formulation of Enhanced Strain Finite Element Methods," invited lecture, Civil Engineering Seminar, Universidad Nacional de Tucuman, Tucuman, Argentina, June 2, 1997.
5. "On the Formulation and Numerical Analysis of Constitutive Models of Solids that Exhibit a Localized Dissipative Mechanism," invited lecture, Civil Engineering Seminar, California Institute of Technology, May 15, 1997.
6. "On the Locking of Standard Finite Element Methods and the Enhanced Strain Formulation," invited lecture, Mechanical Engineering Seminar, ITT, Universidad Pontificia de Comillas, Madrid, Spain, June 17, 1996.

**3. Technical courses.**

1. "Finite Element Methods for Nonlinear Problems," invited course (16 hours) given at the Universidad Nacional del Cuyo, Mendoza, Argentina, May 26-30, 1997.

**4. Attendance to contractors meetings.**

1. "Computational Methods for the Analysis of Failure in Inelastic Solids," ONR Computational Mechanics Program Workshop, Arlington VA, May 22-25, 2000.
2. "Localized Failure of Inelastic Solids: Analysis and Numerical Resolution," ONR Solid Mechanics Program Workshop, Naval Surface Warfare Center, Carderock MD, April 28-30, 1999.
3. "Analysis and Numerical Simulation of Localized Failures in Inelastic Solids," ONR Computational Mechanics Program Workshop, Boulder CO, January 4-6, 1999.
4. "On the Characterization and Numerical Simulation of Localized Dissipative Mechanisms in Inelastic Solids," ONR Computational Mechanics Program Review, San Diego CA, January 27-29, 1998.
5. "Numerical Analysis of Strain Localization in Inelastic Solids," ONR Computational Mechanics Program Review, The University of Texas, Austin, Texas, February 18-21, 1997.

**5. Symposia and other technical meetings organized by the P.I.**

1. Symposium "Computational Failure Mechanics,[ 5<sup>th</sup> US National Congress on Computational Mechanics, Boulder CO, August 3-7 1999 (total of 30 contributions).
2. Symposium "Numerical Analysis of Strain Localization in Inelastic Solids," at the IV World Congress on Computational Mechanics, Buenos Aires, Argentina, June 29-July 2, 1998 (total of 20 contributions).
3. Symposium "High-Performance Finite Elements in Nonlinear Solid Mechanics," co-organized with Professor E.N. Dvorkin, at the IV World Congress on Computational Mechanics, Buenos Aires, Argentina, June 29-July 2, 1998 (total of 11 contributions).
4. Symposium "Computational Methods for Predicting and Simulating Failure," ASCE 12th Engineering Mechanics Conference, La Jolla, CA May 17-20, 1998; session on behalf of the ASCE Inelastic Behavior Committee (total of 5 contributions).
5. Symposium "Second Symposium Recognizing the Contributions of Juan C. Simo," 4<sup>th</sup> US National Congress on Computational Mechanics, San Francisco CA, August 6-8 1997 (total of 40 contributions).

6. Symposium "The Theory and Prediction of Localized Failures in Materials," McNU'97, Joint Summer Meeting of ASCE/ASME/SES, Northwestern University, June 29 to July 2 1997 (total of 28 contributions).

**6. Special issues edited by the P.I. in technical journals.**

1. Special issue on "Computational Failure Mechanics," *International Journal of Solids and Structures*, in press.
2. Special issue on "Finite Elements for Nonlinear Solid Mechanics," in *Computers & Structures*, vol. 75, no. 3, March 2000.
3. Special issue on "The Theory and Prediction of Localized Failure in Materials," in the *Mechanics of Cohesive-Frictional Materials*, vol. 4, no. 2, March 1999.

## **APPENDIX I**

### **Large-Scale Modeling of Localized Dissipative Mechanisms in a Local Continuum**

**Based on the paper:**

Armero, F. [1999], "Large-Scale Modeling of Localized Dissipative Mechanisms in a Local Continuum: Applications to the Numerical Simulation of Strain Localization in Rate-Dependent Inelastic Models," *Mechanics of Cohesive-Frictional Materials*, 4, 101-132.

## I.1. Introduction

Highly localized patterns of the deformation in the form of bands are often observed preceding the failure of solids and structures. Characteristic examples are shear bands in metals (see e.g. NEEDLEMAN & TVERGAARD [1984], and references therein) and soils (see e.g. VARDOULAKIS [1978]), or the localization bands of cracking in brittle materials like concrete or rocks (see e.g. READ & HEGEMEIER [1984], and references therein), among many other representative articles. An overall softening response of the solid leading to its final failure is often observed accompanying this phenomenon. The small scale associated to these bands, compared to the large-scale response of the solid or structure, is to be noted. For example, shear bands of order of microns can be found in metals (BAI & DODD [1992]) or of order of millimeters (MUHLHAUS & VARDOULAKIS [1987]) in the case of soils, whereas characteristic lengths of typical applications are of the order of meters, or even kilometers in geological problems. In this way, the smooth pattern of the deformation of the solid previous to the appearance of strain localization gives rise to highly non-smooth solutions with *localized dissipative mechanisms* in the small scale, especially when observed from the large structural scale. The practical importance of capturing these localization modes while solving the large-scale (structural) problem is clear.

Classical (local) rate-independent constitutive models are known to lack an internal characteristic length, thus leaving undefined the small scales associated to the localized solution. Furthermore, the introduction of strain-softening in the local continuum is known to lead to inconsistencies in the resulting mechanical models. The classical work of THOMAS [1961], HILL [1962] and MANDEL [1966], and the more recent analyses in RICE [1976], OTTOSEN & RUNESSON [1991] and NEILSEN & SCHREYER [1993], among others, have identified the ill-posedness of problems involving a continuum with strain-softening. The leading part of the governing equations (the tangent operator) loses ellipticity, resulting in a change of type of the boundary value problem. The reader is referred also to the illustrative dynamic analysis of a one dimensional rod presented in BAZANT & BELYTSCHKO [1985]. Briefly, these inconsistencies can be traced back again to the lack of an internal characteristic length defining a material volume where the energy dissipation per unit volume imposed by a softening stress/strain relation can take place. As a consequence, the finite element solutions obtained in this context exhibit the well-known pathological dependence on the mesh size; see e.g. TVERGAARD et al. [1981], and PIETRSZCZAK & MRÓZ [1981], among many others.

Mathematical analyses of the perfectly plastic rate-independent problem (see JOHNSON [1976], MATTHIES et al [1979], SUQUET [1981], and TEMAM [1984], among others) have identified the existence of non-smooth solutions involving discontinuous displacement fields, the so-called *strong discontinuities*, thus reproducing the highly non-homogeneous states of strain associated to the localized deformations. The observation that perfect plasticity defines a hyperbolic boundary value problem goes back to PRANDTL [1920], and leads to the classical slip line theory of rigid-plasticity. The slip lines define in this context

possible surfaces of discontinuity of the displacement field, identifying the failure mechanism of the solid; see e.g. the accounts in HILL [1950] or LUBLINER [1990], among others. The introduction of a localized dissipative mechanism along these discontinuities, through a stress/displacement relation as in the so-called discrete crack approaches of cracking in concrete (see HILLERBORG et al [1976]), is required for the proper characterization of the final localized failure of the material. The formulation of a general framework that incorporates these localized effects in the local continuum is the first objective of the present work.

The identification of these inconsistencies has motivated the formulation of many regularization techniques to avoid the associated difficulties. The main idea in these regularized formulations is the incorporation of internal length scales in the constitutive model. We can find along these lines the formulation of non-local models defining the constitutive relations at one point through the state of deformation in a finite neighborhood of it (see e.g. BAZANT et al [1984]); higher-gradient models incorporating higher order effects in the local constitutive relation, leading to higher order boundary value problems (see e.g. COLEMAN & HODGON [1985]); and the consideration of Cosserat continua accommodating rotational degrees of freedom and, hence, defining a length scale when related to the displacement field (see e.g. DEBORST & SLUYS [1991]), to mention just some few representative references.

Similarly, it is known that rate-dependent models introduce a length scale in the constitutive relation, even in the local continuum framework; see e.g. NEEDLEMAN [1988]. More precisely, the presence of a material viscosity defines a characteristic material time that together with the existence of a characteristic velocity in dynamic problems leads to the appearance of a length scale. The boundary-value problem remains well-posed (i.e., no change of type occurs). The onset of strain localization has been related in this case to the appearance of unstable (growing in time) modes in a spectral analysis of the linearized equations of motion. See MOLINARI & CLIFTON [1987] and references therein for complete details of these ideas. The well-posedness of the problem still holds in the quasi-static limit, but then the presence of imperfections highly influences the final localized solution. See NEEDLEMAN [1988] and BELYTSCHKO et al [1991], among others.

The common idea behind all these regularized approaches is the introduction of the small length scales characterizing the localized solutions. Consequently, the regularization will be effective if these small length scales are resolved by the tools employed in the analysis, e.g., the spatial discretization employed in their numerical simulation. The appropriateness of this approach is clear when the main objective is the understanding the details of the localized mechanisms that appear in the small scale of the material response. The multi-scale character of the problem needs to be brought up again. In this context, it may be difficult to motivate complex detailed analyses when the large-scale response of the structural system is the main objective. The issue is not only of computational cost, but also the appropriateness of maintaining standard formulations of the mechanical

problem in stages previous to the failure of the structure and in the large scale, away from the localized deformation patterns, where traditional numerical techniques are known to perform well.

The considerations above identify the need for the formulation of constitutive models that capture the localized dissipation observed in the failure of solids while maintaining the local continuum framework of the large scale. In this context, the goals of the work presented herein are twofold. The first objective is the formulation of a large-scale model that incorporates localized dissipative mechanisms, but treat the small scales associated to strain localization as unresolvable otherwise. The second goal is then the formulation of numerical methods (finite element methods, in particular) that implement these ideas and are able to capture these highly non-smooth solutions accurately. In particular, it is our goal to develop numerical techniques that capture effectively the localized dissipation of regularized rate-dependent models without the need of resolving the associated small length scales. One can talk in this last case of the “large-scale regularization of regularized models.”

Early attempts of the formulation of large-scale model capturing the localized dissipative effects can be traced back to smeared crack models of the cracking of concrete. See e.g. BAZANT & OH [1983] and ROTS et al [1985], among others. In this context, the formulation of continuum models capturing objectively the localized energy dissipation is accomplished through the proper definition of the softening law depending on the mesh size employed in the finite element analysis. In this way, the so-called *characteristic length* is introduced in the formulation of the mechanical model; see e.g. PIETRSZCZAK & MRÓZ [1981] and OLIVER [1989]. Related approaches can be found in the formulation of finite elements involving a-priori defined internal length scales as in BELYTSCHKO et al [1988].

The analysis of strong discontinuities in inelastic continuum models has been presented in SIMO et al [1993], ARMERO & GARIKIPATI [1995,96], and OLIVER [1996]. The extension of these analyses to the finite strain range has been presented in ARMERO & GARIKIPATI [1996]. See also LARSSON & RUNESSON [1996] for a related approach involving a regularized discontinuity. The formulation of locally enhanced finite elements with regularized discontinuities can be found in SIMO et al [1993], and OLIVER [1996], with the limit case involving no regularization presented in ARMERO & GARIKIPATI [1995,96] for elastoplastic models, and ARMERO [1997b] for damage models of cracking. Finite elements incorporating embedded localization lines have been also presented in DVORKIN et al. [1990]. The related approach presented in ORTIZ et al [1987] and NACAR et al [1989], involving also a local enhancement of the finite element interpolation with discontinuous displacements but with no added dissipative mechanism, can also be mentioned.

We present in this paper a general framework for the characterization of the dissipative mechanisms that appear in the failure of solids. The singular fields associated with strong discontinuities are introduced *locally* in a neighborhood of a continuum solid. This formalism allows a full decoupling of the characterization of the bulk and localized response of

the material. Both responses are then modeled independently, with the localized contributions involving a stress/displacement relation that dissipates energy objectively. No length scales are required at this stage. It is the incorporation of these local effects in the large-scale problem, involving smooth fields, that identifies the length scale characteristic of the problem. The limit of vanishing small scales (the large-scale limit) is then taken, leading to a large-scale model involving a local continuum that captures correctly the localized dissipation in the solid. Furthermore, this constructive incorporation of the small-scale effects in the large-scale problem allows not only for the simple numerical implementation of these ideas through a local enhancement of the finite element interpolations, but also for the formulation of the large-scale regularization of rate-dependent models. The numerical implementation of the latter involves the correct scaling of the localized dissipative mechanism along the strong discontinuity, thus capturing the proper dissipation depending on the degree of resolution of the small scales by the assumed spatial discretization. The developments considered herein focus on elastoplastic models characteristic of ductile materials, in both the infinitesimal and finite deformation ranges. The formulation of large-scale models incorporating the localized damage mechanism characteristic of brittle materials can be found in ARMERO [1997b].

An outline of the rest of the paper is as follows. Section I.2 describes the large-scale problem of interest in this work, consisting of the principle of virtual work with the standard regularity assumptions. The infinitesimal case is considered. Section I.3 develops the constitutive modeling of localized dissipative mechanism in the small scale of the material characterized by a local neighborhood of a given material point. These mechanisms are characterized by the singular fields of strong discontinuities, with their constitutive modeling fully characterized in a thermodynamical framework based on the principle of maximum plastic dissipation. Section I.4 effectively bridges the two problems, the small and large scale problems, leading in the large scale limit to a consistent formulation of the local continuum that captures the dissipative effects identified previously in the small scales. The proposed approach is then used for the formulation of the large-scale regularization of rate-dependent models in Section I.4.2, and the formulation of finite element methods incorporating these ideas in Section I.4.3. The extension of all these considerations to the finite strain range in Section I.5. Representative numerical simulations are presented in Section I.6 to assess the performance of the proposed finite element formulations. Finally, Section I.7 concludes with some final remarks.

## I.2. The Large-Scale Problem

This section summarizes the equations governing the large-scale mechanical problem, in the weak form of interest for the development of finite element methods as presented in Section I.6. Regardless of the details particular to the constitutive model defined in Section 3, the equations for the large-scale problem as assumed in this section retain the usual smoothness properties.

Let a domain  $\Omega \subset \mathbb{R}^{n_{\text{dim}}}$  ( $n_{\text{dim}} = 1, 2$  or  $3$ ) define the reference placement of a solid body, identified with its current placement under the assumption of infinitesimal strains assumed in this section. Extensions to the finite deformation case are considered in Section I.5. We denote by  $\mathbf{u} : \Omega \times [0, T] \rightarrow \mathbb{R}^{n_{\text{dim}}}$  the displacement field  $\mathbf{u}(\mathbf{x}, t)$  in a certain time interval  $T$ . This displacement field is imposed to satisfy the essential boundary conditions

$$\mathbf{u} = \bar{\mathbf{g}} \quad \text{on } \partial_u \Omega , \quad (\text{I.2.1})$$

for some specified function  $\bar{\mathbf{g}}$  in part of the boundary  $\partial_u \Omega \subset \partial \Omega$ . We define the space of admissible displacement variations

$$\mathcal{V} = \left\{ \boldsymbol{\eta} : \Omega \rightarrow \mathbb{R}^{n_{\text{dim}}} : \boldsymbol{\eta} = 0 \quad \text{on} \quad \partial_u \Omega \right\} , \quad (\text{I.2.2})$$

that is, satisfying homogeneous boundary conditions on  $\partial_u \Omega$  where the displacement field is imposed. Standard regularity conditions are assumed for the displacement fields  $\boldsymbol{\eta} \in \mathcal{V}$ , the motivation being the tools of analysis available. In particular, the assumed large-scale fields can be easily resolved by standard techniques of finite element analysis, as illustrated in Section I.4.3. Additional contributions due to the specific response of the material (e.g., discontinuities) are introduced in Section I.3.

The infinitesimal *large-scale strains* are obtained as

$$\boldsymbol{\varepsilon}(\mathbf{u}) := \nabla^s \mathbf{u} := \frac{1}{2} [\nabla \mathbf{u} + (\nabla \mathbf{u})^T] , \quad (\text{I.2.3})$$

with  $(\cdot)^T$  denoting the matrix transpose. Let  $\boldsymbol{\sigma} = \boldsymbol{\sigma}(\mathbf{x}) \in \mathbb{R}^{n_{\text{dim}} \times n_{\text{dim}}}$  (symmetric) be the stress field in the solid. We denote the applied body force by  $\mathbf{b} : \Omega \rightarrow \mathbb{R}^{n_{\text{dim}}}$  (per unit mass) and the imposed boundary tractions by  $\bar{\mathbf{t}} : \partial_T \Omega \rightarrow \mathbb{R}^{n_{\text{dim}}}$  acting on the part  $\partial_T \Omega \subset \partial \Omega$  of the boundary of the solid. The usual assumptions

$$\partial_u \Omega \cap \partial_T \Omega = \emptyset \quad \text{and} \quad \overline{\partial_u \Omega \cup \partial_T \Omega} = \partial \Omega , \quad (\text{I.2.4})$$

in each of the  $n_{\text{dim}}$  components of the displacement/traction are assumed for a well-posed problem. See Figure I.3.1 for an illustration. Finally, we denote by  $\ddot{\mathbf{u}} := d^2 \mathbf{u} / dt^2$  and by  $\rho_o$  the acceleration and the reference density of the solid, respectively.

The large-scale problem of the mechanical initial boundary value problem can then be written as

**The Infinitesimal Large Scale Problem.** Find  $\mathbf{u} \in \mathcal{V} + \bar{\mathbf{g}}$  satisfying

$$\int_{\Omega} \rho_o \ddot{\mathbf{u}} \cdot \boldsymbol{\eta} \, d\Omega + \int_{\Omega} \boldsymbol{\sigma} : \nabla^s \boldsymbol{\eta} \, d\Omega = \int_{\Omega} \rho_o \mathbf{b} \cdot \boldsymbol{\eta} \, d\Omega + \int_{\partial_T \Omega} \bar{\mathbf{t}} \cdot \boldsymbol{\eta} \, d\Gamma \quad \forall \boldsymbol{\eta} \in \mathcal{V} , \quad (\text{I.2.5})$$

where the stress field  $\boldsymbol{\sigma}$  is given by the constitutive model developed in the following section, and for given initial conditions  $\mathbf{u}(\mathbf{x}, 0) = \mathbf{u}_o(\mathbf{x})$  and  $\dot{\mathbf{u}}(\mathbf{x}, 0) = \mathbf{v}_o(\mathbf{x})$  in the displacements and velocities, respectively.  $\square$

A standard argument based on the weak form (I.2.5) of the equilibrium equations shows the continuity of tractions for a given orientation defined by a unit vector  $\mathbf{n}$ . Indeed, let  $\Gamma$  be a generic smooth *material* surface passing through a point  $\mathbf{x} \in \Omega$  with unit normal  $\mathbf{n}$ . Assume that the stress field  $\boldsymbol{\sigma}$  is smooth in each of the components that  $\Gamma$  defines in  $\Omega$ . Integration by parts of (I.2.5) under this assumption, and accounting for the internal surface  $\Gamma$  with unit normal  $\mathbf{n}$  at  $\mathbf{x} \in \Omega$  leads to the strong form of the balance of linear momentum equation and natural boundary conditions

$$\operatorname{div} \boldsymbol{\sigma} + \rho_o \mathbf{b} = 0 \quad \text{in } \Omega \setminus \Gamma , \quad (\text{I.2.6})$$

$$\boldsymbol{\sigma} \mathbf{n} = \bar{\mathbf{t}} \quad \text{on } \partial_T \Omega , \quad (\text{I.2.7})$$

together with the local form of the equilibrium across  $\Gamma$  given by

$$[\![\boldsymbol{\sigma}]\!] \mathbf{n} = 0 . \quad (\text{I.2.8})$$

where  $[\![\boldsymbol{\sigma}]\!]$  denotes the jump in the stress. Therefore, we have the well-defined vector

$$\mathbf{T}_\Gamma := \boldsymbol{\sigma} \mathbf{n} \Big|_\Gamma , \quad (\text{I.2.9})$$

the traction vector on  $\Gamma$  for all directions  $\mathbf{n}$ , where the restriction at  $\mathbf{x} \in \Gamma \subset \Omega$  is understood in this last formula.

### I.3. Characterization of Localized Dissipative Mechanisms in the Local Continuum

The previous section introduced the large-scale problem leaving undefined the constitutive relation between the stress and the strain fields. The assumed regularity of the large-scale displacements and corresponding strains may not incorporate all the effects observed in the response of the material. In this context, the main goal of this section is the characterization of a localized dissipative mechanism characterized by a discontinuity in the displacement field, a *strong discontinuity*. As discussed in the introduction, the consideration of non-smooth solutions describing the localized response of the material may be of practical use, even if the solutions are smooth but close to the limit situation of a singular strain field. These ideas are developed further in Section I.4 and illustrated in the numerical examples of Section I.6.

#### I.3.1. The kinematics of strong discontinuities

Let  $\Omega_x \subset \Omega$  be a local neighborhood of a material point  $\mathbf{x} \in \Omega$ , whose dimensions and full characterization will be considered in Section I.4. Our goal is to model the response of the material when it exhibits a localized dissipative mechanism at  $\mathbf{x}$ . As noted in

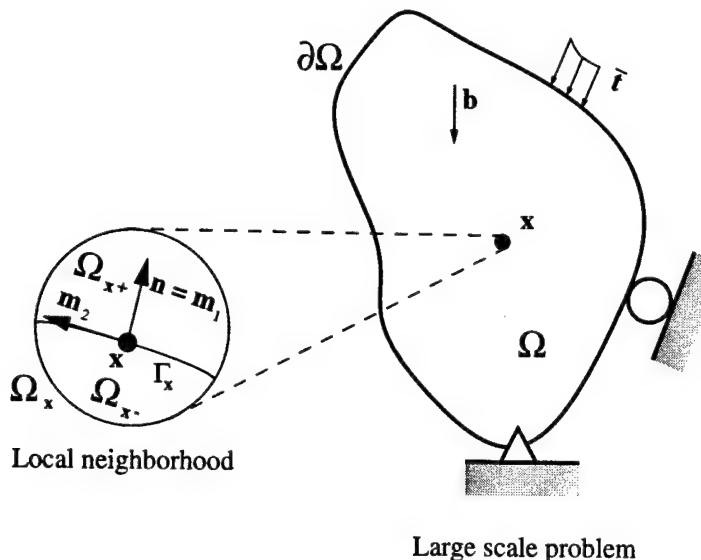


**FIGURE I.3.1** Large scale problem with standard boundary conditions. Definition of the local neighborhood  $\Omega_x \subset \Omega$  at a material point  $x$ , with the smooth surface  $\Gamma_x$  and the corresponding orthogonal reference system  $\{m_1 \equiv n, \dots, m_{n_{\text{dim}}}\}$  ( $n_{\text{dim}} = 2$  in the figure).

the introduction, we consider the large-scale limit characterized by the case of a strong discontinuity.

Assume the existence of a discontinuity in the displacement field across a surface  $\Gamma_x \subset \Omega_x$  passing through  $x \in \Omega_x$  with unit normal  $n$ . The discontinuous displacement field across the surface  $\Gamma_x$  can be written *locally in*  $\Omega_x$  using the decomposition

$$\mathbf{u}_\mu(\mathbf{y}) = \mathbf{u}(\mathbf{y}) + \boldsymbol{\xi}(\mathbf{y}) M_{\Gamma_x}(\mathbf{y}) \quad \mathbf{y} \in \Omega_x , \quad (\text{I.3.1})$$

where the function  $M_{\Gamma_x} : \Omega_x \rightarrow \mathbb{R}$  is smooth in  $\Omega_x \setminus \Gamma_x$  and is normalized to have a unit jump across the discontinuity  $\Gamma_x$ , that is,

$$[M_{\Gamma_x}] = 1 \quad \text{on } \Gamma_x . \quad (\text{I.3.2})$$

Let  $H_{\Gamma_x}$  denote the Heaviside function across  $\Gamma_x$ , defined by

$$H_{\Gamma_x}(\mathbf{y}) = \begin{cases} 1 & \mathbf{y} \in \Omega_{x+} , \\ 0 & \mathbf{y} \in \Omega_{x-} , \end{cases} \quad (\text{I.3.3})$$

where  $\Omega_{x+}$  and  $\Omega_{x-}$  denote each of the two connected components of the neighborhood  $\Omega_x$  defined by  $\Gamma_x$ ; see Figure I.3.1. Given the definition (I.3.3) of the Heaviside function, the function  $M_{\Gamma_x}$  can be written

$$M_{\Gamma_x} = H_{\Gamma_x} + N_x , \quad (\text{I.3.4})$$

for some smooth function  $N_x$  in  $\Omega_x$ . We note that no compatibility requirements between the displacement fields  $\mathbf{u}$  and  $\mathbf{u}_\mu$  are imposed a-priori on the local decomposition (I.3.1). The decomposition (I.3.1) is characteristic of the approach presented in SIMO et al [1993].

With these considerations the jump across  $\Gamma_x$  is given by

$$[\mathbf{u}_\mu] = \boldsymbol{\xi} . \quad (\text{I.3.5})$$

For later use, we introduce the space of displacement jumps

$$\mathcal{J} = \{\boldsymbol{\xi} : \Omega_x \rightarrow \mathbb{R}^{n_{\text{dim}}}\} , \quad (\text{I.3.6})$$

a smooth extension in  $\Omega_x$  of the displacement jump  $\boldsymbol{\xi}_x$  at  $x$  (i.e.,  $\boldsymbol{\xi}_x = \boldsymbol{\xi}(x)$ ). The displacement field  $\mathbf{u}_\mu : \Omega_x \rightarrow \mathbb{R}^{n_{\text{dim}}}$  defines the displacements observed locally in the small scale around the material point  $x$ , incorporating the localized effects of the assumed discontinuous solution.

The infinitesimal strains corresponding to the displacement (I.3.1) are given by

$$\boldsymbol{\varepsilon}_\mu := \nabla^s \mathbf{u}_\mu = \underbrace{\boldsymbol{\varepsilon}(\mathbf{u}) + \boldsymbol{\xi} \otimes \nabla^s N_x}_{\text{regular distribution}} + \underbrace{(\boldsymbol{\xi} \otimes \mathbf{n})^s \delta_{\Gamma_x}}_{\text{singular distribution}} \quad \text{in } \Omega_x , \quad (\text{I.3.7})$$

where the superscript  $s$  denotes the symmetric part. The singular part is expressed in terms of the singular distribution  $\delta_{\Gamma_x}$ , the Dirac delta across  $\Gamma_x$ , after using the classical result

$$\nabla H_{\Gamma_x} = \mathbf{n} \delta_{\Gamma_x} ; \quad (\text{I.3.8})$$

see STAKGOLD [1979] (page 100) for the mathematical details involved in the derivation of (I.3.8). We define

$$\bar{\boldsymbol{\varepsilon}}_\mu := \boldsymbol{\varepsilon}(\mathbf{u}) + (\boldsymbol{\xi} \otimes \nabla N_{\Gamma_x})^s + \nabla^s \boldsymbol{\xi} H_{\Gamma_x} \quad \text{in } \Omega_x , \quad (\text{I.3.9})$$

for the regular part of  $\boldsymbol{\varepsilon}_\mu$ , and the singular strains

$$\tilde{\boldsymbol{\varepsilon}}_\delta := (\boldsymbol{\xi} \otimes \mathbf{n})^s \quad \text{on } \Gamma_x . \quad (\text{I.3.10})$$

With this notation, the strains (I.3.7) in  $\Omega_x$  are given by

$$\boldsymbol{\varepsilon} = \bar{\boldsymbol{\varepsilon}}_\mu + \tilde{\boldsymbol{\varepsilon}}_\delta \delta_{\Gamma_x} . \quad (\text{I.3.11})$$

Alternatively, the total strains  $\boldsymbol{\varepsilon}_\mu$  in  $\Omega_x$  can be decomposed as

$$\boldsymbol{\varepsilon}_\mu = \boldsymbol{\varepsilon}(\mathbf{u}) + \underbrace{\bar{\boldsymbol{\varepsilon}}_{\text{unres}} + \tilde{\boldsymbol{\varepsilon}}_\delta \delta_{\Gamma_x}}_{:= \boldsymbol{\varepsilon}_{\text{unres}}} . \quad (\text{I.3.12})$$

where

$$\bar{\boldsymbol{\varepsilon}}_{unres} := \mathbf{G}(\boldsymbol{\xi}) := \bar{\boldsymbol{\varepsilon}}_\mu - \boldsymbol{\varepsilon}(\mathbf{u}) = (\boldsymbol{\xi} \otimes \nabla N_{\Gamma_x})^s + \nabla^s \boldsymbol{\xi} H_{\Gamma_x} \quad \text{in } \Omega_x . \quad (\text{I.3.13})$$

Physically, the strain field  $\boldsymbol{\varepsilon}_{unres}$  is the part of the strains in  $\Omega_x$  which is *unresolved* by the strains  $\boldsymbol{\varepsilon}(\mathbf{u})$  of the large-scale problem. The decomposition (I.3.12) identifies the regular and singular part of these unresolved strains. Therefore, the unresolved strains (I.3.13) are given by

$$\boldsymbol{\varepsilon}_{unres} = \mathbf{G}(\boldsymbol{\xi}) + (\boldsymbol{\xi} \otimes \mathbf{n})^s \delta_{\Gamma_x} , \quad (\text{I.3.14})$$

being a linear function of the displacement jumps  $\boldsymbol{\xi}$ .

### I.3.2. The localized dissipation

Given the kinematics of the strong discontinuities described in the previous section, we consider the following dissipation functional

$$\mathcal{D}_\mu := \int_{\Omega_x} [\boldsymbol{\sigma} : \dot{\boldsymbol{\varepsilon}}_\mu - \dot{W}] d\Omega_x , \quad (\text{I.3.15})$$

in the local neighborhood  $\Omega_x$ , for a *stored energy function*

$$W = \hat{W}(\boldsymbol{\varepsilon}_\mu, \mathcal{I}) , \quad (\text{I.3.16})$$

in terms of the small-scale strains  $\boldsymbol{\varepsilon}_\mu$  and a set of internal variables  $\mathcal{I}$  to be specified. Uncoupled thermal conditions are assumed for simplicity (e.g. isothermal conditions with  $W$  corresponding to the free energy of the material). Our goal is the complete characterization of a localized dissipative mechanism along  $\Gamma_x$ . To this purpose, we assume the following constitutive decomposition of the stored energy in  $\Omega_x$

$$W = \bar{W}(\bar{\boldsymbol{\varepsilon}}_\mu, \bar{\mathcal{I}}) + \tilde{W}(\boldsymbol{\xi}, \tilde{\mathcal{I}}) \delta_{\Gamma_x} , \quad (\text{I.3.17})$$

that is, we assume that the stored energy function of the material can be decomposed in a regular part  $\bar{W}$  in  $\Omega_x \setminus \Gamma_x$  and a singular part  $\tilde{W}$  on  $\Gamma_x$ , depending respectively on the regular and singular parts of the small-scale strains as defined by (I.3.11) and internal variables. In this way, the generic internal variables  $\bar{\mathcal{I}}$  characterize a bulk inelastic response in  $\Omega_x$ , whereas its singular counterparts  $\tilde{\mathcal{I}}$  do so along the discontinuity  $\Gamma_x$ . We observe that the main consequence of assumption (I.3.17) is the decoupling of the response of the continuum and the localized dissipative mechanism. This decoupling allows a separate characterization of both deformation responses as described next.

The introduction of the decomposition (I.3.17) in (I.3.15) together with the decomposition (I.3.7) of the strains leads to the final expression of the dissipation functional

$$\mathcal{D}_\mu = \underbrace{\int_{\Omega_x} [\boldsymbol{\sigma} : \dot{\boldsymbol{\varepsilon}}_\mu - \dot{W}] d\Omega_x}_{:= \tilde{\mathcal{D}}_\mu} + \underbrace{\int_{\Gamma_x} [\mathbf{T} \cdot \dot{\boldsymbol{\xi}} - \dot{W}] d\Gamma_x}_{:= \tilde{\mathcal{D}}_\mu} , \quad (\text{I.3.18})$$

after using the relation

$$\int_{\Omega_x} \boldsymbol{\sigma} : (\boldsymbol{\gamma} \otimes \mathbf{n})^s \delta_{\Gamma_x} d\Omega_x = \int_{\Gamma_x} \mathbf{T} \cdot \boldsymbol{\gamma} d\Gamma_x \quad \forall \boldsymbol{\gamma} \in \mathcal{J}, \quad (I.3.19)$$

defining the vector field  $\mathbf{T}$  on  $\Gamma_x$  in the small scale  $\Omega_x$ . Clearly, a completely decoupled expression of the dissipation is obtained, accounting for the contributions of the continuum and localized dissipative mechanisms, respectively. As expected, the latter is given by the difference between the power done by the tractions  $\mathbf{T}$  on the jump displacement rates  $\dot{\boldsymbol{\xi}}$  and the change in the stored energy of the localized dissipative mechanism  $\dot{\tilde{W}}$ .

The characterization of the constitutive equations in the bulk of the material follows standard arguments based on the dissipation functional  $\bar{\mathcal{D}}_\mu$ , after the decoupling of the localized dissipative mechanism. For example, (visco) elastoplastic models can be found developed to all the extent in SIMO & HUGHES [1997]. We proceed in the next section with a similar characterization of the localized dissipative mechanism.

### I.3.3. The localized constitutive relations

We develop in this section an elastoplastic model of the localized dissipative mechanism identified in the previous section. As shown in Section I.3.3.1, this framework is appropriate for the modeling of strain localization in ductile materials. The reader is referred to ARMERO [1997b] for the case of a localized anisotropic damage mechanism in the study of cracking of brittle materials.

A general elastoplastic model of the localized dissipative mechanism on  $\Gamma_x$  can be characterized by the additive decomposition of the displacement jumps

$$\boldsymbol{\xi} = \boldsymbol{\xi}^e + \boldsymbol{\xi}^p, \quad (I.3.20)$$

in elastic and plastic parts, respectively. Furthermore, we assume that the localized strain energy  $\tilde{W}$  is a function of the elastic (or reversible) part of the displacement jump

$$\tilde{W} = \tilde{W}(\boldsymbol{\xi}^e, \tilde{\alpha}), \quad (I.3.21)$$

where we have introduced a single scalar variable  $\tilde{\alpha}$  to model the evolution of the irreversible processes along  $\Gamma_x$  for simplicity in the exposition that follows, and without loss of generality. The general case involving a different set of internal variables,  $\tilde{\mathcal{I}}$  as in (I.3.17), follows easily. Note that  $\tilde{\mathcal{I}} = \{\boldsymbol{\xi}^p, \tilde{\alpha}\}$  in (I.3.21). The introduction of the stored energy (I.3.21) in the localized dissipation (I.3.18)<sub>2</sub> leads to the expression

$$\tilde{\mathcal{D}}_\mu = \left( \mathbf{T} - \frac{\partial \tilde{W}}{\partial \boldsymbol{\xi}^e} \right) \cdot \dot{\boldsymbol{\xi}}^e + \mathbf{T} \cdot \boldsymbol{\xi}^p - \frac{\partial \tilde{W}}{\partial \tilde{\alpha}} \dot{\tilde{\alpha}}. \quad (I.3.22)$$

Following standard arguments known as Coleman's method (see e.g. TRUESDELL & NOLL [1965]), that is, imposing the physically motivated constraint

$$\tilde{\mathcal{D}}_\mu \geq 0 , \quad (\text{I.3.23})$$

for all processes and, in particular, for arbitrary changes of the reversible part  $\xi^e$  of the displacement jumps, we arrive at the localized constitutive relation for the traction vector

$$\mathbf{T} = \frac{\partial \tilde{W}}{\partial \xi^e} , \quad (\text{I.3.24})$$

and the final expression of the localized dissipation

$$\tilde{\mathcal{D}}_\mu = \mathbf{T} \cdot \dot{\xi}^p + q \dot{\alpha} . \quad (\text{I.3.25})$$

The notation

$$q = -\frac{\partial \tilde{W}}{\partial \dot{\alpha}} , \quad (\text{I.3.26})$$

has been introduced in (I.3.25) for the stress-like internal variable  $q$ .

The localized elastoplastic response can be characterized then by a yield surface

$$\tilde{\phi} = \tilde{\phi}(\mathbf{T}, q) , \quad (\text{I.3.27})$$

depending on the thermodynamical forces  $\mathbf{T}$  and  $q$  conjugate to the rate of internal variables, as identified by the expression of the localized dissipation (I.3.25). The stationarity of the dissipation functional (I.3.25) constrained by the yield condition  $\tilde{\phi} \leq 0$  leads to the plastic evolution equations for the rate-independent case. Following e.g. SIMO & HUGHES [1997] we construct the unconstrained function

$$\tilde{\mathcal{L}}_\mu(\mathbf{T}, q) := -\tilde{\mathcal{D}}_\mu(\mathbf{T}, q) + \tilde{\gamma} \tilde{\phi}(\mathbf{T}, q) , \quad (\text{I.3.28})$$

for a (localized) consistency parameter  $\tilde{\gamma}$  satisfying the Kuhn-Tucker loading/unloading conditions

$$\tilde{\phi} \leq 0 , \quad \tilde{\gamma} \geq 0 , \quad \text{and} \quad \tilde{\gamma} \tilde{\phi} = 0 , \quad (\text{I.3.29})$$

and the consistency condition

$$\tilde{\gamma} \dot{\tilde{\phi}} = 0 . \quad (\text{I.3.30})$$

The minimization of  $\mathcal{L}_\mu$  for given rates  $\dot{\xi}^p$  and  $\dot{\alpha}$  leads to the associated plastic evolution equations

$$\left. \begin{aligned} \dot{\xi}^p &= \tilde{\gamma} \frac{\partial \tilde{\phi}}{\partial \mathbf{T}} , \\ \dot{\alpha} &= \tilde{\gamma} \frac{\partial \tilde{\phi}}{\partial q} , \end{aligned} \right\} \quad (\text{I.3.31})$$

A Perzyna-type viscous regularization is obtained by replacing the Kuhn-Tucker loading/unloading conditions (I.3.29) and the consistency relation (I.3.30) by the evolution equation

$$\tilde{\gamma} = \frac{< g(\tilde{\phi}) >}{\eta_L}, \quad (\text{I.3.32})$$

for a localized viscous material parameter  $\eta_L$ , general scalar function  $g(\cdot)$ , and Macaulay brackets  $< \cdot >^*$  while retaining the evolution equations (I.3.31).

In conclusion, the consideration of strong discontinuities in a local neighborhood of the local continuum allows for a complete characterization of the bulk and localized responses of the material. In both cases, the variational structure given by the principle of maximum internal dissipation can be used for the modeling of the corresponding inelastic effects. We present in the following section the example furnished by a rigid (visco)plastic slip model. Still, the above developments have been developed in the local neighborhood  $\Omega_x$ . The inclusion of the resulting localized constitutive model is undertaken in Section I.4.

**Remark I.3.1** The above developments assumed a given unit normal  $\mathbf{n}$  to the discontinuity surface  $\Gamma_x$ . For the rate-independent limit, this normal is defined by the loss of ellipticity condition of the underlying continuum model; see e.g. SIMO et al [1993] and references therein. For rate-dependent solids, a case of special interest herein, it is known that the problem remains elliptic; see e.g. NEEDLEMAN [1988]. In particular, no strong discontinuities will appear. As noted in the introduction, and illustrated in Section I.6, we still consider the limit situation defined by a strong discontinuity as an efficient mechanism to model and capture the localized dissipative mechanism associated to the onset of strain localization, without the need of resolving the corresponding small length scales. The numerical simulations presented in Section I.6 consider a Perzyna-type viscoplastic  $J_2$ -flow theory model (see e.g. SIMO & HUGHES [1997]). In this context, we make use the result presented in LEROY & ORTIZ [1990] which indicates that a lower-bound for the appearance of strain localization in a rate-dependent model is obtained by considering the loss of ellipticity of the underlying rate-independent limit. The argument is based on a spectral analysis of the linearized governing equations, as studied in detail in e.g. MOLINARI & CLIFTON [1987], among others. The normal  $\mathbf{n}$  is then obtained as making singular the corresponding rate-independent acoustic tensor. This approach is employed in NACAR et al [1989] for the enhancement of finite elements. Note that the formulation proposed in this last reference does not incorporate a dissipative mechanism along the assumed discontinuities, in contrast with the approach proposed herein.  $\square$

---

\*  $< x > := \begin{cases} 0 & \text{if } x \leq 0 \\ x & \text{if } x \geq 0 \end{cases}$

### I.3.3.1. Model example: a rigid (visco)plastic slip model

We consider in this section the model example of a rigid-plastic slip model as it is observed in the strong discontinuities resulting from the analysis of continuum models of the  $J_2$ -flow theory of plasticity (see ARMERO & GARIKIPATI [1995,96] for details). The extension accommodating a viscous response is developed as well.

To this purpose, the rigid response is characterized by the lack of reversible displacement jumps

$$\boldsymbol{\xi}^e \equiv 0 \implies \boldsymbol{\xi}^p \equiv \boldsymbol{\xi}, \quad (\text{I.3.33})$$

so the localized stored energy function  $\tilde{W}$  is simply given in terms of the scalar internal variable  $\tilde{\alpha}$

$$\tilde{W}(\boldsymbol{\xi}, \tilde{\alpha}) = \mathcal{H}(\tilde{\alpha}), \quad (\text{I.3.34})$$

for some scalar function  $\mathcal{H}(\cdot)$  defining the cohesive opening of the discontinuity  $\Gamma_x$ . The localized slipping mechanism is characterized by the slip surface

$$\tilde{\phi}(\mathbf{T}, q) = \|\mathbf{T}_T\| + q - \tau_y, \quad (\text{I.3.35})$$

where  $\tau_y$  is the initial shear stress upon activation of the localized slip mechanism, and  $\|\mathbf{T}_T\|$  denotes the Euclidean norm of the tangential component of the traction vector, defined by

$$\mathbf{T}_T = \sum_{\beta=2}^{n_{\text{dim}}} T_\beta \mathbf{m}_\beta \quad \text{with} \quad T_\beta := \mathbf{T} \cdot \mathbf{m}_\beta \quad \text{and} \quad \|\mathbf{T}_T\|^2 := \sum_{\beta=2}^{n_{\text{dim}}} (T_\beta)^2, \quad (\text{I.3.36})$$

for an orthonormal basis  $\{\mathbf{m}_1 \equiv \mathbf{n}, \dots, \mathbf{m}_{n_{\text{dim}}}\}$  (see Figure I.3.1). A softening law (I.3.26) is considered, with

$$q = \hat{q}(\tilde{\alpha}) := -\frac{d\mathcal{H}}{d\tilde{\alpha}} \in [0, -\tau_y], \quad (\text{I.3.37})$$

describing the irreversible response along the discontinuity. The general plastic evolution equations (I.3.31) read in this case

$$\left. \begin{aligned} \dot{\xi}_\beta &= \tilde{\gamma} \frac{T_\beta}{\|\mathbf{T}_T\|} \quad (\beta = 2, n_{\text{dim}}), \\ \dot{\xi}_1 &= 0, \\ \dot{\tilde{\alpha}} &= \tilde{\gamma}, \end{aligned} \right\} \quad (\text{I.3.38})$$

for the displacement jump components

$$\xi_1 := \boldsymbol{\xi} \cdot \mathbf{n} \quad \text{and} \quad \xi_\beta := \boldsymbol{\xi} \cdot \mathbf{m}_\beta, \quad (\text{I.3.39})$$

together with the Kuhn-Tucker loading/unloading conditions (I.3.29) and consistency condition (I.3.30) for the rate-independent case, or the Perzyna viscous regularization (I.3.32)

for the viscous case. The connections with classical Schmid models of micromechanics are to be noted (see e.g. ASARO [1983]). Note that in this rigid case ( $\xi^e \equiv 0$ ) the relation (I.3.24) does not hold, and the traction  $\mathbf{T}$  on  $\Gamma_x$  can only be defined in terms of equilibrium considerations as described in the next section.

## I.4. The Construction of the Local Continuum Formulation

As discussed in Section I.2, we consider the large-scale problem governing the evolution of the solid under the standard regularity conditions for the different fields of interest, including the large-scale displacements  $\mathbf{u}$  and stresses  $\boldsymbol{\sigma}$ . The developments in Section I.3 characterize completely the localized dissipative mechanism that may appear in the limit case of a strong discontinuity. It is important to emphasize that the arguments presented in these developments did not consider any length scale parameter. However, the arguments were developed locally in a fixed neighborhood  $\Omega_x$  of the material point  $\mathbf{x} \in \Omega$ , the small-scale problem, when our main interest is the solution of the large-scale problem described in Section I.2. These two problems have been disconnected to all practical purposes.

The goal of this section is to connect these two problems by introducing the local constitutive model developed in Section I.3 in the large-scale problem as defined in Section I.2. In particular, this step identifies the length scales that appear in the problem. The limit case as  $\text{measure}(\Omega_x) \rightarrow 0$  is considered leading to the final formulation involving a local continuum. Section I.4.2 presents the application of these developments for the large-scale regularization of rate-dependent constitutive models. The finite element implementation of these ideas is summarized in Section I.4.3.

### I.4.1. The final governing equations

The framework developed in the previous sections led to the development of the constitutive relations for the continuum in the local neighborhood  $\Omega_x$  and the localized dissipative mechanism on the discontinuity  $\Gamma_x$  independently. In particular, the tractions  $\mathbf{T}$  appearing in the localized constitutive relations were defined by the weak relations (I.3.19) on  $\Gamma_x$ , but otherwise unrelated to the stress field  $\boldsymbol{\sigma}$  in  $\Omega_x/\Gamma_x$ . We note also that the local neighborhood  $\Omega_x$  has not been specified. For the case of a fixed and finite neighborhood, the resulting formulation defines a non-local relation of the constitutive variables  $\xi$ , as it is characteristic of the non-local constitutive models as proposed in BAZANT et al [1984], among others. As noted in the introduction, our goal is the development of a formulation that maintains the local continuum structure (i.e., the neighborhood  $\Omega_x$  is to be considered in the limit as  $\text{measure}(\Omega_x) \rightarrow 0$ ), and it is therefore consistent with the large-scale problem described in Section I.2. In particular, the large-scale problem defines the local equilibrium relation (I.2.9).

Define the following geometric quantities

$$V_x = \text{measure}(\Omega_x) = \int_{\Omega_x} d\Omega_x , \quad (\text{I.4.1})$$

and

$$A_x = \text{measure}(\Gamma_x) = \int_{\Omega_x} \delta_{\Gamma_x} d\Omega_x = \int_{\Gamma_x} d\Gamma_x . \quad (\text{I.4.2})$$

With this notation in hand, we introduce the weak equation

$$-\frac{1}{V_x} \int_{\Omega_x} \boldsymbol{\gamma} \cdot \boldsymbol{\sigma} \mathbf{n} \, d\Omega_x + \frac{1}{A_x} \int_{\Gamma_x} \boldsymbol{\gamma} \cdot \mathbf{T} \, d\Gamma_x = 0 \quad \forall \boldsymbol{\gamma} \in \mathcal{J} ,$$

(I.4.3)

imposed locally in  $\Omega_x$ . Note that the consideration of a material surface  $\Gamma_x$ , assumed massless in addition, results in no transient terms in (I.4.3).

A simple argument based on Taylor's expansion shows formally that equation (I.4.3) recovers the local equilibrium equation (I.2.9). To this purpose, define the length parameter

$$h_x := \frac{V_x}{A_x} . \quad (\text{I.4.4})$$

The case of interest corresponds to the limit  $h_x \rightarrow 0$ , with  $V_x = O(h_x^{n_{\text{dim}}})$  and  $A_x = O(h_x^{(n_{\text{dim}}-1)})$ , so the neighborhood  $\Omega_x$  reduces to the point  $x$  in the limit. The length scale  $h_x$  is chosen as the controlling parameter in this limit process. In this context, we consider the expansions

$$\boldsymbol{\sigma}(y) = \boldsymbol{\sigma}_x + O(h_x) , \quad \boldsymbol{\gamma}(y) = \boldsymbol{\gamma}_x + O(h_x) \quad \forall y \in \Omega_x , \quad (\text{I.4.5})$$

and

$$\mathbf{T}(y) = \mathbf{T}_x + O(h_x) \quad \forall y \in \Gamma_x , \quad (\text{I.4.6})$$

where  $(\cdot)_x = (\cdot)(x)$ , that is, the value of the corresponding quantity at the fixed point  $x \in \Omega$ . The standard notation for the “big oh”  $O(\cdot)$ , that is,

$$\lim_{h_x \rightarrow 0} \frac{O(h_x^k)}{h_x^k} < \infty , \quad (\text{I.4.7})$$

is considered in (I.4.7) and (I.4.6). Introducing the expansions (I.4.7) into (I.4.6), we obtain

$$[-\boldsymbol{\sigma}_x \mathbf{n} + \mathbf{T}_x] \cdot \boldsymbol{\gamma}_x + O(h_x) = 0 \quad \forall \boldsymbol{\gamma} \in \mathcal{J} , \quad (\text{I.4.8})$$

so we recover formally the local equilibrium equation (I.2.9) in the local limit as  $h_x \rightarrow 0$ . We note that the Taylor's expansions considered in (I.4.7) and (I.4.6) involve regular fields. In particular, we consider the (smooth) displacement jumps and not the singular strains.

This situation is to be contrasted with the typical argument that relates traditional non-local models with higher-order models in terms of a Taylor's expansion of the total strain field, which becomes singular (unbounded), making the expansion argument questionable. See PIJAUDIER-CABOT et al [1995] for a discussion of these issues.

### Remarks I.4.1.

- As presented in ARMERO [1997b], an alternative argument shows that the relation (I.4.3) can be understood as the limit  $h_x \rightarrow 0$  of the imposed orthogonality condition

$$\int_{\Omega_x} \boldsymbol{\sigma} : \boldsymbol{\varepsilon}_{unres}^* d\Omega_x = 0, \quad (\text{I.4.9})$$

between the stresses and the unresolved strain variations  $\boldsymbol{\varepsilon}^*$  defined as

$$\boldsymbol{\varepsilon}_{unres}^* = -\frac{1}{h_x} (\boldsymbol{\gamma} \otimes \mathbf{n})^s + (\boldsymbol{\gamma} \otimes \mathbf{n})^s \delta_{\Gamma_x} + O(1), \quad (\text{I.4.10})$$

for variations  $\boldsymbol{\gamma} \in \mathcal{J}$ . The inclusion of (I.4.10) in (I.4.9) and the use of the relation (I.3.19) leads to the weak equation (I.4.3) in the case of interest  $h_x \rightarrow 0$ . The relation (I.4.9) imposes physically the vanishing of the stress power on the variations (I.4.10). Given (I.3.12), indicating that the large and small-scale strains ( $\boldsymbol{\varepsilon}(\mathbf{u})$  and  $\boldsymbol{\varepsilon}_\mu$ ) differ by the unresolved strains  $\boldsymbol{\varepsilon}_{unres}$ , the condition (I.4.9) equates the dissipation  $\mathcal{D}_\mu$  defined by (I.3.15) in the small scale to the dissipation observed in the local neighborhood  $\Omega_x$  by the large-scale problem involving the large-scale strains  $\boldsymbol{\varepsilon}(\mathbf{u})$ . Hence, the formulation developed above effectively incorporates then the localized dissipation of the small-scale response of the material in the (smooth) large-scale problem.

- Furthermore, by understanding the unresolved strains as an enhancement of the large-scale strains  $\boldsymbol{\varepsilon}(\mathbf{u})$ , the orthogonality relation (I.4.9) falls within the class of enhanced strain methods, as described in SIMO & RIFAI [1990] in the context of finite element formulations. It is important to note, however, that in this case the enhanced strains do not vanish in the limit  $h_x \rightarrow 0$ , but resolve the contributions of the localized strains associated to the strong discontinuity.  $\square$

### I.4.2. Large-scale regularization of rate-dependent models

The formulation presented in the previous section leads to a local continuum formulation in the limit  $h_x \rightarrow 0$ , incorporating the localized dissipation associated to the localized dissipative mechanism characterized in Section I.3 by a strong discontinuity. As noted in Remark I.4.1.1, the small-scale dissipation  $\mathcal{D}_\mu$  given by (I.3.15) is incorporated in the large-scale problem (I.2.5) by construction. Given the localized evolution equations (I.3.31), the localized part  $\tilde{\mathcal{D}}_\mu$  of the small-scale dissipation can be expressed as

$$\tilde{\mathcal{D}}_\mu = \tilde{\boldsymbol{\gamma}} \tau_y \quad \text{on } \Gamma_x, \quad (\text{I.4.11})$$

as a simple calculation shows. The Perzyna viscoplastic regularization defined by (I.3.32) leads then to

$$\tilde{\mathcal{D}}_\mu = \frac{\langle g(\tilde{\phi}) \rangle}{\eta_L} \tau_y \quad \text{on } \Gamma_x . \quad (\text{I.4.12})$$

Therefore, for a finite value of the localized viscous parameter  $\eta_L$  we obtain a finite contribution to the final dissipation along the strong discontinuity  $\Gamma_x$ , even in the local continuum limit  $h_x \rightarrow 0$  (or, equivalently,  $1/h_x \rightarrow \infty$  emphasizing the idea of the large-scale limit).

As noted in the introduction, classical rate-dependent model with strain-softening incorporating a (continuum) viscosity are known to result in well-posed problems, still exhibiting the phenomena of strain localization and corresponding localized dissipation but now in a band of finite width  $w_s$ . Therefore, the consideration of a strong discontinuity and the corresponding finite dissipation on it does not comply with this observation. However, in the large-scale limit (that is, when  $h_x \gg w_s$ ), the above developments prove to be very useful for the actual numerical modeling of the localized dissipation observed in the small scale of the material. We note that in typical large-scale structural applications  $w_s \gg L$ , for a characteristic length scale  $L$  of the spatially discretized solid. The constructive procedure developed above (that is, the development of the constitutive relations in a finite neighborhood, and its actual incorporation in the large-scale problems) leads naturally to the finite element implementation of these ideas. As discussed in Section I.4.3, this implementation is based on the identification of the local neighborhood  $\Omega_x$  with a finite element  $\Omega_e$ . The case  $h_x \gg w_s$  is then of the main interest, since it allows capturing the localized dissipation without the actual resolution of the small-scale length scales of order  $w_s$ . Still, the bulk dissipation needs to be recovered as  $h_x$  becomes of the order of the length scale  $w_s$ . This limit can be easily obtained by the proper scaling of the localized softening along  $\Gamma_x$  as developed next.

Given these considerations, we impose the condition

$$\tilde{\mathcal{D}}_\mu \sim \begin{cases} O(h_x) & \text{for } h_x/w_s \rightarrow 0 , \\ O(1) & \text{for } h_x/w_s \gg 1 , \end{cases} \quad (\text{I.4.13})$$

for some estimate  $w_s$  of the width of the shear band. Given (I.4.12), this requirement is easily accomplished by defining the localized viscous parameter  $\eta_L$  through the scaling law

$$\eta_L^{-1} = \eta^{-1} l \quad \text{where } l = \min\{h_x, w_s\} , \quad (\text{I.4.14})$$

for some finite viscous parameter  $\eta$  (units of stress/time). With this scaling and using (I.3.31)<sub>3</sub> and (I.3.32), we conclude that

$$\dot{\alpha} = \dot{\gamma} = \frac{\langle g(\tilde{\phi}) \rangle}{\eta_L} \sim O(h_x) \quad \text{as } h_x \rightarrow 0 . \quad (\text{I.4.15})$$

Therefore, the localized softening modulus  $\mathcal{H}_L$ , defined by

$$\mathcal{H}_L = \widehat{\mathcal{H}}_L(\tilde{\alpha}) := -\frac{dq(\tilde{\alpha})}{d\tilde{\alpha}}, \quad (\text{I.4.16})$$

is of the order

$$\mathcal{H}_L \sim \tau_y \cdot O(h_x^{-1}) \quad \text{as } h_x \rightarrow 0, \quad (\text{I.4.17})$$

after normalizing with  $\tau_y$  (units of stress) given (I.3.37). The scaling (I.4.17) is obtained by considering in this viscous case

$$\mathcal{H}_L^{-1} = \mathcal{H}^{-1} l, \quad (\text{I.4.18})$$

for a softening modulus  $\mathcal{H}$  (units of stress), and  $l$  defined in (I.4.14)<sub>2</sub>. The reader is referred to Section I.6 for several numerical examples illustrating these ideas.

### I.4.3. The finite element implementation

The numerical implementation of the ideas developed in the previous sections follows along the lines of the finite element methods proposed in ARMERO & GARIKIPATI [1995,96], without the need of any regularization (smoothing) of the strong discontinuities. We summarize in this section the main ideas behind these methods and refer to these last references for further details.

The finite element implementation of the formulation developed above follows naturally by identifying the local neighborhood  $\Omega_x$  with a finite element  $\Omega_e$  of the assumed spatial discretization. We consider a piecewise constant approximation of the displacement jumps

$$\mathcal{J}^h = \{\boldsymbol{\xi}_e \in \mathbb{R}^{n_{\text{dim}}} \quad \text{in} \quad \Omega_e\}, \quad (\text{I.4.19})$$

for each element  $\Omega_e$  where localization has been detected, admitting a straight discontinuity surface  $\Gamma_e$ . Higher order interpolations can be accommodated.

The interpolated total strain  $\boldsymbol{\epsilon}_{\mu}^h$  is then given by

$$\boldsymbol{\epsilon}_{\mu}^h = \boldsymbol{\epsilon}(\mathbf{u}^h) + \boldsymbol{\epsilon}_{unres}^h, \quad (\text{I.4.20})$$

with the unresolved strain is given by (I.3.14) as

$$\boldsymbol{\epsilon}_{unres}^h = -\frac{1}{h^{(i)}} \left( \boldsymbol{\xi}_e^h \otimes \mathbf{n}^{(i)} \right)^s + \left( \boldsymbol{\xi}_e^h \otimes \mathbf{n} \right)^s \delta_{\Gamma_e}, \quad (\text{I.4.21})$$

the gradient of the discontinuous interpolation function

$$\boldsymbol{\epsilon}_{unres}^h = \nabla^s \left[ (H_{\Gamma_e} + N_{\Gamma_e}^h) \boldsymbol{\xi}_e^h \right] \quad \text{with} \quad N_{\Gamma_e}^h = 1 - \frac{(\mathbf{x} - \mathbf{x}^{(i)}) \cdot \mathbf{n}^{(i)}}{h^{(i)}}, \quad (\text{I.4.22})$$

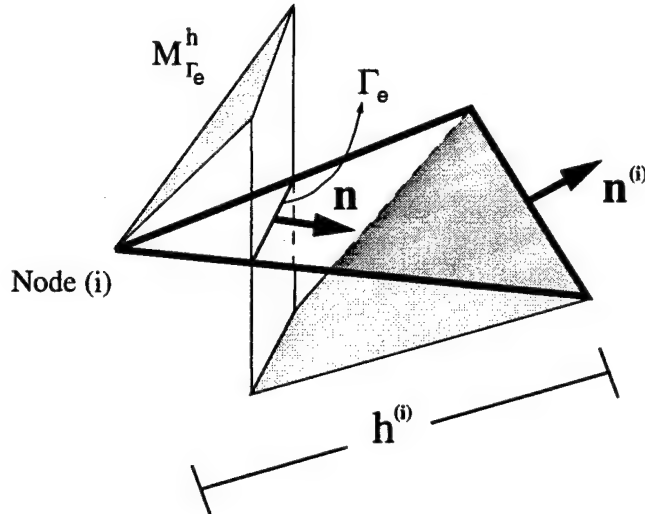


**FIGURE I.4.1** Discontinuous interpolation function motivating the choice of enhanced strain field.

as depicted in Figure I.4.1. See this figure for the notation employed in (I.4.21) and (I.4.22).

In (I.4.20), the discretized large-scale strains are defined as

$$\boldsymbol{\epsilon}(\mathbf{u}^h) = \mathbf{B}\mathbf{d}, \quad (\text{I.4.23})$$

in a typical finite element  $\Omega_e$ , where  $\mathbf{B}$  denotes the standard linearized strain operator given by a standard finite element interpolation. For example, it may arise from some isoparametric interpolation of the large-scale displacements

$$\mathbf{u}^h = \mathbf{N}^h \mathbf{d}, \quad (\text{I.4.24})$$

for the corresponding nodal displacements  $\mathbf{d}$ , or more generally from an assumed or mixed interpolation of the strains. The simulations in Section I.6 consider mixed quadratic triangles with linear (discontinuous) interpolations of the pressure. See Figure I.6.4.b.

The finite element formulation is based on the discrete counterpart of the weak equation (I.2.5) and the local nonlinear equation (I.4.3), leading to the set of algebraic system of equations in the nodal displacements  $\mathbf{d}$  and the local parameters  $\xi_e^h$ .

$$\left. \begin{aligned} \mathbf{R} &:= \mathbf{f}_{ext} - \sum_{e=1}^{n_{elem}} \int_{\Omega_e} \mathbf{B}^T \boldsymbol{\sigma}(\mathbf{d}, \xi_e^h) d\Omega - \mathbf{M} \ddot{\mathbf{d}} = 0 \\ \mathbf{s}_e &:= \frac{1}{V_e} \int_{\Omega_e} \boldsymbol{\sigma}(\mathbf{d}, \xi_e^h) \mathbf{n} d\Omega - \mathbf{T}(\xi_e^h) = 0 \quad \text{in } \Omega_e \end{aligned} \right\}, \quad (\text{I.4.25})$$

where  $V_e = \text{measure}(\Omega_e)$ ,  $\sum_{e=1}^{n_{elem}}$  refers to the standard assembly operator over the  $n_{elem}$  elements, and  $\mathbf{M}$  denotes the finite element mass matrix. We note the independence of

these parameters from element to element, consistent with the local character of the decomposition (I.3.1). As a practical consequence, this fact allows the efficient implementation of the proposed formulation through the static condensation of the local parameters  $\xi_e^h$ , leading to a final system of equations in the large-scale nodal displacements  $\mathbf{d}$ , after the consistent linearization of the equations. The resulting large-scale formulation incorporates the localized dissipation, as it was the original goal of the proposed approach.

## I.5. The Extension to the Finite Deformation Range

We extend in this section the previous developments to the finite strain range. To this purpose, we summarize in Section I.5.1 the finite kinematics of strong discontinuities, and develop in Section I.5.2 the constitutive relations of localized dissipative mechanisms in the finite deformation range. Finally, Section I.5.3 summarizes the finite element implementation in this geometrically nonlinear range.

### I.5.1. The finite kinematics of strong discontinuities

The finite deformation of a solid occupying the reference placement  $\Omega \subset \mathbb{R}^{n_{\text{dim}}}$  is characterized in the large scale by the *smooth deformation* mapping  $\varphi : \Omega \rightarrow \mathbb{R}^{n_{\text{dim}}}$ . As it is customary, we denote the material points  $\mathbf{X} \in \Omega$  with the corresponding current position vectors as  $\mathbf{x} = \varphi(\mathbf{X})$ .

As in the infinitesimal case discussed in Section I.3.3.1, the response of the material in a local neighborhood  $\Omega_X \subset \Omega$  of a material point  $\mathbf{X}$  may not be characterized completely by a smooth deformation field  $\varphi$ . We consider the case of a strong discontinuity given by the decomposition

$$\varphi_\mu = \varphi + \xi M_{\Gamma_x} \quad \text{in } \Omega_X , \quad (\text{I.5.1})$$

with the function  $M_{\Gamma_x}$  defined as in (I.3.1), so  $\xi = [\varphi_\mu]$  across  $\Gamma_X \subset \Omega_X$ , a discontinuity surface with unit normal  $\mathbf{N}$  (a material vector). Considering the gradient of  $\varphi_\mu$  in  $\Omega_X$ , we obtain the expression

$$\mathbf{F}_\mu = \text{Grad}\varphi + \underbrace{\mathbf{G}_F(\xi) + \xi \otimes \mathbf{N} \delta_{\Gamma_X}}_{\mathbf{F}_{\text{unres}}} , \quad (\text{I.5.2})$$

for the small-scale deformation gradient  $\mathbf{F}_\mu$ , with a regular part given by

$$\bar{\mathbf{F}}_\mu = \text{Grad}\varphi + \mathbf{G}_F(\xi) . \quad (\text{I.5.3})$$

The symbol  $\text{Grad}(\cdot)$  denotes the material gradient, with respect to the material coordinates  $\mathbf{X}$ . The regular part of the unresolved deformation gradient  $\mathbf{F}_{\text{unres}}$  is given by

$$\mathbf{G}_F(\xi) := \xi \otimes \text{Grad}N_{\Gamma_x} + \text{Grad}\xi H_{\Gamma_x} \quad \text{in } \Omega_x , \quad (\text{I.5.4})$$

the counterpart of (I.3.9).

The expression (I.5.2) can be written alternatively as

$$\mathbf{F}_\mu = \bar{\mathbf{F}}_\mu (\mathbf{1} + \mathbf{J} \otimes \mathbf{N}) , \quad (\text{I.5.5})$$

for the material displacement jump vector

$$\mathbf{J} := \bar{\mathbf{F}}_\mu^{-1} [\varphi_\mu] . \quad (\text{I.5.6})$$

We decompose this material displacement jump in a material coordinate system

$$\mathbf{J} = \xi^i \mathbf{M}_i \quad (\text{summation implied}) , \quad (\text{I.5.7})$$

with  $\mathbf{M}_1 = \mathbf{N}$  and  $\mathbf{M}_i \cdot \mathbf{M}_j = \delta_{ij}$  (orthonormal), defining the convected coordinates  $\xi^i$ . We observe that the spatial displacement jump is given then as

$$[\varphi_\mu] = \xi = \xi^i \mathbf{m}_i^\sharp \quad \text{with} \quad \mathbf{m}_i^\sharp := \bar{\mathbf{F}}_\mu \mathbf{M}_i , \quad (\text{I.5.8})$$

in the spatial configuration.

The nominal traction  $\mathbf{T}$  is introduced in this geometrically nonlinear setting as in (I.3.19) by the relation

$$\int_{\Omega_x} \mathbf{P} : (\boldsymbol{\gamma} \otimes \mathbf{N}) \delta_{\Gamma_x} d\Omega_x = \int_{\Gamma_x} \mathbf{T} \cdot \boldsymbol{\gamma} d\Gamma_x \quad \forall \boldsymbol{\gamma} \in \mathcal{J} , \quad (\text{I.5.9})$$

in terms of the nominal stresses  $\mathbf{P}$  (first Piola-Kirchhoff stress tensor). Similarly, we define the covariant components of the traction as

$$\mathbf{T} = T_i \mathbf{m}_\beta^i \quad \text{with} \quad \mathbf{m}_\beta^i = \bar{\mathbf{F}}_\mu^{-T} \mathbf{M}_i . \quad (\text{I.5.10})$$

We note the orthogonality relations  $\mathbf{m}_j^\sharp \cdot \mathbf{m}_\beta^i = \delta_j^i$  (the Kronecker delta). In particular, we define the spatial normal vector

$$\mathbf{n}_\beta \equiv \mathbf{m}_\beta^1 = \bar{\mathbf{F}}_\mu^{-T} \mathbf{N} , \quad (\text{I.5.11})$$

not a unit vector, in general.

As shown in ARMERO & GARIKIPATI [1996], the response of the strong discontinuities in finite strain models of multiplicative plasticity can be characterized by the Lie derivative of the displacement jumps defined as

$$\mathbf{L}_v [\varphi_\mu] := \bar{\mathbf{F}}_\mu \frac{d}{dt} [\bar{\mathbf{F}}_\mu^{-1} [\varphi]] = \bar{\mathbf{F}}_\mu \dot{\mathbf{J}} . \quad (\text{I.5.12})$$

The vector  $\mathbf{f}_v[\varphi_\mu]$  defines a frame-indifferent (objective) rate of the change of the displacement jump  $[\varphi_\mu]$ . Furthermore, combining (I.5.12) with (I.5.8) we obtain

$$\mathbf{f}_v[\varphi_\mu] = \dot{\xi}^i \mathbf{m}_i^\sharp, \quad (\text{I.5.13})$$

in the coordinate system defined in (I.5.8)<sub>2</sub>.

### I.5.2. Localized dissipative mechanisms in the finite deformation range

Motivated by the results in the infinitesimal case, we consider similarly a decomposition of the stored energy of the material in a continuum and localized contributions

$$W(\mathbf{F}_\mu, \mathcal{I}) = \bar{W}(\bar{\mathbf{F}}_\mu^T \bar{\mathbf{F}}_\mu, \bar{\mathcal{I}}) + \tilde{W}(\mathbf{J}, \bar{\mathcal{I}}) \delta_{\Gamma_X}, \quad (\text{I.5.14})$$

where the dependence on the right Cauchy-Green tensor  $\bar{\mathbf{F}}_\mu^T \bar{\mathbf{F}}_\mu$  for the continuum contribution and  $\mathbf{J}$  (or alternatively, the components  $\xi^i$ ) for the localized part is imposed in accordance with the *principle of material frame indifference*, as a classical argument shows. The regular part  $\bar{W}$  of the stored energy function leads to standard continuum models in  $\Omega_X/\Gamma_X$  for, say, the nominal stresses  $\mathbf{P}$  (first Piola-Kirchhoff stress tensor). Furthermore, we define the *frame-indifferent measure*

$$\tilde{D}_\mu := T_i \dot{\xi}^i - \dot{\tilde{W}}, \quad (\text{I.5.15})$$

along the discontinuity  $\Gamma_X$  to base the arguments of the derivation of the localized constitutive relations. Equation (I.5.15) has the same form as its infinitesimal counterpart (I.3.18) in the considered convected basis.

The formulation of a localized elastoplastic model follows then by considering the elastoplastic decomposition

$$\mathbf{J} = \mathbf{J}^e + \mathbf{J}^p, \quad (\text{I.5.16})$$

in a elastic and a plastic part. We note that the spatial decomposition

$$\boldsymbol{\xi} = \boldsymbol{\xi}^e + \boldsymbol{\xi}^p, \quad (\text{I.5.17})$$

follows with the definitions

$$\boldsymbol{\xi}^e := \bar{\mathbf{F}}_\mu \mathbf{J}^e \quad \text{and} \quad \boldsymbol{\xi}^p := \bar{\mathbf{F}}_\mu \mathbf{J}^p, \quad (\text{I.5.18})$$

with  $\boldsymbol{\xi} = \bar{\mathbf{F}}_\mu \mathbf{J}$  by (I.5.3). The corresponding expressions in the considered convected basis read

$$\mathbf{J}^e = \xi^{ei} \mathbf{M}_i \quad \text{and} \quad \mathbf{J}^p = \xi^{pi} \mathbf{M}_i, \quad (\text{I.5.19})$$

with the elastoplastic decomposition

$$\xi^i = \xi^{ei} + \xi^{pi} \quad (i = 1, n_{\text{dim}}), \quad (\text{I.5.20})$$

of the convected components of the displacement jumps follows.

The same arguments employed in the infinitesimal case lead then to the constitutive relation

$$T_i = \frac{\partial \tilde{W}}{\partial \xi^{e_i}} \quad (i = 1, n_{\text{dim}}), \quad (\text{I.5.21})$$

for the nominal tractions, and

$$\tilde{\mathcal{D}}_\mu = T_i \dot{\xi}^p{}^i + q \dot{\alpha}, \quad (\text{I.5.22})$$

for the localized measure, with stress-like internal variable  $q$  defined again by (I.3.26). The stationarity of (I.5.22) among all admissible stress states  $\tilde{\phi}(\mathbf{T}, q) \leq 0$ , as done in Section I.3 for the infinitesimal case, leads to the associated plastic evolution equations

$$\left. \begin{aligned} \dot{\xi}^p{}^i &= \tilde{\gamma} \frac{\partial \tilde{\phi}}{\partial T_i} \quad (i = 1, n_{\text{dim}}), \\ \dot{\alpha} &= \tilde{\gamma} \frac{\partial \tilde{\phi}}{\partial q}, \end{aligned} \right\} \quad (\text{I.5.23})$$

together with the Kuhn-Tucker loading/unloading conditions

$$\tilde{\phi} \leq 0, \quad \tilde{\gamma} \geq 0, \quad \text{and} \quad \tilde{\gamma} \tilde{\phi} = 0, \quad (\text{I.5.24})$$

and the consistency condition

$$\tilde{\gamma} \dot{\tilde{\phi}} = 0, \quad (\text{I.5.25})$$

as their infinitesimal counterparts. The Perzyna viscoplastic regularization is given by

$$\tilde{\gamma} = \frac{\langle g(\tilde{\phi}) \rangle}{\eta_L}, \quad (\text{I.5.26})$$

as developed in Section I.3.

A rigid (visco)plastic slip model is obtained in the same way as discussed in Section I.3.3.1 for the infinitesimal case. The slip surface (I.3.36) is considered again with the norm of the tangential traction vector defined by

$$\mathbf{T}_T = \sum_{\beta=2}^{n_{\text{dim}}} T_\beta \mathbf{M}^\beta \quad \text{and} \quad \|\mathbf{T}_T\|^2 = \sum_{\alpha, \gamma=2}^{n_{\text{dim}}} T_\alpha \delta^{\alpha\beta} T_\beta, \quad (\text{I.5.27})$$

for the dual basis  $\mathbf{M}^i \equiv \mathbf{M}_i$  given the orthonormal character assumed for the material basis  $\{\mathbf{M}_i\}$ . The rigid plastic slip equations (I.3.38) hold then in this case

$$\left. \begin{aligned} \delta_{\beta\alpha} \dot{\xi}^\alpha &= \tilde{\gamma} \frac{T_\beta}{\|\mathbf{T}_T\|} \quad (\beta = 2, n_{\text{dim}}), \\ \dot{\xi}^1 &= 0, \\ \dot{\alpha} &= \tilde{\gamma}, \end{aligned} \right\} \quad (\text{I.5.28})$$

with  $\xi^e \equiv 0$ , as a simple calculation shows.

**Remark I.5.1** The above formulation corresponds to a fully material characterization of a localized dissipative mechanism on  $\Gamma_x$ . As shown above, it leads to governing equations possessing the same form as their infinitesimal counterparts. Alternative formulations that, for example, do not consider a fixed (orthonormal) material basis  $\{M_i\}$ , with the slip yield condition defined in terms of a spatial norm of the tangential traction vector (involving spatial, true stress components) can also be developed. Details are omitted. This situation is similar to the modeling of frictional contact of solids, as discussed in LAURSEN [1994].  $\square$

### I.5.3. The governing equations and their finite element implementation

The counterpart of the large-scale problem (I.2.5) in the finite deformation considered in this section can be similarly expressed in terms of the unknown (smooth) deformation  $\varphi \in \mathcal{V} + \bar{\mathbf{g}}$ ,

$$\int_{\Omega} \rho_o \ddot{\varphi} \cdot \boldsymbol{\eta} \, d\Omega + \int_{\Omega} \mathbf{P} : \text{Grad} \boldsymbol{\eta} \, d\Omega = \int_{\Omega} \rho_o \mathbf{b} \cdot \boldsymbol{\eta} \, d\Omega + \int_{\partial_T \Omega} \bar{\mathbf{t}} \cdot \boldsymbol{\eta} \, d\Gamma \quad \forall \boldsymbol{\eta} \in \mathcal{V}, \quad (\text{I.5.29})$$

for given initial conditions  $\varphi(\mathbf{x}, 0) = \varphi_o(\mathbf{x})$  and  $\dot{\varphi}(\mathbf{x}, 0) = \mathbf{v}_o(\mathbf{x})$ , with the nominal stresses  $\mathbf{P}$  given by the constitutive relations as described in the previous section. Equivalently, the internal virtual work term can be written as

$$\int_{\Omega} \mathbf{P} : \text{Grad} \boldsymbol{\eta} \, d\Omega = \int_{\Omega} \boldsymbol{\tau} : \nabla^s \boldsymbol{\eta} \, d\Omega, \quad (\text{I.5.30})$$

in terms of the Kirchhoff stress field  $\boldsymbol{\tau}$  defined as

$$\boldsymbol{\tau} = \mathbf{P} \bar{\mathbf{F}}_{\mu}^T, \quad (\text{I.5.31})$$

and the spatial gradient defined by

$$\nabla \boldsymbol{\eta} := \bar{\mathbf{F}}_{\mu}^{-T} \text{Grad} \boldsymbol{\eta}, \quad (\text{I.5.32})$$

both using the regular part of the deformation gradient  $\bar{\mathbf{F}}_{\mu}$ .

The localized constitutive model developed in the previous section is incorporated in the large-scale problem (I.5.29) as in the infinitesimal case by considering the weak form of the local equilibrium equation across the *material* surface  $\Gamma_X$

$$-\frac{1}{V_X} \int_{\Omega_X} \boldsymbol{\gamma} \cdot \boldsymbol{\tau} \mathbf{n}_{\beta} \, d\Omega_x + \frac{1}{A_X} \int_{\Gamma_X} \boldsymbol{\gamma} \cdot \mathbf{T} \, d\Gamma_x = 0 \quad \forall \boldsymbol{\gamma} \in \mathcal{J}, \quad (\text{I.5.33})$$

with  $\mathbf{n}_{\beta}$  given by (I.5.11), and  $V_X = \text{measure}(\Omega_X)$  and  $A_X = \text{measure}(\Gamma_X)$  defined as in (I.4.1) and (I.4.2), respectively.

The finite element implementation follows then as in the infinitesimal case, leading to the discrete equations

$$\left. \begin{aligned} \mathbf{R} &:= \mathbf{f}_{ext} - \sum_{e=1}^{n_{elem}} \int_{\Omega_e} \mathbf{b}^T \boldsymbol{\tau} d\Omega - \mathbf{M} \ddot{\mathbf{d}} = 0 , \\ \mathbf{s}_e &:= \frac{1}{V_e} \int_{\Omega_e} \boldsymbol{\tau} \mathbf{n}_\beta d\Omega - \mathbf{T}(\boldsymbol{\xi}_e^h) = 0 \quad \text{in } \Omega_e , \end{aligned} \right\} \quad (\text{I.5.34})$$

for a spatial linearized discrete strain operator  $\mathbf{b}$  and finite element  $\Omega_e$  in the reference configuration of the solid. The efficient numerical implementation of the equations (I.5.34) involves again the static condensation of the element parameters  $\boldsymbol{\xi}_e^h$  after their consistent linearization. Further details can be found in ARMERO & GARIKIPATI [1996], and are omitted here.

**Remark I.5.2** The general elastoplastic framework developed in Section I.5.2 allows the elastic regularization of the rigid localized mechanism defined by (I.5.28). In this way, we consider the elastic relation

$$T_i = \kappa_i \xi^{ei} \quad i = 1, n_{\text{dim}} \quad (\text{no sum}) , \quad (\text{I.5.35})$$

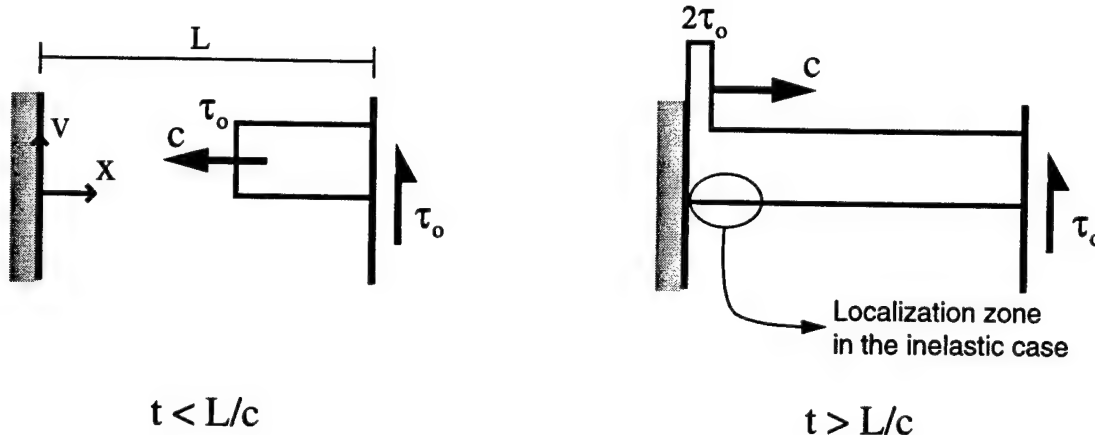
for large (penalty) parameters  $\kappa_i$ . The final governing equations (I.5.23) possess then the same structure of (infinitesimal) elastoplasticity, allowing then the application of standard return mapping algorithms for their numerical integration. The reader is referred to SIMO & HUGHES [1997] for details. Implementations not involving the regularization (I.5.35) can be found in ARMERO & GARIKIPATI [1995].  $\square$

## I.6. Representative Numerical Simulations

We present in this section the results obtained for two representative examples that assess the performance of the numerical modeling of viscoplastic strain localization through strong discontinuities as described in the previous sections. Section I.6.1 includes the results obtained in the 1D wave propagation problem in an infinitesimal viscoplastic shear layer. The benchmark problem given by the simulation of the plane strain tension test at finite strains is discussed in Section I.6.2.

### I.6.1. 1D wave propagation problem in a softening viscoplastic shear layer

We consider the one-dimensional dynamic problem of the propagation of shear waves in a viscoplastic shear layer. Infinitesimal conditions are assumed. A layer width  $L = 100$  and unit thickness is considered, under simple shear conditions, with a fixed left end ( $v = 0$  at  $x = 0$  and all times) and an imposed sudden shear stress  $\tau_o$  at the right end  $x = L$ .



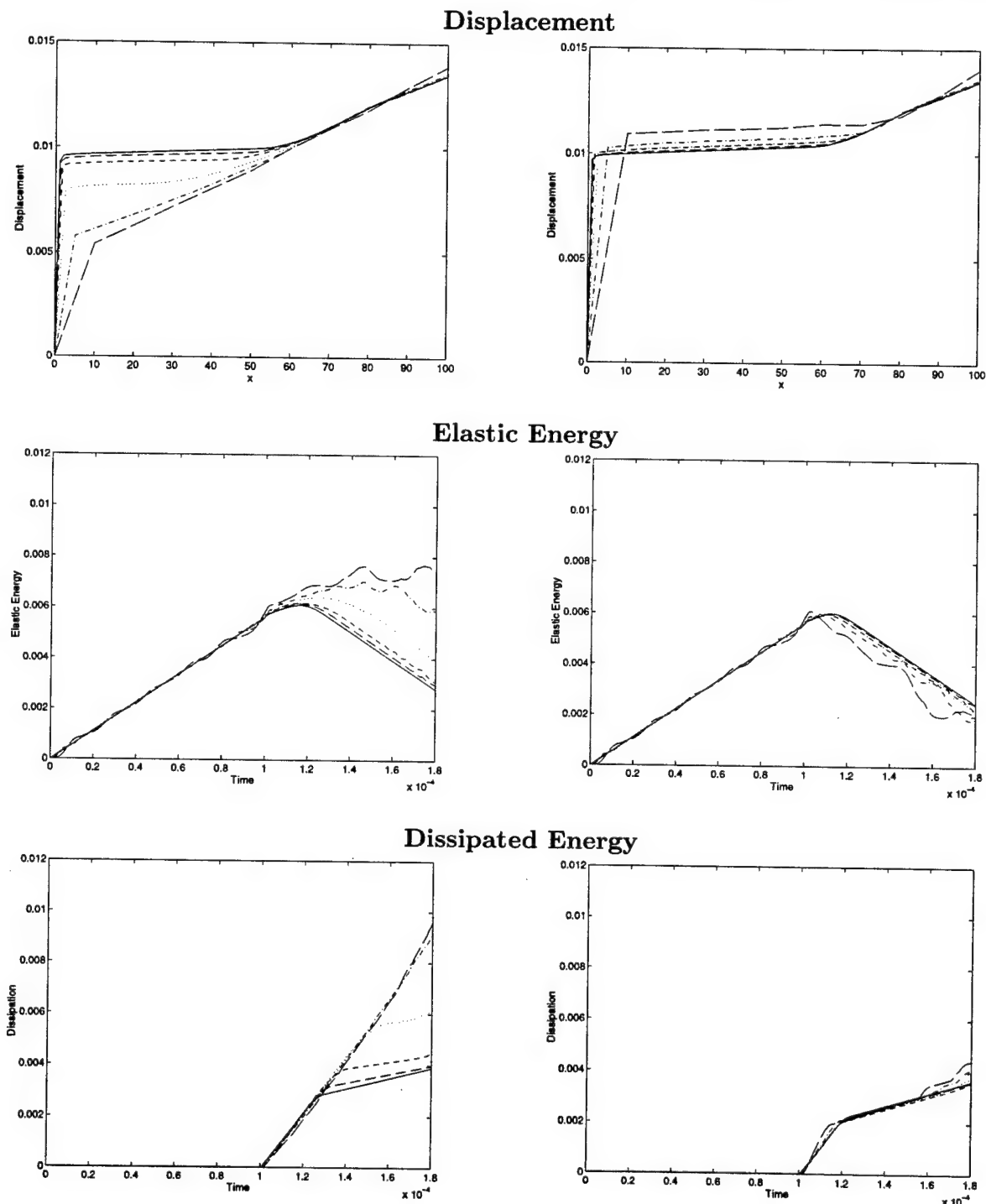
**FIGURE I.6.1** 1D wave propagation problem. Sketch of the elastic solution. After reflection at the fixed end the stress doubles in the elastic case. In the inelastic case, the material yields and softens creating a shear band.

Figure I.6.1 depicts the definition of the problem, as well as the elastic solution. In this case, a pulse of constant stress  $\tau_0$  travels along the layer at a constant wave speed  $c = \sqrt{G/\rho}$ , for a shear modulus  $G$  and density  $\rho$ . Upon reaching the fixed end, the stress doubles in this elastic case, and is reflected back along the shear layer.

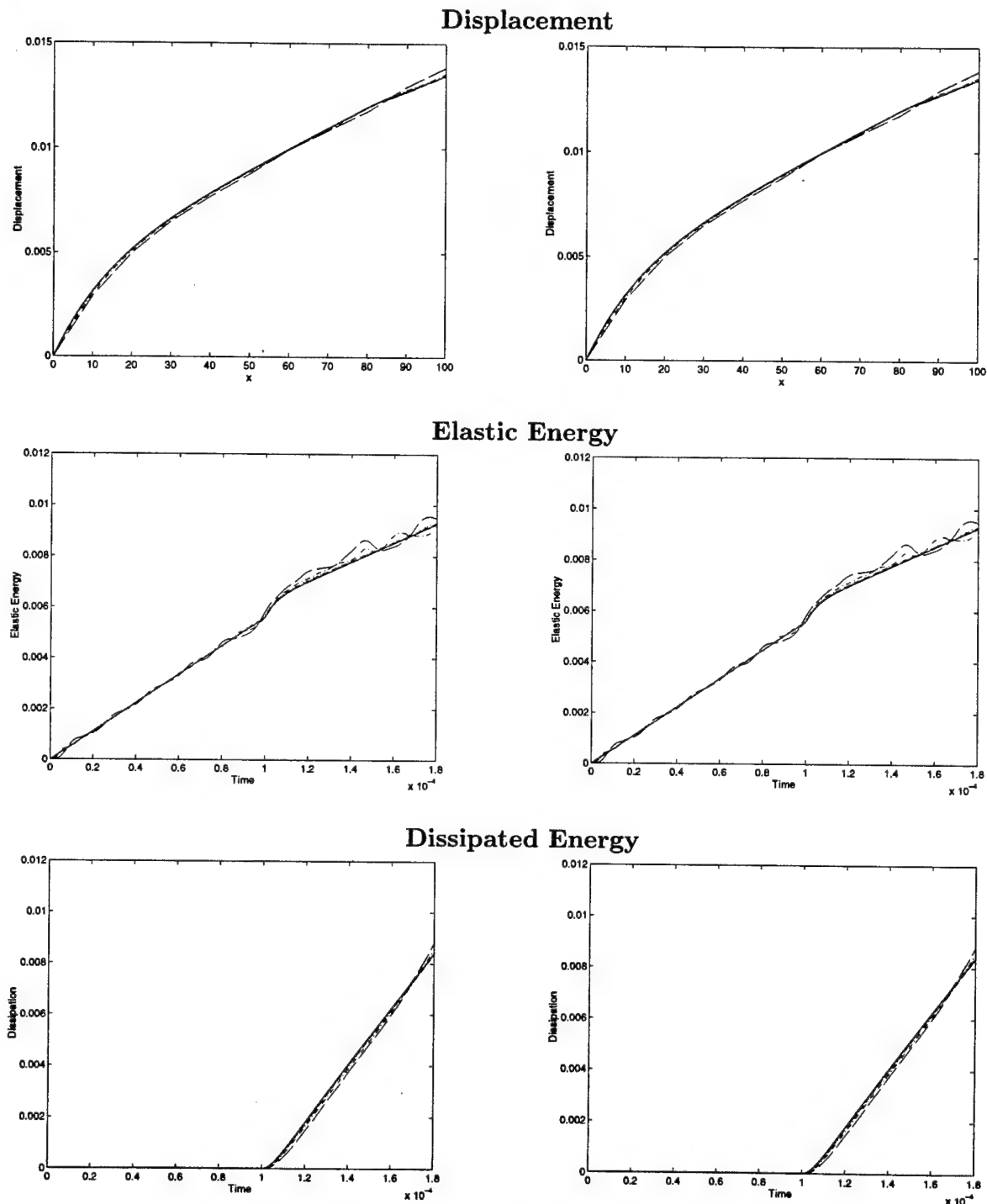
In the case of a softening material, a shear band appears at the fixed end upon reflection if the yield limit of the material is reached. The problem of a rate-independent strain-softening material (in its completely equivalent form involving an axial bar) has been considered in BAZANT & BELYTSCHKO [1985]. In this case, the well-known pathological mesh-size dependence of the finite element solution appears as a consequence of the inability of a rate-independent material model involving a fixed softening strain/stress relation to capture the localized dissipative mechanism associated to the shear band. As noted in the introduction, these difficulties can be traced back to the absence of a material length scale in such a model.

Closed-form solutions of the wave propagation in a rate-independent localized softening bar, exhibiting an inviscid strong discontinuity, have been presented in ARMERO [1997a]. Similarly, we have presented in this last reference the analysis of discrete approximations that incorporate the singular fields of the strong discontinuity and thus avoiding the aforementioned mesh-size pathology in this inviscid limit.

The results presented in NEEDLEMAN [1988] and SLUYS [1992] for this same problem show the regularizing effects of the inclusion of viscosity in the inelastic material law. A material length scale is introduced in the material model, leading to finite element solutions converging to a finite shear band width, and avoiding the pathological mesh-dependence *in the limit, as this material length scale is resolved by the mesh*. See the

SOFTHENING VISCOPLASTICITYLOCALIZED VISCOS MODEL

**FIGURE I.6.2** 1D wave propagation problem. Solutions obtained with a classical viscoplastic model with strain-softening and a localized viscous model for a viscosity  $\eta = 1 \cdot 10^{-3}$ . The mesh-dependence for the classical viscoplastic model for coarse meshes can be seen alleviated with the use of a localized dissipative mechanism. Legend: — (h = 10), - - - (h = 5), ··· (h = 2.5), - · - (h = 1.67), - - - - (h = 1.25), — (h = 1).

SOFTENING VISCOPLASTICITYLOCALIZED VISCOS MODEL

**FIGURE I.6.3** 1D wave propagation problem. Solutions obtained with a classical viscoplastic model with strain-softening and a localized viscous model for a viscosity  $\eta = 1 \cdot 10^{-1}$ . The same solution is obtained in both cases, exhibiting a very low mesh dependence in this case of high viscosity. Legend: — ( $h = 10$ ), - - - ( $h = 5$ ), - · - - ( $h = 2.5$ ), - - - - - ( $h = 1.67$ ), - - - - - - ( $h = 1.25$ ), — ( $h = 1$ ).

aforementioned references for details. However, we should expect a bad performance by meshes not resolving the very small scale associated to typical materials of interest.

Figure I.6.2, left column, depicts the results obtained for the viscoplastic model characterized by the elastic relation  $\tau = G(\gamma - \gamma^p)$  in terms of the shear stress  $\tau$ , engineering shear strain  $\gamma = \partial v / \partial x$  and the plastic shear strain  $\gamma^p$ . The latter is defined by the viscoplastic evolution equations

$$\left. \begin{aligned} \dot{\gamma}^p &= \frac{<\phi>}{\eta} \text{sign}(\tau), \\ \dot{\alpha} &= \frac{<\phi>}{\eta}, \\ \phi &= |\tau| - \max\{\tau_y + \mathcal{H}\alpha, 0\}. \end{aligned} \right\} \quad (\text{I.6.1})$$

The following material properties are assumed: shear modulus  $G = 2 \cdot 10^4$ , initial yield limit  $\tau_y = 2$ , softening modulus  $\mathcal{H} = -1 \cdot 10^3$ , and viscosity parameter  $\eta = 1 \cdot 10^{-3}$ . The density of the material is  $\rho = 2 \cdot 10^{-8}$ , leading to an elastic wave speed of  $c = 2 \cdot 10^6$ . The initial sudden shear stress pulse applied to the layer is  $\tau_o = 0.75 \tau_y$ , leading to the yielding of the material upon the reflection of the wave. The dynamic governing equations are integrated through the trapezoidal rule with a consistent mass matrix. A time step of  $\Delta t = L/(200 c)$  is employed. The shear layer is discretized with different number of linear finite elements to study the effectiveness in resolving the localized shear band.

The top, left plot in Figure I.6.2 shows the displacement distribution along the bar for this case of (continuum) softening viscoplasticity. We observe for the fine meshes the sharp gradient of this distribution at the left end  $x = 0$ , thus obtaining the expected formation of the shear band. We can observe the converging approximation as the finite element size  $h$  is reduced. But we can observe at the same time the bad resolution of the final localized solution for large mesh sizes, leading to a strong mesh dependence for the coarse meshes. This dependence is illustrated by the plots in Figure I.6.2. We have included the evolution in time of the elastic energy in the shear layer

$$W_{elas} = \int_0^L \frac{1}{2} \frac{\tau^2}{G} dx, \quad (\text{I.6.2})$$

and the total dissipated energy

$$\mathcal{D} = W_{ext} - W_{elas} - K, \quad (\text{I.6.3})$$

for the applied external work (due to the applied stress at the right end)

$$W_{ext} = \int_0^t \tau_o v(L, t) dt, \quad (\text{I.6.4})$$

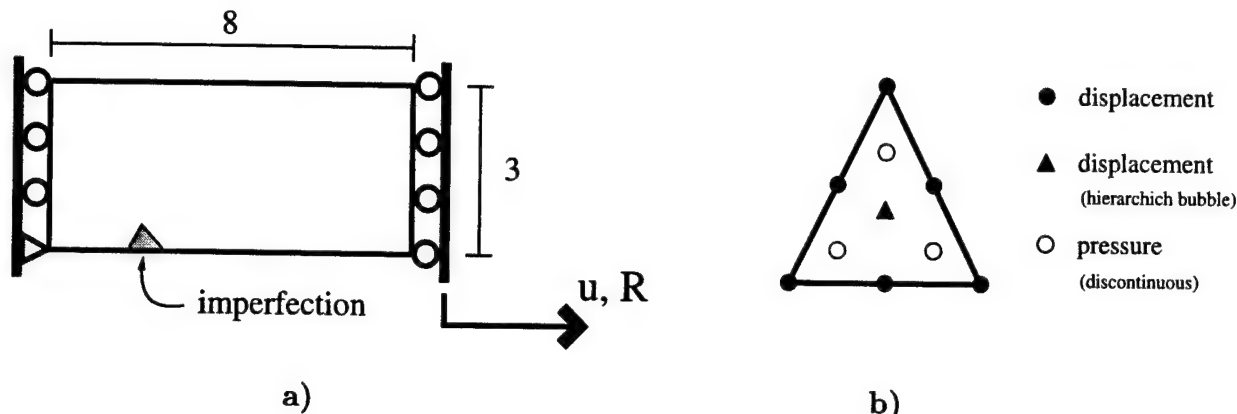


**FIGURE I.6.4** Plane strain tension test. a) Problem definition, with an imposed displacement  $\bar{u}$  at the right end and measured load  $R$ ; b) P2  $\oplus$  bubble /P1 element.

and the kinetic energy

$$K = \int_0^L \frac{1}{2} \rho v^2 dx . \quad (\text{I.6.5})$$

The strong dependence on the mesh-size if the localized zone is not resolved by the mesh is apparent.

To capture the localized dissipative mechanism associated to the shear band, we consider the localized viscous model developed in Section I.3 instead of the continuum inelastic equations (I.6.1), maintaining the linear elastic relation for the continuum. This is done only in the first element of the fixed end, once yielding is detected. The rest of the shear layer remains viscoplastic. We note that in this simple one-dimensional example the loss of ellipticity of the underlying rate-independent softening model occurs at the initiation of yielding; see Remark I.3.1. We note also that  $n \equiv 1$  in this one-dimensional case.

The localized softening modulus  $\tilde{\eta}_L$  and  $\tilde{\mathcal{H}}_L$  are defined through the scaling relations (I.4.14) and (I.4.18), respectively. The parameter  $w_s$  in (I.4.14)<sub>2</sub> is chosen as the element size that resolves the shear band. We note that this parameter is to be understood a numerical parameter and *not a material property*. The relation (I.4.14)<sub>2</sub> effectively switches from the localized dissipated mechanism associated to the strong discontinuity to a continuum dissipative as the element size goes below  $w_s$ .

Figure I.6.2, right column shows the result obtained with the localized viscous model. A value  $w_s = L/100$  is considered. We observe the completely different solutions for the coarse meshes, resolving more accurately the localized solution associated to the appearance of the shear band. Coarse meshes that were unable to give accurate solutions for the continuum model lead in this case to meaningful displacement distributions. In particular, the numerical solutions are seen to capture more accurately the evolution of the

**TABLE I.6.1** Plane strain tension test. Material properties.

|                               |                         |                   |
|-------------------------------|-------------------------|-------------------|
| Bulk Modulus                  | $\kappa$                | 164.206           |
| Shear Modulus                 | $\mu$                   | 80.1938           |
| Uniaxial Yield Limit          | $\sigma_y$              | 45.0              |
| Viscosity                     | $\eta$                  | $1 \cdot 10^{-3}$ |
| Localized softening modulus   | $\tilde{\mathcal{H}}_L$ | -12.0             |
| Localized viscosity parameter | $\tilde{\eta}_L$        | $1 \cdot 10^{-3}$ |

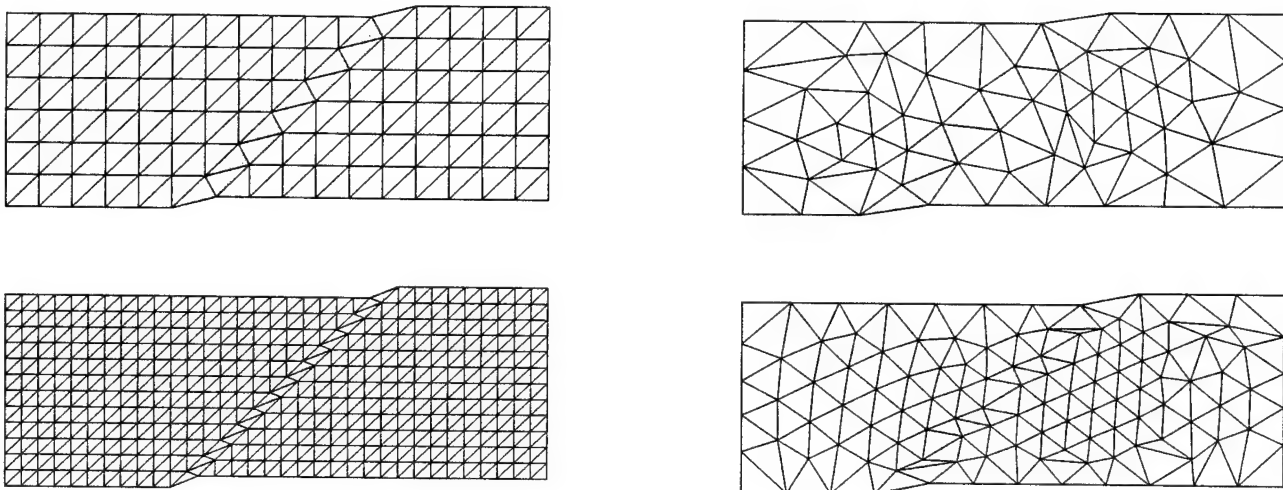
dissipation in time.

Figure I.6.3 shows the result obtained for a large viscosity  $\eta = 1 \cdot 10^{-1}$ . The solution in this case is essentially smooth, as shown in the displacement distribution. The localized viscous model is considered with  $w_s = L/2$ , leading for the assumed mesh sizes to a scaling parameter  $l = h$ . In this situation, the mesh resolves the details of the solution, leading both the continuum and the localized viscous models to the same solution in this 1D setting. A simple calculation shows that the localized viscous model (I.3.31) is obtained from the continuum model (I.6.1) with the identifications  $\gamma^p \leftarrow \xi/h$  (the regular part of the unresolved strains) and  $\alpha \leftarrow \tilde{\alpha}/h$  in this particular case ( $h < w_s$ ) of the one dimensional problem.

In conclusion, the proposed formulation, consisting basically of the appropriate scaling in this simple one dimensional setting, recovers the continuum solution as the spatial discretizations resolves the details of the localized solution, while leading to a more accurate resolution of the same in coarse meshes. The “large-scale regularization” of the localization of the strains in rate-dependent models is effectively obtained.

## I.6.2. The plane strain tension test

We consider the plane strain tension test in this second example. Complete numerical analyses of this benchmark problem can be found in TVERGAARD et al. [1981] and references therein. Figure I.6.4 depicts the problem under consideration. A  $8 \times 3$  block is stretched under an imposed displacement at one edge, while considering smooth boundary conditions at both ends. Quasi-static conditions are assumed in this case. The finite strain  $J_2$ -flow theory of viscoplasticity with the numerical implementation as discussed in SIMO [1992] is considered for the bulk response, in combination with the finite strain localized viscous model described in Section I.5. The material properties are summarized in Table I.6.1. In particular, perfect viscoplasticity is considered for the continuum model, and a linear localized softening law given by  $\tau_y = \sigma_y/\sqrt{3}$  and the localized softening modulus  $\tilde{\mathcal{H}}_L$ . See Table I.6.1. Due to the symmetry in the problem a small imperfection (0.1% reduction of the uniaxial yield limit  $\sigma_y$ ) is considered in an element of the lower boundary.



**FIGURE I.6.5** Plane Strain Tension test. Localized viscous model ( $\eta = 1 \cdot 10^{-3}$ ). Solutions computed with the P2⊕Bub/P1 triangle and enhanced localization modes in structured (192 and 768 elements) and unstructured (102 and 199 elements) meshes (End displacement = 0.08, deformations scaled by 5).

Different spatial discretizations, including structured and unstructured meshes, based on the  $P2 \oplus$ bubble /  $P1$  quadratic triangle depicted in Figure I.6.4.b are considered. This element can be shown to pass the LBB condition in the incompressible infinitesimal case (as proposed in CROUZEIX & RAVIART [1973]), avoiding the volumetric locking common in elastoplastic calculations. We note in this respect, and as discussed below, the appearance of the localized solution is preceded by a certain amount of bulk plastic flow.

The localized inviscid solution for this problem was reported in ARMERO & GARIKIPATI [1996]. Figure I.6.5 depicts the solution obtained in the case of a viscous discontinuity. The elements exhibiting active enhanced localization modes are shown in gray in Figure I.6.5. A perfectly viscoplastic material is assumed until localization is detected, resulting then in the consideration of the enhanced modes modeling the strong discontinuity with the corresponding localized softening law. A linear softening law is assumed. Elements outside the path of the discontinuity remain viscoplastic. As discussed in Remark I.3.1, the loss of ellipticity condition of the underlying rate-independent solid is considered to determine the orientation of the discontinuity. A closed-form expression for the current case of  $J_2$ -flow theory can be found in ARMERO & GARIKIPATI [1995]. We note that the discontinuity is propagated as the solution is computed, with no predetermined path. The reader is referred to ARMERO & GARIKIPATI [1996] for details on the initiation and propagation of the discontinuities.

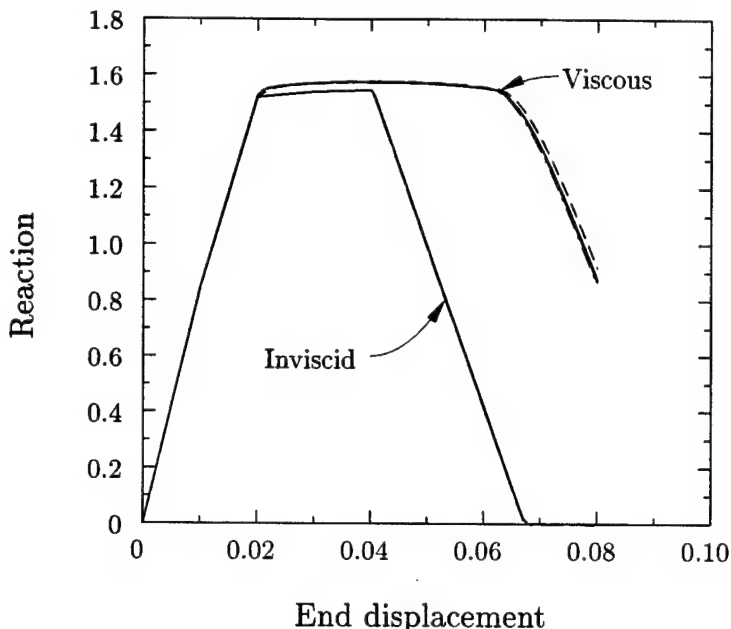


**FIGURE I.6.6** Plane Strain Tension test. Load/displacement curves for the localized viscous model and the inviscid limit model, computed with the P2+Bub/P1 triangle and enhanced localization modes in structured and unstructured meshes. Legend: Coarse unstructured mesh, 102 elements (—); Fine unstructured mesh, 199 elements (— · —); Coarse structured mesh, 192 elements (— · —); Fine structured mesh, 768 elements (—).

Figure I.6.6 depicts the load/displacement curves obtained in this case. The rate-independent solution is also included. In both the viscous and inviscid problems the solutions for four different meshes are included. Structured and unstructured meshes, involving from 102 to 768 elements, are considered; see Figure I.6.5. Almost a perfect overlapping of the curves can be observed. The low mesh sensitivity of the proposed methodology is apparent in this problem. We observe the stiffer response of the viscoplastic solution, with the appearance and propagation of the localized solution at a later deformation compared to the inviscid solution.

## I.7. Conclusions

The modeling of localized dissipative mechanisms in a local continuum has been accomplished with the use of the formalism of strong discontinuities. The case of elastoplastic discontinuities, and their viscous regularization, has been considered in both the infinitesimal and finite deformation ranges. In both cases, localized constitutive models have been

developed locally without the need of the introduction of (smearing) length scales. The inclusion of these models in the smooth problem governing the large-scale response of the solid identifies the length scales appearing in the modeling of localized solutions. The limit of interest as these scales vanish (the large-scale limit) identifies the structure of a local continuum incorporating the localized dissipation characteristic of the localized failure of common materials.

A first application of the previous developments is the formulation of sound constitutive models incorporating objectively a localized dissipation. Rate-independent continuum models are known for the absence of a characteristic length defining the small scales of the final localized solutions, leading to the limit case of strong discontinuity. The proposed formulation identifies the localized dissipation characteristic of these solutions, thus leading to a large-scale model of the phenomenon of strain localization with the correct (objective) energy dissipation.

The large-scale regularization of rate-dependent models has been introduced as a second application of the proposed approach. In this viscous case, the continuum models are known to incorporate the length scales required to define the observed localized dissipation. The small scales involved in these solutions when compared with typical scales of the practical applications of interest lead to numerical solutions with a strong mesh-dependence, unless costly spatial discretizations resolving the small scales are considered. The proposed approach models effectively the unresolved scales through the consideration of strong discontinuities, the large-scale limit. Furthermore, the proper scaling of the associated localized mechanism allows the recovery of the proper dissipation as the small scales are resolved.

## References

- ARMERO, F. [1997a] "On the Characterization of Localized Solutions in Inelastic Solids: An Analysis of Wave Propagation in a Softening Bar," SEMM/UCB Report no. 97/18, submitted for publication.
- ARMERO, F. [1997b] "Formulation and Numerical Analysis of a Localized Anisotropic Damage Model," SEMM/UCB Report no. 97/11.
- ARMERO, F. & GARIKIPATI, K. [1995] "Recent Advances in the Analysis and Numerical Simulation of Strain Localization in Inelastic Solids," *Proc. COMPLAS IV*, eds. D.R.J. Owen, E. Onate, and E. Hinton, CIMNE, Barcelona.

- ARMERO, F. & GARIKIPATI, K. [1996] "An Analysis of Strong Discontinuities in Multiplicative Finite Strain Plasticity and their Relation with the Numerical Simulation of Strain Localization in Solids," *Int. J. Solids and Structures*, **33**, 2863-2885.
- ASARO, R.J. [1983] "Micromechanics of Crystals and Polycrystals," in *Advances in Applied Mechanics*, **23**, 1-115.
- BAI, Y. & DODD, B. [1992] *Adiabatic Shear Localization; Occurrence, Theories and Localization*, Pergamon Press, Oxford.
- BAZANT, Z.P.; BELYTSCHKO, M. & CHANG, T.P. [1984] "Continuum Theory for Strain-Softening", *J. Eng. Mech., ASCE*, **110**, 1666-1691.
- BAZANT, Z. & BELYTSCHKO, T. [1985] "Wave Propagation in a Strain Softening Bar," *ASCE J. Eng. Mech.*, **111**, 381-389.
- BAZANT & OH [1983] "Crack Band Theory for Fracture of Concrete," *Materials and Structures*, RILEM, **16**, 155-177.
- BELYRSCHKO, T.; FISH, J. & ENGELMANN, B.E. [1988] "A Finite Element with Embedded Localization Zones," *Comp. Meth. Appl. Mech. Eng.*, **70**, 59-89.
- BELYTSCHKO, T.; MORAN, B. & KULKARNI M. [1991] "On the Crucial Role of Imperfections in Quasi-Static Viscoplastic Solutions," *Journal of Applied Mechanics*, **58**, 658-665.
- DEBORST, R. & SLUYS, L.J. [1991] "Localization in a Cosserat Continuum under Static and Loading Conditions", *Comp. Meth. Appl. Mech. Eng.*, **90**, 805-827.
- COLEMAN, B.D. & HODGON, M.L. [1985] "On Shear Bands in Ductile Materials", *Arch. Rat. Mech. Anal.*, **90**, 219-247.
- CROUZEIX, M.& RAVIART, P.A. [1973] "Conforming and nonconforming finite element methods for solving the stationary Stokes equations", *R.A.I.R.O. Anl. Numer.*, **7**, 33-76.
- DVORKIN, E.; CUITIÑO, A. & GOIA, G. [1990] "Finite Elements with Displacement Interpolated Embedded Localization Lines Insensitive to Mesh and Distortions," *Int. J. Num. Meth. Eng.*, **30**, 541-564.
- HILL, R. [1950] *The Mathematical Theory of Plasticity*, Clarendon Press, Oxford.
- HILL, R. [1962] "Acceleration Waves in Solids," *J. Mech. Phys. Solids*, **16**, 1-10.
- HILLERBORG, A.; MODEER, M. & PETERSSON, P. [1976] "Analysis of Crack Formation and Crack Growth in Concrete by Means of Fracture Mechanics and Finite Elements," *Cement and Concrete Research*, **6**, 773-782.
- PIJAUDIER-CABOT, G.; BODE, L. & HUERTA, A. [1995] "Arbitrary Lagrangian-Eulerian

- Finite Element Analysis of Strain Localization in Transient Problems," *Int. J. Numer. Meth. Eng.*, **38**, 4171-4191.
- JOHNSON, C. [1976] "Existence Theorems for Plasticity Problems," *J. Math. Pures et Appliq.* **55**, 431-444.
- LARSSON, R. & RUNESSON, K. [1996] "Element Embedded Localization Band Based on Regularized Displacement Discontinuity", *J. Eng. Mech.*, **122**, 402-411.
- LAURSEN, T.A. [1994] "The Convected Description in Large Deformation Frictional Contact Problems," *Int.J. Solids Structures*, **31**, 669-681.
- LEROUY, Y. & ORTIZ, M. [1990] "Finite Element Analysis of Transient Strain Localization Phenomena in Frictional Solids", *Int.J. Numer. Analyt. Meth. Geom.*, **14**, 93-124.
- LUBLINER, J. [1990] *Plasticity Theory*, Macmillan Publishing Company, New York.
- MANDEL, J. [1966] "Conditions de Stabilité et Postulat de Drucker", in *Rheology and Soli Mechanics*, IUTAM Symposium, Grenoble 1964, ed. by J. Kravtchenko and P.M. Sirieys, 58-68.
- MATTHIES, H.; STRANG, G. & CHRISTIANSEN, E. [1979] "The Saddle Point of a Differential Program," in *Energy Methods in Finite Element Analyses*, edited by Glowinski, Rodin & Zienkiewicz, John Wiley & Sons, London.
- MOLINARI, A. & CLIFTON, R.J. [1987] "Analytical Characterization of Shear Localization in Thermoviscoplastic Materials," *Journal of Applied Mechanics*, **54**, 806-812.
- MÜHLHAUS, H.B. & VARDOLAKIS, I. [1987] "The Thickness of Shear-Bands in Granular Materials," *Geotechnique*, **35**, 299-317.
- NACAR, A.; NEEDLEMAN, A. & ORIZ, M. [1989] "A Finite Element Method for Analyzing Localization in Rate Dependent Solids at Finite Strains," *Comp. Meth. Appl. Mech. Eng.*, **73**, 235-258.
- NEEDLEMAN, A. [1988] "Material Rate Dependence and Mesh Sensitivity in Localization Problems," *Comp. Meth. Appl. Mech. Eng.*, **67**, 69-85.
- NEEDLEMAN, A. & TVERGAARD, V. [1984] "Finite Element Analysis of Localization in Plasticity," in *Finite Elements. Special Problems in Solid Mechanics*, Volume V, ed. by J.T. Oden and G.F. Carey, Prentice Hall, Englewood Cliffs.
- NEILSEN, M.K. & SCHREYER, H.L. [1993] "Bifurcation in Elastic-Plastic Materials," *Int. J. Solids Struct.*, **30**, 521-544.
- OLIVER, J. [1989] "A Consistent Characteristic Length for Smeared Cracking Problems", *Int. J. Num. Meth. Eng.*, **28**, 461-474.
- OLIVER, J. [1996] "Modelling Strong Discontinuities in Solid Mechanics via Strain Soft-

- ening Constitutive Equations. Part 1: Fundamentals. Part 2: Numerical Simulation," *Int. J. Num. Meth. Eng.*, **39**, 3575-3623.
- ORTIZ, M.; LEROY, Y. & NEEDLEMAN, A. [1987] "A Finite Element Method for Localized Failure Analysis," *Comp. Meth. Appl. Mech. Eng.*, **61**, 189-214.
- OTTOSEN, N.S. & RUNESSON, K. [1991] "Properties of Discontinuous Bifurcation Solutions in Elasto-Plasticity," *Int. J. Solids Struct.*, **27**, 401-421.
- PIETRSZCZAK, ST. & MRÓZ, Z. [1981] "Finite Element Analysis of Deformation of Strain-Softening Materials," *Int. J. Numer. Meth. Eng.*, **17**, 327-334.
- PRANDTL, L. [1920] "Ueber die Haerte Plastischer Koerper," *Goettinger Nachrichten*, 74-84.
- READ, H.E. & HEGEMEIER, G.A. [1984] "Strain Softening of Rock, Soil and Concrete; a Review Article," *Mechanics of Materials*, **3**, 271-294.
- RICE, J. [1976] "The Localization of Plastic Deformations", in *Theoretical and Applied Mechanics*, ed. by W.T. Koiter, 207-219.
- ROTS, J.G.; NAUTA, P.; KUSTERS, G. & BLAAUWENDRAA, T. [1985] "Smeared Crack Approach and Fracture Localization in Concrete," *Heron*, **30**.
- SIMO, J.C. [1992] "Algorithms for Multiplicative Plasticity that Preserve the Form of the Return Mappings of the Infinitesimal Theory," *Comp. Meth. Appl. Mech. Eng.* **99**, pp.61-112.
- SIMO, J.C. & HUGHES, T.J.R. [1997] *Plasticity and Viscoplasticity, Formulation and Numerical Analysis*, Springer Verlag, preprint.
- SIMO, J.C; OLIVER, J. & ARMERO, F. [1993] "An Analysis of Strong Discontinuities Induced by Softening Solutions in Rate Independent Solids," *J. Comput. Mech.*, **12**, 277-296.
- SIMO, J.C. & RIFAI, S. [1990] "A Class of Mixed Assumed Strain Methods and the Method of Incompatible Modes," *Int. J. Num. Meth. Eng.*, **29**, 1595-1638.
- SLUYS, L.J. [1992] "Wave Propagation, Localisation and Dispersion in Softening Solids" Ph.D. Dissertation, Delft Technologycal University, The Netherlands.
- STAKGOLD, I. [1979] *Green's Functions and Boundary Value Problems*, Wiley, New York.
- SUQUET, P.M. [1981] "Sur les Equations de la Plasticité: Existence et Régularité des Solutions," *Journal de Mécanique*, **20**, 3-39.
- TEMAM, R. [1984] *Mathematical Problems in Plasticity*, Gauthier-Villars, Paris.
- THOMAS, T.Y. [1961] *Plastic Flow and Fracture in Solids*, Academic Press.

- TRUESDELL & NOLL [1965] "The Nonlinear Field Theories of Mechanics," *Handbuch der Physik Bd. III/3*, ed. by S. Fluegge, Springer Verlag, Berlin.
- TVERGAARD, V.; NEEDLEMAN, A. & LO, K.K. [1981] "Flow Localization in the Plane Strain Tensile Test," *Jour. Mech. Phys. Solids*, **29**, 115-142.
- VARDOULAKIS, I. [1979] "Formation of Shear Bands in Sand Bodies as a Bifurcation Problem," *Int. J.*, **32**, 35-54.

## **APPENDIX II**

### **Analysis of Strong Discontinuities under Fully Coupled Thermomechanical Conditions**

**Based on the paper:**

Armero, F. and Park, J.G. [1999] "An Analysis of Wave Propagation in a Softening Shear Layer under Fully Coupled Thermo-Mechanical Conditions," to be submitted to *International Journal of Solids and Structures*.

## II.1. Introduction

The failure of many engineering materials is often preluded by the localization of strain in a narrow zone. In typical metals and soils, these zones involve the localization of the shear strain and are, therefore, called shear bands. Shear bands are the results of large plastic deformation and usually a precursor to the abrupt collapse of the material or structure. Due to its practical and theoretical importance, shear banding has been extensively studied during the last decades. Typical cases of strain localization include adiabatic shear banding in metals (BAI & DODD [1992]) and shear banding in soils (VARDOULAKIS [1978]), or the localization of cracking in brittle materials (READ & HEGEMEIER [1984]), among others. All these phenomena have been observed together with an overall strain-softening response of the material.

The *narrowness* of a localized band is a relative term related to its geometrical dimension. It can be of order of microns in a ductile metal, or in order of milimeters in geological problems. This fact shows the existence of internal length scale corresponding to each material, which requires a multi-scale mechanism to capture the characteristics of the different scales correctly.

Standard rate-independent constitutive models lack this internal length scale. Therefore, a localized band of finite length is not possible without further modification of the constitutive relation. Furthermore, the strain-softening behavior in a local continuum makes the problem ill-posed, as it has been extensively studied by THOMAS [1961], HILL [1962], RICE [1976], and NEILSEN & SCHREYER [1993], among many others. In this case, the mechanical tangent loses its ellipticity, and as a result, the type of the boundary value problem changes. Due to this inconsistency, finite element solutions are known to exhibit spurious mesh-size dependence; see e.g. TVERGAARD et al. [1981] and PIETRSZCZAK & MRÓZ [1981].

The relative narrowness of the localization bands leads to the idea of the infinite strain in a band of zero width. This limiting process corresponds to a discontinuous displacement across a surface. The term *strong discontinuity* comes from the fact that the solution exhibits a discontinuity in the displacement field, to be contrasted with a *weak discontinuity*. In the latter case, the solution has a discontinuity in the strain field. The existence of strong discontinuities has been shown through mathematical analyses of the boundary value problem of rate-independent perfect plasticity by JOHNSON [1976] and MATTHIES et al [1979], among others.

An analysis of wave propagation in a softening bar was done in BAZANT & BE-LYTSCHKO [1985]. A one-dimensional bar under a stress pulse at both ends starts yielding when the two pulses meet at the center of the bar. The exact closed-form solution was obtained by these authors under the assumption of continuum strain-softening upon yielding. Since the inelastic effect were localized on a surface (volume of zero width), no energy is dissipated in this solution. Clearly, this is not physically meaningful.

These considerations clearly motivate the introduction of a localized dissipative mechanism. In this way, we study in this report the same one-dimensional problem accounting for these localized effects in the general coupled thermo-mechanical range, extending the analysis presented in ARMERO [1997a] for the isothermal case. It is well-known that a large proportion of plastic work is converted into heat (see e.g. BAI & DODD [1992] Ch.1). This heat increases the temperature field in a shear band and usually reduces the yield limit of the material as it is the case in ductile metals. This phenomenon is referred to as thermal softening. When thermal softening is stronger than mechanical hardening, an instability may appear and lead to the localization of the inelastic effects in the form of a band. Furthermore, if it yields fast enough such that there is no time for the heat to diffuse away from the shear band, the yield process might be called to be *adiabatic*. For all these cases, the modeling of the interaction between mechanical and temperature fields is crucial for the correct characterization of the material response. It should be noted that due to the nature of heat conduction, perfect adiabatic conditions are always approximate.

The analyses presented herein make use of the concept of strong discontinuity to model the resulting localized effects. As mentioned above, a localized dissipative mechanism is required to explain the energy loss during yielding. In this context, SIMO et al [1993] and ARMERO & GARIKIPATI [1995] presented a *localized dissipative mechanism* satisfying this requirement. The final models consist of large-scale stress-strain constitutive relation and small-scale stress-displacement relation along the discontinuity. We use this mechanism to simulate the behavior of a strain-softening material. It is also noted that this mechanism is activated when the problem becomes ill-posed otherwise. The governing field equations, the linear momentum and energy balance are considered under the assumption of small strain and small deformation. The temperature field remains continuous, while the heat flow becomes discontinuous accounting for the localized heat source associated to the plastic dissipation along the discontinuity.

An outline of the rest of this report is as follows. The first part presents a spectral analysis of the linearized thermo-elastoplastic initial boundary value problem involving a classical continuum model with strain-softening. The definition of the problem and several main concepts are defined in Section 2.1. Then, the linearized stability analyses follow in Sections 2.2 and 2.3. The existence of an internal length-scale is briefly remarked here. The implication of these results based on the linearized problem for the finite element simulations of the localized solutions are presented in Section 2.4. The appearance of the mesh-size dependence is illustrated in the ill-posed problems.

The second part of this report deals with the one-dimensional problem of the wave propagation in a softening shear layer. An inviscid-elasto-thermoplastic model is considered. Section 3 summarizes the problem definition and the closed-form exact solutions in the case of vanishing thermal softening. In fully coupled cases, numerical solutions using a finite difference scheme are presented. Next, we consider the approximate solution of the same problem in Section 4. A finite local neighborhood accounting for the localized

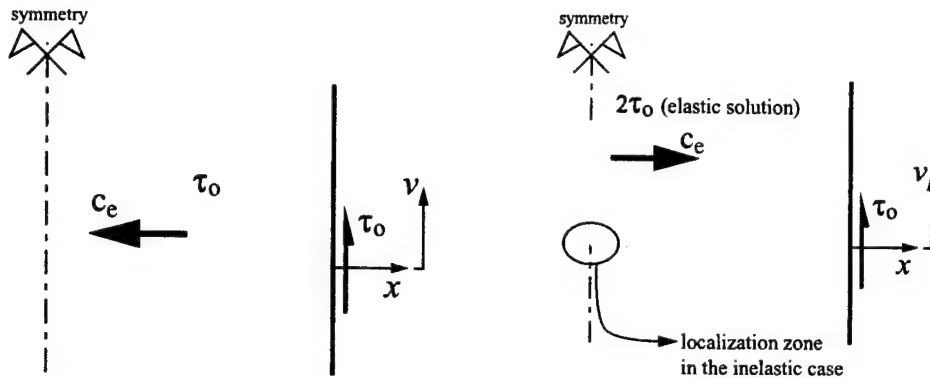


**FIGURE II.2.1** One-dimensional shear layer: problem definition and elastic solution. A stress pulse propagates at the elastic wave speed  $c_e$  from both ends. On reaching the center, the stress pulse doubles in intensity in the elastic solution. For the inelastic case with  $\tau_o > \tau_y$  the localization zones appears at the center.

softening is introduced to model the finite element spatial discretization. The effect of this discretization is discussed here analytically. Finally, we compare representative finite element simulations with the analytic solutions. The extentions to multi-dimensional problems are presented in Section 5.

## II.2. A Spectral Analysis of the Linearized Problem

This section introduces the linearized local form of the governing equations , consisting of the equation of motion and the heat equation. These equations are coupled by the thermal softening of the material and by the energy release induced by the plastic flow. No thermoelastic coupling effects are present for the pure shear problem of interest.

In purely mechanical problems, when the mechanical tangent modulus becomes negative, the equation of motion loses its hyperbolic form and becomes elliptic for the general dynamic problem. This transition changes the characteristics of its solution. We investigate these issues in this section through a spectral analysis of the linearized problem.

### II.2.1. Problem definition

We consider the one-dimensional problem of a layer under shear stress (see Figure II.2.1).

The governing coupled partial differential equations are

$$\left. \begin{aligned} \rho \dot{v} &= \frac{\partial \tau}{\partial x}, \\ \dot{\tau} &= G(\dot{\gamma} - \dot{\gamma}^p), \\ \eta \dot{\gamma}^p &= \phi(\tau, \gamma^p, \vartheta), \\ \rho c_v \dot{\vartheta} &= \kappa \frac{\partial^2 \vartheta}{\partial x^2} + \chi \tau \dot{\gamma}^p. \end{aligned} \right\} \quad (\text{II.2.1})$$

Here,  $\kappa$  and  $c_v$  denote the thermal conductivity and the specific heat capacity, respectively. The velocity  $v$ , shear modulus  $G$ , shear stress  $\tau$ , shear strain  $\gamma$ , plastic strain  $\gamma^p$ , relative temperature  $\vartheta$  and hardening modulus  $H$  follow conventional notations. The elastic limit is denoted by  $\tau_e$ . The equation of motion is expressed in (II.2.1)<sub>1</sub>, elastic stress-strain relation in (II.2.1)<sub>2</sub>, flow rule in (II.2.1)<sub>3</sub>, and heat equation in (II.2.1)<sub>4</sub>. The time derivative of a quantity is expressed by single dot. An associated plastic potential function

$$\phi := \tau - [\tau_e(1 - w_0 \vartheta) + H \gamma^p] \quad (\text{II.2.2})$$

is assumed in this report, with the linear thermal softening constant  $w_0$ . Viscoplastic effects are considered by a constant viscosity  $\eta$ . The last term of (II.2.1)<sub>4</sub> represents the heat source produced by the mechanical energy release. In particular, the Taylor coefficient  $\chi$  represents the fraction of the plastic work converted into heat.

The linearized version of (II.2.1) at a solution  $\tau_o$ ,  $v_o$ ,  $\vartheta_o$ ,  $\gamma_o^p$ , and  $\dot{\gamma}_o^p$  are

$$\left. \begin{aligned} \rho \dot{v} &= \frac{\partial \tau}{\partial x}, \\ \dot{\tau} &= G(\dot{\gamma} - \dot{\gamma}^p), \\ \dot{\tau} &= -\tau_e w_0 \dot{\vartheta} + H \dot{\gamma}^p + \eta \ddot{\gamma}^p, \\ \rho c_v \dot{\vartheta} &= \kappa \frac{\partial^2 \vartheta}{\partial x^2} + \chi(\tau_o \dot{\gamma}^p + \tau \dot{\gamma}_o^p). \end{aligned} \right\} \quad (\text{II.2.3})$$

A general wave type small perturbations of this problem is given by

$$\left. \begin{aligned} \tau &= \hat{\tau} e^{I(\lambda x - \omega t)}, \\ v &= \hat{v} e^{I(\lambda x - \omega t)}, \\ \vartheta &= \hat{\vartheta} e^{I(\lambda x - \omega t)}, \\ \gamma^p &= \hat{\gamma}^p e^{I(\lambda x - \omega t)}, \end{aligned} \right\} \quad (\text{II.2.4})$$

with  $I := \sqrt{-1}$ . A complex wave number  $\lambda$  and an angular frequency  $\omega$  are assigned with full generality. For convenience of the calculations to follow, we use  $\alpha := -\omega I$  (the complex angular frequency), alternatively.

The introduction of the expressions (II.2.4) into the governing equations (II.2.3) leads to the dispersion equation

$$[\alpha + \bar{\kappa}\lambda^2][(1 + \alpha T)\alpha^2 + c_e^2(S + \alpha T)\lambda^2] - R\alpha[-V\alpha + (\alpha^2 + c_e^2\lambda^2)] = 0. \quad (\text{II.2.5})$$

This is the main equation that we analyze in the following sections. Several parameters have been introduced in (II.2.5). They are defined as

$$\left. \begin{aligned} S &:= \frac{H}{G+H}, & R &:= \frac{\chi\tau_e^2 w_0}{\bar{c}_v(G+H)}, & \bar{c}_v &:= \rho c_v, \\ \bar{\kappa} &:= \frac{\kappa}{\bar{c}_v}, & T &:= \frac{\eta}{G+H}, \\ c_e^2 &:= \frac{G}{\rho}, & V &:= \frac{G\dot{\gamma}^p o}{\tau_e}. \end{aligned} \right\} \quad (\text{II.2.6})$$

The nondimensional parameters  $S$  and  $R$  represent the relative mechanical hardening and the relative thermal softening, respectively. The range of these parameters is

$$\left. \begin{aligned} \bar{c}_v &> 0, & G &> 0, & \rho &> 0, & G+H &> 0, \\ 0 &\leq R < 1, & \bar{\kappa} &\geq 0, & T &\geq 0, \\ -\infty &< S < 1. \end{aligned} \right\} \quad (\text{II.2.7})$$

Before proceeding to the analysis, we define first several fundamental concepts employed in the discussions that follow. A solution is called (linearly) *stable* when the real part of  $\alpha$  is negative, so that the amplitude of a perturbation decreases in time. The term (linearly) *unstable* describes the opposite case. In other words, we have

$$\begin{aligned} Re(\alpha) &> 0 \rightarrow \text{instability}, \\ Re(\alpha) &< 0 \rightarrow \text{stability}. \end{aligned} \quad (\text{II.2.8})$$

For the case  $Re(\alpha) = 0$ , the multiplicity of the roots (II.2.5) needs to be investigated.

A related concept is the *well-posedness* of the problem, as first introduced by HADAMARD [1903]. It describes the conditions under which the governing equations have a unique solution depending continuously on the data. Defining  $\Omega := \sup_{\lambda} [Re(\alpha)]$  following ZAUDERER [1989], we have

$$\begin{aligned} \Omega &< +\infty \rightarrow \text{well-posed}, \\ \Omega &= +\infty \rightarrow \text{ill-posed}. \end{aligned} \quad (\text{II.2.9})$$

Compared with (II.2.8), it is clear that instability precedes ill-posedness.

In this context, the following analysis is divided into two parts. First, we investigate the stability for several material properties. Second, the well-posedness of the problem is studied. Additionally, internal length scales of the problem is remarked.

### II.2.2. Linearized stability analysis

We rewrite the dispersion equation (II.2.5) as a fourth order polynomial in  $\alpha$ , namely,

$$a_0\alpha^4 + a_1\alpha^3 + a_2\alpha^2 + a_3\alpha + a_4 = 0 \quad (\text{II.2.10})$$

with real coefficients  $a_0$  to  $a_4$  for real wave numbers  $\lambda$ , as it is assumed in this section. Simple algebraic manipulations lead to

$$\begin{aligned} a_0 &= T, \\ a_1 &= 1 - R + \lambda^2 \bar{\kappa}T, \\ a_2 &= \lambda^2(\bar{\kappa} + c_e^2 T) + RV, \\ a_3 &= \lambda^2 c_e^2(S - R) + \lambda^4 c_e^2 \bar{\kappa}T, \\ a_4 &= \lambda^4 \bar{\kappa} c_e^2 S. \end{aligned} \quad (\text{II.2.11})$$

The stability (i.e.,  $\operatorname{Re}(\alpha) < 0$ ) of the general quartic equation (II.2.10) is characterized by the Routh-Hurwitz criterion (GANTMACHER [1964]). This criterion states that the roots of (II.2.10) have negative real parts if and only if

$$\begin{aligned} P_1 &:= a_1 > 0, & P_2 &:= a_1 a_2 - a_3 a_0 > 0, \\ P_3 &:= a_1 a_2 a_3 - a_1^2 a_4 - a_3^2 a_0 > 0, & \text{and} & P_4 := a_4 > 0. \end{aligned} \quad (\text{II.2.12})$$

These criteria need to be satisfied for all real wave number  $\lambda > 0$ . It is clear from (II.2.11) that  $P_1 > 0$  when  $R < 1$ . Manipulations (II.2.11) and (II.2.12), we obtain

$$P_2 = (1 - R)(\lambda^2 \bar{\kappa}^2 + RV) + \lambda^2 \bar{\kappa} T RV + \lambda^2 c_e^2 T(1 - S) + \lambda^4 \bar{\kappa}^2 T \quad (\text{II.2.13})$$

and

$$\begin{aligned} P_3 &= \lambda^8(1 - S)\bar{\kappa}^3 c_e^2 T^2 \\ &+ \lambda^6(c_e^2 \bar{\kappa}^2 T[(S - 1)(2R - 1) + RTV] + c_e^4 T^2 \bar{\kappa}(1 - S)) \\ &+ \lambda^4([c_e^2 \bar{\kappa}(1 - 2R + S)RV - c_e^4(S - R)(S - 1)]T - c_e^2 \bar{\kappa}(1 - R)R(1 - S)) \\ &+ \lambda^2 c_e^2(1 - R)R(S - R). \end{aligned} \quad (\text{II.2.14})$$

From (II.2.13), since  $S < 1$  always,  $P_2 > 0$  if  $R < 1$ . In addition, the coefficients of  $\lambda^6$  and  $\lambda^4$  in (II.2.14) are positive when

$$T > \frac{\bar{\kappa}}{c_e^2} \max \left[ \frac{(S - 1)(1 - 2R)}{(1 - S) + \bar{\kappa} RV/c_e^2}, \frac{(1 - R)R(1 - S)}{(S - R)(1 - S) + VR\bar{\kappa}(1 - 2R + S)/c_e^2} \right] \quad (\text{II.2.15})$$

and

$$S > R, \quad R < 1. \quad (\text{II.2.16})$$

The above conditions show that when we have linear thermal softening, mechanical hardening needs to be stronger than thermal softening, and additionally, enough viscosity is needed for the solution to be stable. This result takes full account of the heat conduction effects (through  $\bar{\kappa}$ ) and, more importantly, of the elastic effects of the material (finite  $c_e$ ). This situation is to be contrasted with the classical linearized stability analyses based on a rigid-thermo-visco-plastic stress-strain law (see the complete survey in BAI & DODD [1992]).

We consider next several particular cases. First, the inviscid problem is characterized by the dispersion relation

$$b_0\alpha^3 + b_1\alpha^2 + b_2\alpha + b_3 = 0 \quad (\text{II.2.17})$$

with

$$\begin{aligned} b_0 &= 1 - R, & b_1 &= \lambda^2\bar{\kappa} + RV, \\ b_2 &= \lambda^2c_e^2(S - R), & b_3 &= \lambda^4\bar{\kappa}c_e^2S, \end{aligned} \quad (\text{II.2.18})$$

from (II.2.5) by setting  $T = 0$ . The Routh-Hurwitz criterion for this case is given by

$$P_i := b_i > 0 (i = 0, 1, 2, 3), \quad P_4 := b_1b_2 - b_0b_3 > 0. \quad (\text{II.2.19})$$

The first condition in (II.2.19) is satisfied if  $R < 1$  and  $S > R$ . However,

$$P_4 = \lambda^4c_e^2\bar{\kappa}[-1 + S]R + \lambda^2c_e^2P(S - R) \quad (\text{II.2.20})$$

and since  $S < 1$ , the second condition can not be satisfied for all  $\lambda$ . In other words, the solution is always unstable under the presence of thermal softening  $R > 0$  when  $T = 0$  (inviscid), for  $c_e$  finite and  $\bar{\kappa} \neq 0$ , consistent with the remarks above.

In the adiabatic limit  $\bar{\kappa} = 0$ , the dispersion equation reduces to (II.2.17) with coefficients

$$\begin{aligned} b_0 &= T, & b_1 &= 1 - R, \\ b_2 &= \lambda^2c_e^2T + RV, & b_3 &= \lambda^2c_e^2(S - R). \end{aligned} \quad (\text{II.2.21})$$

It is observed that  $P_0$ ,  $P_1$ ,  $P_2$ , and  $P_3$  are positive if  $T > 0$ ,  $R < 1$  and  $S > R$  using (II.2.19) and (II.2.21). Additionally,

$$P_4 = T(1 - S)\lambda^2c_e^2 + (1 - R)RV, \quad (\text{II.2.22})$$

is positive when  $R < 1$ . These results indicate that the solution is stable when  $S > R$  and  $R < 1$ , with viscosity  $T > 0$ . Here, the existence of viscosity  $T$  is sufficient for the stability regardless of its magnitude.

The case of vanishing  $T$  in (II.2.21) represents the inviscid-adiabatic case. The complex frequency  $\alpha$  is given in this case by the closed-form solution

$$\alpha = \frac{-RV}{2(1 - R)} \pm \frac{\sqrt{R^2V^2 - 4(1 - R)(S - R)}}{2(1 - R)}c_e\lambda. \quad (\text{II.2.23})$$

Clearly when  $S > R$ ,  $\text{Re}(\alpha) < 0$ , independently of the underlying rate V; in other words, stability.

### II.2.3. Investigation of the ill-posedness

The complex frequency  $\alpha$  is the root of the polynomial (II.2.5) with real coefficients. The roots of a polynomial can only become unbounded when the coefficients of the polynomial become unbounded; in our case,  $\lambda \rightarrow \infty$ . We are interested in the limit values of  $\text{Re}(\alpha)$  to decide *ill-posedness* of a given problem as defined in (II.2.9). In the following asymptotic analysis, the solutions in the limit  $\lambda \rightarrow \infty$  are investigated to that purpose.

For the dispersion relation (II.2.5), a general asymptotic solution  $\alpha = a\lambda^n$  is assumed ( $n \geq 0$ ) for a general complex number  $a$ . The introduction of this solution into (II.2.5) leads to

$$\begin{aligned} a^4\lambda^{4n}T + a^3\lambda^{3n}[(1-R) + \lambda^2\bar{\kappa}T] + a^2\lambda^{2n}[\lambda^2(\bar{\kappa} + c_e^2T) + RV] \\ + a\lambda^n[\lambda^2c_e^2(S-R) + \lambda^4c_e^2\bar{\kappa}T] + \lambda^4\bar{\kappa}c_e^2S = 0. \end{aligned} \quad (\text{II.2.24})$$

The leading term of the resulting polynomial needs to be zero to satisfy the above dispersion equation *asymptotically*. When  $n = 0$ , the leading term is  $\lambda^4$ , so we must have

$$[ac_e^2\bar{\kappa}T + \bar{\kappa}c_e^2S] = 0. \quad (\text{II.2.25})$$

Therefore, we conclude that

$$a = -\frac{S}{T}. \quad (\text{II.2.26})$$

For  $n = 1$ , the leading term is  $\lambda^5$ , and its coefficient is

$$a\bar{\kappa}T[a^2 + c_e^2] = 0 \implies a = \pm Ic_e. \quad (\text{II.2.27})$$

For all other cases of  $n$ ,  $a = 0$ . In summary, we conclude that

$$\Omega := \sup_{\lambda}[\text{Re}(\alpha)] < +\infty \quad (\text{II.2.28})$$

for all the possible n's ( $\geq 0$ ), showing that the viscosity makes problem well-posed regardless of thermal softening or mechanical hardenings.

Likewise, the dispersion relation of the inviscid problem (II.2.17) and (II.2.18) becomes

$$a^3\lambda^{3n}(1-R) + a^2\lambda^{2n}[\lambda^2\bar{\kappa} + RV] + a\lambda^{2+n}c_e^2(S-R) + \lambda^4\bar{\kappa}c_e^2S = 0. \quad (\text{II.2.29})$$

For  $n = 1$ , the leading term is  $\lambda^4$  and

$$[a^2\bar{\kappa} + \bar{\kappa}c_e^2S] = 0 \implies a = \pm c_e\sqrt{SI}. \quad (\text{II.2.30})$$

The above equation shows that the real part of the solution is unbounded when  $S < 0$ , that is, when we have mechanical softening. To make  $\lambda^6$  a leading term,  $n = 2$  is set and

$$[a^3(1 - R) + a^2\bar{\kappa}] = 0 \implies a = -\frac{\bar{\kappa}}{1 - R}. \quad (\text{II.2.31})$$

When  $R > 1$ ,  $a > 0$  and the solution is unbounded. The solution of the inviscid problem is ill-posed then when  $S < 0$  or  $R > 1$ .

The dispersion equation of the adiabatic problem (II.2.17) and (II.2.21) becomes

$$a^3\lambda^{3n}T + a^2\lambda^{2n}(1 - R) + a(\lambda^2c_e^2T + RV) + \lambda^2c_e^2(S - R) = 0. \quad (\text{II.2.32})$$

When  $\lambda^2$  is the leading term,  $n = 0$  and its limit becomes

$$[ac_e^2T + ce^2(S - R)] = 0, \implies a = -\frac{S - R}{T} \quad (\text{II.2.33})$$

as  $\lambda \rightarrow \infty$ . When  $\lambda^3$  is the leading term,  $n = 1$  and

$$[a^3T + c_e^2aT] = 0, \implies a = \pm c_e I \quad (\text{II.2.34})$$

asymptotically. The real part of  $a$  goes to zero for all  $n \geq 1$  as  $\lambda \rightarrow \infty$ ; i.e., the solution of the adiabatic problem is always bounded and well-posed if  $T > 0$ .

The dispersion relation of the inviscid-adiabatic material is presented in (II.2.23). It is clear that when  $S < R$ , the problem is unstable and ill-posed at the same time since the second term has  $\lambda$ .

Figure II.2.2 presents a summary of the stability and well-posedness analyses. The differences of the plots (a) and (b) or of the plots (c) and (d) show the regularizing effect of the viscosity. The problem is always well-posed in the presence of a viscosity based on the present linearized spectral analysis. Our interest is in the ill-posed problems. In this way, an inviscid model will be analyzed in the next sections. Comparison of the two inviscid models (b) and (d) reveals also the regularizing effect of the thermal conductivity  $\bar{\kappa}$ . However, the effect is weaker than that of viscosity in the sense that it can not regularize the mechanical softening ( $S < 0$ ) and excessive thermal softening ( $R > 1$ ).

### Remarks II.2.1.

For the well-posed problem, we can define an internal length-scale  $l$  as

$$l^{-1} = \lambda_{max} = arg \left[ \sup_{\lambda} [Re(\alpha)] \right]. \quad (\text{II.2.35})$$

Note that for the ill-posed problems  $\lambda_{max} \rightarrow \infty$ , implying no internal length-scale.

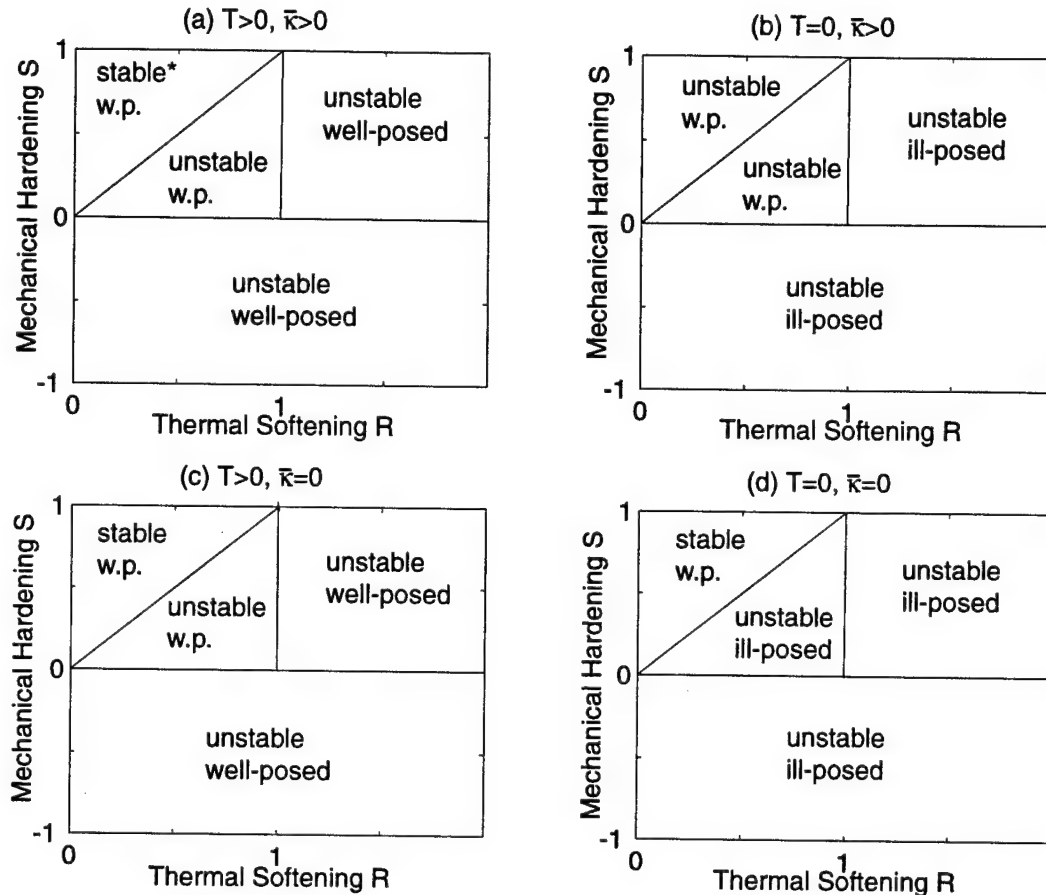


**FIGURE II.2.2** Summary of the stability and the ill-posedness conditions: (a) General thermo-viscoplastic material (b) Inviscid thermoplastic material (c) Adiabatic viscoplastic material (d) Adiabatic inviscid material. (\*) if condition (II.2.15) of enough viscosity is satisfied for (a)

#### II.2.4. Evaluation of the mesh-size dependence of the finite element solutions

Previous subsections deal with linearized problems analytically. To evaluate the generality of those results from the linearized model, the fully nonlinear problem is solved using the finite element method. The one-dimensional problem of interest is considered, with a Heaviside step function type dynamic loads at both ends. When both waves meet at the center, its magnitude doubles in the purely elastic solution. In the inelastic case, the material starts yielding. This situation is described by the governing equations (II.2.1). The initial yielding time is set as  $t = 0$  and the time when the bar yields completely is denoted as  $t_b$ . The problem are run using meshes with a different number of equally

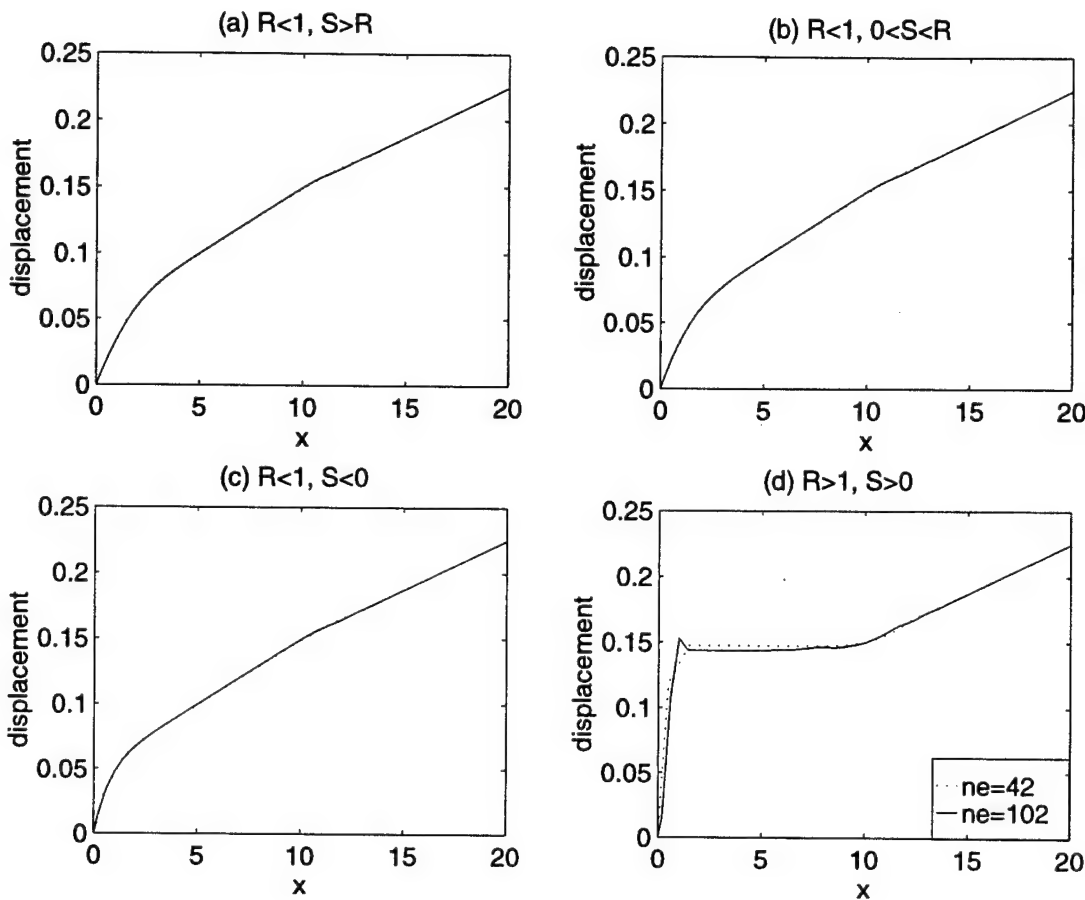


**FIGURE II.2.3** Spatial distribution of the displacement with four different material properties for the *elasto-thermo-viscoplastic* material.  $S$  and  $R$  denotes relative material hardening and relative thermal softening, respectively.

distributed linear elements in the displacement and temperature.

To see the characteristics of four different types of materials modes discussed in the previous sections, four different simulations are carried out. We set the a general material as one for which the thermal conductivity  $\kappa$  and viscosity  $\eta$  do not vanish. By considering the inviscid limit and the adiabatic limit, four types of materials can exist; i.e., Thermo-viscoplasticity, inviscid thermo-plasticity, adiabatic-viscoplasticity, and inviscid adiabatic-plasticity.

Also, each material has the possible range of thermal softening  $R$  and mechanical hardening  $S$ . It is assumed that  $R < 1$  and three possible domains of  $S > R$ ,  $0 < S < R$ , and  $S < 0$  are selected for the study. In the last case,  $R > 1$  is tested.

The displacement distribution in half of the domain  $[0, L/2]$  at  $t = 2.5t_b$  is for each

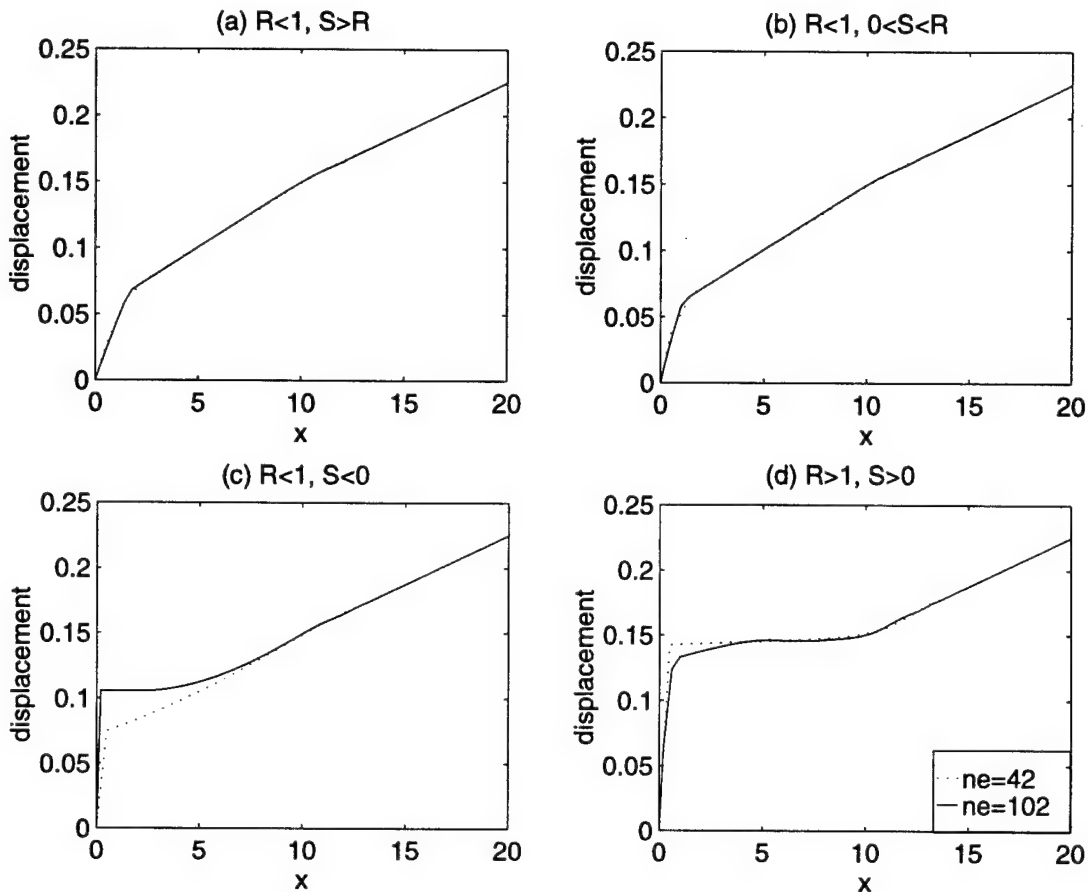


**FIGURE II.2.4** Spatial distribution of the displacement with four different material properties in the *inviscid elasto-thermo-plastic* material.  $S$  and  $R$  denotes relative material hardening and relative thermal softening, respectively. Cases (c) and (d) correspond to ill-posed problems according to the analyses of Section II.2.3.

case presented in Figures II.2.3, II.2.4, II.2.5, and II.2.6. The general viscous material in Figure II.2.3 shows convergence in all cases, which is consistent with the conclusion of the linearized spectral analyses. Smooth lines of the displacement due to the viscous effect match closely for different meshes. As expected, a large displacement is developed at  $x = 0$  in the case of  $R > 1$  due to the strong thermal softening. Comparing with the three other materials (i.e., inviscid, adiabatic, and inviscid-adiabatic), solutions are almost identical for  $R > 1$ . The strong thermal softening leads to a localized solution at  $x = 0$ ; note the sharp increase of the displacement at that point.

An inviscid material is tested in Figure II.2.4 with positive conductivity. When  $S > 0$ , the finite element solutions for different meshes converge to a unique one as long as  $R < 1$ . The viscous adiabatic solutions are presented in Figure II.2.5. Based on the

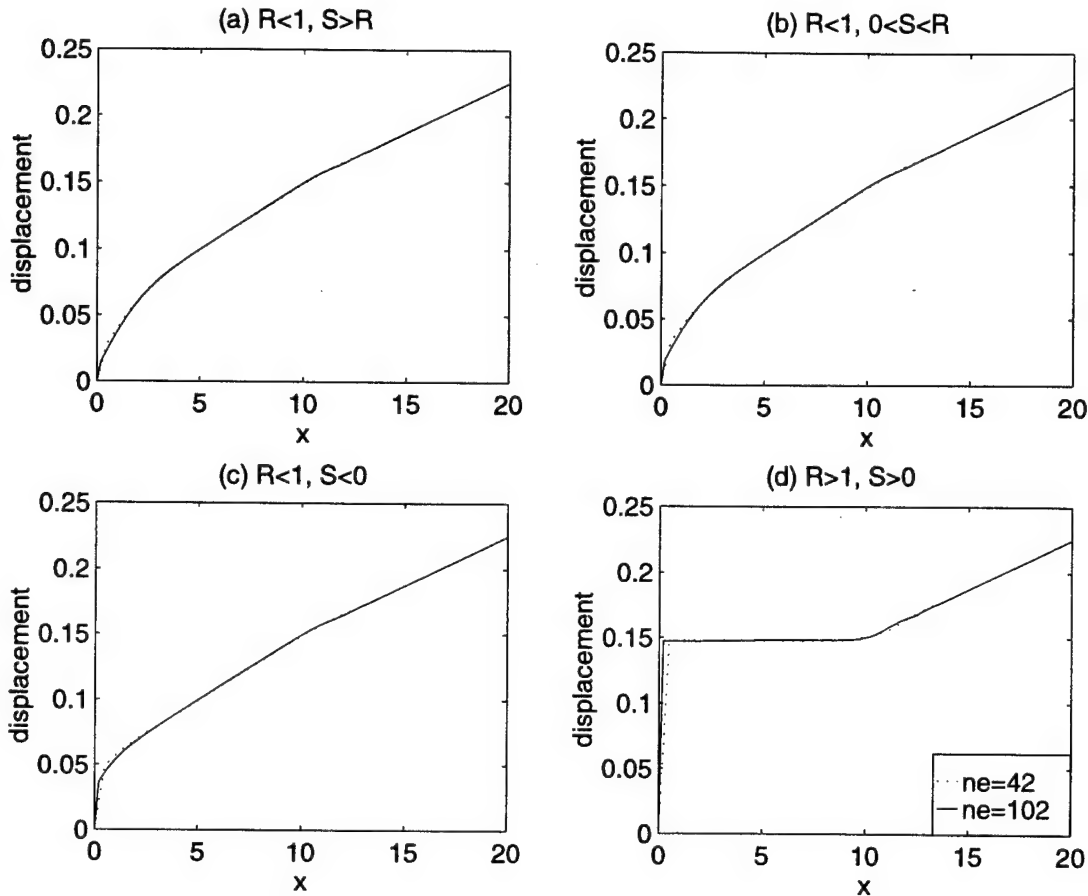


**FIGURE II.2.5** Spatial distribution of the displacement with four different material properties in the *elasto-adiabatic-viscoplastic* material.  $S$  and  $R$  denotes relative material hardening and relative thermal softening, respectively. All four cases define a well-posed problem according to the analysis of Section II.2.3.

analysis of Section II.2.3, the problem is always well-posed, as shown by the displacement distributions. show it well. Figure II.2.5(d) shows the development of a sharp localization band due to the lack of enough viscosity. Compared with the general viscous problem with positive conductivity, this adiabatic problem is seen to be more unstable. Figure II.2.6 presents the solutions for the inviscid adiabatic material. When  $S < R$ , the displacement distribution shows mesh-size dependence reflecting the ill-posedness of the given problem. The last graph has a unique solution, in which the material yields almost instantly due to very strong thermal softening and the left end of a bar moves freely. Then the whole domain of a bar is elastic and it is a well-posed dynamic problem.

These results allows to conclude the close relation between the ill-posedness of the

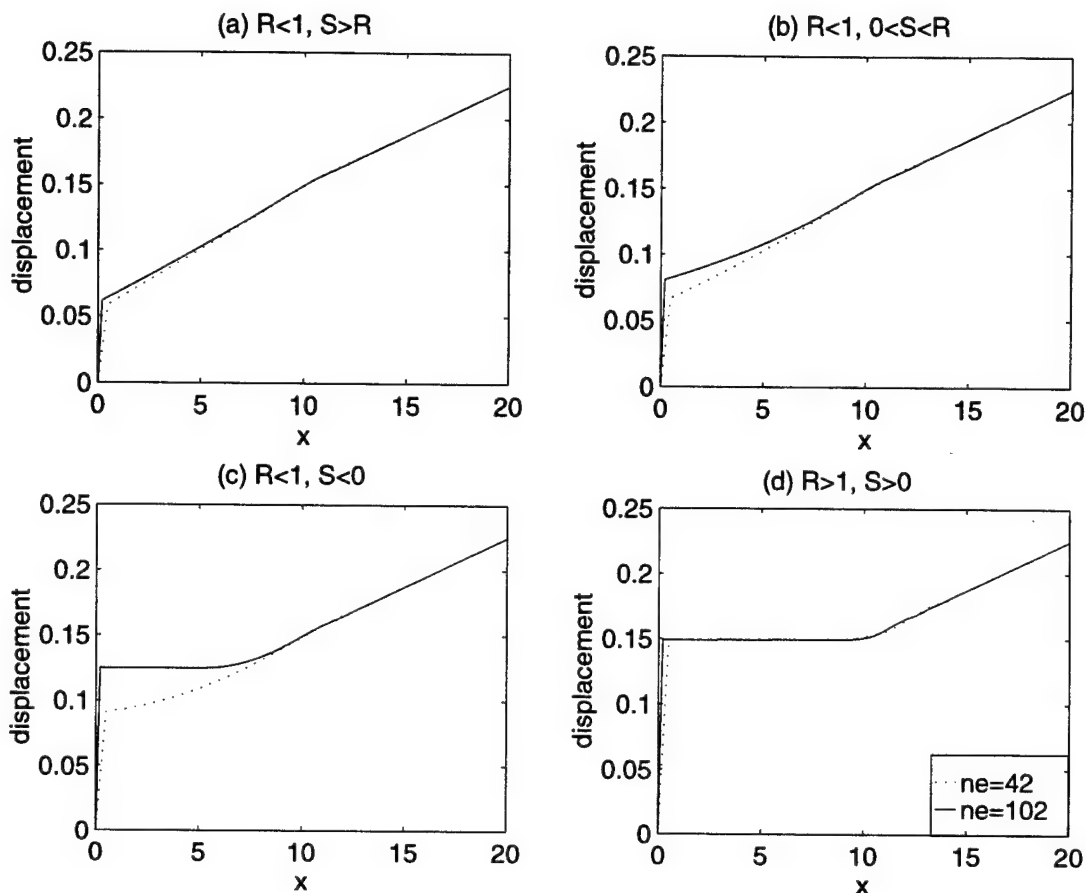


**FIGURE II.2.6** Spatial distribution of the displacement with four different material properties in the *inviscid elasto-adiabatic-plastic* material.  $S$  and  $R$  denotes relative material hardening and relative thermal softening, respectively. The only well-posed case is (a), according to the analysis of Section II.2.3.

linearized boundary value and the mesh-size dependence of the finite element solutions. The ill-posedness of these problems is studied in the following sections. In fact, the ill-posedness is removed by the introduction of the localized dissipative mechanism associated to a strong discontinuity. As shown next, this consideration leads to a problem exhibiting a physically meaningful solution; a solution that can be obtained analytically.

### II.3. An Analysis of Wave Propagation in A Localized Thermo-ElastoPlastic Shear Layer

In the previous section, we investigated the ill-posed problems and observed that those problems have spurious mesh-dependence in standard finite element method simulations.

To eliminate this ill-posedness (and, in addition, the mesh dependence of the numerical solutions), we introduce a local dissipative mechanism as developed in ARMERO [1997a] to the analysis of wave propagation of the shear layer. The problem is described in Section 3.1, with the analytic solution to this problem derived in Section 3.2 for a particular simple case. Several parametric studies are presented next to characterize the thermo-plastic behavior.

### II.3.1. Problem description

Consider a homogeneous shear layer occupying  $\Omega = [-L, L]$  with constant unit cross section and density  $\rho$ , initially at rest. This layer has constant specific heat  $c_v$  and thermal conductivity  $\kappa$ . The elastic limit stress is the function of relative temperature increase  $\vartheta(x, t)$ . We write this limit stress as  $\tau_e \Theta(t)$  for convenience, with  $\tau_e$  being the elastic limit at the reference temperature with  $\Theta(0) = 1$  without loss of generality. Upon yielding, the material follows a softening law  $\tilde{y}(\tilde{\alpha}, \vartheta)$ . Here,  $\tilde{\alpha}$  is the displacement-like internal variable on a surface.

The assumed thermal boundary conditions at  $x = \pm L$  are of zero heat flow (insulated boundaries). A constant stress  $0 < \tau_o < \tau_e$  is applied at both ends  $x = \pm L$ . A purely mechanical linear elastic response is obtained initially. The one-dimensional equation of motion expressed in displacement  $u$  is,

$$\frac{\partial^2 u}{\partial t^2} = c_e^2 \frac{\partial u^2}{\partial x^2} \quad \text{with} \quad c_e := \sqrt{\frac{G}{\rho}}. \quad (\text{II.3.1})$$

In the elastic range, the solution of (II.3.1) involves a rectangular stress pulse of value  $\tau_o$  propagating toward the center of the layer from both ends. Strain and velocity pulses are easily obtained as

$$\gamma_o = \frac{\tau_o}{G} \quad \text{and} \quad v_o = c_e \gamma_o. \quad (\text{II.3.2})$$

The two pulses meet at the center of the bar at a time that we set to  $t = 0$ . At this stage, the whole layer is at a stress  $\tau_o$  and strain  $\gamma_o$ , so we can write

$$u(x, t)|_{t=0} = u(x, 0) = \gamma_o x. \quad (\text{II.3.3})$$

The equations (II.3.2) and (II.3.3) are the initial conditions of the problem. When  $\tau_e > 2\tau_o$ , the material does not yield upon at the center, and the displacement solution of (II.3.1) is

$$u(x, t) = \gamma_o \cdot (x + c_e t) + \gamma_o \cdot (x - c_e t) H(c_e t - x) \quad \text{for } x \geq 0 \quad \text{and} \quad c_e t \leq L. \quad (\text{II.3.4})$$

Here,  $H(x)$  denotes the Heaviside step function. We assume that  $L \gg ct$ , so the need to consider the reflections at  $x = \pm L$  is avoided. Our interest is in the case of  $\tau_e < 2\tau_o$ , and following sections deal with the analysis of this problem.

### II.3.2. Exact solution for a localized softening model

We obtain the exact and numerical solution under the consideration of a strong discontinuity with a localized dissipative mechanism with thermal softening. For the case of a localized rigid-plastic mechanism (ARMERO [1997a]), the displacement jump  $\xi$  does not have elastic part and the  $\xi$  is assumed to follow similar rules as classical plasticity theory. In case of associative plastic flow, we can write the equations

$$\left. \begin{array}{l} \tilde{\phi} = |T| - \tilde{y}(\tilde{\alpha}, \vartheta) \leq 0 \\ \dot{\xi} = \tilde{\gamma} \operatorname{sign}(T) \\ \dot{\tilde{\alpha}} = \tilde{\gamma} \\ \tilde{\gamma} \geq 0, \quad \tilde{\gamma}\tilde{\phi} = 0, \quad \dot{\tilde{\gamma}}\tilde{\phi} = 0 \end{array} \right\} \quad (\text{II.3.5})$$

for the displacement jump  $\xi(t)$  at  $x = 0$ . The function  $\tilde{\phi}$  represents yield function, which consists of the surface traction  $T$  and yield stress  $\tilde{y}$ . The positive parameter  $\tilde{\gamma}$  identifies the rate of evolution of the displacement-like internal variable  $\tilde{\alpha}$ . The relations (II.3.5)<sub>4</sub> correspond to the Kuhn-Tucker loading/unloading conditions. Under the monotonic loading with  $T \geq 0$ ,

$$0 \leq \xi(t) = \tilde{\alpha}(t) \quad (\text{II.3.6})$$

since both are initially zero. Instead of using  $\xi(t)$  explicitly, we introduce the notation

$$d_0(t) = u(0^+, t) = -u(0^-, t) = \xi(t)/2, \quad t \geq 0, \quad (\text{II.3.7})$$

for the displacement at the center of the layer  $x = 0^+$ .

Upon releasing at  $x = 0$ , the rest of the bar remains elastic so that the elastic solution is valid with additional  $d_0$  contribution.

$$u(x, t) = \gamma_o \cdot (x + c_e t) + \left[ \gamma_o \cdot (x - c_e t) + d_0(t - \frac{x}{c_e}) \right] H(c_e t - x) \quad (\text{II.3.8})$$

for  $t \geq 0$  and  $x \geq 0$ . The entire layer, except at  $x = 0$ , is elastic and the stress distribution is given by

$$\tau(x, t) = \tau_o + [\tau_o - \frac{G}{c_e} \dot{d}_0(t - \frac{x}{c_e})] H(c_e t - x), \quad (\text{II.3.9})$$

and in particular, at  $x = 0^+$ ,

$$\tau_{0+}(t) = 2\tau_o - \frac{G}{c_e} \dot{d}_0(t). \quad (\text{II.3.10})$$

Given this stress distribution, the velocity distribution is given by

$$v(x, t) = v_o - \left[ v_o - \dot{d}_0(t - \frac{x}{c_e}) \right] H(c_e t - x). \quad (\text{II.3.11})$$

The traction  $T$  at  $x = 0$  in (II.3.5) is the same as  $\tau_{0+}(t)$  by local-equilibrium condition,

$$T = \tau_{0+}. \quad (\text{II.3.12})$$

Given the definition of  $d_0$ , we have  $\tilde{y}(\tilde{\alpha}, \vartheta_0) = \tilde{y}(2d_0, \vartheta_0)$ . Here,  $\vartheta_0 := \vartheta|_{x=0}$ . Note that the temperature field remains continuous. Upon yielding, the traction  $T$  at  $x = 0$  becomes identical to  $\tilde{y}$ . As a result,

$$T = \tilde{y}(2d_0, \vartheta_0) = 2\tau_o - \frac{G}{c_e} \dot{d}_0(t). \quad (\text{II.3.13})$$

The energy release rate  $D_p$  is defined as the difference between the external power and the rate of change of total mechanical energy. This released energy is mainly transformed into heat flux considering global energy conservation. These two results are explained by the relations

$$\begin{aligned} \frac{1}{2}D_p(t) &:= \tau_o v_o - \frac{d}{dt} \left[ \int_0^L \left[ \frac{1}{2}\rho v^2 + \frac{1}{2}\frac{\tau^2}{G} \right] dx \right] \\ &= \tau_{0+} \dot{d}_0(t) \\ &= q_{0+}(t), \end{aligned} \quad (\text{II.3.14})$$

with the heat flux  $q$  given in terms of the temperature by

$$q_{0+} = -\kappa \frac{\partial \vartheta}{\partial x} \Big|_{x=0^+}, \quad (\text{II.3.15})$$

the  $1/2$  factor accounts for the symmetry in the problem. The problem then reduces to the heat equation and the ODE (II.3.13), with relation (II.3.14) appearing as a boundary condition at  $x = 0^+$ . The complete system of equations to be solved simultaneously is then,

$$\left. \begin{aligned} c_v \rho \dot{\vartheta} &= \kappa \frac{\partial^2 \vartheta}{\partial x^2} \quad \text{in } (0, L] \\ \tilde{y}(2d_0, \vartheta_0) &= 2\tau_o - \frac{G}{c_e} \dot{d}_0(t) \\ q_{0+}(t) &= -\kappa \frac{\partial \vartheta}{\partial x} \Big|_{x=0^+}. \end{aligned} \right\} \quad (\text{II.3.16})$$

This represents a coupled system of differential equations and, generally, these equations are nonlinear due to (II.3.16)<sub>2</sub>. In some simple cases, though, the exact closed-form solution can be obtained. This solution will become a basis for the verification of more complex models.

The softening law  $\tilde{y}(2d_0, \vartheta_0)$  has  $\tilde{y}(0, 0) = \tau_e$  and is assumed monotonically decreasing to  $\tilde{y} = 0$  for some value of  $d_0$  and  $\vartheta_0$ . A simple case is given by the linear function of  $d_0$  and  $\vartheta_0$ ,

$$\tilde{y}(2d_0, \vartheta_0) = \tau_e(1 - w_0 \vartheta_0) + H_L \cdot 2d_0 \quad (\text{II.3.17})$$

with linear hardening/softening modulus  $H_L$  and linear thermal softening constant  $w_0$ . It should be noted that  $H_L$  has the units of *stress/length*. In this case, the equations (II.3.16) can be written as,

$$\left. \begin{aligned} c_v \rho \frac{\partial \vartheta}{\partial t} &= \kappa \frac{\partial^2 \vartheta}{\partial x^2} \\ 2\tau_o - \frac{G}{c_e} \dot{d}_0 &= \tau_e(1 - w_0 \vartheta_0) + 2H_L d_0 \\ \tau_{0+}(t) \dot{d}_0(t) &= -\kappa \frac{\partial \vartheta}{\partial x} \Big|_{x=0^+} \end{aligned} \right\} \quad (\text{II.3.18})$$

If thermal softening constant  $w_0$  vanishes, (II.3.18)<sub>2</sub> becomes uncoupled, consisting of the ODE (II.3.18)<sub>2</sub>, with closed form solutions,

$$d_0(t) = \frac{AG}{2H_L c_e} \left[ 1 - \exp \left( \frac{-2H_L c_e t}{G} \right) \right] \quad (\text{II.3.19})$$

where  $A := \frac{c_e}{G} (2\tau_o - \tau_e)$ . This solution is valid up to the time when  $\tau_{0+} = 0$ . We refer to this time as *the uncoupled breaking time*  $t_{b_o}$  and is given by

$$t_{b_o} = -\frac{G}{2H_L c_e} \log \left( \frac{2\tau_o c_e}{GA} \right). \quad (\text{II.3.20})$$

After complete yielding, (that is, setting (II.3.17) to zero) it results in

$$\left. \begin{aligned} \dot{d}_0(t) &= \frac{2\tau_o c_e}{G} = 2v_o, \\ d_0(t) &= d_0(t_b) + 2v_o \cdot (t - t_b), \end{aligned} \right\} \quad (\text{II.3.21})$$

for  $t \geq t_{b_o}$ . During the time between  $t = 0$  and  $t = t_{b_o}$ , the rate of energy release is calculated from  $d_0(t)$  as

$$\begin{aligned} q_{0+} &= \left[ 2\tau_o - \frac{G}{c_e} \dot{d}_0(t) \right] \cdot \dot{d}_0(t) \\ &= \left[ 2\tau_o - \frac{GA}{c} \exp \left( \frac{-2H_L c_e t}{G} \right) \right] \cdot \exp \left( \frac{-2H_L c_e t}{G} \right). \end{aligned} \quad (\text{II.3.22})$$

In the above equation,  $q_{0+}$  is the heat flux generated by the mechanical energy release. We relate heat flux  $q$  to temperature gradient through *Fourier's law*

$$q = -\kappa \frac{\partial \vartheta}{\partial x}, \quad (\text{II.3.23})$$

so a *Neumann boundary condition* is obtained  $x = 0$ . Using Green's function (ZAUDERER [1989]) for semi-infinite bar ( $L \gg c_e t$  is assumed) with initial condition  $\vartheta(x, 0) = 0$  and

boundary condition above, the temperature evolution of the layer at  $x = 0$  is exactly expressed as

$$\vartheta_0(t) = -\frac{b}{2a} \exp(2at)\sqrt{2a} \operatorname{Erf}\left(\sqrt{2at}\right) + \frac{d}{a} \exp(at)\sqrt{a} \operatorname{Erf}\left(\sqrt{at}\right), \quad (\text{II.3.24})$$

for  $0 \leq t \leq t_{b_o}$  with constants  $a = \frac{-2H_L c_e}{G}$ ,  $b = \frac{GA^2}{c_e \sqrt{\rho c_v \kappa}}$ ,  $d = \frac{2\tau_o A}{\sqrt{\rho c_v \kappa}}$ . The error function  $\operatorname{Erf}(t)$  is defined as

$$\operatorname{Erf}(t) := \frac{2}{\sqrt{\pi}} \int_0^t \exp(-z^2) dz. \quad (\text{II.3.25})$$

In summary, equations (II.3.8), (II.3.9), (II.3.11) and (II.3.24) correspond to the exact closed-form solution of the considered problem, defining the distributions in space and time of displacement, stress, velocity and temperature, respectively.

**Remark II.3.1** The above considerations assume that the response outside the strong discontinuity at the center of the shear layer is thermoelastic. No consideration is given to the possible thermal softening, and corresponding inelastic response, outside the discontinuity. Numerical experiments show that these effects are small compared with the main contribution given by the response along the discontinuity. In fact, the finite element solutions presented in the following sections consider the full thermoplastic response outside the discontinuity and still a good comparison is observed with the analytical solutions presented in this section. We plan to present a more detailed analysis of these considerations in a forthcoming publication.  $\square$

### II.3.3. Parametric study

We obtained the exact solution for localized softening model with no thermal softening ( $w_0 = 0$ ) in the previous section. We consider in this section the solution of the general case  $w_0 \neq 0$ . These solutions are obtained numerically by solving (II.3.18) with Forward Cauchy-Euler (for time derivative) and Centered difference (for spatial derivative).

#### II.3.3.1. Nondimensional parameters

The solution (II.3.24) leads to the consideration of the non-dimensional parameters

$$\left. \begin{aligned} \vartheta_N &\equiv \vartheta/\vartheta_r, \\ t_N &\equiv t/t_r, \\ x_N &\equiv x/x_r, \end{aligned} \right\} \quad (\text{II.3.26})$$

with

$$\left. \begin{aligned} \vartheta_r &:= \frac{\tau_e^2}{\rho \sqrt{-H_L c_e c_v \kappa}}, \\ t_r &:= \frac{G}{H_L c_e}, \\ x_r &:= \sqrt{t \kappa / (\rho c_v)}. \end{aligned} \right\} \quad (\text{II.3.27})$$

With all these nondimensional variables, two parameters are found to govern the evolution of the distribution of the normalized temperature. The two parameters are defined as

$$p_1 := \frac{w_0^4 \tau_e^8}{G \rho^3 \kappa^2 c_v^2 H_L^2} \quad \text{and} \quad p_2 := \frac{2\tau_o}{\tau_e}. \quad (\text{II.3.28})$$

The parameter  $p_1$  includes all the material properties of the layer. The parameter  $p_2$  measures the relative strength of the initial stress pulse. It can be said that we have all the same behaviors in normalized space of time and distance if  $p_1$  and  $p_2$  are fixed. In this context,  $p_1$  can be considered as the intensity factor of thermal softening because all other material properties can not vanish generally.

The default geometric and material properties of the layer are listed in the table,

$$\left. \begin{array}{l} \tau_o = 150 \text{N/mm}^2 \\ \tau_y = 200 \text{N/mm}^2 \\ G = 20000 \text{N/mm}^2 \\ \rho = 2 \cdot 10^{-6} \text{Ns}^2/\text{mm}^4 \\ c_e = 100000 \text{mm/s} \\ w_0 = 1.7321 \cdot 10^{-4} \text{1/K}^{-1} \\ H_L = 3000 \cdot (-1) \text{N/mm}^2/\text{mm} \\ \kappa = 40 \text{N/sK} \\ c_v = 1000 \text{mm}^2/\text{s}^2 \text{K} \\ L = \geq 4c_e t_{b_o} (20 \text{mm}) \end{array} \right\} \quad (\text{II.3.29})$$

where  $L$  is the length of the layer,  $\kappa$  is the thermal conductivity, and  $c_v$  is the specific heat. The assumed parameters correspond to  $p_1 = 1.0$  and  $p_2 = 1.5$ . These parameters are then varied by changing the thermal constant  $w_0$ .

### II.3.3.2. Properties of the solution

Figure II.3.1 includes the spatial distribution and Figure II.3.2 the temporal evolution of different thermo-mechanical quantities for the four different values of the non-dimensional parameter  $p_1$ . The general trend of the solution is that thermal effect accelerates material softening, especially in an early stage of yielding.

In the limit as  $p_1$  becomes large, it yields almost instantly. In other words, the left boundary behaves like a free end. We can also observe that in that limit, returning stress wave vanishes in Figure II.3.1(c). Consequently, at  $x = 0^+$  it loses its whole stiffness and displacement jump evolves at constant rate  $2c_e \tau_o / G$ . This behavior is expressed as the

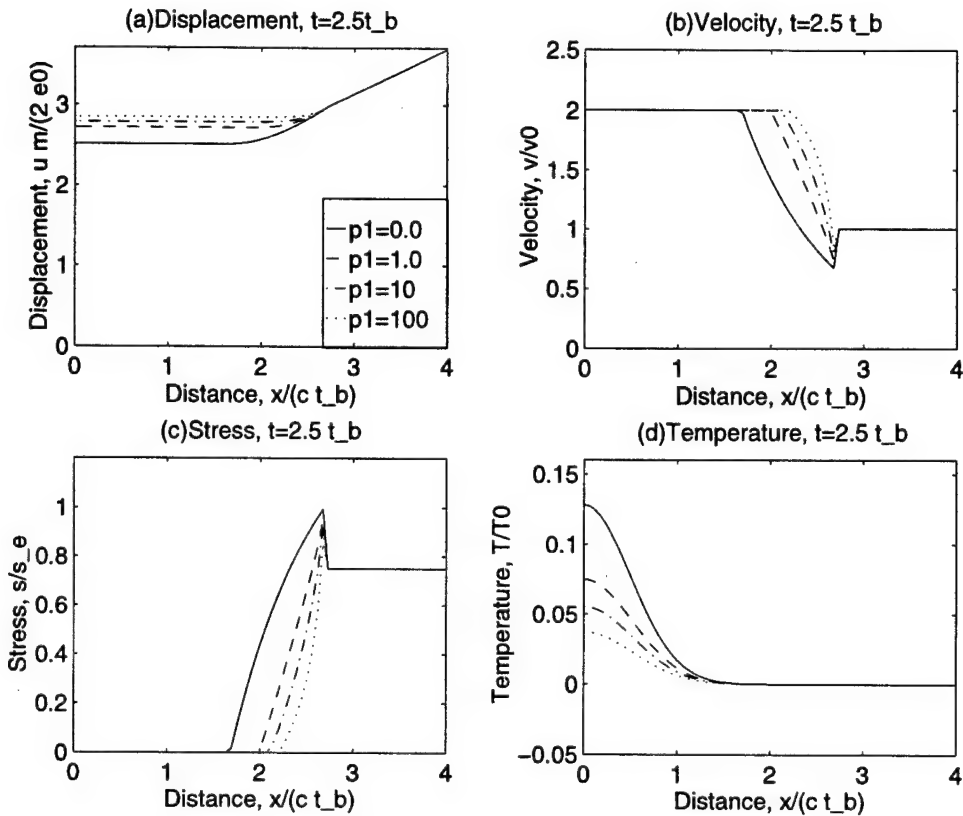


**FIGURE II.3.1** Displacement, velocity, stress, and temperature distribution along the shear layer with four different material parameter  $p_1 := \frac{w_0^4 \tau_e^8}{G \rho^3 \kappa^2 c_v^2 H_L^2}$ . The parameter  $p_1$  is a nondimensional factor for the intensity of thermal softening.

near straight line in Figure II.3.1(a) and II.3.2(a) (for  $p_1 = 100$ ). However, this numerical simulation was done to exaggerate the thermal softening effects by intensity  $p_1$ . Real materials have  $0 < p_1 < 1.0$  generally. With linear thermal softening, breaking time  $t_b$  decreased and the shape of stress curve changed in Figure II.3.1(c) and Figure II.3.2(c).

The localized zone of temperature is generally a function of density, specific heat and conductivity because it is based on the solution of heat equation. In normalized space, the length of localized zone is almost fixed in Figure II.3.1(d) regardless of the value of  $p_1$ . Figure II.3.2(d) shows time evolution of temperature increase at  $x = 0$ . We observe that initial curves of each value of  $p_1$  follows the same path. As  $p_1$  increases the elastic

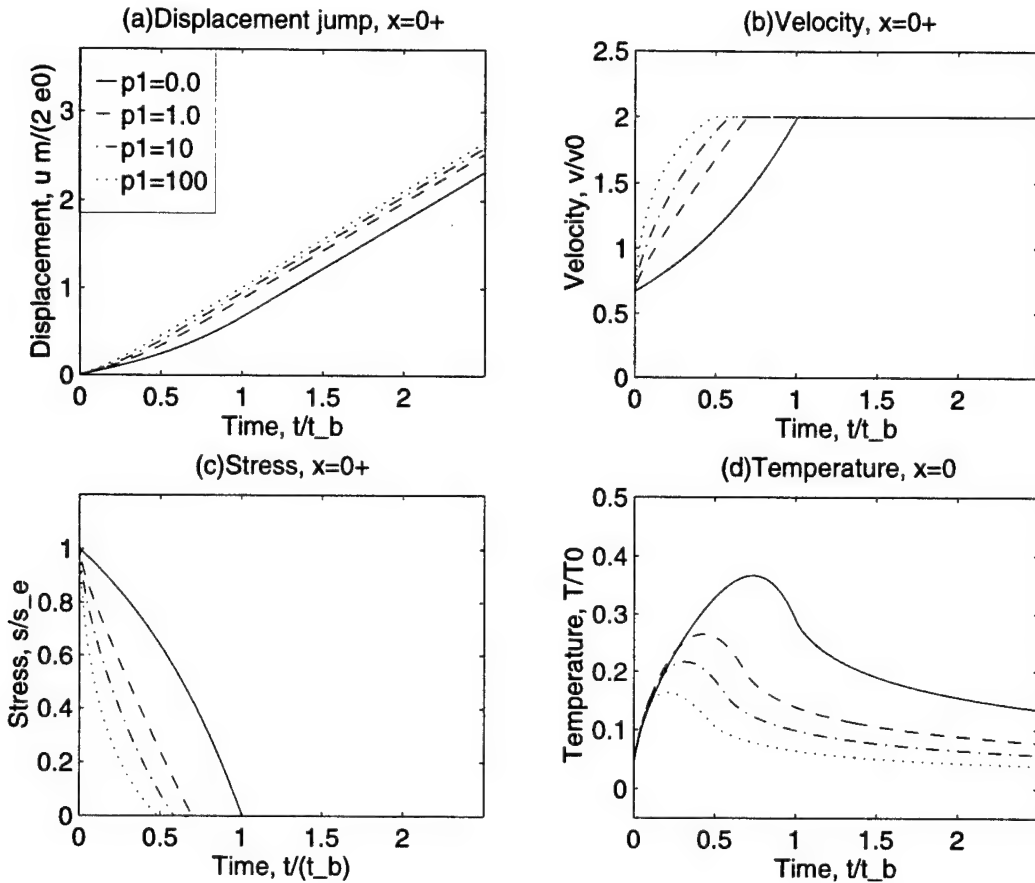


**FIGURE II.3.2** Displacement, velocity, stress, and temperature evolution in time at  $x = 0^+$  with four different material parameter  $p_1 := \frac{w_0^4 \tau_e^8}{G \rho^3 \kappa^2 c_v^2 H_L^2}$ . The parameter  $p_1$  is a nondimensional factor for the intensity of thermal softening.

limit stress decreases and it bifurcates from the increasing curve of  $p_1 = 0$ . This is the direct result of energy release. Figure II.3.5(a) is the graph of released energy versus time. Each curve follows one path and makes branch by the value of  $p_1$ . Parameter  $p_1$  does not change the rate of energy release, but makes  $t_b$  smaller. Finally, the level of total released energy is determined by  $t_b$ .

Second experiments deal with four different values of  $p_2$  with  $p_1 = 1.0$ . Figure II.3.3 and Figure II.3.4 are spatial distribution and time evolution of thermo-mechanical quantities. The effect of  $p_2$  is that it magnifies responding mechanical quantities because  $p_2$  directly represents relative strength of external loads.

Parameter  $p_2$  has finite range of  $1.0 < p_2 < 2.0$  so that  $t_b$  has its limit which is larger than zero (Figure II.3.4(c)). In the tested range of parameters, breaking time  $t_b$  decreases

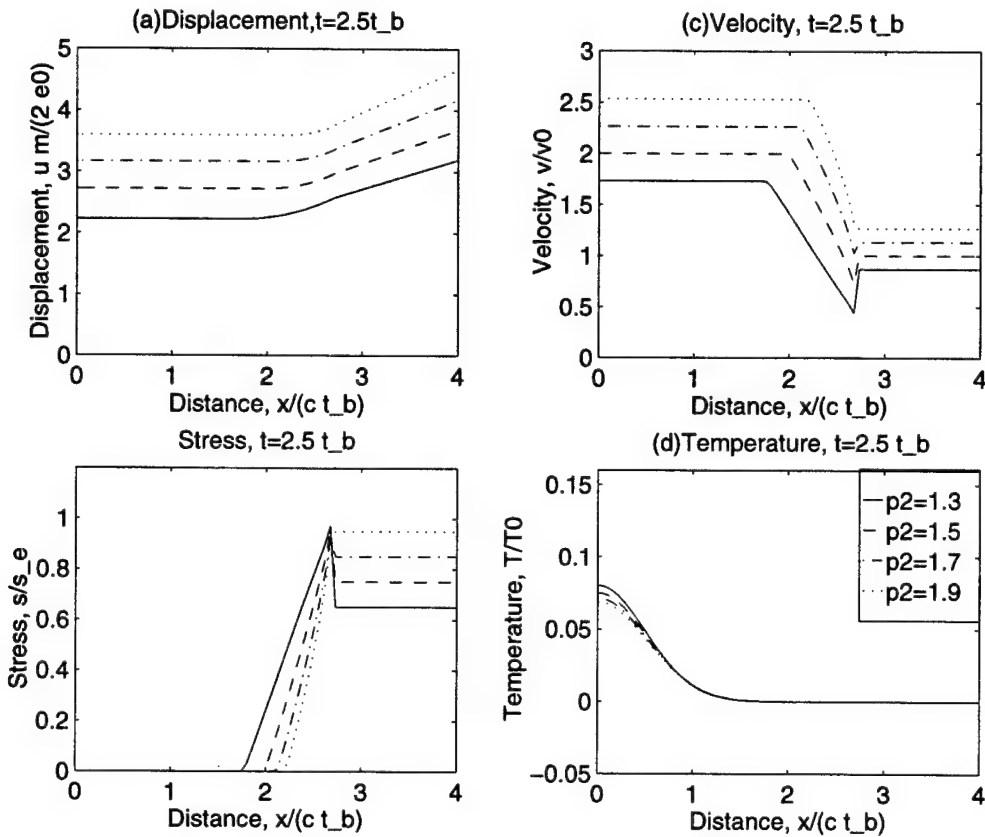


**FIGURE II.3.3** Displacement, velocity, stress, and temperature distribution along the shear layer with four different boundary condition parameter  $p_2 := \frac{2\tau_0}{\tau_e}$ . The parameter  $p_2$  is a nondimensional factor for the external load.

in II.3.5(d) as  $p_2$  increases.

The parameter  $p_2$  changes the rate of energy release: Larger load increases the rate. We can see this result in Figure II.3.5(c). It shows that it breaks earlier with almost the same total released energy as  $p_2$  increases. Consequently, it has higher peaks in temperature evolution when  $p_2$  is larger (Figure II.3.4(d)). Due to the same level of total released energy, temperature distribution becomes closer for all cases after some time (Figure II.3.3(d), Figure II.3.4(d)).

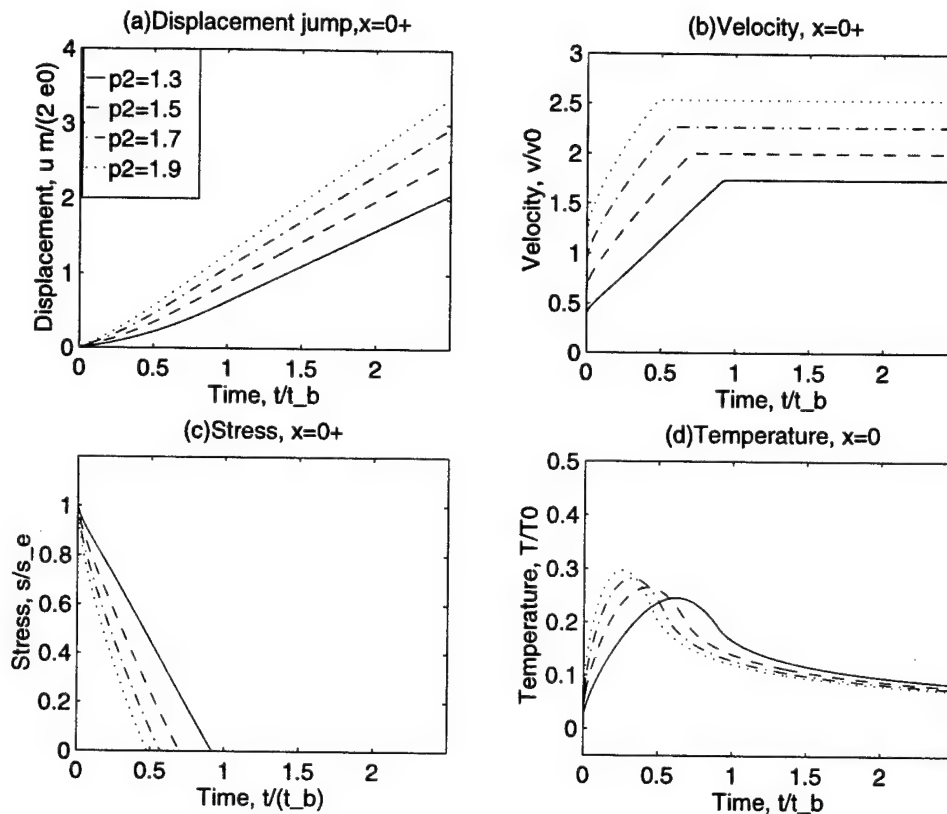


**FIGURE II.3.4** Displacement, velocity, stress, and temperature evolution in time at  $x = 0^+$  with four different boundary condition parameter  $p_2 := \frac{2\tau_0}{\tau_e}$ . The parameter  $p_2$  is a nondimensional factor for the external load.

## II.4. An Analysis of the Approximation of Strong Discontinuities

In this section an analysis of the approximation of the exact model is presented. The approximated model is important in the sense that it can predict the behavior of finite element model if we identify the local neighborhood  $\Omega_x$  as  $\Omega_e$ , *finite element*.

We approximate the step function type strong discontinuity by a ramp function type continuous displacement in a finite local neighborhood  $\Omega_x$  with size  $h_x > 0$ . The temperature field is assumed to be regular throughout the domain. Our main goal is to investigate the effect of spatial discretization to energy release and its interaction to thermo-mechanical behavior. Every result is based on exact closed-form solutions discussed in the following sections.

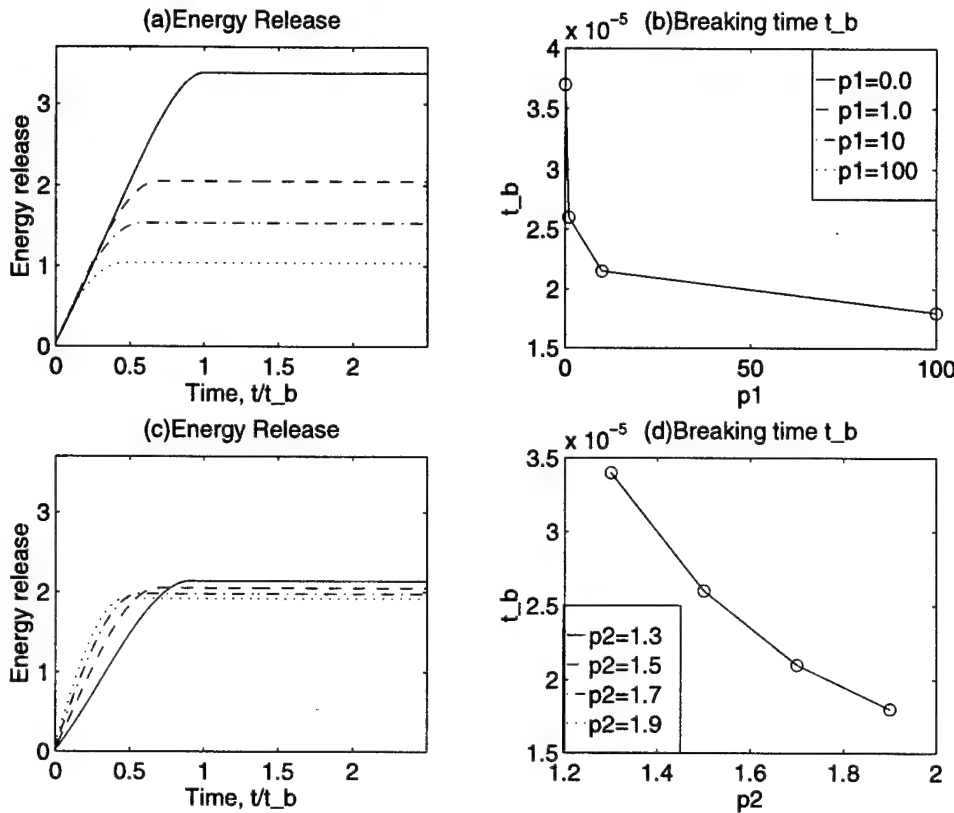


**FIGURE II.3.5** (a) Time evolution of the energy release, (b) Breaking time variations with  $p_1$ . (c) Time evolution of the energy release, (d) Breaking time variations with  $p_2$ .

#### II.4.1. An approximate solution for $h > 0$ : analytic results

The regularized displacement field is described by

$$u(x, t) = \begin{cases} d_{\frac{h}{2}}(t) \frac{2x}{h}, & \text{for } 0 \leq x \leq h/2, \\ \hat{u}(x, t), & \text{for } x \geq h/2, \end{cases} \quad (\text{II.4.1})$$

for a fixed parameter  $h > 0$ . That is, we consider a linear approximation of the displacement  $u(x, t)$  in the local neighborhood  $\Omega_o = (-h/2, h/2)$  of  $x = 0$ . The displacement  $\hat{u}(x, t)$  is a general function assumed outside  $\Omega_o$ . For continuity of displacement,

$$\hat{u}\left(\frac{h}{2}, t\right) = d_{\frac{h}{2}}(t). \quad (\text{II.4.2})$$

The effect of spatial discretization is neglected and assumed to be exact outside  $\Omega_o$ . The relative temperature field  $\vartheta$  is considered to be continuous everywhere. We only consider

the effect of regularization of strong discontinuities within  $\Omega_o$ . The domain outside of  $\Omega_o$  is always in elastic range and then

$$\tau = G \frac{\partial \hat{u}}{\partial x} \quad \text{for } x > h/2. \quad (\text{II.4.3})$$

From (II.4.1), the material response inside the local neighborhood  $\Omega_o$  is calculated as

$$\tau_{\Omega_o} = G \frac{2}{h} d_{\frac{h}{2}} \quad \text{in } \Omega_o \quad (\text{II.4.4})$$

until the elastic limit of material  $\tau_e$  is reached. After this limit, the material response in  $\Omega_o$  is determined by the displacement jump  $\xi(t)$  of the small-scale displacements at  $x = 0$ .

$$\tau_{\Omega_o} = G \left( \frac{2}{h} d_{\frac{h}{2}} - \frac{1}{h} \xi \right) \quad \text{in } \Omega_o \quad (\text{II.4.5})$$

for the material response in  $\Omega_o/\Gamma_0$ . Given the constant approximation of strain and stress (4.5) in  $\Omega_o$ , small-scale equilibrium equation is derived

$$T(\xi, \vartheta) = \frac{2}{h} \int_0^{h/2} \tau dx = \tau_{\Omega_o}, \quad (\text{II.4.6})$$

with  $T(\xi, \vartheta)$  given by the localized model at  $x = 0$ . Combining (II.4.4) and (II.4.6) gives the equation showing relation between the displacement jump  $\xi(t)$  and  $d_{\frac{h}{2}}$ ,

$$\xi + \frac{h}{G} T(\xi, \vartheta) = 2d_{\frac{h}{2}}. \quad (\text{II.4.7})$$

For linear softening function of  $\xi$  and general one of  $\vartheta$ , the softening law is defined as

$$T(\xi, \vartheta) = \tau_e \Theta(\vartheta) + H_L \xi \quad (\text{II.4.8})$$

with linear softening modulus  $H_L < 0$  and  $\Theta(0) = 1$ . Now (II.4.7) is expressed for  $\xi$  with the help of (II.4.8),

$$\begin{aligned} \xi &= \frac{2}{1-\delta} \left[ d_{\frac{h}{2}} - \delta \frac{\gamma_e \Theta}{m} \right] \\ \tau_{\Omega_o} &= \frac{Gm}{1-\delta} \left[ \frac{\gamma_e \Theta}{m} - d_{\frac{h}{2}} \right] \end{aligned} \quad (\text{II.4.9})$$

using (II.4.5). Here,  $m := -\frac{2H_L}{G}$ ,  $\delta := m \frac{h}{2} = -\frac{hH_L}{G}$  and these equations are valid up to the breaking time  $t_b$ , which corresponds to the displacement  $d_{\frac{h}{2}}(t_b) = \Theta \gamma_e / m$ . After breaking time, displacement jump  $\xi$  is determined by (II.4.7) with  $T \equiv 0$ .

$$\xi = 2d_{\frac{h}{2}}, \quad \text{and} \quad \tau_{\Omega_o} = 0, \quad (\text{II.4.10})$$

during assumed monotonic loading.

From the weak form of linear momentum balance, we reversely have two strong forms

$$\frac{\partial^2 \hat{u}}{\partial t^2} = c_e^2 \frac{\partial^2 \hat{u}}{\partial x^2} \quad \text{for } x > \frac{h}{2}, \quad \text{with} \quad \frac{\partial \hat{u}}{\partial x}(L, t) = \gamma_o, \quad (\text{II.4.11})$$

and

$$\boxed{\alpha \frac{\rho \delta}{m} \ddot{d}_{\frac{h}{2}} + \tau_{\Omega_o} - \tau_{\frac{h}{2}+} = 0,} \quad (\text{II.4.12})$$

in the unknown function  $d_{\frac{h}{2}}(t)$  and  $\alpha = 1/3$  for the consistent mass approximation. The solution of equation (4.12) is given by

$$\hat{u}(x, t) = \gamma_o(x + c_e t) + \left[ \gamma_o(x - c_e t - h) + d_{\frac{h}{2}}(t - \frac{x - h/2}{c_e}) \right] H(c_e t - x + \frac{h}{2}), \quad (\text{II.4.13})$$

and

$$\begin{aligned} \hat{\tau}(x, t) &= \tau_o + \left[ \tau_o - \frac{G}{c_e} \dot{d}_{\frac{h}{2}} \right] H(c_e t - x + \frac{h}{2}), \\ \hat{v}(x, t) &= v_o + \left[ -v_o + \dot{d}_0(t - \frac{x - h/2}{c_e}) \right] H(c_e t - x + \frac{h}{2}), \end{aligned} \quad (\text{II.4.14})$$

for  $x \geq h/2$ . Inside the local neighborhood  $\Omega_o$ ,

$$\left. \begin{aligned} u(x, t) &= \frac{2x}{h} d_{\frac{h}{2}} \\ v(x, t) &= \frac{2x}{h} \dot{d}_{\frac{h}{2}} \end{aligned} \right\} \quad (\text{II.4.15})$$

for  $x \leq h/2$ . Substituting (II.4.13) in (II.4.3), we obtain

$$\tau_{\frac{h}{2}+}(t) = 2\tau_o - \frac{G}{c_e} \dot{d}_{\frac{h}{2}}(t). \quad (\text{II.4.16})$$

Using (II.4.4) and (II.4.16), differential equation (II.4.12) reads

$$\alpha \frac{\delta}{mc_e} \ddot{d}_{\frac{h}{2}} + \dot{d}_{\frac{h}{2}} + \frac{mc_e}{\delta} d_{\frac{h}{2}} = 2\gamma_o c \quad (\text{II.4.17})$$

for  $t \leq t_e$ , which denotes the time when the elastic limit is reached. The time  $t_e$  is defined as

$$\tau_{\Omega_o}(t_e) = \tau_e \quad \text{and} \quad d_{\frac{h}{2}}(t_e) = \delta \frac{\gamma_e}{m} = \delta \frac{2\gamma_o}{mr}, \quad (\text{II.4.18})$$

from (II.4.4). In this time period,  $\dot{\vartheta} = 0$  and temperature field is uncoupled with displacement field. The initial conditions for  $d_{\frac{h}{2}}$  are determined by initial elastic solutions,

$$d_{\frac{h}{2}}(0) = \gamma_o x|_{x=h/2} = \delta \frac{\gamma_o}{m}, \quad \text{and} \quad \dot{d}_{\frac{h}{2}}(0) = v_o. \quad (\text{II.4.19})$$

Upon activation of the softening response on the discontinuity  $x = 0$  at  $t_e$ , (II.4.5) and (II.4.16) leads to another differential equation of  $d_{\frac{h}{2}}$

$$\alpha \frac{\delta}{mc_e} \ddot{d}_{\frac{h}{2}} + \dot{d}_{\frac{h}{2}} - \frac{mc_e}{1-\delta} d_{\frac{h}{2}} = \left[ 2\gamma_o - \frac{\gamma_e \Theta}{1-\delta} \right] c_e \quad (\text{II.4.20})$$

for  $t_e \leq t \leq t_b$ . The breaking time  $t_b$  is determined by

$$T(\xi(t_b), \vartheta(x=0, t_b)) = \tau_{\Omega_o}(t_b) = 0 \quad \text{and} \quad d_{\frac{h}{2}}(t_b) = \frac{\gamma_e \Theta}{m} \quad (\text{II.4.21})$$

After breaking, equation (II.4.12) reads

$$\alpha \frac{\delta}{mc} \ddot{d}_{\frac{h}{2}} + \dot{d}_{\frac{h}{2}} = 2\gamma_o c_e \quad (\text{II.4.22})$$

for  $t \geq t_b$ .

We set up all the governing differential equations with initial condition (II.4.19). The closed form solutions of (II.4.17), (II.4.20) and (II.4.22) are respectively

$$d_{\frac{h}{2}}(t) = \delta \frac{2\gamma_o}{m} - \delta \frac{\gamma_o}{m} \left[ \cos(\omega_1 t) - \frac{2\alpha - 1}{\sqrt{4\alpha - 1}} \sin(\omega_1 t) \right] \exp(-\epsilon t) \quad (\text{II.4.23})$$

for  $0 < t \leq t_e$ ,

$$d_{\frac{h}{2}}(t) = (\Theta - (1-\delta)r) \frac{2\gamma_o}{mr} + \frac{\gamma_o}{m} \left[ \frac{\epsilon}{\omega_2} \left( \frac{\alpha\delta}{v_o} \dot{d}_{\frac{h}{2}}(t_e) - (1-\delta) \right) \sinh(\omega_2(t-t_e)) + \frac{2}{1}(1-\delta) \cosh(\omega_2(t-t_e)) \right] \exp(-\epsilon(t-t_e)) \quad \text{for } t_e \leq t \leq t_b, \quad (\text{II.4.24})$$

$$d_{\frac{h}{2}}(t) = \left[ \frac{2\gamma_o \Theta(t_b)}{mr} - \frac{2v_o - \dot{d}_{\frac{h}{2}}(t_b)}{2\epsilon} \right] + \frac{2v_o - \dot{d}_{\frac{h}{2}}(t_b)}{2\epsilon} \exp(-2\epsilon(t-t_b)) + 2v_o(t-t_b) \quad \text{for } t \geq t_b, \quad (\text{II.4.25})$$

where

$$\epsilon := \frac{mc_e}{2\alpha\delta}, \quad \omega_1 := \epsilon\sqrt{4\alpha - 1}, \quad \text{and} \quad \omega_2 := \epsilon\sqrt{1 + \frac{4\delta}{1-\delta}}.$$

Temperature field  $\vartheta$  and  $\Theta(\vartheta(0, t))$  is calculated by energy release rate  $\mathcal{D}_p$ , which is given by

$$\mathcal{D}_p = 0 \quad \text{for } t \leq t_e \quad \text{and} \quad \mathcal{D}_p = \tau_{\Omega_o} \dot{\xi} \quad \text{for } t_e \leq t \leq t_b. \quad (\text{II.4.26})$$

The approximated temperature field is described by

$$\vartheta(x, t) = \begin{cases} \vartheta_o + \frac{2x}{h}[\vartheta_{\frac{h}{2}} - \vartheta_o], & \text{for } 0 \leq x \leq h/2, \\ \hat{\vartheta}(x, t), & \text{for } x \geq h/2, \end{cases} \quad (\text{II.4.27})$$

The introduction of the variations  $\eta$  corresponding to the class of functions (II.4.27) in the weak form of the heat equation

$$\int_0^L \rho c_v \dot{\vartheta} \eta \, dx - \int_0^L q \frac{\partial \eta}{\partial x} \, dx = \kappa \eta \frac{\partial \vartheta}{\partial x} \Big|_0^L \quad (\text{II.4.28})$$

leads to

$$\begin{aligned} & \int_0^{\frac{h}{2}} \rho c_v [\dot{\vartheta}_o + (\dot{\vartheta}_{\frac{h}{2}} - \dot{\vartheta}_o) \frac{2x}{h}] [\eta_o + (\eta_{\frac{h}{2}} - \eta_o) \frac{2x}{h}] \, dx - \int_0^{\frac{h}{2}} q \cdot (\eta_{\frac{h}{2}} - \eta_o) \frac{2}{h} \, dx \\ & + \int_{\frac{h}{2}}^L \rho c_v \dot{\vartheta} \hat{\eta} \, dx - \int_{\frac{h}{2}}^L q \frac{\partial \hat{\eta}}{\partial x} \, dx = \eta_o \mathcal{D}_p / 2, \end{aligned} \quad (\text{II.4.29})$$

for all variations  $\eta_o$  and  $\hat{\eta}$  with  $\hat{\eta}(h/2, t) = \eta_{\frac{h}{2}}$ . After integration by parts, we arrive at the equations

$$\rho c_v \dot{\vartheta} = \kappa \frac{\partial^2 \vartheta}{\partial x^2} \quad \text{for } x > \frac{h}{2}, \quad \text{with} \quad \frac{\partial \vartheta}{\partial x}(L, t) = 0, \quad (\text{II.4.30})$$

and the equation

$$\begin{aligned} & \rho c_v h \left[ \frac{1}{6} \dot{\vartheta}_o + \frac{1}{12} \dot{\vartheta}_{\frac{h}{2}} \right] + q_{\Omega_o} = \mathcal{D}_p / 2, \\ & \rho c_v h \left[ \frac{1}{12} \dot{\vartheta}_o + \frac{1}{6} \dot{\vartheta}_{\frac{h}{2}} \right] - q_{\Omega_o} + q_{\frac{h}{2}+} = 0. \end{aligned} \quad (\text{II.4.31})$$

Here, heat flux are defined as

$$\begin{aligned} q_{\Omega_o} &= -\kappa \frac{2}{h} (\vartheta_{\frac{h}{2}} - \vartheta_o) \\ q_{\Omega_{\frac{h}{2}}} &:= -\kappa \frac{\partial \vartheta}{\partial x} \Big|_{x=\frac{h}{2}}. \end{aligned} \quad (\text{II.4.32})$$

## II.4.2. Properties of the solution

In this section, parametric study of  $\delta$  is presented. Figure II.4.1 depicts the distribution of the displacement, velocity, stress and temperature field along the bar at  $t = 2.5t_b$ . Figure II.4.2 is the graph of the evolution of displacement, velocity, stress and temperature at  $x = h/2$  in time. Eleven different values of length parameter  $\delta$  -0.001, 0.1, 0.2, 0.3, 0.4,

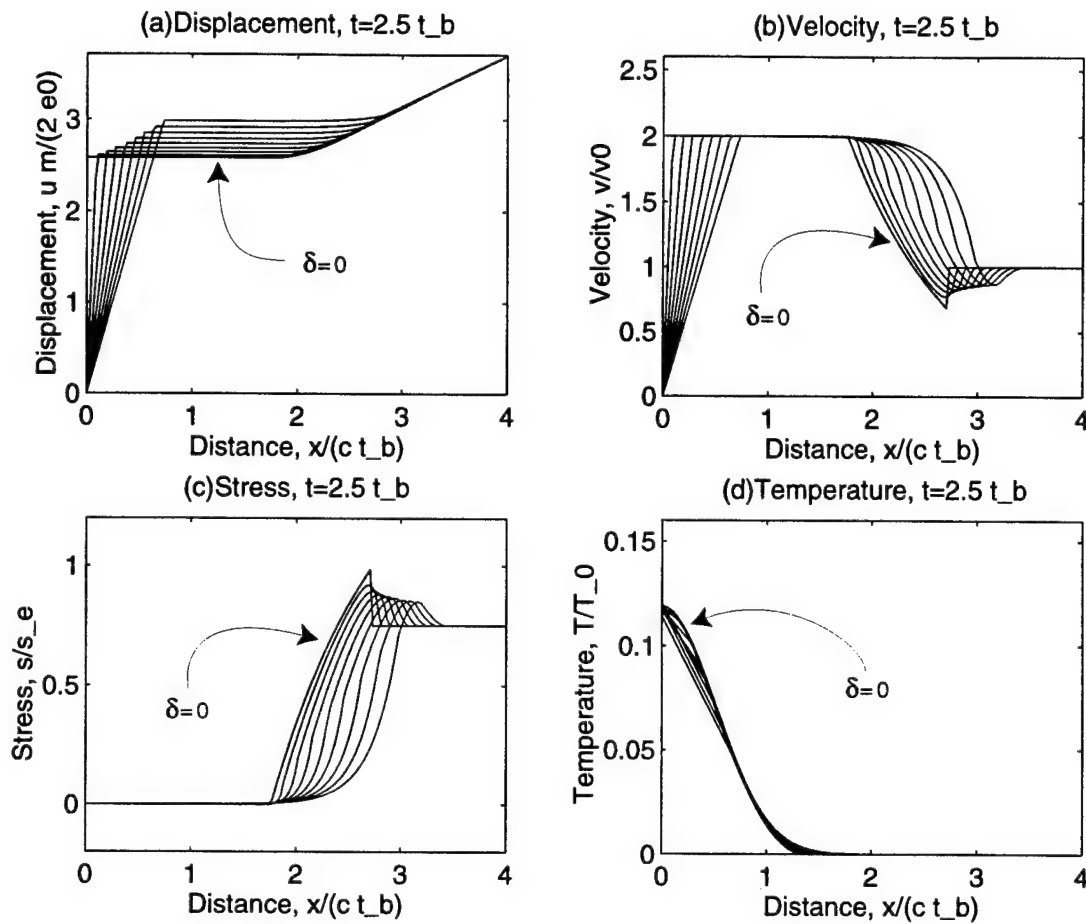


**FIGURE II.4.1** Displacement, velocity, stress, and temperature distribution along the shear layer for nine different values of  $\delta = 0.0, 0.1, 0.2, 0.3, 0.4, 0.5, 0.6, 0.7, 0.8$ . Parameter  $p_1 = 1.0 \times 10^{-4}$  and  $p_2 = 1.5$  are fixed.

0.5, 0.6, 0.7, 0.8 – are considered with linear softening law. Thermal softening function  $\Theta$  is also considered to be linear, namely,

$$\Theta(\vartheta(0, t)) = 1 - w_0 \vartheta(0, t) \quad (\text{II.4.33})$$

with thermal softening constant fixed. For comparison with pure mechanical results, parameters  $p_1 = 1.0 \times 10^{-4}$  and  $p_2 = 1.5$  are selected. A consistent mass approximation ( $\alpha = 1/3$ ) is assumed.

The kinematic quantities have similar characteristics of purely mechanical results in ARMERO [1997a]. The noticeable differences in  $t_b$  is the main effect of thermal softening. In Figure II.4.2(b)- II.4.2(d), we can see that the breaking time  $t_b$  comes earlier than normalized time 1.0 regardless of  $\delta$ . Increased temperature lowered the elastic limit  $\tau_e$ ,

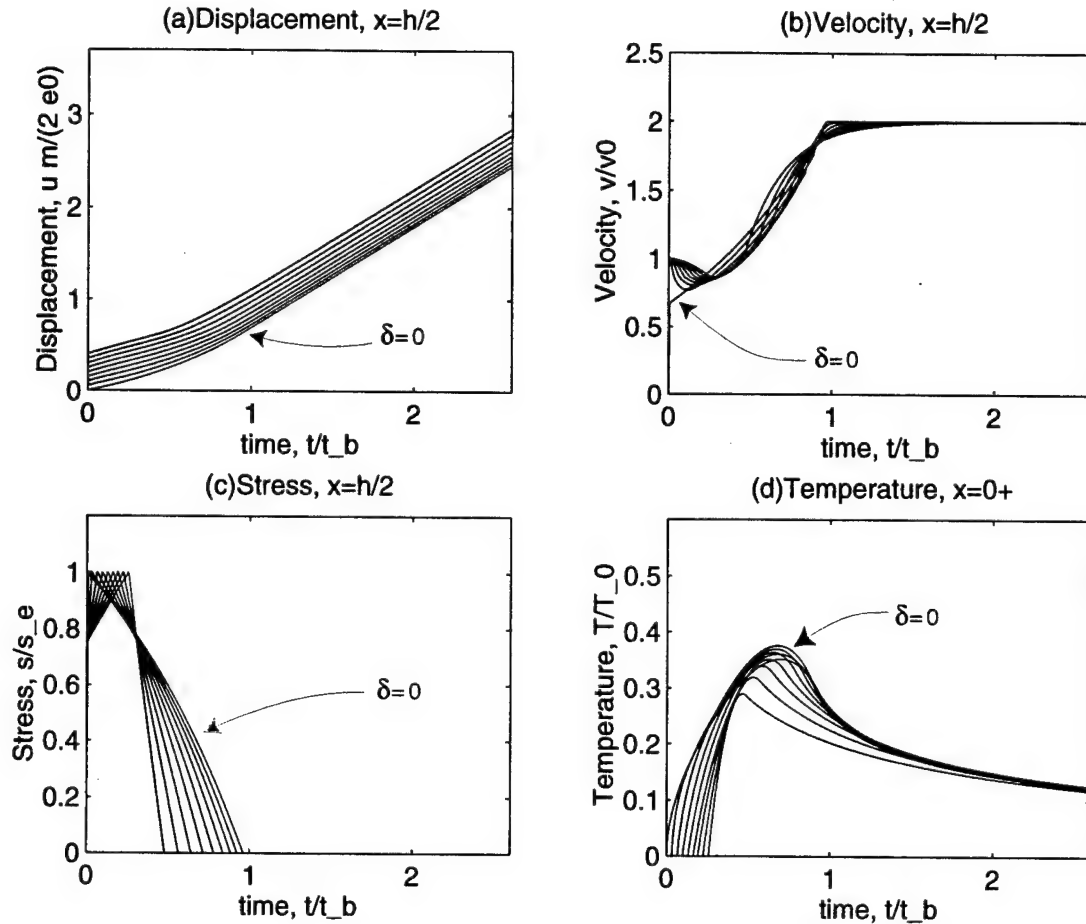


**FIGURE II.4.2** Displacement, velocity, stress, and temperature evolution in time at  $x = \frac{h}{2}$  for nine different values of  $\delta = 0.0, 0.1, 0.2, 0.3, 0.4, 0.5, 0.6, 0.7, 0.8$ . Parameter  $p_1 = 1.0 \times 10^{-4}$  and  $p_2 = 1.5$  are fixed.

which causes  $t_b$  smaller. This phenomenon was examined in Section II.3.1 and can be predicted by the uncoupled relation

$$t_{b_o} = -\frac{1}{mc_e} \log \left( 1 - \frac{1}{r} \right), \quad (\text{II.4.34})$$

with  $r = 2\tau_o/\tau_e$ .

In Figure II.4.2(c), time evolution of stress  $\tau_{\Omega_o}$  is depicted. It also shows similar results to ARMER [1997a] of pure mechanical problem:  $t_e$  and  $t_b$  move closer to each other as  $\delta$  increases. One notable difference is that slope of stress evolution curve slightly increases as time goes on. This is related to the stabilizing effect of thermal conductivity and this topic was discussed in Section II.2.

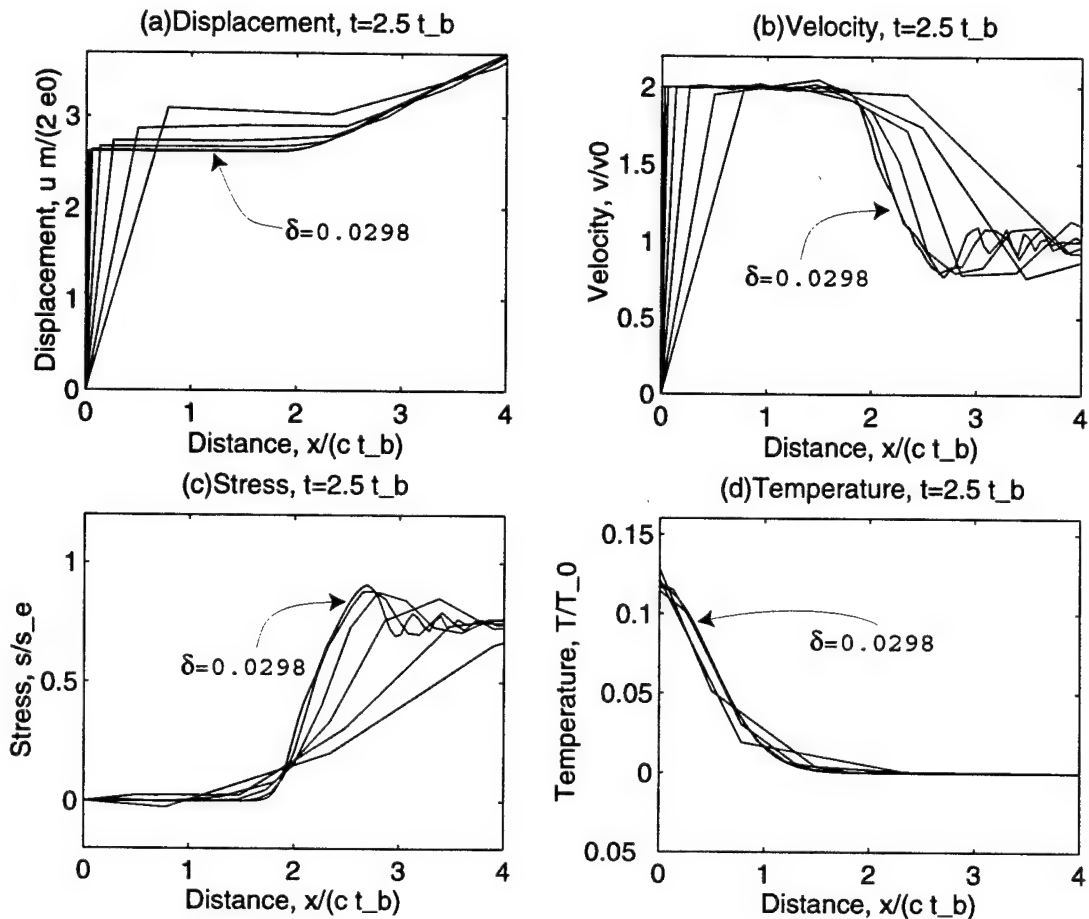


**FIGURE II.4.3** Displacement, velocity, stress, and temperature distribution along the shear layer for six different values of  $\delta = 0.0298, 0.0594, 0.1463, 0.2857, 0.5455, 0.8571$ . Finite Element solution for comparison with Figure II.4.1. Parameter  $p_1 = 1.0 \times 10^{-4}$  and  $p_2 = 1.5$  are fixed.

Time evolution of temperature is in Figure II.4.2(d). Maximum temperature decreases as  $\delta$  increases up to  $\delta = 0.8$ . However, it converges to one after complete breaking.

### II.4.3. Representative finite element simulations

We consider the shear layer which is described in Section II.3.1. The model of this layer is discretized symmetrically by an odd number of equal length finite elements. In real setting for analysis, half of the bar is considered and as a result, the first (central) element has half the dimension of other elements.

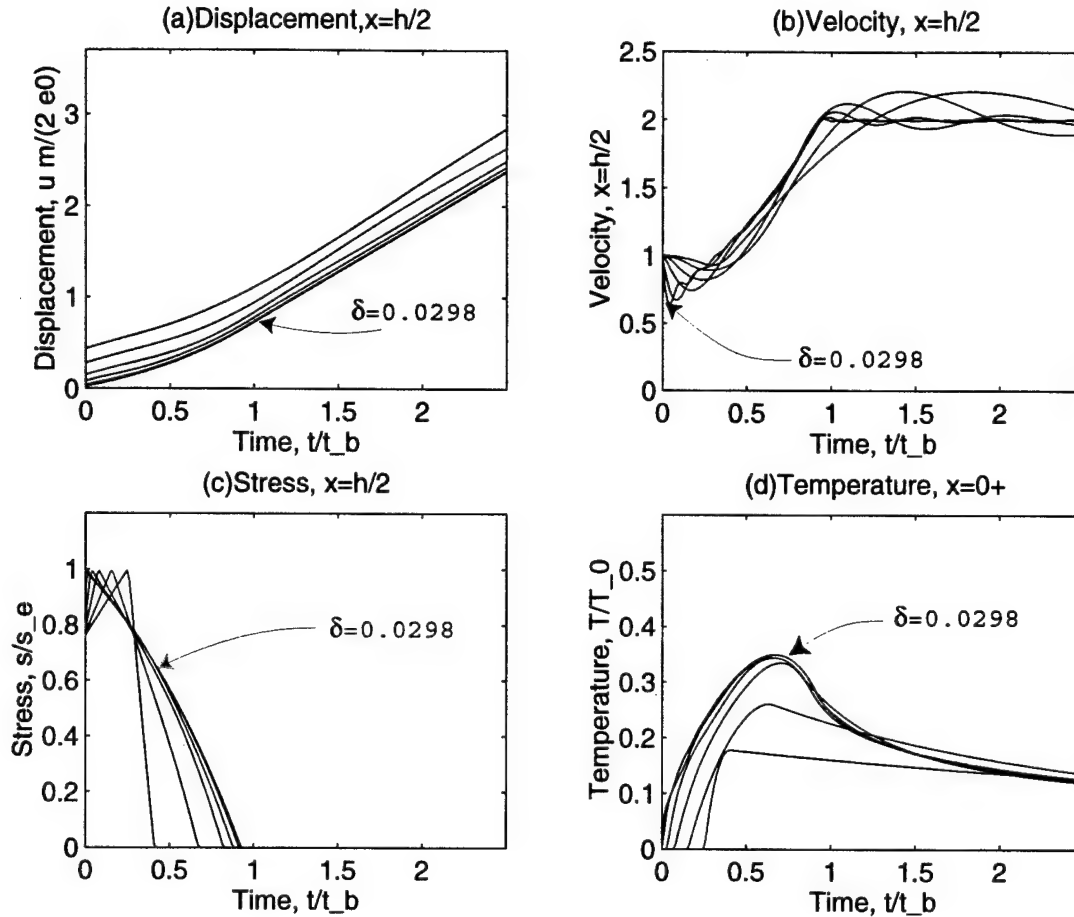


**FIGURE II.4.4** Displacement, velocity, stress, and temperature time evolution at  $x = \frac{h}{2}$  for six different values of  $\delta = 0.0298, 0.0594, 0.1463, 0.2857, 0.5455, 0.8571$ . Finite Element solution for comparison with Figure II.4.2. Parameter  $p_1 = 1.0 \times 10^{-4}$  and  $p_2 = 1.5$  are fixed.

The initial conditions (II.3.2) and (II.3.3) is imposed at  $t = 0$ , with initial constant velocity  $v_o$ . A stress of  $r = 1.5$  is imposed at the end of the layer. We adopt the average acceleration Newmark approximation of the governing equations in time with consistent mass matrix and constant time step  $\Delta t = t_{b_o}/80$  for all simulations. This is to be done to validate the results in the previous section. One difference between the present finite element analysis and the approximated analysis in the previous section is that in the elastic domain the finite element analysis is still approximate solution to the problem. Figure II.4.3 and Figure II.4.4 depict the results obtained with different number of elements. All other material quantities are fixed as  $p_1 = 1.0 \times 10^{-4}$ .

The trend of solutions with different values of  $\delta$  are the same as analytically approx-

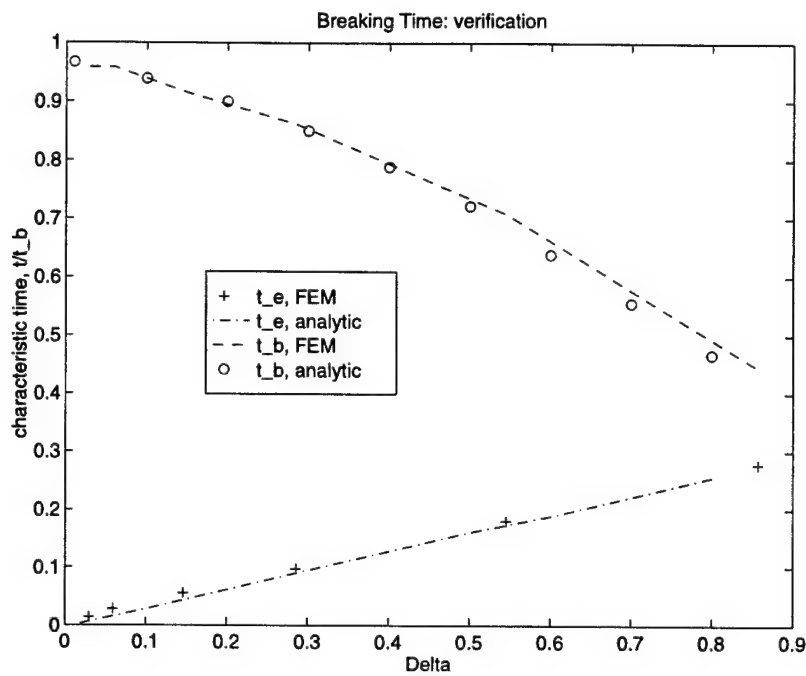


**FIGURE II.4.5** Comparison plot of the breaking time between analytic solutions of approximate theory and finite element solutions. They are expected to match and the result is in good agreement with expectations.

imated solutions in Figure II.4.2. The solutions with highly discretized models are quite exactly in agreement with exact analytic solutions (Figure II.4.1, II.4.2). Figure II.4.4(d) shows decreasing peak as  $\delta$  increases, which is also in good agreement with the analytic solution II.4.2(d). This is the main effect of spatial discretization of temperature field in the finite element solutions.

As another way of verification,  $t_e$  and  $t_b$  from both analytical approximation and finite element analysis are investigated with the same condition. Material parameter  $p_1 = 1.0 \times 10^{-4}$  and  $\delta s$  of 0.0298, 0.0594, 0.1463, 0.2857, 0.5455 and 0.8571 are selected. These  $\delta s$  correspond to 201, 101, 41, 21, 11, and 7 elements in finite elemet model. Figure II.4.5 depicts this result. The values of  $t_e$ s and  $t_b$ s are in good agreement with each other.

## II.5. Extensions to General Multi Dimensional Problems

We consider briefly in this section the analysis of strong discontinuities in the general multi dimensional setting. To this purpose, we describe first the continuum thermoplastic model in Section II.5.1 that we consider as the basis of our developments. Section II.5.2 summarizes the results characterizing the strong discontinuities in this general context, with Section II.5.3 describing their finite element implementation. Finally, Section II.5.4 includes some representative numerical simulations.

### II.5.1. The continuum model

Consistent with our developments in the previous sections, we consider a continuum thermoplastic model based in the infinitesimal range on the additive elastoplastic decompositions

$$\boldsymbol{\varepsilon} = \boldsymbol{\varepsilon}^e + \boldsymbol{\varepsilon}^p, \quad \text{and} \quad \eta = \eta^e + \eta^p, \quad (\text{II.5.1})$$

for the infinitesimal strain  $\boldsymbol{\varepsilon}$  and the entropy per unit volume  $\eta$ . The elastic (recoverable) response of the material is assumed given by an elastic potential  $\psi(\boldsymbol{\varepsilon}^e, \vartheta, \alpha)$ , the free energy function, in terms of the elastic part of the strain  $\boldsymbol{\varepsilon}^e$ , the temperature  $\vartheta$ , and internal variables  $\alpha$  characterizing the hardening/softening of the material. For simplicity, we consider a scalar variable  $\alpha$  for isotropic hardening in the following developments.

A classical argument, usually known as Coleman's method (see TRUESDELL & NOLL [1965]), leads to the constitutive relations

$$\boldsymbol{\sigma} = \partial_{\boldsymbol{\varepsilon}^e} \psi, \quad \eta^e = -\partial_{\vartheta} \psi, \quad q = -\partial_{\alpha} \psi, \quad (\text{II.5.2})$$

for the stress tensor  $\boldsymbol{\sigma}$  and the stress-like internal variable  $q$ . The internal dissipation reads then

$$\mathcal{D}_{int}^p = \mathcal{D}_{mech}^p + \mathcal{D}_{therm}^p, \quad (\text{II.5.3})$$

for the mechanical plastic dissipation

$$\mathcal{D}_{mech}^p = \boldsymbol{\sigma} : \dot{\boldsymbol{\varepsilon}}^p + q \dot{\alpha}, \quad (\text{II.5.4})$$

and the thermal dissipation

$$\mathcal{D}_{therm}^p = \vartheta \dot{\eta}^p. \quad (\text{II.5.5})$$

As considered in previous sections, the mechanical dissipation (II.5.4) is typically expressed in terms of the Taylor coefficient  $\chi$  as  $\mathcal{D}^p = \chi \boldsymbol{\sigma} : \dot{\boldsymbol{\varepsilon}}^p$ . The relation (II.5.3) of the internal dissipation leads to the following associated plastic evolution equations

$$\left. \begin{aligned} \dot{\boldsymbol{\varepsilon}}^p &= \lambda \partial_{\boldsymbol{\sigma}} \phi, \\ \dot{\alpha} &= \lambda \partial_q \phi, \\ \dot{\eta}^p &= \lambda \partial_{\vartheta} \phi, \end{aligned} \right\} \quad (\text{II.5.6})$$

in terms of a yield surface  $\phi(\sigma, q, \alpha)$ . The notation of  $\lambda$  for the plastic multiplier in these equations should not be confused with the symbol for the complex wave number employed in the spectral analyses presented in previous sections. The loading/unloading conditions are defined as usual by the Kuhn-Tucker complementary conditions with

$$\lambda \geq 0, \quad \phi \leq 0, \quad \lambda \phi = 0, \quad (\text{II.5.7})$$

and the plastic consistency condition

$$\lambda \dot{\phi} = 0. \quad (\text{II.5.8})$$

We refer to SIMO & MIEHE [1992] and ARMERO & SIMO [1993] for complete details of all these developments. In particular, the relation (II.5.6)<sub>3</sub> identifies the role of the plastic entropy as the field associated to the thermal softening of the material. We refer to LUBLINER [1990] for a discussion of this issue.

Finally, the governing equations read in this three-dimensional setting

$$\left. \begin{aligned} 0 &= \operatorname{div} \sigma + \mathbf{f}_{ext}, \\ c \dot{\vartheta} &= -\operatorname{div} \mathbf{q} - \mathcal{H}^e + \mathcal{D}_{mech}^p, \end{aligned} \right\} \quad (\text{II.5.9})$$

for the thermal flow  $\mathbf{q}$  and the structural thermoelastic heating  $\mathcal{H}^e$ . The numerical simulations presented in Section II.5.4 consider the case of an isotropic material characterized by Fourier's law

$$\mathbf{q} = -\kappa \nabla \vartheta, \quad (\text{II.5.10})$$

for the thermal conductivity  $\kappa$ , and

$$\mathcal{H}^e = \alpha_\vartheta \operatorname{tr}(\dot{\boldsymbol{\varepsilon}}^e), \quad (\text{II.5.11})$$

for the linear coefficient of thermal expansion  $\alpha_\vartheta$ . We also consider the quasi-static assumption considered in (II.5.9)<sub>1</sub> in the numerical simulations presented in Section II.5.4.

### II.5.2. Strong discontinuities in thermoplastic media

The plastic evolution equations (II.5.6) reveal the nature of the localized plastic flows in a thermoplastic material. More specifically, the consideration of a plastic multiplier

$$\lambda = \tilde{\lambda} \delta_\Gamma, \quad (\text{II.5.12})$$

for the Dirac delta function  $\delta_\Gamma$  along a surface  $\Gamma$  imply the singularity of the plastic strains  $\boldsymbol{\varepsilon}^p$ , strain-like hardening/softening variables  $\alpha$  and the plastic entropy  $\eta^p$ . This singular character of these fields (singular in the distributional sense) requires the decompositions

$$\mathbf{u}_\mu = \bar{\mathbf{u}} + [\mathbf{u}] H_\Gamma \quad \text{and} \quad \eta_\mu = \bar{\eta} + \tilde{\eta} \delta_\Gamma, \quad (\text{II.5.13})$$

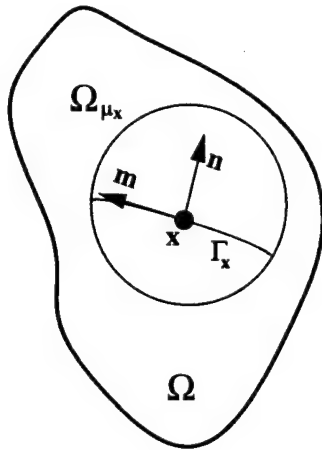


**FIGURE II.5.1** The characterization of the localized dissipative mechanism associated to a strong discontinuity  $\Gamma$  is understood in a local neighborhood  $\Omega_\mu$ .

that is, the discontinuity of the displacement field and the singularity of the entropy field. The notation  $(\cdot)_\mu$  has been employed to refer to the local character of the corresponding fields in a local neighbor of the material point under consideration, with the regular part denoted by  $(\bar{\cdot})$ . We refer to ARMERO [1997a] for complete details of the developments of these ideas in a multi-scale context. Figure II.5.1 illustrates the local character of these considerations in the aforementioned local neighborhood. The local strains associated to the displacement field (II.5.13)<sub>1</sub> are

$$\varepsilon_\mu = \varepsilon(\bar{u}) + ([u] \otimes n)^s \delta_\Gamma , \quad (\text{II.5.14})$$

for the unit normal  $n$  to the discontinuity surface  $\Gamma$ .

The inclusion of the expressions (II.5.12) to (II.5.14) in the constitutive relations presented in the previous sections identifies necessary conditions for the existence of the assumed strong discontinuities exhibiting the localized plastic flow (II.5.12). The analysis follows the same steps as presented in Appendix III of this report for the case of poroplasticity. The details are therefore omitted. The results characterizing the strong discontinuities can be summarized as follows:

1. The temperature  $\vartheta$  remains continuous with a discontinuous thermal flow

$$q_\mu = \bar{q} + [q] H_\Gamma \implies \operatorname{div} q = \operatorname{div} \bar{q} + [q] \cdot n \delta_\Gamma , \quad (\text{II.5.15})$$

in the distributional sense, as it appears in the balance equation (II.5.9)<sub>2</sub>.

2. The energy balance equation (II.5.9)<sub>2</sub> leads then to the local balance equation

$$\tilde{\mathcal{D}}_{\text{mech}}^p = t \cdot [\dot{u}] - \dot{\psi} = -[q] \cdot n , \quad \text{with } t = \sigma n \text{ on } \Gamma , \quad (\text{II.5.16})$$

the traction vector  $\mathbf{t}$  on  $\Gamma$  and the localized free-energy function  $\tilde{\psi}$  associated to the localized response along the strong discontinuity  $\Gamma$ . For the elastoplastic case of interest herein,  $\tilde{\psi}$  corresponds to the potential associate to the softening response on  $\Gamma$ , but rigid otherwise (i.e., no recoverable part of  $[\mathbf{u}]$  is considered). The equation (II.5.16) identifies the discontinuous part of the thermal flow with the localized mechanical dissipation along  $\Gamma$  (power per unit area and not unit volume). Following the developments in the continuum, we express the localized dissipation (II.5.16) as

$$\tilde{\mathcal{D}}^P = \tilde{\chi} \mathbf{t} \cdot [\dot{\mathbf{u}}], \quad (\text{II.5.17})$$

for a “localized Taylor coefficient”  $\tilde{\chi}$ .

3. The normal  $\mathbf{n}$  and the localized flow direction  $\mathbf{m}$  (i.e.,  $[\dot{\mathbf{u}}] = \dot{\zeta} \mathbf{m}$  with  $\|\mathbf{m}\| = 1$ ) satisfy the acoustic tensor relation

$$\mathbf{Q}_{iso}^{ep} \mathbf{m} = [\mathbf{n} \cdot \mathbf{C}_{iso}^{ep} \mathbf{n}] \mathbf{m} = 0 \quad (\text{II.5.18})$$

for the isothermal continuum perfect tangent  $\mathbf{C}_{iso}^{ep}$ . In the case of  $J_2$ -flow theory, this relation leads to the orthogonality of the two vectors  $\mathbf{n}$  and  $\mathbf{m}$ , thus defining an slip relation along  $\Gamma$ .

4. The localized softening relation

$$\dot{\zeta} = \frac{1}{\tilde{\mathcal{H}} \Xi} [\partial_{\sigma} \phi : \dot{\sigma} + \partial_{\vartheta} \phi \dot{\vartheta}] \quad \text{and} \quad \dot{\eta} = \dot{\zeta} \partial_{\theta} \phi. \quad (\text{II.5.19})$$

for

$$\Xi = \frac{(\partial_q \phi)^2}{\partial_{\sigma} \phi : \mathbf{C}_{iso}^{ep} \partial_{\sigma} \phi} \mathbf{C}_{iso}^{ep} \partial_{\sigma} \phi : (\mathbf{m} \otimes \mathbf{n}) \quad (\text{II.5.20})$$

at the bifurcation leading to the strong discontinuity. In general, we identify a localized softening relation  $t([\mathbf{u}], \vartheta)$  for the traction vector in terms of the displacement jump and temperature.

These results identify clearly the fundamental role of the strong discontinuity introducing a localized dissipation (dissipation per unit area) on  $\Gamma$  and leading to the localized heating of the material. The need for the introduction of these effects in the numerical solution of the governing equations is then clear as developed next in the context of the finite element method.

### II.5.3. The finite element implementation

Following the developments presented in Appendix I of this report, we consider an enhanced interpolation of the strains in the context of the finite element method to accommodate their singular character. In particular, we consider the strains

$$\boldsymbol{\epsilon}^h = \bar{\mathbf{B}} \mathbf{d} - \underbrace{\frac{1}{h_e^{(i)}} (\boldsymbol{\xi}_e^h \otimes \mathbf{n}^{(i)})^s}_{\text{conforming}} + \underbrace{(\boldsymbol{\xi}_e^h \otimes \mathbf{n})^s \delta_{\Gamma_e}}_{\text{enhanced (unresolved)}}, \quad (\text{II.5.21})$$

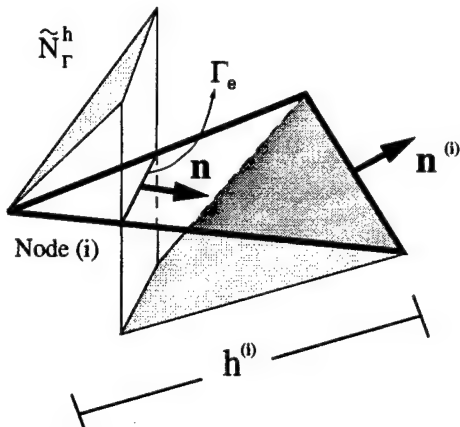


**FIGURE II.5.2** Discontinuous shape function leading to the singular strain at an element where localization has been detected

starting with a conforming interpolation of the strain field defined by the linear strain operator  $\bar{\mathbf{B}}$ . This includes any assumed strain interpolation in the context of mixed treatment of the governing equations. Here  $\xi_e^h$  are the enhanced parameters modeling the jump across the strong discontinuity  $\Gamma$  for an element where localization has been detected through the relation (II.5.18). A piece-wise constant approximation of the jump at the element level is assumed. The strain interpolations (II.5.21) can be motivated as the (symmetric) gradient of the discontinuous shape function depicted in Figure II.5.2.

To capture the discontinuous thermal flow, we also consider a local enhancement of the thermal flux vector that arises from a standard thermal element characterized by a gradient operator  $\bar{\mathbf{B}}_\vartheta$ . In this way, we consider

$$\bar{\mathbf{q}}^h = -\kappa \underbrace{\bar{\mathbf{B}}_\vartheta \vartheta}_{\text{conforming}} \quad \text{in } \Omega_e \setminus \Gamma_e \quad \text{and} \quad [\![\mathbf{q}^h]\!] \cdot \mathbf{n} = q_{ne}^h \quad \text{on } \Gamma_e ,$$

for the regular part  $\bar{\mathbf{q}}^h$  and the localized normal thermal flow  $q_{ne}^h$ . Here,  $\vartheta$  denotes a set of nodal temperatures defining the conforming interpolation of the temperature field.

**Remark II.5.1** The acoustic tensor condition (II.5.18) identifies the orthogonality of the unit normal  $\mathbf{n}$  and the direction of the displacement jump  $[\mathbf{u}]$  for  $J_2$ -flow theory. The check for the singularity of the acoustic tensor can in fact be expressed in closed form; see ARMERO & GARIKIPATI [1995]. In this case, a fixed slip direction  $\xi_e^h = \xi_e^h \mathbf{m}$ , for the tangent  $\mathbf{m}$  to  $\Gamma_e$ , is considered, thus reducing the number of enhanced parameters in the strain field to one scalar.  $\square$

The introduction of the previous considerations in the weak form of the governing

**TABLE II.5.1** Finite element implementation of enhanced strain finite elements incorporating strong discontinuities in the thermomechanical range

```
do n = 1,nsteps
```

```
  do while (convergence in  $z_{n+1}^{(k)} := [d \theta]_{n+1}^{(k)}$ ,  $k = 0, 1, \dots$ )
```

```
    do e = 1,nelem
```

Update enhanced parameters:  $\xi_{en+1}^{(k+1)} = \xi_{en+1}^{(k)} + K_{e22}^{-1} (r_e - K_{e21} \Delta z_e)$

**Standard finite element**

with  $\epsilon = \bar{B}d + \tilde{\epsilon}(\xi_e)$

$$\Rightarrow R_e = \begin{cases} R_{e \text{ mech}} \\ R_{e \text{ ther}} \end{cases}, \quad K_e = \frac{\partial R_e}{\partial z_e}$$

Enhanced strain module:

Enhanced residual:  $r_e = \frac{I}{A_e} \int_{\Omega_e} \sigma n d\Omega - t (\xi_{en+1}^{(k+1)}, \bar{\theta}_{en+1}^{(k+1)})$

and tangent:  $K_{e12} = \frac{\partial R_e}{\partial \xi_e}, \quad K_{e21} = \frac{\partial r_e}{\partial z_e}, \quad K_{e22} = \frac{\partial r_e}{\partial \xi_e}$

Localized dissipation:  $R_{e \text{ ther}} \leftarrow R_{e \text{ ther}} - \bar{N}_e^T \tilde{D}_{mech e}^p$

where  $\tilde{D}_{mech e}^p = t \cdot (\xi_{en+1}^{(k+1)} - \xi_{en}) / \Delta t$ ,

$\bar{N}_e = \int_{T_e} N_e d\Gamma$  (in closed form) and  $\bar{\theta}_e = \bar{N}_e \theta$

Static condensation:

$R_e \leftarrow R_e - K_{e12} K_{e22}^{-1} r_e$

$K_e \leftarrow K_e - K_{e12} K_{e22}^{-1} K_{e21}$

```
end do !e
```

Assemble ( $R = \sum_e R_e$ ,  $K = \sum_e K_e$ ) and solve ( $K \Delta z = R$ ).

Update ( $z_{n+1}^{(k+1)} = z_{n+1}^{(k)} + \Delta z$ ) and check convergence on  $R$ .

```
end do !convergence
```

Propagate discontinuities through the mesh graph, if necessary.

```
end do !n
```

equations lead to the finite element residuals

$$\left. \begin{aligned} \mathbf{R}_{\text{mech}}(\mathbf{d}, \boldsymbol{\vartheta}) &:= \mathbf{f}^{\text{ext}} - \sum_{e=1}^{n_{\text{el}}} \int_{\Omega_e} \bar{\mathbf{B}}^T \boldsymbol{\sigma}(\boldsymbol{\varepsilon}(\mathbf{d}, \boldsymbol{\vartheta}; \boldsymbol{\xi}_e^h)) d\Omega = 0, \\ \mathbf{R}_{\text{ther}}(\mathbf{d}, \boldsymbol{\vartheta}) &:= \mathbf{s}^{\text{ext}} - \sum_{e=1}^{n_{\text{el}}} \left\{ \int_{\Omega_e} \left[ \mathbf{N}_\vartheta^T \left( c \dot{\boldsymbol{\vartheta}} + \mathcal{H}^e - \tilde{\mathcal{D}}_{\text{mech}}^p \right) + \kappa \bar{\mathbf{B}}_\vartheta^T \bar{\mathbf{B}}_\vartheta \boldsymbol{\vartheta} \right] d\Omega \right. \right. \\ &\quad \left. \left. - \int_{\Gamma_e} \mathbf{N}_\vartheta^T \tilde{\mathcal{D}}_{\text{mech}}^p d\Gamma \right\} = 0, \right. \end{aligned} \right\} \quad (\text{II.5.22})$$

where we have enforced  $-q_{ne}^h = \tilde{\mathcal{D}}_{\text{mech}}^p = \tilde{\chi} \mathbf{t} \cdot \dot{\boldsymbol{\xi}}_e^h$  on  $\Gamma_e$ . The local enhanced parameters are obtained as  $\boldsymbol{\xi}_e^h(\mathbf{d}, \boldsymbol{\vartheta})$  by imposing the local equilibrium relation

$$\tilde{\mathbf{r}}_e(\mathbf{d}, \boldsymbol{\vartheta}; \boldsymbol{\xi}_e^h) := \frac{1}{A_{\Omega_{e,\text{loc}}}} \int_{\Omega_{e,\text{loc}}} \boldsymbol{\sigma}(\boldsymbol{\varepsilon}(\mathbf{d}, \boldsymbol{\vartheta}; \boldsymbol{\xi}_e^h)) \mathbf{n} d\Omega - \mathbf{t}_\Gamma(\boldsymbol{\xi}_e^h, \bar{\boldsymbol{\vartheta}}_e) = 0, \quad (\text{II.5.23})$$

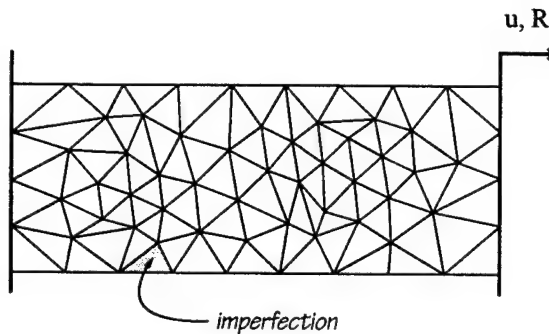
We refer to ARMERO [1997a] for details.

Table II.5.1 includes complete details of the numerical implementation of the preceding equations. It involves the static condensation of the local enhanced parameters  $\boldsymbol{\xi}_e^h$  leading to the solution of a global system of equations in terms of the nodal displacements and temperatures  $\mathbf{z} := \{\mathbf{d}, \boldsymbol{\vartheta}\}$  (the large-scale problem). The simplicity of the implementation is to be noted, reducing simply to the construction of the local residual (II.5.23) and its static condensation after the standard calculations in a general continuum finite element. The numerical simulations of Section II.5.4 consider quadratic triangles with discontinuous linear pressures (Q2/P1). In particular, no regularization of the Dirac-delta functions is required, without the need for special quadrature rules either. A piece-wise constant approximation of the displacement jump contributions is assumed in these considerations. We also note the simplicity of the inclusion of the term with the localized dissipation  $\tilde{\mathcal{D}}^p$  on  $\Gamma_e$ , with the value  $\bar{N}_e$  in Table II.5.1 calculated in closed form. On converging the nonlinear problem the discontinuities are propagated through the mesh using a mesh graph and based on the criterion given by (II.5.18) identifying the unit normal  $\mathbf{n}$ . We refer to ARMERO & GARIKIPATI [1996] for further details on this aspect.

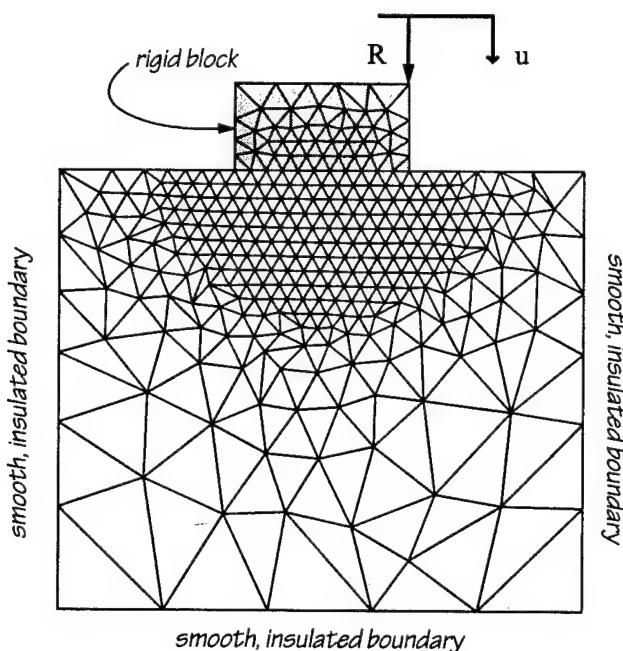
#### II.5.4. Representative numerical simulations

We present in this section several representative numerical simulations to illustrate the performance of the proposed formulation. We consider the two examples depicted in Figure II.5.3 under plane strain conditions. A continuum  $J_2$ -flow theory thermoplastic model based on the Mises yield condition

$$\phi(\boldsymbol{\sigma}, \alpha, \boldsymbol{\vartheta}) = \|\text{dev}(\boldsymbol{\sigma})\| - \sqrt{\frac{2}{3}} y(\alpha, \boldsymbol{\vartheta}) \leq 0, \quad (\text{II.5.24})$$



### Example #1



### Example #2

**FIGURE II.5.3** Problem definitions: 1) plane strain tension test; 2) rigid block pushed against a thermoplastic domain. Plane strain conditions are assumed in both cases, with imposed displacements and measured reactions as shown. Unstructured meshes are used in all cases, without the mesh knowing a-priori any information about the strong discontinuity. An imperfection in the form of a reduced yield limit is assumed in Example #1 to break the symmetry due to the constant state of stress prior to localization.

**TABLE II.5.2** Assumed material properties.  $J_2$ -flow theory with perfect plasticity is assumed for the continuum with linear thermal softening. The localized softening law giving the resolved shear on the discontinuity in terms of the slip is assumed linear, with linear thermal softening.

|   |                         |                      |
|---|-------------------------|----------------------|
| Young modulus                           | $E$                     | 200.0                |
| Poisson ratio                           | $\nu$                   | 0.3                  |
| Flow stress                             | $\sigma_{y_o}$          | 0.45                 |
| Thermal softening (linear)              | $w_o$                   | $3.0 \cdot 10^{-3}$  |
| Localized softening modulus (linear)    | $\tilde{\mathcal{H}}_L$ | -10.0                |
| Localized thermal softening (linear)    | $\tilde{w}_L$           | $3.0 \cdot 10^{-3}$  |
| Thermal conductivity                    | $k$                     | $45.0 \cdot 10^{-3}$ |
| Thermal capacity                        | $\rho c_v$              | $3.68 \cdot 10^{-3}$ |
| Linear coefficient of thermal expansion | $\alpha_\vartheta$      | $1.0 \cdot 10^{-6}$  |
| Taylor coefficient                      | $\chi$                  | 1.0                  |
| Localized Taylor coefficient            | $\tilde{\chi}$          | 1.0                  |

is considered. We assume perfect plasticity and linear thermal softening for the continuum yield properties of the material, that is,

$$y(\alpha, \vartheta) = \sigma_{y_o} (1 - w_o \vartheta), \quad (\text{II.5.25})$$

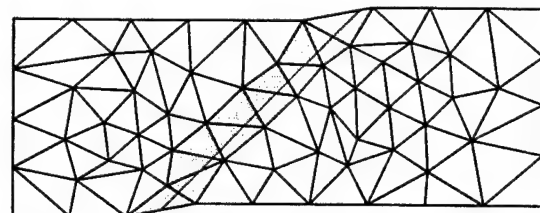
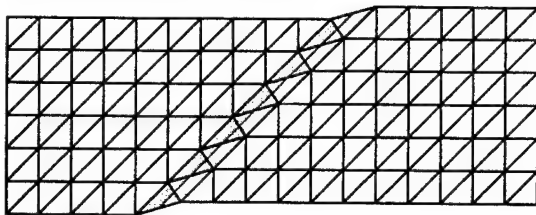
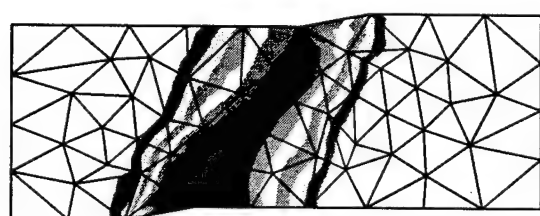
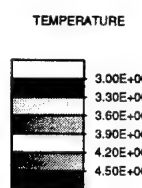
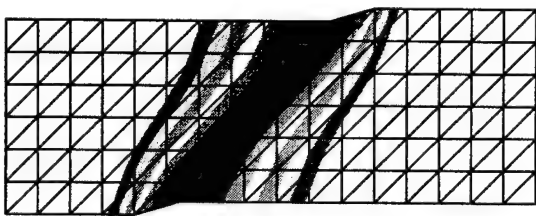
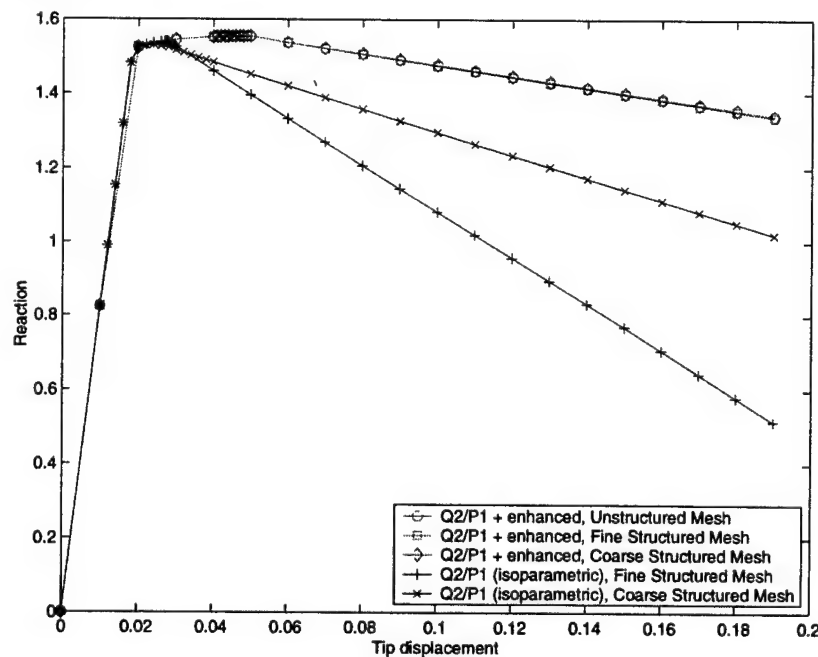
for the two material parameters  $\sigma_{y_o}$  and  $w_o$ . The acoustic tensor condition (II.5.18) leads then to a slipping relation along the discontinuity between the resolved shear  $r_s := \mathbf{t} \cdot \mathbf{m} = \boldsymbol{\sigma} \mathbf{n} \cdot \mathbf{m}$  (with  $\mathbf{n} \perp \mathbf{m}$ ) and the tangential slip  $\zeta$  (with  $[\mathbf{u}] = \zeta \mathbf{m}$ ). The linear softening relation

$$r_s = \frac{\sigma_{y_o}}{\sqrt{3}} (1 - \tilde{w}_L \vartheta) + \tilde{\mathcal{H}}_L \zeta, \quad (\text{II.5.26})$$

is assumed. The stresses are given by a linear elastic response, defined by the Young modulus  $E$  and Poisson ratio  $\nu$ . Table II.5.2 summarizes the values assumed for the different material parameters in the numerical simulations presented next.

#### II.5.4.1. Plane strain tension test

We consider first the classical benchmark problem of the plane strain tension test. To this purpose, we consider the specimen of dimensions  $3 \times 8$  depicted in Figure II.5.3. An equal tensile displacement is imposed at one end under quasi-static plane strain conditions, with the specimen free to contract laterally, leading to a state of constant strain and stress. A unit rate of imposed displacement is considered. To break the symmetry, a small imperfection is assumed by reducing the yield value  $\sigma_{y_o}$ . Under these conditions, the strains are expected to localize at  $45^\circ$  degrees with the axis of the load. Note that the mesh or the finite elements do not have any a-priori knowledge of this, with the

**Discontinuity path:****Temperature distribution:****Load displacement curves:**

**FIGURE II.5.4** Plane strain tension test. 1) Discontinuity path in a unstructured and a structured mesh. The same path is obtained in both cases, with a good resolution of the localized deformation pattern of the specimen. 2) Temperature distribution capturing the dissipative effects along the discontinuity. 3) Load/displacement curves obtained for different meshes. In all cases (fine and coarse, structured and unstructured meshes), the proposed localized formulations based on strong discontinuities results in essentially the same solution, reflecting the resolution of the localized dissipative mechanism. This situation is to be contrasted with the numerical solutions obtained with a standard isoparametric solution based on a continuum model with strain softening.

discontinuity propagating automatically after checking the localization condition (II.5.18); see also ARMERO & GARIKIPATI [1996] for details.

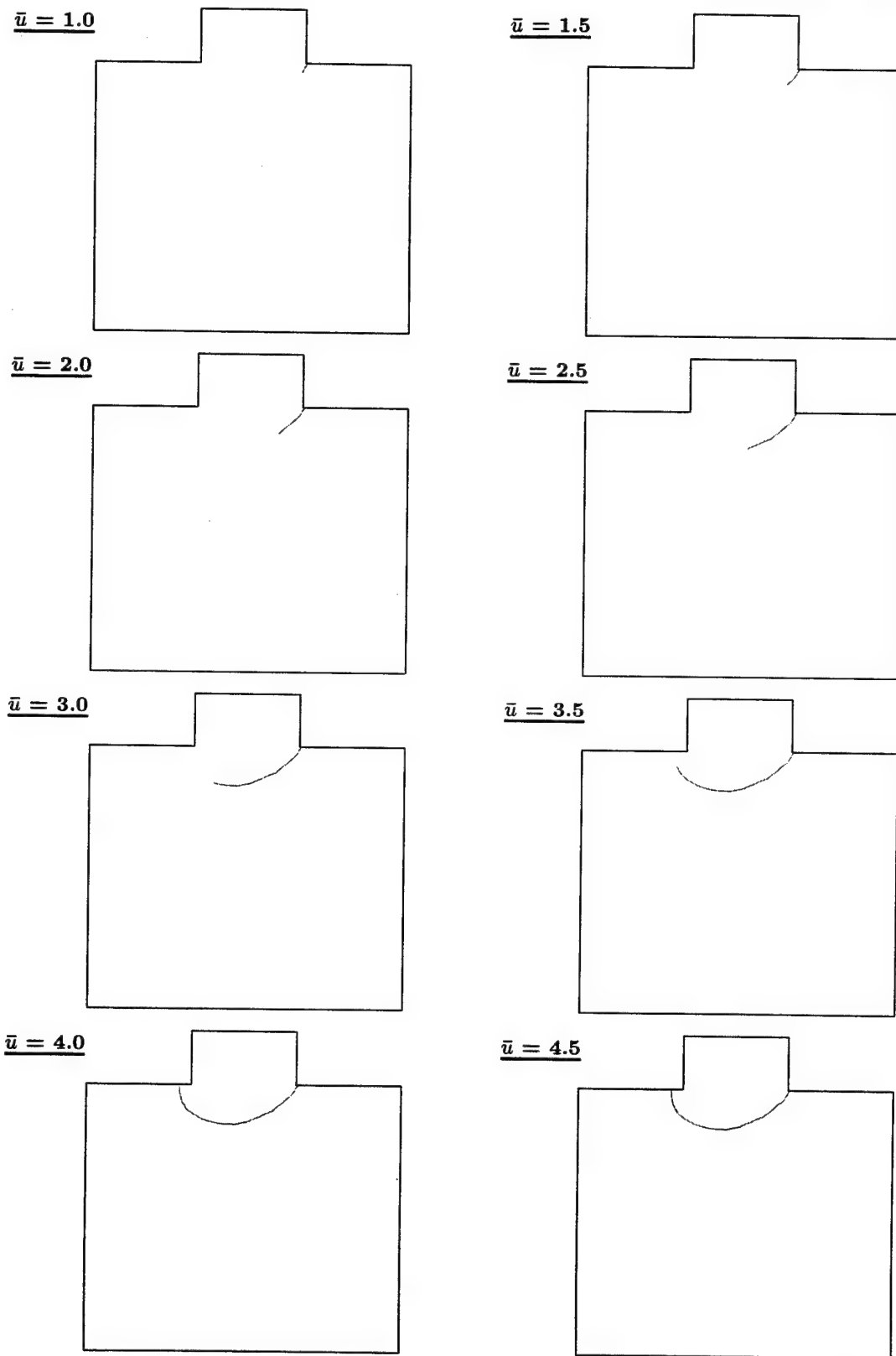
Several spatial discretizations are considered, involving all quadratic triangles with a mixed linear discontinuous interpolation of the pressure to avoid volumetric locking. Figure II.5.4.1 depicts the solution obtained with this element enhanced with the strong discontinuity fields discussed in the previous sections. The path of the discontinuity is depicted. The finite elements with active enhanced modes are shown in color, for two discretizations, structured and unstructured, respectively. The same path can be observed in both cases, concluding the good properties of the proposed formulations in terms of the independence on the mesh alignment. We emphasize again that the finite elements do not have any a-priori information of the directionality of the strong discontinuity. Figure II.5.4.2 depicts the distribution of the temperature in the specimen, showing clearly the heating resulting from the localized slipping along the discontinuity. This heat, and other heating produced in the volume of the specimen due to the bulk plasticity, is dissipated through the heat conduction process.

Figure II.5.4.3 includes the load displacement curves obtained with several spatial discretizations, including coarser meshes than the ones considered above (half the number of elements). We observe the overlapping solutions measured by all the meshes when the proposed enhanced strain formulation is considered. For comparison, we also report the results obtained with the same discretizations but with a continuum model with strain softening. The pathological mesh-size dependence of these numerical solutions is evident in contrast with the procedure developed herein.

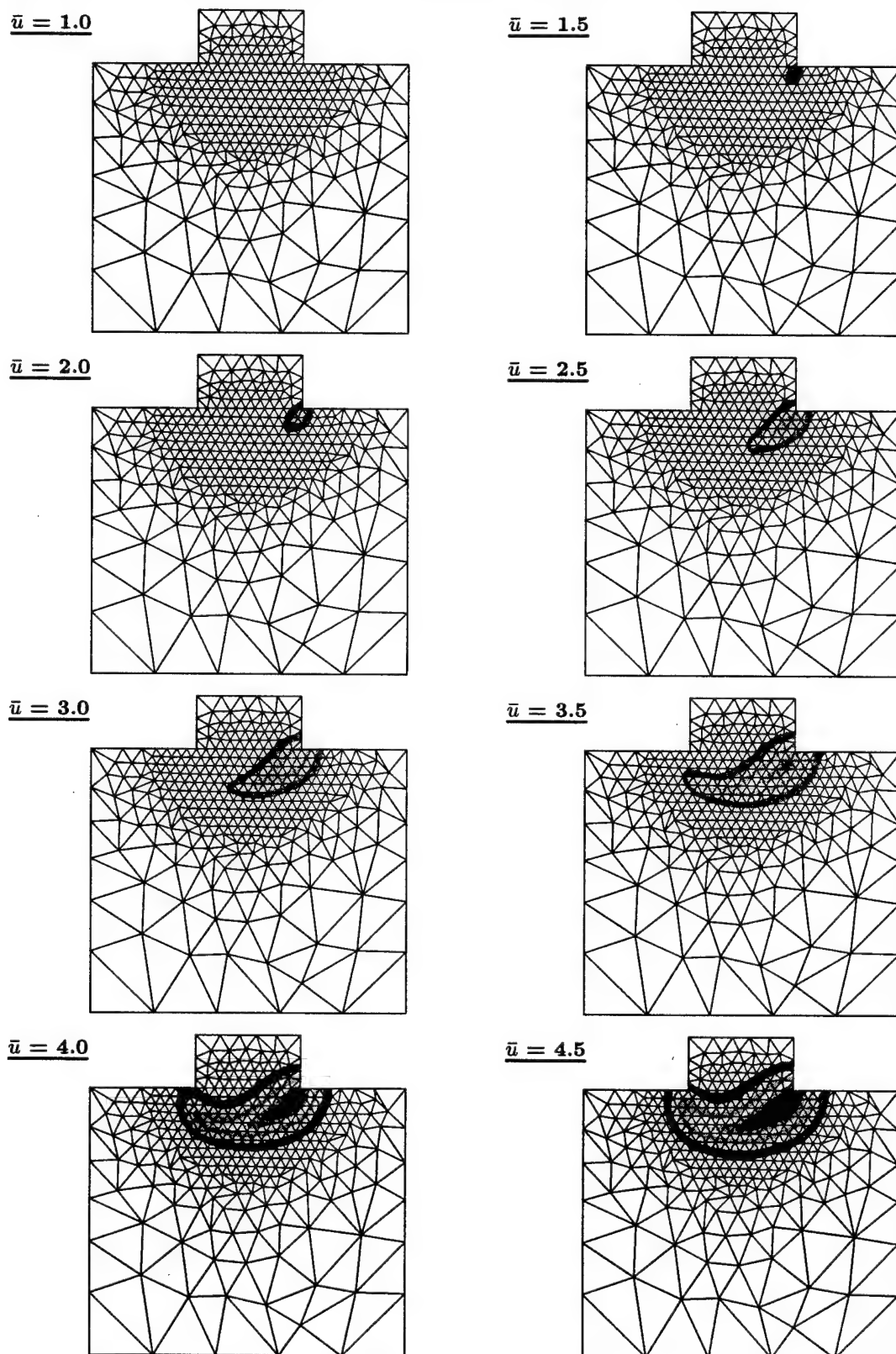
### II.5.4.2. Rigid block pushed against a thermoplastic foundation

We consider next the Example #2 in Figure II.5.3 consisting of a rigid block being pushed against a thermoplastic foundation. The rigid block has dimensions of  $0.4 \times 0.8$  with the thermoplastic domain of  $2 \times 2.4$ . The block is pushed with an imposed displacement at the right top corner, with the corresponding reactions measured. Plane strain conditions are assumed again, with the boundary conditions depicted in Figure II.5.3. The material parameters considered in the simulation are summarized in Table II.5.2. The rigid block is modeled by considering a Young modulus of  $200 \cdot 10^3$ , with a purely elastic law.

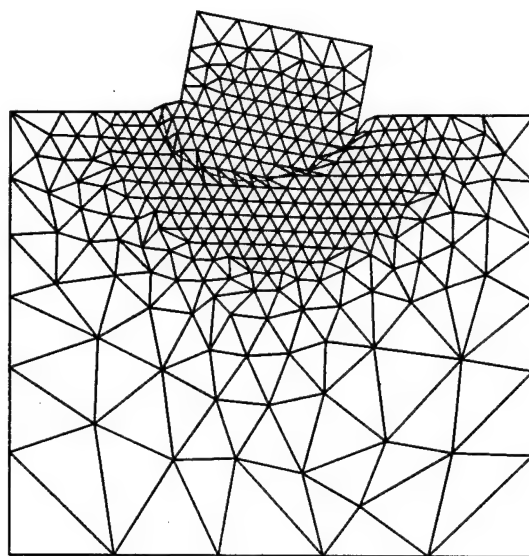
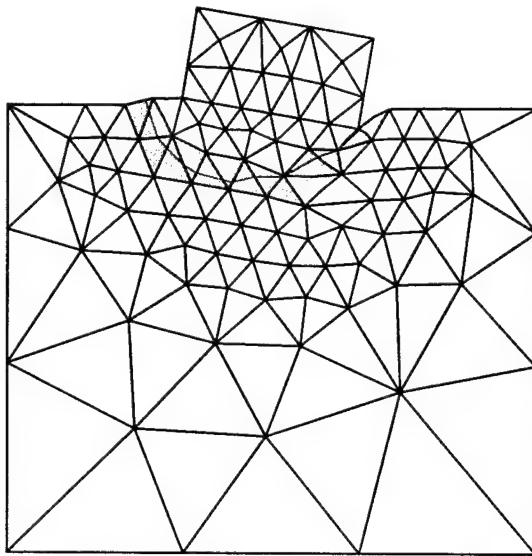
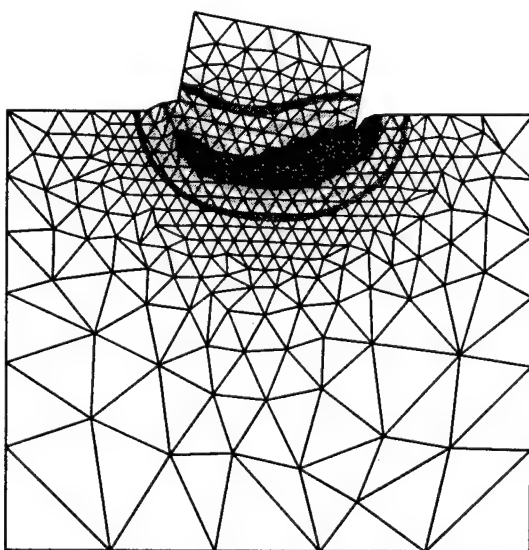
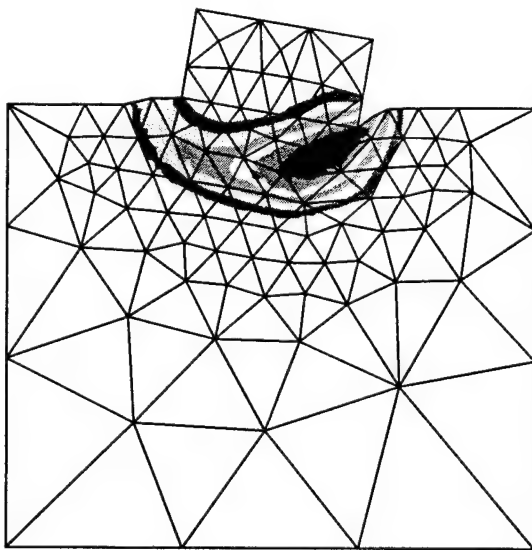
We consider again spatial discretizations involving quadratic triangles with discontinuous linear pressures. No imperfections are required in this case, with the strong discontinuity activated automatically when the condition (II.5.18) is detected. As expected, this occurs at the right corner of the block in contact with the substrate. The path of propagation afterwards is depicted in Figure II.5.5. This path is obtained automatically by the condition (II.5.18). We note that in this case this condition can be evaluated in closed form; see ARMERO & GARIKIPATI [1995]. The curvature of the path is to be noted in this



**FIGURE II.5.5** Rigid block pushed on an elastoplastic foundation.  
Automatic propagation of the discontinuity for different imposed dis-  
placements.



**FIGURE II.5.6** Rigid block pushed on an elastoplastic foundation. Temperature distribution at different imposed displacements (plotting range [5, 30]). Plots shown over the original undeformed mesh.

**Discontinuity path:****Temperature distribution:**

**Coarse unstructured  
mesh**

**Fine unstructured  
mesh**

**FIGURE II.5.7** Rigid block pushed on an elastoplastic foundation. Temperature distribution for two different spatial discretizations. Plots over deformed configuration at  $\bar{u} = 10$  (temperature range [35, 55]). Note the similar paths of the discontinuity for different meshes.

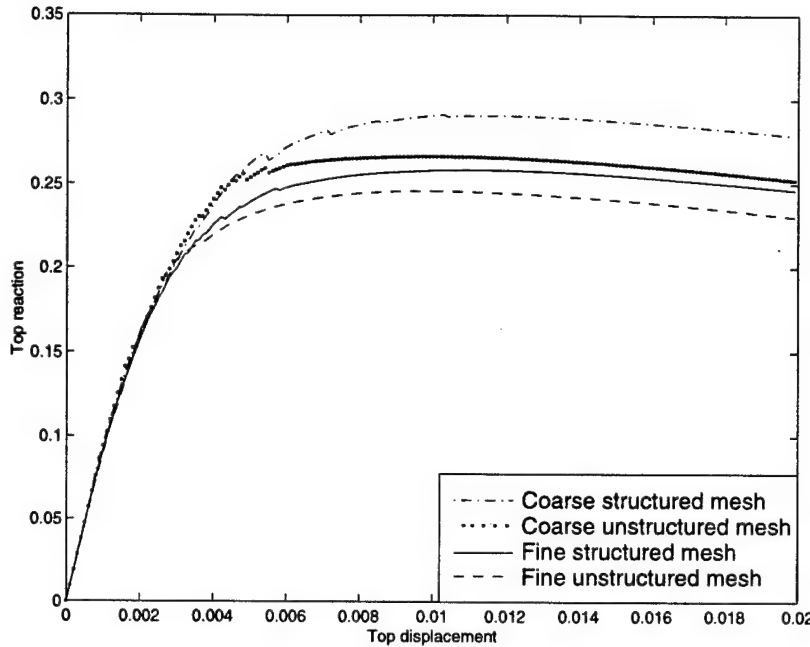


**FIGURE II.5.8** Rigid block pushed on an elastoplastic foundation. Load/displacement curves for several discretizations. Note that the coarse meshes lead to a stiffer solution, as expected, leading to a smaller temperature rise. Observe, however, that the descending slope post-peak is the same, corresponding to an objective resolution of the localized dissipative mechanism (i.e. not showing pathological mesh-size dependence).

case. Figure II.5.6 depicts the distribution of the temperature. The heating associated to the localized slip relation along the strong discontinuity is apparent.

Figure II.5.7 compares this solution with the solution obtained with a coarser mesh. We can observe again the good resolution of the path of the discontinuity confirming the good mesh-alignment independence of the proposed methodology. When comparing the temperature distributions (both depicted at the same scale), we can observe less heating in the coarser mesh. This situation is to be traced back to the stiffer response of the coarser discretization, as expected. This is confirmed in Figure II.5.8 where the measured load displacement curves have been included. The solutions with two additional structured meshes (not shown) have also been included. The post-peak response follows the same slope, indicating the same resolution of the localized dissipative mechanism. The stiffer response of the coarser mesh is confirmed. These differences are to be expected and are directly related to the accuracy of the different level of discretization, with a convergence to a solution as the mesh is refined. This situation is to be contrasted with the pathological mesh-size dependence of the solutions based on a continuum model with strain softening.

## II.6. Concluding Remarks

The main purpose of this appendix is the characterization of the behavior of thermo-elastoplastic material. The concept of a local dissipative mechanism through the introduction of a strong discontinuity is used to model a strain-softening material. The released energy on the discontinuity surface is converted into localized heat flux on that surface. Based on small-strain theory, the deformation process is governed by the coupled system of linear momentum balance and heat equation. This framework was applied to one-dimensional softening shear layer under a pulse type dynamic load. Proper parameters were found and investigated by numerical simulations.

The investigation was done in two steps. The method of linearized spectral analysis was used to predict the real behavior of nonlinear problem. It revealed that in general condition with positive thermal conductivity, the ill-posedness can be characterized in terms of the sign of the mechanical hardening/softening modulus, and its relation with the thermal softening. The ill-posedness of a problem is shown to be directly related to the mesh-dependence of finite element analysis. For these ill-posed problems, an objective dissipation mechanism is required to get physically reasonable solutions.

The ill-posed problems in the continuum framework were next studied analytically after considering the aforementioned localized dissipative mechanism of a strong discontinuity, thus removing the ill-posedness of the problem. In this context, the analytic solution of thermo-mechanical problem was obtained rigorously. The linear momentum balance constitutes a wave equation and the energy balance leads to a heat equation. The solution for the uncoupled case was obtained analytically and used to predict the behavior of the fully coupled case. The conclusions of these analyses were verified extensively through numerical simulations of the coupled nonlinear problems.

An analytic solution of the approximated model of a regularized strong discontinuity was calculated with discretization parameter  $\delta$ . Based on these results, a finite element analysis was done and verified. These comparisons show the objectivity and consistency of strong discontinuity formulations. The effects of the spatial discretization in the modeling of localized dissipative mechanism have been completely characterized by the proposed analysis.

Extensions to the general multi dimensional problem have been presented in the context of the infinitesimal theory. After characterizing the strong discontinuities in a fully coupled thermoplastic model, we have presented their finite element implementation. The numerical results show the objectivity of the proposed framework in contrast to standard isoparametric finite element solutions based on a continuum softening model. The independence on the mesh alignment has been also noted.

---

## References

- ARMERO, F. [1997a] "Large-Scale Modeling of Localized Dissipative Mechanisms in a Local Continuum: Applications to the Numerical Simulation of Strain Localization in Rate-Dependent Inelastic Solids," SEMM/UCB Report no. 97/12, *Mech. Cohesive-Frictional Mat.*, in press.
- ARMERO, F. [1997b] "On the Characterization of Localized Solutions in Inelastic Solids: An Analysis of Wave Propagation in a Softening Bar," SEMM/UCB Report no. 97/18, submitted to *Comp. Meth. Appl. Mech. Eng.*
- ARMERO, F. & GARIKIPATI, K. [1995] "Recent Advances in the Analysis and Numerical Simulation of Strain Localization in Inelastic Solids," *Proc. COMPLAS IV*, eds. D.R.J. Owen, E. Onate, and E. Hinton, CIMNE, Barcelona.
- ARMERO, F. & GARIKIPATI, K. [1996] "An Analysis of Strong Discontinuities in Multiplicative Finite Strain Plasticity and their Relation with the Numerical Simulation of Strain Localization in Solids," *Int. J. Solids and Structures*, **33**, 2863-2885.
- Armero, F. and Simo, J.C. [1993] "A-Priori Stability Estimates and Unconditionally Stable Product Formula Algorithms for Non-Linear Coupled Thermoplasticity", *International Journal of Plasticity*, **9**, 149-182.
- BAI, Y. [1982] "Thermo-plastic Instability in Simple Shear," *J. Mech. Phys. Solids*, **30**, 195-207.
- BAI, Y. & DODD, B. [1992] *Adiabatic Shear Localization; Occurrence, Theories and Localization*, Pergamon Press, Oxford.
- BAZANT, Z. & BELYTSCHKO, T. [1985] "Wave Propagation in a Strain Softening Bar," *ASCE J. Eng. Mech.,* **111**, 381-389.
- GANTMACHER F.R. [1964] *The Theory of Matrices*, vol. II, Chelsea Publishing Co., New York.
- HADAMARD [1903] *Lecons sur la Propagation des ondes et les Equations de l'hydrodynamique.*
- HILL, R. [1962] "Acceleration Waves in Solids," *J. Mech. Phys. Solids*, **16**, 1-10.
- JOHNSON, C. [1976] "Existence Theorems for Plasticity Problems," *J. Math. Pures et Appliq.* **55**, 431-444.
- LUBLINER, J. [1990] *Plasticity Theory*, Macmillan Publishing Company, New York.
- MATTHIES, H.; STRANG, G. & CHRISTIANSEN, E. [1979] "The Saddle Point of a Differential Program," in *Energy Methods in Finite Element Analyses*, edited by Glowinski, Rodin & Zienkiewicz, John Wiley & Sons, London.

- MOLINARI, A. & CLIFTON, R.J. [1987] "Analytical Characterization of Shear Localization in Thermoviscoplastic Materials," *Journal of Applied Mechanics*, **54**, 806-812.
- NEILSEN, M.K. & SCHREYER, H.L. [1993] "Bifurcation in Elastic-Plastic Materials," *Int. J. Solids Struct.*, **30**, 521-544.
- PIETRSZCZAK, ST. & MRÓZ, Z. [1981] "Finite Element Analysis of Deformation of Strain-Softening Materials," *Int. J. Numer. Meth. Eng.*, **17**, 327-334.
- READ, H.E. & HEGEMEIER, G.A. [1984] "Strain Softening of Rock, Soil and Concrete; a Review Article," *Mechanics of Materials*, **3**, 271-294.
- RICE, J. [1976] "The Localization of Plastic Deformations", in *Theoretical and Applied Mechanics*, ed. by W.T. Koiter, 207-219.
- SIMO, J.C. & MIEHE C. [1992] "Associative coupled thermoplasticity at finite strains: formulation, numerical analysis and implementation", *Comp. Meth. App. Mech. Engr.*, **98**, 41-104.
- SIMO, J.C; OLIVER, J. & ARMERO, F. [1993] "An Analysis of Strong Discontinuities Induced by Softening Solutions in Rate Independent Solids," *J. Comput. Mech.*, **12**, 277-296.
- SIMO, J.C. & RIFAI, S. [1990] "A Class of Mixed Assumed Strain Methods and the Method of Incompatible Modes," *Int. J. Num. Meth. Eng.*, **29**, 1595-1638.
- SLUYS, L.J. [1992] "Wave Propagation, Localisation and Dispersion in Softening Solids" Ph.D. Dissertation, Delft Technologycal University, The Netherlands.
- THOMAS, T.Y. [1961] *Plastic Flow and Fracture in Solids*, Academic Press.
- TRUESDELL & NOLL [1965] "The Nonlinear Field Theories of Mechanics," *Handbuch der Physik Bd. III/3*, ed. by S. Fluegge, Springer Verlag, Berlin.
- TVERGAARD, V.; NEEDLEMAN, A. & LO, K.K. [1981] "Flow Localization in the Plane Strain Tensile Test," *Jour. Mech. Phys. Solids*, **29**, 115-142.
- VARDOULAKIS, I. [1979] "Formataion of Shear Bands in Sand Bodies as a Bifurcation Problem," *Int. J.*, **32**, 35-54.
- ZAUDERER, E. [1989] *Partial Differential Equations of Applied Mathematics*, John Wiley & Sons, New York.

## **APPENDIX III**

### **Analysis of Strong Discontinuities in Coupled Poroplasticity**

**Based on the paper:**

Armero, F. and Callari, C. [1999], "An Analysis of Strong Discontinuities in a Saturated Poroplastic Solid," *Int. J. Numerical Methods in Engineering*, 46, 1673-1698.

### III.1. Introduction

The study of localized failures of solids is of the main interest given its important practical applications. In the case of porous materials, like typical geomaterials, the coupling of the flow of a fluid through the porous space is known to have significant effects in this type of failures. In this way, the localization of the strains in narrow bands, referred to as shear bands given their nature, results also in the concentration of the fluid flow along them, leading altogether to the final collapse of the solid. Theoretical and numerical analyses of these phenomena abound in the literature; representative examples are given by RUDNICKI & RICE [1975], RICE [1975], LORET & PREVOST [1991], PIETRUSZCZAK [1995], SCHREFLER et al [1995], VARDOLAKIS [1996], and RUNESSON et al [1996], among many others.

The phenomenon of strain localization is common to many other materials including, for example, metals. In all the cases, the final stages of the deformation before failure are characterized by the localization of the dissipative effects along these band-type structures. Different approaches can be found in the literature to model and simulate numerically this phenomenon; a complete review falls outside the scope of this work. Of interest to the developments presented in this paper is the so-called strong discontinuity approach. This approach can be found developed for the purely mechanical problem in SIMO et al [1993], ARMERO & GARIKIPATI [1996] and OLIVER [1996], with the consideration of regularized strong-discontinuities in LARSSON & RUNESSON [1996] and STEINMANN et al [1997], among others. The resulting formulations consider the limit case of solutions involving a discontinuous displacement field, as they are necessarily obtained in (uncoupled) rate-independent plasticity models of the local continuum. The key feature, however, is the addition of a *localized dissipative mechanism* along these discontinuities, a feature not present in the original local continuum model. The resulting problem of evolution avoids the ill-posedness of the classical continuum problem (that is, it leads to unique solutions depending continuously on the data), as it has been shown in the closed-form analytical solutions presented in ARMERO [1997b] for the problem of wave propagation in a localized softening bar. Similarly, these ideas have been shown in ARMERO [1997a] to furnish a very general tool for the efficient modeling in the large scale of the localized effects of regularized models exhibiting a finite length scale (rate-dependent models, to be specific), while treating these small scales as unresolvable.

We present in this paper the extension of these ideas to the coupled case of a saturated poro-plastic solid. The goals are two-fold. The first objective is the characterization of strong discontinuities in this type of models. In particular, we consider poro-elastoplastic models in the infinitesimal range characterized by an additive decomposition of the strains and the fluid content (fluid mass per unit volume), that is, in the framework first proposed in the pioneering work of BIOT [1941] in the visco-elastic range. Complete details of these models can be found in the recent account in COUSSY [1995], including also several analyses of the resulting boundary value problems. In this context, discontinuous solutions in the

displacements, with the corresponding strains being a singular distribution, are shown to be consistent with the consideration of a localized fluid content (that is, with a fluid mass distributed per unit area of a dilatant surface), as a consequence of a discontinuity of the fluid flow in a permeable porous solid. Importantly, the pore pressure field remains continuous (or, more precisely, with regular gradients). This situation is to be contrasted with the analyses presented in RUNESSON et al [1996] and LARSSON et al [1996] for the limit undrained case, where a discontinuity of the pressure field was considered. For the case of a finite permeability in Darcy's law, this assumption would require to evaluate second derivatives of a discontinuous field. This mathematical structure of the equations for a positive permeability, as well as experimental evidence (see e.g. VARDOULAKIS [1996]), seems then to indicate as more appropriate the continuity assumption on the pressure field. We develop then in this context an analysis of the considered strong-discontinuities in the displacement field for classical continuum models with strain softening (following closely the work that we presented in SIMO et al [1993]), as a motivation for the form of the localized stress-displacement-fluid content relations characterizing the localized dissipative mechanisms in these solutions.

An understanding of these analyses is gained by the consideration of a saturated shear layer of a dilatant porous solid; see e.g. RICE [1975] for a linearized stability analysis of this case. We derive complete localized laws for this model problem based on the Mohr-Coulomb associated plastic potential. In particular, the dilatancy associated with the discontinuity for this model is identified as the origin of the localized fluid content. In the context considered herein, and in agreement with RUDNICKI & RICE [1975] and this last reference, among others, the inception of localization is observed to be determined by the drained response of the material. The case of a strain softening drained response leads to a lack of a length scale associated with the strain localization in the shear component of the deformation, as indicated in RICE [1975] or, in a more general context, in ZHANG & AL [1998].

All these relations lead directly to the formulation of enhanced strain finite element methods for the solution of this particular model problem, the second goal of this paper. The methodology proposed in ARMERO & GARIKIPATI [1995,96], without introducing a regularization of the singular strain field, is considered. We present complete details for the geometrically one-dimensional problem of the dilatant shear layer; extensions to more general situations are currently under further investigation. The proposed enhanced finite elements involve a constant approximation at the element level of the displacement jumps appearing in the expressions of the singular strains and of the localized fluid content. The new methods lead to a correct resolution of the energy dissipation associated to the localized solutions, thus avoiding the pathological mesh-dependence observed in standard isoparametric formulations of continuum softening models in this shear driven problem.

An outline of the rest of the paper is as follows. Section III.2 includes a complete characterization of strong discontinuities in porous media. More specifically, the large-

scale problem defining the equilibrium of the solid is summarized in Section III.2.1, with the introduction of the strong discontinuities in the small scale done in Section III.2.2. The consequences of these considerations in the flow of a fluid through the porous solid are studied in Section III.2.3. Section III.3.2 derives the localized stress-displacement-fluid content laws motivated by a general continuum model presented in Section III.3.1. The applications of these developments to the model problem of the dilatant shear layer is undertaken in Section III.4, including the development of the enhanced finite element formulation for this case in Section III.4.2. After the discussion of several numerical simulations in Section III.5, we present in Section III.6 several concluding remarks as well as a discussion of additional aspects of the problem currently under investigation.

## III.2. A Characterization of Discontinuous Solutions in Porous Media

We describe in this section the general equations of the coupled problem of evolution for the saturated porous solid of interest in this work. The presentation follows the ideas originally proposed in ARMERO [1997a] for the uncoupled mechanical problem, characterizing the localized effects in the deformation processes of solids through the consideration of strong discontinuities *locally* in the small scales. In this context, Section III.2.1 describes the mechanical governing equations of the classical local continuum problem, the *large-scale problem* as referred to in this work, involving regular displacement fields. The kinematics of strong discontinuities is described next in Section III.2.2. The addition of the fluid flow fields in this context is developed in Section III.2.3.

### III.2.1. The large-scale mechanical problem

We consider a porous solid, composed of a solid skeleton and (non-occluded) porous space, occupying the reference placement  $\Omega \subset \mathbb{R}^{n_{\text{dim}}}$  ( $n_{\text{dim}} = 1, 2$  or  $3$ ) identified with its current placement under the usual assumption of infinitesimal strains. In this context, the deformation of the solid in the large scale can be characterized by the displacement  $\mathbf{u} : \Omega \times [0, T] \rightarrow \mathbb{R}^{n_{\text{dim}}}$  of the solid's skeleton for a typical time interval  $T$ . Essential boundary conditions  $\mathbf{u} = \bar{\mathbf{u}}$  are imposed on  $\partial_u \Omega \subset \partial \Omega$ , the boundary of the domain  $\Omega$ ; see Figure III.2.1. The space of admissible displacement variations, satisfying the homogeneous counterpart of these essential boundary conditions,

$$\mathcal{V}_u = \{\boldsymbol{\eta} : \Omega \rightarrow \mathbb{R}^{n_{\text{dim}}} : \boldsymbol{\eta} = 0 \text{ on } \partial_u \Omega\}, \quad (\text{III.2.1})$$

is considered as usual.

The large-scale property attached to the displacement field  $\mathbf{u}$  and corresponding variations in  $\mathcal{V}_u$  refers to the fact that standard regularity conditions are assumed for these

fields. By standard, we refer to functions having integrable absolute first derivatives at the least (that is, the first derivatives being regular distributions as opposed to singular distributions, in the usual sense; see e.g. STAKGOLD [1979]). Additional localized effects, in the form of discontinuous displacement fields with strains being singular distributions, are considered separately in Section III.2.2 below. In this context, the infinitesimal *large-scale strain* field is given by the standard relation

$$\boldsymbol{\varepsilon} = \nabla^s \mathbf{u} = \frac{1}{2} [\nabla \mathbf{u} + (\nabla \mathbf{u})^T], \quad (\text{III.2.2})$$

for the symmetric part of the gradient operator  $\nabla(\cdot)$ , with  $(\cdot)^T$  denoting the transpose of a tensor.

Denoting the (total) stress field in the solid by  $\boldsymbol{\sigma} \in \mathbb{R}^{n_{\text{dim}} \times n_{\text{dim}}}$  (symmetric), the quasi-static equilibrium of the solid can then be expressed by the classical relation

$$\int_{\Omega} \boldsymbol{\sigma} : \nabla^s \boldsymbol{\eta} \, d\Omega = \int_{\Omega} \mathbf{f} \cdot \boldsymbol{\eta} \, d\Omega + \int_{\partial_t \Omega} \bar{\mathbf{t}} \cdot \boldsymbol{\eta} \, dA, \quad \forall \boldsymbol{\eta} \in \mathcal{V}_u, \quad (\text{III.2.3})$$

for the volume  $d\Omega$  and area  $dA$  elements (i.e., the Lebesgue measures in  $\Omega \subset \mathbb{R}^{n_{\text{dim}}}$  and  $\partial\Omega \subset \mathbb{R}^{n_{\text{dim}}-1}$ , respectively), volumetric body force  $\mathbf{f}$ , and imposed tractions  $\bar{\mathbf{t}}$  on  $\partial_t \Omega \subset \partial\Omega$ . The assumptions

$$\partial_u \Omega \cap \partial_t \Omega = \emptyset \quad \text{and} \quad \overline{\partial_u \Omega \cup \partial_t \Omega} = \partial\Omega, \quad (\text{III.2.4})$$

are considered as usual. The equation (III.2.3) corresponds to the classical form of the principle of virtual work and leads, after a standard argument, to the local equilibrium equations. In particular, we also have the continuity relation across any material surface  $\Gamma$  with unit normal  $\mathbf{n}$

$$[\![\boldsymbol{\sigma}]\!] \mathbf{n} = \mathbf{0}, \quad (\text{III.2.5})$$

for the jump in the stress  $[\![\boldsymbol{\sigma}]\!]$  across  $\Gamma$ . The classical notion of the traction vector on  $\Gamma$

$$\mathbf{t}_{\Gamma} := \boldsymbol{\sigma} \mathbf{n} \Big|_{\Gamma} \quad (\text{III.2.6})$$

is then recovered.

### III.2.2. The kinematics of strong discontinuities

The large-scale problem defined in the previous section accounts for solutions involving standard regularity conditions of the different fields, as indicated above. However, it is of the main interest to characterize more general solutions and, in particular, discontinuities in the displacement field, the so-called *strong discontinuities*, leading to strains being singular distributions. The purpose of this generalization is to model efficiently (both

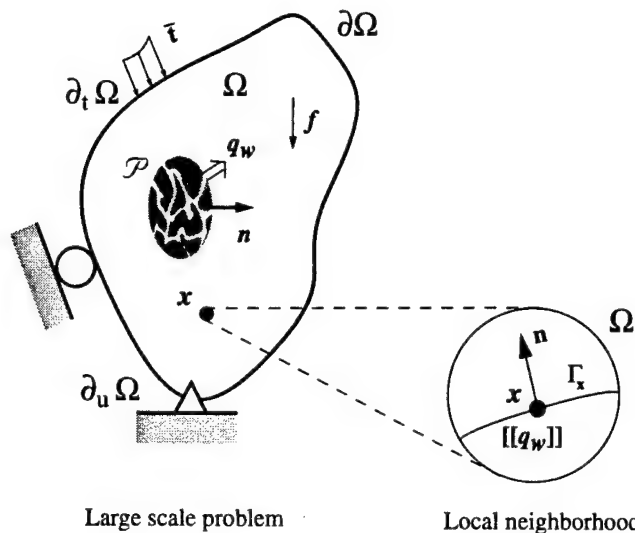


**FIGURE III.2.1** Kinematics of strong discontinuities. Large-scale problem defining the equilibrium of the solid, with standard loading and boundary conditions, and the local neighborhood  $\Omega_x$  incorporating the effects of the strong discontinuities. The flow of fluid in the porous solid is characterized by the flow vector  $\mathbf{q}_w$ , which exhibits a discontinuity across  $\Gamma_x$ .

theoretically and numerically) the localized response of inelastic solids as discussed in Section III.3 below. Following ARMERO [1997a], these localized (non-smooth) effects are introduced at the local level as follows.

Let  $\Omega_x \subset \Omega$  be a local neighborhood of a material point  $\mathbf{x} \in \Omega$ . The case of interest corresponds to the appearance of a discontinuity in the displacement field across a certain orientation  $\mathbf{n}$  at  $\mathbf{x} \in \Omega_x$ . Let  $\Gamma_x$  denote a surface in  $\Omega_x$  with such orientation; see Figure III.2.1 for an illustration of these ideas. As indicated below, the case of  $\text{measure}(\Omega_x) \rightarrow 0$  is of the interest herein, thus allowing for this general local definitions. In this context, we consider a general function  $\Psi_{\Gamma_x} : \Omega_x \rightarrow \mathbb{R}$  exhibiting a unit jump across the surface  $\Gamma_x$ , that is,  $[\Psi_{\Gamma_x}] = 1$  on  $\Gamma_x$ . Denoting by  $H_{\Gamma_x}$  the Heaviside step function across  $\Gamma_x$  the function  $\Psi_{\Gamma_x}$  can be expressed as

$$\Psi_{\Gamma_x} = H_{\Gamma_x} - N_{\Gamma_x} \quad \text{in } \Omega_x , \quad (\text{III.2.7})$$

for a smooth function  $N_{\Gamma_x}$ .

With this notation, we consider the small-scale displacement field

$$\mathbf{u}_\mu = \mathbf{u} + \boldsymbol{\xi} \Psi_{\Gamma_x} \quad \text{in } \Omega_x , \quad (\text{III.2.8})$$

in terms of the large-scale displacement  $\mathbf{u}$  and the local field  $\boldsymbol{\xi} : \Omega_x \rightarrow \mathbb{R}^{n_{\text{dim}}}$  defining the displacement jump  $[\mathbf{u}_\mu] = \boldsymbol{\xi}$  across  $\Gamma_x$ . The infinitesimal strains corresponding to the

local displacement field  $\mathbf{u}_\mu$ , which we refer to as the *small-scale strains*, are given by

$$\varepsilon(u_\mu) = \underbrace{\varepsilon(u) + G(\xi)}_{\substack{\text{regular} \\ \text{distribution}}} + \underbrace{(\xi \otimes n) \delta_{\Gamma_x}}_{\substack{\text{singular} \\ \text{distribution}}}, \quad (\text{III.2.9})$$

for the regular function

$$G(\xi) := \nabla^s \xi \cdot H_{\Gamma_\xi} - \xi \otimes \nabla^s N_{\Gamma_\xi}, \quad (\text{III.2.10})$$

and the Dirac delta function  $\delta_{\Gamma_x}$  across  $\Gamma_x$ . We note the result  $\nabla H_{\Gamma_x} = \mathbf{n} \cdot \delta_{\Gamma_x}$  for the unit normal  $\mathbf{n}$ ; see STAKGOLD [1979]. The relation (III.2.9) identifies the decomposition of the small-scale strain  $\boldsymbol{\varepsilon}(\mathbf{u}_\mu)$  in regular and singular parts, the latter corresponding to the localized effects along the strong discontinuity  $\Gamma_x$ . Similarly, the decomposition (III.2.9) can be understood as defining the *unresolved strain*  $\boldsymbol{\varepsilon}_{unres} = \boldsymbol{\varepsilon}(\mathbf{u}_\mu) - \boldsymbol{\varepsilon}(\mathbf{u})$  by the large-scale strain  $\boldsymbol{\varepsilon}(\mathbf{u})$ .

The considerations above have introduced the new unknown field  $\xi$ , in addition to the large-scale displacements  $\mathbf{u}$ . As shown in ARMERO [1997a], a well-posed local continuum formulation can be constructed by considering the local weak equation for all variations  $\gamma$  of the local jumps  $\xi$

$$-\frac{1}{\text{measure}(\Omega_x)} \int_{\Omega_x} \boldsymbol{\gamma} \cdot \boldsymbol{\sigma} \mathbf{n} \, d\Omega + \frac{1}{\text{measure}(\Gamma_x)} \int_{\Gamma_x} \boldsymbol{\gamma} \cdot \mathbf{t}_{\Gamma_x} \, dA = 0 , \quad (\text{III.2.11})$$

in the limit  $h_x := \text{measure}(\Omega_x)/\text{measure}(\Gamma_x) \rightarrow 0$ , imposing then the equilibrium equation (III.2.11). The whole formulation is to be understood in this local limit, thus avoiding the precise definition of the neighborhood  $\Omega_x$ . The resulting large-scale local problem incorporates effectively the dissipative effects of the discontinuous solutions, and leads to a well-posed problem. See ARMERO [1997b] for the closed-form analysis of the wave propagation in a one-dimensional bar considering the resulting dynamic problem, showing the uniqueness of the solution and its continuous dependence on the data.

### III.2.3. The characterization of the fluid flow

The porous solid is assumed to be fully saturated with a fluid. Following BIOT [1941], we consider the *fluid content*  $\tilde{M} : \Omega \times [0, T] \rightarrow \mathbb{R}$  increment (units of fluid mass per unit volume) over an initial value  $M_o : \Omega \rightarrow \mathbb{R}$ . Given the developments above for the discontinuous solutions in the displacements  $u_\mu$ , and the corresponding singular strains  $\varepsilon(u_\mu)$ , we consider similarly the *localized fluid content*  $\tilde{M}$  increment (units of fluid mass per unit area) on the set

$$\Gamma = \cup \Gamma_x = \{x \in \Omega \ : \ \Gamma_x \neq \emptyset\} , \quad (\text{III.2.12})$$

composed by all the material points exhibiting locally strong discontinuities. We assume that this set defines a measure space (being, in general, of lower dimension than  $\Omega$ , e.g., a surface), thus allowing the decomposition

$$M := \bar{M} + \tilde{M} \delta_{\Gamma}, \quad (\text{III.2.13})$$

for the total fluid content  $M$ . In equation (III.2.13), we have introduced the notation  $\delta_{\Gamma}$  for the delta function satisfying the integral relation

$$\begin{aligned} \text{Total fluid mass} \\ \text{in } \Omega \end{aligned} := \int_{\Omega} M d\Omega = \int_{\Omega} \bar{M} d\Omega + \int_{\Gamma} \tilde{M} dA, \quad (\text{III.2.14})$$

for the corresponding measure  $dA$  on  $\Gamma$  and the usual Lebesgue measure  $d\Omega$  in  $\mathbb{R}^{n_{\text{dim}}}$ . Physically, this relation identifies the fluid mass stored along all the strong discontinuities of the displacement. As discussed in Section III.3 below, the decomposition (III.2.13) is consistent with continuum local models of poro-plasticity, with the localized fluid content  $\tilde{M}$  given by the dilatancy associated to the strong discontinuities  $\Gamma$ .

Assuming that no fluid sources exist, the conservation of fluid mass in any part  $\mathcal{P} \subset \Omega$  is given by

$$\int_{\mathcal{P}} \dot{M} d\Omega = - \int_{\partial\mathcal{P}} \mathbf{q}_w \cdot \mathbf{n} dA, \quad (\text{III.2.15})$$

defining a vector field  $\mathbf{q}_w$  that characterizes the local flow of fluid mass due to fluid conduction through the porous space of the solid. These ideas are illustrated in Figure III.2.1. In (III.2.15), the time derivative has been denoted by  $(\cdot)$ . A standard argument based on integration by parts leads to the relations

$$\dot{\tilde{M}} = - \operatorname{div} \mathbf{q}_w \quad \text{in } \Omega \setminus \Gamma, \quad (\text{III.2.16})$$

and the localized balance law

$$\dot{\tilde{M}} = -[\mathbf{q}_w] \cdot \mathbf{n} \quad \text{on } \Gamma, \quad (\text{III.2.17})$$

for the unit normal  $\mathbf{n}$  to  $\Gamma$  (the smoothness of  $\Gamma$  is assumed, for simplicity), identifying the discontinuity of the fluid flow with the jump term  $[\mathbf{q}_w]$  on  $\Gamma$ . We observe that the relations (III.2.16) and (III.2.17) can be written equivalently in distributional form as

$$\dot{\tilde{M}} = - \operatorname{div} \mathbf{q}_w \quad (= - \operatorname{div} [\mathbf{q}_w|_{\Omega \setminus \Gamma}] - [\mathbf{q}_w] \cdot \mathbf{n} \delta_{\Gamma}), \quad (\text{III.2.18})$$

see e.g. STAKGOLD [1979].

The classical local relation given by Darcy's law is assumed in the following developments for the fluid flow vector  $\mathbf{q}_w$  in  $\Omega \setminus \Gamma$ , that is,

$$\mathbf{q}_w = -\rho_w^2 \mathbf{k}(\nabla \mu_w - \mathbf{g}), \quad (\text{III.2.19})$$

in terms of the density of the fluid  $\rho_w$ , the permeability tensor of the porous solid  $\mathbf{k}$ , gravity  $\mathbf{g}$ , and the free enthalpy (or chemical potential)  $\mu_w$  of the fluid. We consider the case of a barotropic fluid characterized by its *pore pressure*  $p : \Omega \times [0, T] \rightarrow \mathbb{R}$  and the constitutive relation

$$\hat{\mu}_w(p) = \int^p \frac{d\eta}{\hat{\rho}_w(\eta)}, \quad (\text{III.2.20})$$

in the developments that follow. In this case, Darcy's law (III.2.19) takes the classical form

$$\mathbf{q}_w = -\rho_w \mathbf{k}(\nabla p - \rho_w \mathbf{g}), \quad (\text{III.2.21})$$

for the fluid mass flow vector  $\mathbf{q}_w$  in  $\Omega \setminus \Gamma$ . The discontinuous part of the fluid flow  $[\mathbf{q}_w]$  on  $\Gamma$  is given by the localized fluid content  $\dot{M}$  through (III.2.17) and is obtained by the localized constitutive relations derived in the following section for a general elastoplastic porous solid. We note that the locality of all the previous arguments, that is, arising at a material point  $\mathbf{x} \in \Omega$ , leads to the pointwise relation (III.2.17), not accounting explicitly for flow conduction along the discontinuity surface  $\Gamma$ .

Finally, the weak form of the governing equations (III.2.16) and (III.2.17), as employed in the finite element methods developed in Section III.4.2, are obtained multiplying equation (III.2.16) by a smooth test function  $w : \Omega \rightarrow \mathbb{R}$ , and integrating by parts, thus leading to

$$\int_{\Omega} \dot{M} w \, d\Omega = \int_{\Omega} \mathbf{q}_w \cdot \nabla w \, d\Omega - \int_{\partial\Omega} \mathbf{q}_w \cdot \mathbf{n} w \, dA + \int_{\Gamma} [\mathbf{q}_w] \cdot \mathbf{n} w \, dA. \quad (\text{III.2.22})$$

Assuming that the normal flow of fluid mass  $\bar{q}_{wn}$  is known on the part of the boundary  $\partial_q \Omega$  (possibly as a function of the pore pressure  $p$ ), that is,

$$\mathbf{q}_w \cdot \mathbf{n} = \bar{q}_{wn} \quad \text{on } \partial_q \Omega \subset \partial\Omega, \quad (\text{III.2.23})$$

with the part of the boundary with an imposed pressure denoted by  $\partial_p \Omega$ , equation (III.2.22) reduces to

$$\int_{\Omega} \dot{M} w \, d\Omega + \int_{\Gamma} \dot{M} w \, dA = \int_{\Omega} \mathbf{q}_w \cdot \nabla w \, d\Omega - \int_{\partial_q \Omega} \bar{q}_{wn} w \, dA \quad \forall w \in \mathcal{V}_p, \quad (\text{III.2.24})$$

after making use of the local relation (III.2.17). The notation

$$\mathcal{V}_p = \{w : \Omega \rightarrow \mathbb{R} : w = 0 \text{ on } \partial_p \Omega\}, \quad (\text{III.2.25})$$

for the space of admissible pressure variations has been employed in (III.2.24). The assumptions (III.2.4) are similarly imposed for the parts of the boundary  $\partial_p \Omega$  and  $\partial_q \Omega$ .

**Remark III.2.1** We emphasize the important fact that the pressure field  $p$  and the chemical potential  $\mu_w = \hat{\mu}_w(p)$ , as well as their variations, remain continuous (or, to be more

precise, with integrable absolute value derivatives) in all the previous developments, a situation to be contrasted with the formulations presented in e.g. LARSSON et al [1996] for the undrained limit, considering discontinuous pressure fields with the corresponding gradients being singular distributions. Mathematically, the structure of the local equation (III.2.18) with the flow vector given by (III.2.21), involving then the second spatial derivatives of the pressure field for a positive permeability, precludes these discontinuities, but not of the fluid flow vector. In addition, the presence of pressure shocks has not been observed experimentally; see e.g. VARDOLAKIS [1996]. In the proposed context, the flow jump  $[q_w]$  can be related to a discontinuity in the pressure gradient instead. The discussion presented next identifies the consistency of this approach with a continuum poro-elastoplastic model.

□

### **III.3. Localized Dissipative Mechanisms in Coupled Poro-Elastoplastic Solids**

The governing equations described in the previous section characterize the kinematics as well as the quasi-static equilibrium and the conservation of fluid mass in a general porous media exhibiting strong discontinuities. In this context, the kinematic variables, consisting of the large-scale displacements  $\mathbf{u}$  and the local displacement jumps  $\boldsymbol{\xi}$ , and the fluid variables, given by the (continuous) pore pressure  $p$  and the fluid content  $M$  (with its regular  $\tilde{M}$  and singular parts  $\tilde{M}$ ), have been shown to characterize these discontinuous solutions. Still, the resulting equations need to be supplemented by the appropriate constitutive relations for the stresses and the fluid content. In particular, these relations must be developed for the localized quantities on  $\Gamma$ , namely, for the traction vector  $\mathbf{t}_{\Gamma_x}$  and the localized fluid content  $\tilde{M}$ .

The development of these localized constitutive laws is undertaken in this section. More specifically, we show that a poro-plastic continuum model is consistent with localized relations along the discontinuity. These ideas are developed in Section III.3.2 after summarizing in Section III.3.1 a classical continuum poro-plastic model. The assumed continuum model considers an additive elastoplastic decomposition of both the strains and the fluid content fields in the infinitesimal range of interest herein. A complete account of this type of models, following the thermodynamically consistent approach first proposed in the pioneering work of BIOT [1941], can be found in COUSSY [1995]. An extension to the finite deformation range in the framework given by a multiplicative decomposition of the deformation gradient can be found in ARMERO [1998].

#### **III.3.1. The continuum poro-elastoplastic model**

The governing equations described in the previous section are supplemented by the constitutive model characterizing the response of the porous solid, that is, defining the

total stresses  $\sigma$  in terms of the independent unknown fields  $M$  and the infinitesimal strains  $\varepsilon \equiv \varepsilon(u_\mu)$  in the small scale  $\Omega_x$  of the material. A general coupled elastoplastic model can be characterized in this context by the additive decompositions

$$\varepsilon = \varepsilon^e + \varepsilon^p \quad \text{and} \quad M = M^e + M^p , \quad (\text{III.3.1})$$

in elastic and plastic parts. The reversible response of the porous solid is then characterized by a stored energy function  $W = \hat{W}(\varepsilon^e, M^e, \alpha)$ , in terms of the elastic parts of the strains and fluid content increment, and an extra set of internal variables characterizing, for example, the hardening/softening of the material. The analyses presented in this paper consider, for simplicity, the case of isotropic hardening determined by a single scalar internal variable  $\alpha$ . Similarly, isothermal conditions are assumed.

A standard argument based on the imposition of a positive internal dissipation (known as Coleman's method; see, e.g., TRUESDELL & NOLL [1965])

$$\mathcal{D}_{int} = \sigma : \dot{\varepsilon} + \mu_w \dot{M} - \dot{W} \geq 0 , \quad (\text{III.3.2})$$

where the first term in the right-hand side of this expression accounts for the stress power and the second term for the change of internal energy due to fluid transport (the dissipation associated with fluid conduction is defined separately), leads to the constitutive relations

$$\sigma = \partial_{\varepsilon^e} W , \quad \mu_w = \partial_{M^e} W \quad \text{and} \quad q = -\partial_\alpha W , \quad (\text{III.3.3})$$

for total stresses  $\sigma$ , the chemical potential of the fluid  $\mu_w$  and the stress-like hardening internal variable  $q$ . The internal dissipation (III.3.2) can then be expressed equivalently as

$$\mathcal{D}_{int} = \sigma : \dot{\varepsilon}^p + \mu_w \dot{M}^p + q \dot{\alpha} \geq 0 , \quad (\text{III.3.4})$$

as a straightforward calculation shows.

The rate forms of the constitutive relations (III.3.3) are given by

$$\dot{\sigma} = \dot{\sigma}' - b\rho_{wo}\dot{\mu}_w \mathbf{c} , \quad \text{with} \quad \dot{\sigma}' = \mathbb{C}_{sk}\dot{\varepsilon}^e , \quad (\text{III.3.5})$$

for the *effective Biot's stresses*  $\sigma'$ , and

$$\dot{\mu}_w = \dot{p}/\rho_w = \frac{Q}{\rho_{wo}^2} [\dot{M}^e - b\rho_{wo} \dot{\varepsilon}^e : \mathbf{c}] , \quad (\text{III.3.6})$$

for the fluid's chemical potential. Here, we have introduced the notation  $\mathbb{C}_{sk}$  for the solid's skeleton elastic tangent ("drained" tangent),  $\rho_{wo}$  for the fluid's reference density,  $Q$  for the Biot's modulus,  $b$  for the Biot's coefficient, and  $\mathbf{c}$  for the coupling tangent tensor.

In particular, the linear elastic response is recovered through the quadratic stored energy function

$$W(\boldsymbol{\varepsilon}^e, M^e, \alpha) = \frac{1}{2}\boldsymbol{\varepsilon}^e : \mathbb{C}_u \boldsymbol{\varepsilon}^e + \frac{Q}{2\rho_{wo}^2} M^{e2} - \frac{bQ}{\rho_{wo}} \boldsymbol{\varepsilon}^e : \mathbf{c} M^e + H(\alpha), \quad (\text{III.3.7})$$

for a general hardening potential  $H(\alpha)$  and the “undrained” material tangent  $\mathbb{C}_u$  given in terms of the drained elasticities  $\mathbb{C}_{sk}$  by

$$\mathbb{C}_u = \mathbb{C}_{sk} + Qb^2 \mathbf{c} \otimes \mathbf{c}. \quad (\text{III.3.8})$$

The isotropic case is recovered with the choices

$$\mathbb{C}_{sk} = \kappa_{sk} \mathbf{1} \otimes \mathbf{1} + 2\mu_{sk} \left( \mathbb{I} - \frac{1}{3} \mathbf{1} \otimes \mathbf{1} \right) \quad \text{and} \quad \mathbf{c} = \mathbf{1}, \quad (\text{III.3.9})$$

for the drained bulk  $\kappa_{sk}$  and shear  $\mu_{sk}$  moduli, and the rank two  $\mathbf{1}$  and rank four  $\mathbb{I}$  identity tensors, respectively. The undrained tangent  $\mathbb{C}_u$  possesses then the same form (III.3.9)<sub>1</sub>, but with the undrained bulk modulus  $\kappa_u = \kappa_{sk} + Qb^2$ .

The evolution of the plastic internal variables  $\boldsymbol{\varepsilon}^p$ ,  $M^p$  and  $\alpha$  is given by the rate equations

$$\boxed{\begin{aligned} \dot{\boldsymbol{\varepsilon}}^p &= \lambda \partial_{\boldsymbol{\sigma}} f, \\ \dot{\alpha} &= \lambda \partial_q f, \\ \dot{M}^p &= \lambda \partial_{\mu_w} f \quad (= \lambda \rho_w \partial_p f), \end{aligned}} \quad (\text{III.3.10})$$

for the associate case based on a yield surface  $f(\boldsymbol{\sigma}, \mu_w(p), q)$ . Equations (III.3.10) can be derived from the principle of maximum plastic dissipation, after following a standard argument based on (III.3.4). The plastic consistency parameter  $\lambda$  has been introduced in (III.3.10), and it is determined by the Kuhn-Tucker and consistency conditions

$$f \leq 0, \quad \lambda \geq 0, \quad \lambda f = 0, \quad \text{and} \quad \lambda \dot{f} = 0. \quad (\text{III.3.11})$$

defining the loading/unloading conditions.

A common example of the above considerations is furnished by a yield condition  $f(\boldsymbol{\sigma}, p, q) = f_{sk}(\boldsymbol{\sigma}', q)$  defined in terms of the effective stresses (III.5) (that is, characterizing the drained response of the porous solid). This choice leads to the relations

$$\partial_{\boldsymbol{\sigma}} f = \partial_{\boldsymbol{\sigma}'} f_{sk}, \quad \text{and} \quad \partial_p f = b \frac{\rho_{wo}}{\rho_w} \partial_{\boldsymbol{\sigma}'} f_{sk} : \mathbf{c}, \quad (\text{III.3.12})$$

as a simple calculation based on the chain rule shows. In this case, equation (III.3.10)<sub>3</sub> reads

$$\dot{M}^p = \rho_{wo} b \boldsymbol{\varepsilon}^p : \mathbf{c} \quad (= \rho_{wo} b \dot{\boldsymbol{\varepsilon}}_v^p, \quad \text{for the isotropic case}) \quad (\text{III.3.13})$$

a direct relation of the evolution of the irreversible part of the fluid content  $M^p$  with the plastic dilatancy of the solid's skeleton, as characterized in the isotropic case by the volumetric plastic strain

$$\varepsilon_v^p := \text{tr}[\varepsilon^p] , \quad (\text{III.3.14})$$

for the usual trace operator  $\text{tr}[\cdot]$ . Combining (III.3.6) with (III.3.13), we obtain the relation

$$\dot{M} = \frac{\rho_{wo}}{Q} \dot{p} + \rho_{wo} b \dot{\varepsilon}_v , \quad (\text{III.3.15})$$

for the volumetric strain  $\varepsilon_v := \text{tr}[\varepsilon]$ . Here, we have assumed a constant fluid density  $\rho_w = \rho_{wo}$  and the isotropic case of interest in the developments of the sections to follow.

### III.3.2. The localized dissipative mechanism

We show in this section that the developments presented in Section III.2 identifying the regularity of the different fields are consistent with the coupled poro-elastoplastic model described in Section III.3.1. The final goal is the identification of a localized stress-displacement-fluid flow relation along the strong discontinuity. In this context, we consider a localized dissipative mechanism characterized by a localized plastic flow given by

$$\lambda = \tilde{\lambda} \delta_{\Gamma_x} . \quad (\text{III.3.16})$$

The conditions developed below identify then necessary conditions for the appearance of this assumed mechanism (see ARMERO & GARIKIPATI [1996]). The derivation involves basically the same arguments as in the developments presented in SIMO et al [1993], and proceeds as follows.

The traction vector  $\mathbf{t}_{\Gamma_x} = \boldsymbol{\sigma} \mathbf{n}$  remains continuous by equilibrium, implying that  $\dot{\mathbf{t}}_{\Gamma_x}$  is a regular function. After using (III.3.5) and the decomposition of the strains (III.2.9) in regular and singular parts, the rate of the traction can be written as

$$\begin{aligned} \dot{\mathbf{t}}_{\Gamma_x} &= \dot{\boldsymbol{\sigma}} \mathbf{n} = [\mathbb{C}_{sk} \dot{\varepsilon}^e - \rho_{wo} b \dot{\mu}_w \mathbf{c}] \mathbf{n} \\ &= \underbrace{[\mathbb{C}_{sk} (\dot{\bar{\varepsilon}} - \dot{\bar{\varepsilon}}^p) - \rho_{wo} b \dot{\mu}_w \mathbf{c}] \mathbf{n}}_{\text{regular}} + \underbrace{[\mathbb{C}_{sk} ((\dot{\xi} \otimes \mathbf{n})^s - \tilde{\lambda} \partial_{\boldsymbol{\sigma}} f)] \mathbf{n} \delta_{\Gamma_x}}_{\text{singular}} \quad (\text{III.3.17}) \end{aligned}$$

noting again the regularity of the fluid chemical potential; see Remark III.2.1. The regularity of the traction rate  $\dot{\mathbf{t}}_{\Gamma_x}$  implies then that the singular part of (III.3.17) vanishes, that is,

$$\mathbf{Q}_{sk} \dot{\xi} = \tilde{\lambda} \mathbb{C}_{sk} \partial_{\boldsymbol{\sigma}} f \mathbf{n} \quad \text{where} \quad \mathbf{Q}_{sk} = \mathbf{n} \cdot \mathbb{C}_{sk} \cdot \mathbf{n} , \quad (\text{III.3.18})$$

the elastic acoustic tensor of the solid's skeleton.

Furthermore, the consistency condition (III.3.11)<sub>3</sub> implies

$$\begin{aligned}
 0 = \dot{f} &= \partial_{\sigma} f : \dot{\sigma} + \partial_p f \dot{p} + \partial_q f \dot{q} \\
 &= \underbrace{\partial_{\sigma} f : [\mathbb{C}_{sk}(\dot{\bar{\epsilon}} - \dot{\bar{\epsilon}}^p) - \rho_{wo} b \dot{\mu}_w c]}_{\text{regular}} + \partial_p f \dot{p} + \partial_q f \dot{q} \\
 &\quad + \underbrace{\partial_{\sigma} f : \mathbb{C}_{sk}((\dot{\xi} \otimes n)^s - \tilde{\lambda} \partial_{\sigma} f)}_{\text{singular}} \delta_{\Gamma_x}, \tag{III.3.19}
 \end{aligned}$$

Each of the regular and singular parts of this last expression must vanish, leading to

$$\tilde{\lambda} = \frac{1}{\partial_{\sigma} f : \mathbb{C}_{sk} \partial_{\sigma} f} \partial_{\sigma} f : \mathbb{C}_{sk} (\dot{\xi} \otimes n)^s, \tag{III.3.20}$$

for the singular part. Combining this last relation with (III.3.18) we obtain the final condition for the direction of the jump rate  $\dot{\xi} = \|\dot{\xi}\| m$  (with  $\|m\| = 1$ )

$$\mathbf{Q}_{sk}^{ep} m = 0 \quad \text{where} \quad \mathbf{Q}_{sk}^{ep} = \mathbf{n} \cdot \left[ \mathbb{C}_{sk} - \frac{1}{\partial_{\sigma} f : \mathbb{C}_{sk} \partial_{\sigma} f} \mathbb{C}_{sk} \partial_{\sigma} f \otimes \mathbb{C}_{sk} \partial_{\sigma} f \right] \cdot \mathbf{n}, \tag{III.3.21}$$

the *drained* perfectly plastic acoustic tensor.

In addition, the above relations lead to the following localized softening law. Given the regularity of the different fields involved, the softening law (III.3.10)<sub>2</sub> needs to be understood in the distributional sense

$$\mathcal{H}^{-1} \dot{q} := -\dot{\alpha} = -\tilde{\lambda} \partial_q f \delta_{\Gamma_x} \implies \mathcal{H}^{-1} = \tilde{\mathcal{H}}^{-1} \delta_{\Gamma_x}, \tag{III.3.22}$$

for a localized softening modulus  $\tilde{\mathcal{H}}$ . This last equation identifies also the evolution of the localized equivalent plastic strain

$$\dot{\alpha} = \tilde{\lambda} \partial_q f, \tag{III.3.23}$$

having units of displacement. The combination of (III.3.22), the regular part of the consistency condition (III.3.19) and the equation (III.3.20) leads to the following localized relation for the magnitude of the rate of the displacement jump

$$\|\dot{\xi}\| = \frac{1}{\tilde{\mathcal{H}} \Xi_{sk}} \underbrace{[\partial_{\sigma} f : \dot{\sigma} + \partial_p f \dot{p}]}_{\partial_{\sigma'} f_{sk} : \dot{\sigma}'} \quad \text{where} \quad \Xi_{sk} = \frac{(\partial_q f)^2}{\partial_{\sigma} f : \mathbb{C}_{sk} \partial_{\sigma} f} \mathbb{C}_{sk} \partial_{\sigma} f : (m \otimes n), \tag{III.3.24}$$

with  $\|\dot{\xi}\| = 0$  when the right-hand-side of (III.3.24)<sub>1</sub> vanishes (that is, a rigid-plastic response along  $\Gamma_x$ ).

Finally, the origin of the singular character of the fluid content  $M$  can be identified with the plastic (or irreversible) part  $M^p$  through (III.3.10)<sub>3</sub> given (III.3.16). In fact, using (III.3.10)<sub>3</sub> and (III.2.18) the following expression is obtained

$$\dot{\tilde{M}} = -[\![q_w]\!] \cdot \mathbf{n} = \rho_{wo} b \underbrace{\|\dot{\xi}\|}_{\dot{\xi} \cdot \mathbf{n}} \mathbf{m} \cdot \mathbf{n}, \quad (\text{III.3.25})$$

for the singular part of the fluid content  $\tilde{M}$ , and from (III.3.15)

$$\dot{\tilde{M}} = \frac{\rho_{wo}}{Q} \dot{p} + \rho_{wo} b \dot{\bar{\varepsilon}}_v, \quad (\text{III.3.26})$$

for the regular fluid content increment. Equation (III.3.25) clearly indicates the relation of the localized fluid content  $\tilde{M}$  with the dilatancy associated with the strong discontinuity, that is, the component of the displacement jump normal to the discontinuity.

In summary, the developments in this section show the consistency of a classical continuum poro-plastic model with localized relations along the strong discontinuities. In particular, the localized softening law (III.3.24), involving a stress/displacement relation, has been obtained. Similarly, the evolution of the localized fluid content in the fully saturated porous media is given by (III.3.25) through the dilatant response of the strong discontinuity. We consider in the next section the particular case of a dilatant shear layer to illustrate the significance of these localized relations.

**Remark III.3.1** The developments presented in this section have considered a general poro-plastic model, leading to a set of rigid-plastic relations along the discontinuity. As indicated in Section III.1, we understand the developments presented herein as a motivation for the form of the final localized relations. The consistency of these localized laws with the original local continuum model is the main focus. Additional considerations (viscous effects, elastic unloading with or without damage, for example) can be incorporated in a more general framework as presented in ARMERO [1997a,b].  $\square$

### III.4. Model Problem: a Dilatant Shear Layer

As a model example of the considerations presented in the previous sections, we examine in this section the problem of an infinite shear layer. This model problem is defined as follows. We denote by  $L$  the thickness of the layer in the direction  $x$ , perpendicular to the layer, so  $\Omega = [0, L] \subset \mathbb{R}$  in this case. We denote by  $\mathbf{n} = [1 \ 0]^T$  the unit vector in the  $x$ -direction and by  $\mathbf{s} = [0 \ 1]^T$  the unit vector in the perpendicular direction; see Figure

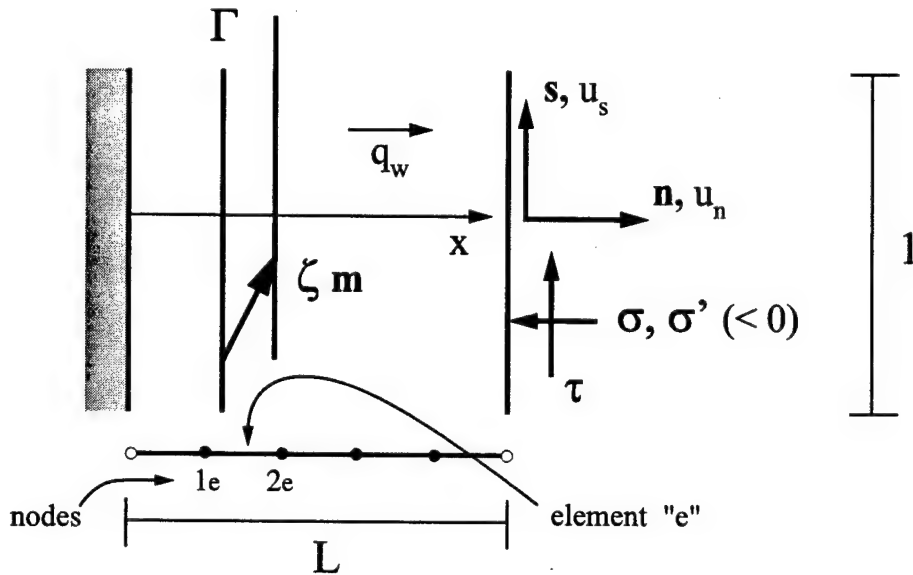


**FIGURE III.4.1** Dilatant shear layer. Problem definition illustrating the notation for the normal and shear components of the displacement and stress, the fluid flow, and the finite element discretization.

III.4.1 for an illustration of the notation. The layer is subjected to the normal and shear strains

$$\varepsilon_n = \frac{du_n}{dx} \quad \text{and} \quad \gamma_s = \frac{du_s}{dx}, \quad (\text{III.4.1})$$

for the normal and shear displacements  $u_n(x)$  and  $u_s(x)$ , respectively. In this setting, the total normal stress  $\sigma$  and the shear stress  $\tau$  act on the layer at  $x = L$  and are constant in  $\Omega$  by equilibrium (no body forces are assumed). The effective normal stress corresponding to  $\sigma$  is denoted by  $\sigma' = \sigma + bp$ . The material is assumed isotropic and characterized by a scalar permeability  $k$  (i.e.,  $\mathbf{k} = k \mathbf{1}$ ), so the fluid flow  $q_w$  is in the  $x$ -direction by symmetry. Gravity effects are neglected, and a constant fluid density  $\rho_w = \rho_{wo}$  is assumed.

### III.4.1. The poro-elastoplastic model

The poro-elasto-plastic model described in Section III.3.1 reduces in this case to the following equations. First, we consider the linear elastic stress-strain laws

$$\dot{\sigma}' = E_{oe} (\dot{\varepsilon}_n - \dot{\varepsilon}_n^p) \quad \text{and} \quad \dot{\tau} = G (\dot{\gamma}_s - \dot{\gamma}_s^p), \quad (\text{III.4.2})$$

for the oedometric modulus  $E_{oe}$  and the shear modulus  $G$ . The Mohr-Coulomb yield criterion

$$f_{sk}(\tau, \sigma', \alpha) = |\tau| + \beta\sigma' - q(\alpha), \quad (\text{III.4.3})$$

is assumed for the elastoplastic response, where  $\beta = \tan \varphi$  for the drained friction angle  $\varphi$ , and  $q(0) (= c)$  is the initial drained cohesion of the material. The continuum plastic evolution equations (III.3.10) read in this case

$$\dot{\varepsilon}_n^p = \lambda \beta, \quad \dot{\gamma}_s^p = \lambda \operatorname{sign}(\tau), \quad \dot{\alpha} = \lambda \quad \text{and} \quad \dot{M}^p = \rho_{wo} \dot{\varepsilon}_n^p. \quad (\text{III.4.4})$$

The loading/unloading and consistency conditions (III.3.11) are added to these equations.

The combination of equations (III.4.2) to (III.4.4) leads to the following rate form of the assumed continuum poro-plastic model

$$\underbrace{\begin{Bmatrix} \dot{\sigma}' \\ \dot{\tau} \end{Bmatrix}}_{\mathbb{C}_{sk}^{ep}} = \frac{1}{G + \beta^2 E + \mathcal{H}} \begin{bmatrix} E(G + \mathcal{H}) & -\beta E G \operatorname{sign}(\tau) \\ -\beta E G \operatorname{sign}(\tau) & G(\beta^2 E + \mathcal{H}) \end{bmatrix} \begin{Bmatrix} \dot{\varepsilon}_n \\ \dot{\gamma}_s \end{Bmatrix}, \quad (\text{III.4.5})$$

in terms of the continuum hardening/softening modulus  $\mathcal{H} := -dq(\alpha)/d\alpha$ . The so-called dilatant hardening can be observed in the term involving the  $\mathcal{H} + \beta^2 E$  combination. Still, the perfectly plastic case  $\mathcal{H} = 0$  leads to a singular tangent  $\mathbb{C}_{sk}^{ep}$  with the eigenvector corresponding to the zero eigenvalue given by

$$\dot{\varepsilon}^{eig} = \begin{Bmatrix} \dot{\varepsilon}_n^{eig} \\ \dot{\gamma}_s^{eig} \end{Bmatrix} = \frac{1}{\sqrt{1 + \beta^2}} \begin{Bmatrix} \beta \\ \operatorname{sign}(\tau) \end{Bmatrix}. \quad (\text{III.4.6})$$

This strain mode can be written as the symmetric part of the rank one update (in the particular notation employed in (III.4.6) for the strain rate vector) as

$$\dot{\varepsilon}^{eig} \leftarrow \operatorname{sym}(\mathbf{m} \otimes \mathbf{n}) \quad \text{for} \quad \boxed{\mathbf{m} = [\mathbf{u}]/\|[\mathbf{u}]\| = \frac{1}{\sqrt{1 + \beta^2}} [\beta \mathbf{n} + \operatorname{sign}(\tau) \mathbf{s}]}, \quad (\text{III.4.7})$$

thus corresponding also to the condition (III.3.21) based on the acoustic tensor  $\mathbb{Q}_{sk}^{ep}$ . Therefore, the localization condition (III.3.21) is satisfied upon yielding, with the normal  $\mathbf{n}$  to the strong discontinuity surface at  $x_I$  given by the normal to the layer, and the constant direction  $\mathbf{m}$  of the displacement jump given by (III.4.7). The dilatant character of the discontinuity jump, as reflected by the normal component of the strain mode  $\dot{\varepsilon}^{eig}$ , is apparent for  $\beta \neq 0$ .

**Remark III.4.1** We note that the conclusion that the dilatant shear layer loses its stability when the underlying drained elastoplastic model reaches the softening range agrees with the analysis presented in RICE [1975] for this very same model example. In this reference, a complete linearized stability analysis of the governing equations, including the conservation of fluid mass through Darcy's law, is presented. This analysis identifies the

short-wavelength limit as leading to the observed instability, with no intrinsic length-scale present in this shear problem.  $\square$

Following the analysis of Section III.3.2 characterizing the resulting strong discontinuities, the strain rates are decomposed upon localization in a regular and a singular parts, namely

$$\dot{\varepsilon}_n = \dot{\bar{\varepsilon}}_n + \dot{\xi}_n \delta_{\Gamma_x} \quad \text{and} \quad \dot{\gamma}_s = \dot{\bar{\gamma}}_s + \dot{\xi}_s \delta_{\Gamma_x}, \quad (\text{III.4.8})$$

where

$$\dot{\xi}_n = \dot{\xi} \cdot n = \dot{\xi} \frac{\beta}{\sqrt{1 + \beta^2}} \quad \text{and} \quad \dot{\xi}_s = \dot{\xi} \cdot s = \dot{\xi} \frac{\text{sign}(\tau)}{\sqrt{1 + \beta^2}}, \quad (\text{III.4.9})$$

are the normal and the shear components of the displacement jump rate, respectively. The magnitude of the rate of the jump  $\dot{\xi}$  is given by the localized relation (III.3.24), which reads in this case

$$\dot{\tau} \text{ sign}(\tau) + \beta \dot{\sigma}' = \frac{\tilde{\mathcal{H}}}{\sqrt{1 + \beta^2}} \dot{\xi}. \quad (\text{III.4.10})$$

A constant softening modulus  $\tilde{\mathcal{H}}$  (i.e., linear softening), up to reaching a zero yield limit, is assumed in the simulations of Section III.5. The localized fluid content in  $\Gamma_x$ , given by (III.3.25), reads in this case

$$\dot{\tilde{M}} = -[\![q_w]\!] = \frac{\rho_{wo} b \beta}{\sqrt{1 + \beta^2}} \dot{\xi}, \quad (\text{III.4.11})$$

in terms of the constant fluid density  $\rho_{wo}$ , the Biot's coefficient  $b$  and the dilatancy factor  $\beta$ . Similarly, the regular part of the fluid content increment, given by equation (III.3.26), can be written for the current case of interest

$$\dot{\tilde{M}} = \frac{\rho_{wo}}{Q} \dot{p} + \rho_{wo} b \dot{\bar{\varepsilon}}_n, \quad (\text{III.4.12})$$

for the Biot's modulus  $Q$  and the regular part of the normal strain  $\bar{\varepsilon}_n$ .

### III.4.2. An enhanced finite element formulation

The above considerations are implemented in the context of enhanced strain finite element methods, following the formulations presented in ARMERO & GARIKIPATI [1995,96] which do not resort to the regularization of the singular Dirac delta functions. In this geometrical one-dimensional setting, we consider the isoparametric interpolation of the large-scale displacement fields  $u_n$  and  $u_s$

$$u_n(x) = \mathbf{N}_e(x) \mathbf{d}_{n_e} \quad \text{and} \quad u_s(x) = \mathbf{N}_e(x) \mathbf{d}_{s_e} \quad \text{for } x \in \Omega_e, \quad (\text{III.4.13})$$

for the piece-wise linear shape functions

$$\mathbf{N}_e(x) = \begin{bmatrix} -(x - x_{2e})/h_e \\ (x - x_{1e})/h_e \end{bmatrix}, \quad (\text{III.4.14})$$

for a typical two-node element  $\Omega_e = [x_{1e}, x_{2e}] \subset \Omega = [0, L]$  (with  $h_e = |x_{2e} - x_{1e}|$ ) in terms of the nodal displacements vectors  $\mathbf{d}_{n_e}$  and  $\mathbf{d}_{s_e}$ , the normal and shear displacements, respectively. The strain field is approximated through the enhanced strategy

$$\varepsilon_{n_e} = \underbrace{\mathbf{B}_e \mathbf{d}_{n_e} - \frac{1}{h_e} \xi_{n_e}}_{\bar{\varepsilon}_{n_e}} + \xi_{n_e} \delta_{\Gamma_x}, \quad \text{and} \quad \gamma_{s_e} = \underbrace{\mathbf{B}_e \mathbf{d}_{s_e} - \frac{1}{h_e} \xi_{s_e}}_{\bar{\gamma}_{n_e}} + \xi_{s_e} \delta_{\Gamma_x}, \quad (\text{III.4.15})$$

in the elements where localization is detected, where

$$\mathbf{B}_e := \nabla \mathbf{N}_e = \frac{1}{h_e} \begin{bmatrix} -1 & 1 \end{bmatrix}, \quad (\text{III.4.16})$$

the standard strain matrix associated with the conforming part of the displacements (the large-scale strain field in the notation of Section III.2). The scalars  $\xi_{n_e}$  and  $\xi_{s_e}$  correspond to a constant approximation over the element of the normal and shear displacement jumps, respectively, and are given in terms of a single enhanced parameter  $\xi_e$  for element  $\Omega_e$  through the relations (III.4.9).

The enhanced interpolation (III.4.15) of the strains can be understood as arising from the displacement interpolation

$$\mathbf{u}_\mu(x) = \mathbf{N}_e(x) \mathbf{d}_e + \boldsymbol{\xi}_e \Psi_{\Gamma_e}(x) \quad x \in [x_{1e}, x_{2e}], \quad (\text{III.4.17})$$

for  $\mathbf{d}_e = [\mathbf{d}_{n_e} \quad \mathbf{d}_{s_e}]^T$  and  $\boldsymbol{\xi}_e = [\xi_{n_e} \quad \xi_{s_e}]^T$ , in terms of the interpolating function

$$\Psi_{\Gamma_e}(x) = H_{x_{\Gamma_e}}(x) - N_{2e}(x), \quad (\text{III.4.18})$$

for the shape function  $N_{2e}(x)$  in (III.4.14)<sub>2</sub> and the Heaviside function  $H_{x_{\Gamma_e}}(x)$  exhibiting a unit jump across the discontinuity at the center of the element

$$x_{\Gamma_e} = \frac{1}{2} (x_{2e} + x_{1e}). \quad (\text{III.4.19})$$

The function  $\Psi_{\Gamma_e}(x)$  is depicted in Figure III.4.2, and corresponds to an approximation of the function  $\psi_\Gamma(x)$  in (III.2.7) as employed in the developments of Section III.2.2 for the continuum problem. The relation

$$\int_{x_{1e}}^{x_{2e}} \Psi_{\Gamma_e}(x) dx = 0, \quad (\text{III.4.20})$$

over an element  $\Omega_e$  is satisfied, in particular. The multi-scale framework developed in Section III.2 clearly applies to the proposed finite element method with simply identifying the local neighborhood  $\Omega_x$  with the element  $\Omega_e$  for the material point  $x_\Gamma$ . We note, however, that the entire formulation only makes use of the enhanced strain as written in (III.4.15). As obtained in the previous section for the one-dimensional problem at hand, a strong discontinuity is activated upon yielding.

The final governing equations for the mechanical problem consist of the principle of virtual work equation (III.2.3) of the large-scale problem for  $\mathbf{u}$ , and the localized equilibrium relation (III.2.11). For the problem at hand, the weak form (III.2.3) reduces to the set of residual equations

$$\left. \begin{aligned} \mathbf{R}_n &:= \mathbf{f}_{n_{ext}} - \sum_{e=1}^{n_{elem}} \int_{x_{1e}}^{x_{2e}} \mathbf{B}_e^T \boldsymbol{\sigma} \, dx = 0, \\ \mathbf{R}_s &:= \mathbf{f}_{s_{ext}} - \sum_{e=1}^{n_{elem}} \int_{x_{1e}}^{x_{2e}} \mathbf{B}_e^T \boldsymbol{\tau} \, dx = 0, \end{aligned} \right\} \quad (\text{III.4.21})$$

for normal and shear external nodal force components  $\mathbf{f}_{n_{ext}}$  and  $\mathbf{f}_{s_{ext}}$ , respectively, including imposed boundary displacements. The symbol  $\mathbf{A}$  has been used in (III.4.21) to denote the assembly of all the  $n_{elem}$  element contributions. The stresses  $\boldsymbol{\sigma}$  and  $\boldsymbol{\tau}$  are obtained through the elastic relations (III.4.2) for the effective stresses, in terms of the regular part of the strains  $\bar{\boldsymbol{\epsilon}}_n$  and  $\bar{\boldsymbol{\gamma}}_s$ , respectively, in (III.4.15), and the pressure contribution discussed below. The corresponding integrals are evaluated through a single quadrature point at the center of the element.

The localized equilibrium relation (III.2.11) reduces in this case, involving a constant approximation of the displacement jumps over the element, to the nonlinear scalar relation

$$\left. \begin{aligned} |\boldsymbol{\tau}| + \beta \boldsymbol{\sigma}' - \tilde{q}(\xi_e) &= 0, & \text{for } \dot{\xi}_e > 0, \\ \xi_e &= \text{constant}, & \text{otherwise,} \end{aligned} \right\} \quad (\text{III.4.22})$$

after using the localized softening relation (III.4.10), in terms of the stresses  $\{\boldsymbol{\sigma}, \boldsymbol{\tau}\}$  and the localized softening stress-displacement law  $\tilde{q}(\xi_e)$  (note that, in this case,  $\tilde{\alpha} = \xi_e$  as defined in (III.3.23)). The rate form of (III.4.22) is given by equation (III.4.10). The normal  $\xi_{n_e}$  and shear  $\xi_{s_e}$  components of the jump are obtained in terms of  $\xi_e$  through the constant relations (III.4.9). The integration of the localized equations (III.4.22) follows the same steps as described in ARMERO & GARIKIPATI [1995].

The fluid flow contributions are interpolated using a similar piece-wise linear interpolation of the pore pressure field  $p$ , that is,

$$p(x) = \mathbf{N}_e(x) \mathbf{p}_e \quad \text{for } x \in \Omega_e = [x_{1e}, x_{2e}], \quad (\text{III.4.23})$$

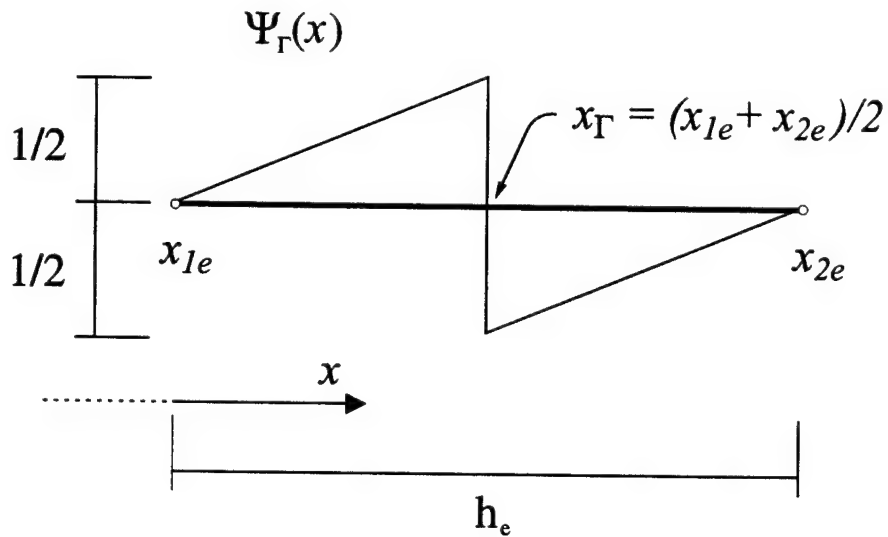


**FIGURE III.4.2** Dilatant shear layer. One-dimensional enhanced finite element with a discontinuous shape function at the mid-point  $x_{\Gamma e} = (x_{1e} + x_{2e})/2$ .

and the same shape functions  $\mathbf{N}_e$  as in (III.4.14)<sub>2</sub> for the nodal pore pressure parameters  $\mathbf{p}_e = [p_{1e} \ p_{2e}]^T$ . The weak form of the fluid mass balance equation (III.2.24) leads in this case to

$$\int_0^L \dot{\tilde{M}} \delta p \, dx + \sum_{e=1}^{n_{loc}} \dot{\tilde{M}}_e \delta p(x_{\Gamma e}) = \int_0^L q_w \frac{d}{dx} (\delta p) \, dx - [q_w \ \delta p]_0^L , \quad (\text{III.4.24})$$

for all admissible variations  $\delta p \in \mathcal{V}_p$  and for  $n_{loc}$  elements exhibiting a strong discontinuity. Consistent with the one-point quadrature assumed for the mechanical contributions and the mid-point location of the discontinuity  $x_{\Gamma e}$  in (III.4.19), the contribution of the localized fluid content involves simply  $\delta p(x_{\Gamma e}) = (\delta p_{1e} + \delta p_{2e})/2$  for the assumed linear pressure interpolation. Alternative locations of the discontinuity in an element can be considered; details are omitted.

The presence of the localized flow  $\dot{\tilde{M}}_e = -[q_w]_e$  appears as an added source term to the fluid mass balance, and it is given by the relation (III.4.11) in terms of the displacement jump rate  $\dot{\xi}_e$ . The associated discontinuity of the fluid flow  $q_w$  is incorporated at the element level through an *enhancement* of the conforming contribution of the gradient of the assumed linear pressure interpolation. More precisely, we consider at the element level the enhanced interpolation

$$q_w(x) = -\rho_{wo} k \mathbf{B}_e \mathbf{p}_e + [q_{w_e}] \Psi_{\Gamma e}(x) \quad x \in [x_{1e}, x_{2e}] , \quad (\text{III.4.25})$$

for the conforming gradient operator  $\mathbf{B}_e$  defined in (III.4.16). Noting the property (III.4.20) for the discontinuous interpolation function  $\Psi_{\Gamma_e}(x)$  and the constant character of the pore pressure gradient variations  $d(\delta p)/dx$ , we observe that the fluid flow jump  $[\![q_w]\!]$  is effectively eliminated from the balance equation (III.4.24). The actual value of  $[\![q_w]\!]$  is obtained from the localized relation (III.4.11) as a post-processing, if desired. Similar to the enhancement of the strains discussed above, the discontinuous contribution to the fluid flow vector in (III.4.25) can be understood as arising from an enhanced interpolation of the pressure field, incorporating the continuous function

$$\Psi_{\Gamma_e}^p(x) := \int_{x_{1e}}^x \Psi_{\Gamma_e}(\eta) d\eta \quad x \in [x_{1e}, x_{2e}] , \quad (\text{III.4.26})$$

exhibiting a discontinuity in the first derivative at  $x_{\Gamma_e}$ . Note that, given (III.4.20), we have the property

$$\Psi_{\Gamma_e}^p(x_{1e}) = \Psi_{\Gamma_e}^p(x_{2e}) = 0$$

thus defining an added hierachic interpolation to the original linear pressure interpolation. The numerical results reported in Section III.5 do not use, however, this alternative more complex post-processing when reporting the spatial distributions of the pore pressure.

The final discrete system of equations corresponding to the fluid mass conservation (III.4.24) is obtained by considering the constitutive relations (III.4.12) and (III.4.11) for the regular and singular parts, respectively, of the fluid content increment. In particular, for the one-dimensional finite element interpolations considered in this section, equation (III.4.12) can be written as

$$\begin{aligned} \dot{\bar{M}} \Big|_{\Omega_e} &= \frac{\rho_{wo}}{Q} \dot{p} + \rho_{wo} b \dot{\bar{\varepsilon}}_n \\ &= \frac{\rho_{wo}}{Q} \dot{p} + \rho_{wo} b \left( \dot{\varepsilon}_n - \frac{1}{h_e} \dot{\xi}_e \right) \\ &= \frac{\rho_{wo}}{Q} \dot{p} + \rho_{wo} b \dot{\varepsilon}_n - \frac{1}{h_e} \dot{\bar{M}}_e \quad \text{in } \Omega_e \end{aligned} \quad (\text{III.4.27})$$

after using (III.4.11) and (III.4.15)<sub>1</sub>. Given the relation

$$\delta p(x_{\Gamma_e}) = \frac{1}{h_e} \int_{x_{1e}}^{x_{2e}} \delta p(x) dx , \quad (\text{III.4.28})$$

for the assumed mid-point location (III.4.19) of  $x_{\Gamma_e}$ , we observe then that the introduction of the relation (III.4.27) in the weak equation (III.4.24) leads to the cancellation of the localized fluid content terms corresponding to  $\dot{\bar{M}}_e$ , as a simple calculation shows. The resulting finite element equation reads

$S\dot{p} + Q^T \dot{d}_n + H\dot{p} - r_{ext} = 0 ,$

(III.4.29)

where we have introduced the notation

$$\begin{aligned} \mathbf{S} &:= \mathbf{A} \sum_{e=1}^{n_{elem}} \int_{\Omega_e} \frac{\rho_{wo}}{Q} \mathbf{N}_e^T \mathbf{N}_e dx, \quad \mathbf{H} := \mathbf{A} \sum_{e=1}^{n_{elem}} \int_{\Omega_e} \rho_{wo} k \mathbf{B}_e^T \mathbf{B}_e dx, \\ \text{and } \mathbf{Q} &:= \mathbf{A} \sum_{e=1}^{n_{elem}} \int_{\Omega_e} \rho_{wo} b \mathbf{B}_e^T \mathbf{N}_e dx, \end{aligned} \quad (\text{III.4.30})$$

and the vector of imposed external fluxes  $\mathbf{r}_{ext}$ , including the corresponding contributions of imposed boundary pressures. Physically, equation (III.4.29) imposes weakly the global (large-scale) balance of fluid mass as given by the regular contributions of the fluid flow fields, whereas the localized balance of fluid mass on the strong discontinuity is handled locally at the element level. For the assumed mid-point location of the discontinuity, the localized accumulation of fluid content  $\tilde{M}$  in the discontinuity is a consequence of the strain  $-\xi_{ne}/h_e$  associated to the normal displacement jump  $\xi_{ne}$  over the rest of the element, as relation (III.4.27) shows. This localized fluid content can then be obtained as a post-processing in terms of the enhanced parameter  $\xi_e$  through (III.4.11).

In summary, the proposed finite element formulation involves the assembly and numerical solution of the nonlinear system of discrete equations (III.4.21) and (III.4.29). The numerical simulations presented in Section III.5 make use of a Newton-Raphson scheme to solve this coupled set of nonlinear equations, with the quasi-static equilibrium equations (III.4.21) imposed at the end of the time step and the evolution equations (III.4.29) discretized in time with a backward-Euler scheme. Equation (III.4.22) is employed for the solution of the local enhanced parameter  $\xi_e$ , and eliminated through its static condensation in the corresponding contributions of the stresses in the mechanical equations (III.4.21). We refer to ARMERO & GARIKIPATI [1995,96] for complete details on this procedure; details are omitted herein. The final formulation involves then a nonlinear discrete problem in the nodal displacements  $\mathbf{d}_e$  and the nodal pressures  $\mathbf{p}_e$  only, *the large-scale problem*, while incorporating effectively the effects of the localized dissipative mechanisms.

### III.5. Representative Numerical Simulations

The purpose of this section is to evaluate the performance of the finite element formulation proposed in Section III.4.2. To this purpose, we present the results obtained for two different problems involving the dilatant shear layer studied in Section III.4. More specifically, Section III.5.1 considers the undrained shear test, referring to the assumed impervious boundaries of the shear layer. In contrast, Section III.5.2 considers the drained shear test characterized by an imposed pore pressure along the boundaries.

**TABLE III.5.1** Material parameters for the poro-plasticity model considered in the numerical simulations presented herein.

|                      |             |                   |               |
|----------------------|-------------|-------------------|---------------|
| Oedometric Modulus   | $E_{oe}$    | 2700              | $kPa$         |
| Shear Modulus        | $G$         | 770               | $kPa$         |
| Initial Cohesion     | $c$         | 30                | $kPa$         |
| Frictional Parameter | $\beta$     | 0.45              |               |
| Permeability         | $k$         | $1 \cdot 10^{-8}$ | $m^2/(kPa s)$ |
| Biot's Modulus       | $Q$         | $3.33 \cdot 10^4$ | $kPa$         |
| Biot's Coefficient   | $b$         | 1                 |               |
| Fluid Density        | $\rho_{wo}$ | $1.0 \cdot 10^3$  | $kg/m^3$      |

### III.5.1. The undrained shear test

We first consider a layer  $L = 0.63 m$  thick with impervious boundaries at  $x = 0$  and  $x = L$ . A constant normal stress of  $\sigma = -200 kPa$  is suddenly imposed at  $t = 0$  and it is maintained constant during the test at  $x = L$ . The simulation is run by imposing a shear displacement at  $x = L$ , with a constant rate of  $\dot{u}_s(L) = a = 4.0 \cdot 10^{-8} m/s$ . Fixed boundary conditions are assumed at  $x = 0$  leading to the shear of the layer. The assumed material parameters have been included in Table III.5.1. In particular, the Biot modulus  $Q$  has been computed by means of the relation

$$\frac{1}{Q} = \frac{\phi_0}{\kappa_w} + \frac{1 - \phi_0}{\kappa_s} \quad (\text{III.5.1})$$

where  $\phi_0 = 0.3$  is the initial porosity, and  $\kappa_w = 10^4 kPa$  and  $\kappa_s = 10^{16} kPa$  are the bulk moduli of the fluid and the solid phases, respectively. We consider a piece-wise linear finite element discretization of the problem, as described in Section III.4.2, with a lumped form (row sum) of the capacity matrix  $\mathbf{S}$ . More specifically, we consider the enhanced finite element formulation presented in the previous section with the response in the discontinuity given by a linear localized softening law (III.4.22) with a localized softening modulus of  $\tilde{\mathcal{H}} = -1000 kPa/m$ . We also perform numerical simulations involving standard isoparametric linear elements based on a continuum local model with strain softening modulus of  $\mathcal{H} = -25 kPa$ .

The shear stress  $\tau$  and the pore pressure  $p$  at the center of the layer versus the imposed shear displacement are depicted in Figure III.5.1.a for the newly proposed enhanced finite element formulation and in Figure III.5.1.b for the standard isoparametric finite elements. In both cases we can observe an initial elastic range, characterized by a linear increase of the shear stress  $\tau$  (constant across the layer by equilibrium) versus the imposed shear strain  $\gamma_s$  together with a constant value of the pore pressure  $p$  and corresponding normal effective  $\sigma'$  and total  $\sigma$  stresses. Due to the assumed undrained boundary conditions in this test, no rate effects appear in this elastic solution.

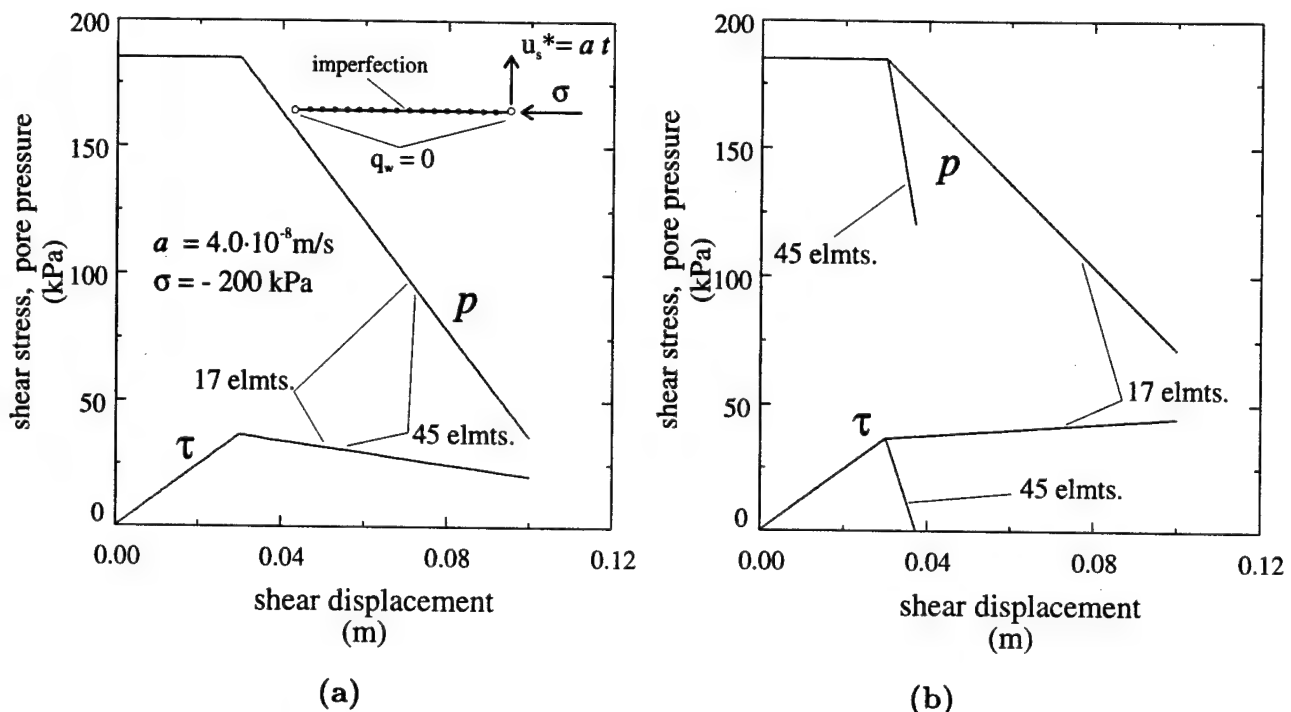


**FIGURE III.5.1** Shear layer of a dilatant material: undrained test. Shear stress and pore pressure at the center versus shear displacement: (a) Enhanced finite elements, and (b) standard isoparametric formulation.

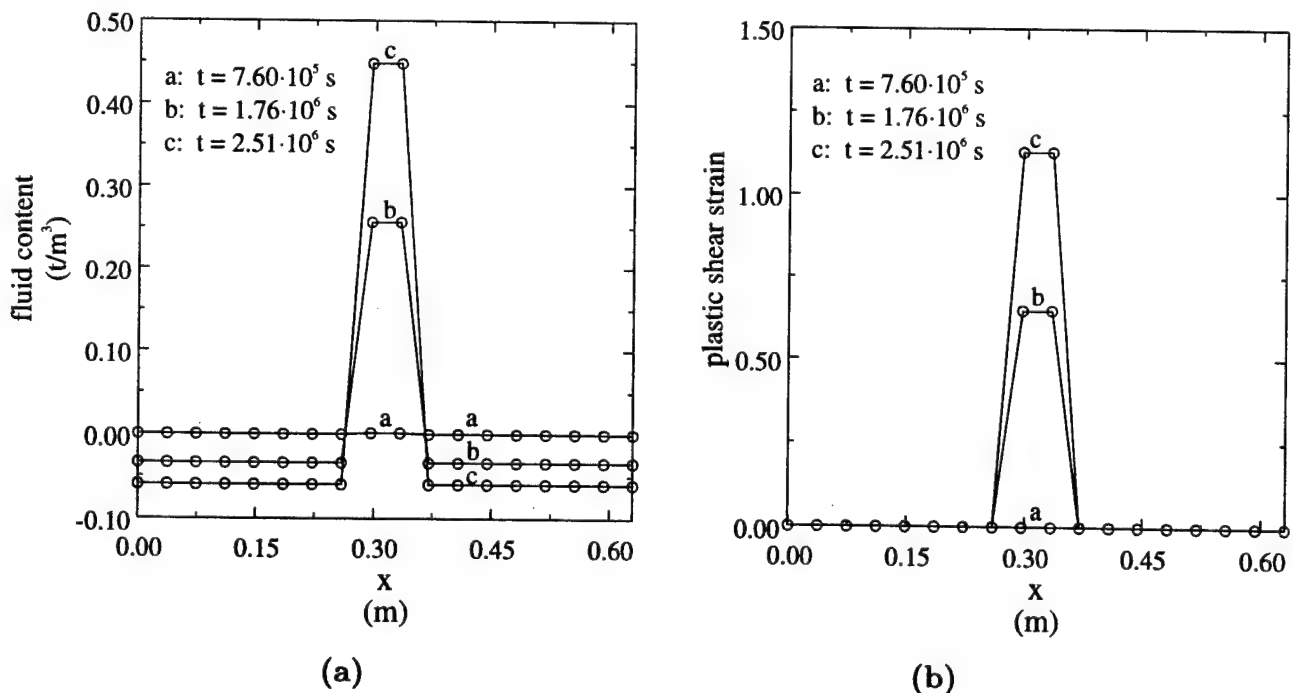


**FIGURE III.5.2** Shear layer of a dilatant material: undrained test. Isochrones of (a) fluid content, (b) plastic shear strain. Solution obtained with the enhanced finite element formulation with the 17 elements mesh; plots obtained with a lumped  $L_2$  projection to the nodes.

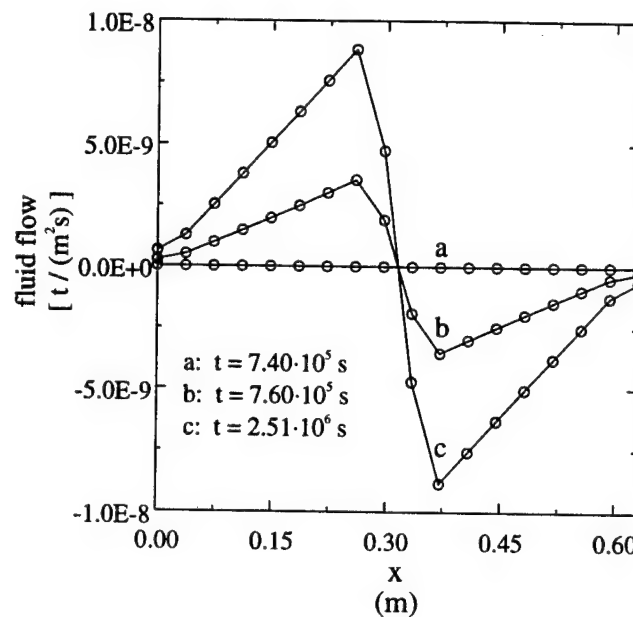


**FIGURE III.5.3** Shear layer of a dilatant material: undrained test. Isochrones of the fluid flow  $q_w$ . Solution obtained with the enhanced finite element formulation with the 17 elements mesh; plots obtained with a lumped  $L_2$  projection to the nodes.

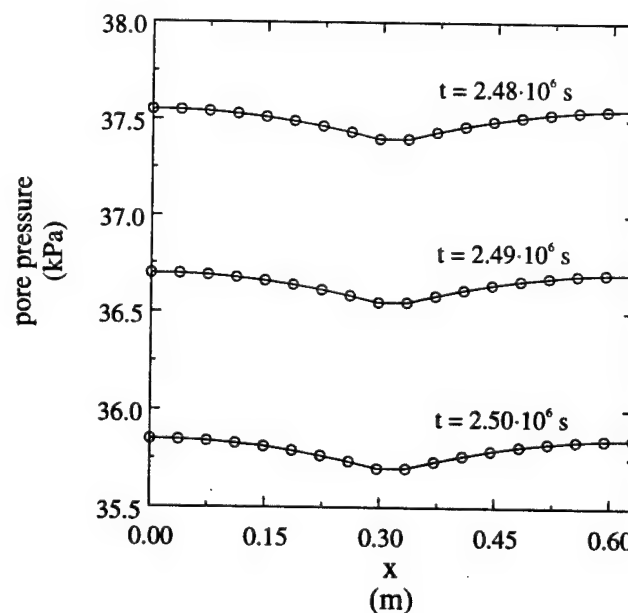


**FIGURE III.5.4** Shear layer of a dilatant material: undrained test. of the pore pressure  $p$ . Solution obtained with the enhanced finite element formulation with the 17 elements mesh.

To trigger the localization of the strain upon reaching yielding, an imperfection in the form of a 1% reduction of the initial cohesion  $c$  is introduced in the element at the center. The solutions thereafter involve a localized pattern, characterized by the activation of the enhanced parameters approximating the jump of the displacements for the simulations involving the enhanced finite elements. Computations are conducted with two different discretizations of the sample, involving 17 and 45 equally spaced finite elements, respectively. As observed in Figure III.5.1.a, the response obtained with the two meshes coincides for the enhanced finite elements, verifying the lack of pathological mesh dependence of the proposed formulation. This situation is to be contrasted by the strong mesh dependence exhibited by standard isoparametric finite elements with continuum strain softening, as depicted in Figure III.5.1.b.

Figures III.5.2.a and III.5.2.b include the distributions of the fluid content and the shear plastic strain, respectively, obtained with the enhanced finite element formulation for the 17 element mesh. The localization of the plastic strain at the center is apparent. Similarly, and due to the dilatant behavior of the discontinuity, the fluid content increases at the center, while it decreases in the adjacent material, leading to the observed localized pattern of the fluid content; see Figure III.5.2.a. This kind of response is also shown in Figure III.5.3 by the induced fluid flow depicting a jump across the strong discontinuity, with the fluid flow on each side towards the discontinuity at the center. We note that these plots have been obtained with the use of a local lumped  $L_2$  projection of the values at the center of the elements to the nodes followed by the averaging of the resulting nodal values; the smooth distribution of the plastic quantities outside the central element is an artifact of this projection. The spatial distribution of the pore pressure along the sample is depicted in Figure III.5.4 at different times for this solution. We can observe the decrease of the pore pressure at the center due to the presence of the dilatant strong discontinuity and the corresponding localized increase of the fluid content.

### III.5.2. The drained shear test

We assume free draining boundaries at both ends in this second test. The same dimensions and material parameters summarized in Table III.5.1 are employed in this case. The simulations are run also with an imposed shear displacement at  $x = L$  after imposing a sudden initial normal stress of  $\sigma = -200 \text{ kPa}$ , which is also maintained constant during the simulations. The draining through the boundaries introduces in this case a non-constant distribution of the pore pressure, leading to rate-dependence even in the elastic range. The goal in this test is to study the influence of these effects in the resulting localization patterns. To this purpose, two constant strain rates  $\dot{\epsilon}_s(L) = a$  of  $a = 2.0 \cdot 10^{-5} \text{ m/s}$  and  $a = 6.0 \cdot 10^{-5} \text{ m/s}$  are considered. The higher strain rates in this case are required for the yield in the specimen to occur before the total dissipation of the pore pressures.

As in the previous section, we consider simulations based on the proposed enhanced finite elements and standard isoparametric finite elements. A linear localized softening

stress-displacement law of the form given in (III.4.22) is assumed in the former, with a localized modulus of  $\tilde{\mathcal{H}} = -3000 \text{ kPa}/\text{m}$ . The continuum strain softening modulus assumed in this test is  $\mathcal{H} = -75 \text{ kPa}$ . Spatial discretizations involving 9 and 17 piecewise linear elements in an equally spaced distribution are assumed.

Figure III.5.5 depicts the evolution of the shear stress and the pore pressure at the center of the specimen versus the imposed shear strain. The rate-dependent effects are clear in these plots. Figure III.5.6 depicts the pore pressure distribution for the enhanced finite element solution based on the 17 element mesh. The gradual dissipation of the pore pressure after an initial build up due to the applied constant normal stress can be observed in this figure, with its characteristic spatial distribution corresponding to one-dimensional elastic consolidation. Since the total normal compressive stress  $\sigma$  is maintained constant, the effective normal stress  $\sigma' = \sigma + b p$  follows a similar distribution. Note that during the initial elastic stages the normal and shear components of the deformation process are entirely uncoupled, thus the applied shear strain has no effect on the fluid motion in this range.

The specimen eventually yields at the center. To avoid the strong numerical sensitivity that we have observed in capturing this yielding at the exact center, we also consider in this case a 1% reduction of the initial cohesion  $c$  at the center element. The plastic strains localize at the center, leading to a sudden increase of the rate of dissipation of the pore pressure, as observed in Figure III.5.6 at  $t \approx 700 \text{ s}$  for the strain rate of  $a = 6 \cdot 10^{-5} \text{ m/s}$  and the enhanced finite element formulation. This spatial distribution of the pore pressure clearly changes with the formation of the discontinuity, which acts as an internal drainage. Note that negative pressures will eventually appear at the center; the simple model considered in this work does not account for any limitation in this respect, like the cavitation of the fluid.

Comparing the solutions obtained for the two different meshes in Figure III.5.5 we can conclude the following. For the proposed enhanced finite element formulation depicted in Figure III.5.5.a, a slight difference can be observed between each mesh. The observed differences can be traced back to the different approximation of the fluid flow process by the different spatial discretization and not by the non-objectivity of the localized dissipative mechanism upon localization. This conclusion is drawn from the same slope obtained in the shear stress plot by both meshes for each imposed strain rate. This situation is to be contrasted with the solutions obtained with the standard isoparametric formulation shown in Figure III.5.5.b. The mesh dependence in this case is not only caused by the approximation introduced by the integration of the fluid flow, but clearly also caused by a non-objective resolution of the localized dissipative mechanism. Note the entirely different slopes obtained in the shear stress evolution by the different meshes for each imposed strain rate.

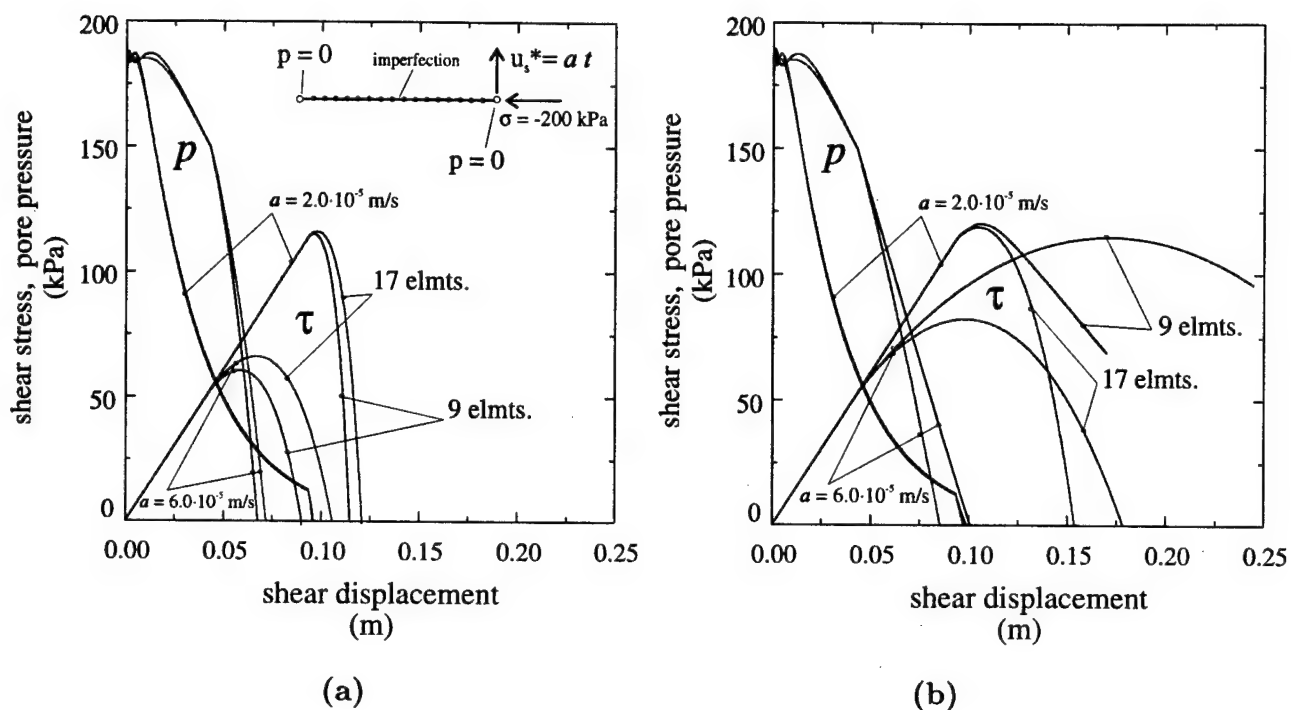


**FIGURE III.5.5** Shear layer of a dilatant material: drained test. Shear stress and pore pressure at the center versus shear displacement: (a) Enhanced finite elements, and (b) standard isoparametric formulation.

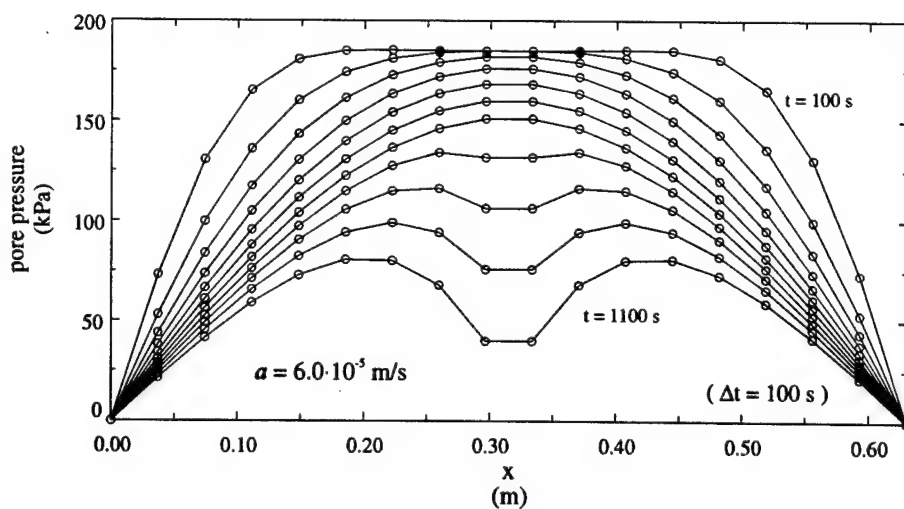


**FIGURE III.5.6** Shear layer of a dilatant material: drained test. Isochrones of the pore pressure  $p$  obtained with the enhanced finite elements for  $a = 6 \cdot 10^{-5}$  m/s (isochrones shown every 100 s).

### III.6. Concluding Remarks

We have presented in this paper a general framework for the characterization of strong discontinuities in fully saturated porous media. Discontinuities in the displacements, with the corresponding singular measures of the strains through the associated plastic strains, have been shown to be consistent with a singular distribution of the fluid content. Physically this is a consequence of the dilatant response of these discontinuities, leading to the accumulation of fluid mass along these surfaces of discontinuity and creating a discontinuity of the fluid flow vector across them. The model example of a shear layer of a dilatant material has been used to illustrate these ideas, including the formulation of enhanced strain finite element methods incorporating without regularization these singular fields of the strains and fluid content, as well as the discontinuous fluid flow vectors. The resulting formulation has been shown to avoid the mesh-dependence observed when employing standard isoparametric finite elements based on a local continuum model in the shear driven problems considered herein.

Furthermore, the appearance of these discontinuities has been directly related to the response of the underlying drained material model, as in the discontinuous linearized instabilities observed in the analyses in RICE [1975] and RUDNICKI & RICE [1975], among others. It is important to emphasize that the fundamental consideration in the developments of the previous sections leading to this result is the continuity of the pressure field (or, more precisely, the regular distributional character of the fluid flow). This consideration is motivated by the structure of the mathematical equations, namely, the involvement of second spatial derivatives of the pressure field in the conservation of fluid mass equation for a *positive permeability*. We also pointed out similar considerations based on experimental observations as reported, for example, in VARDOULAKIS [1996]. As shown in the linearized stability analysis presented in RICE [1975] for a dilatant shear layer, disturbances in the short wave-length limit (zero length scale limit) lead to the instability of the shear layer for the case of a strain softening drained response and physically positive permeability. For the ideal purely undrained case, that is, for zero permeability, the above continuity condition on the pressure is no longer required. As a consequence, the appearance of localization is to be derived from the undrained, rate-independent response of the solid in this ideal limit. The stiffer response of the porous solid under purely undrained conditions puts then a severe demand in the numerical simulations near this limit case, due to the need to capture very accurately the details of the local flow associated to fluid mass conduction. These arguments seem to explain the very sensitive response in the numerical simulations involving a very high strain rate, shown by the difficulty to capture the localized solutions, as indicated in the previous section. Careful analyses of the effects of the spatial and temporal discretizations in the development of these coupled phenomena, including the interaction of the length scales associated to the numerical discretization, the dissipative conduction processes, the assumed imperfections, and strain localization itself, are required. We plan to address these issues in a forthcoming publication.

Similarly, we are currently extending the finite element formulations presented herein to the multi-dimensional case. General states of stress need to be considered, as well as the interaction of possible different length scales in particular states of stress, like the uniaxial compressive examples presented recently in ZHANG & AL [1998]. As shown in ARMERO [1997a], strong discontinuities furnish a very efficient tool for the modeling of localized effects while treating the involved small length scales as unresolvable. The general framework presented in this paper will show to be crucial for this purpose, as it is the current focus of our work in this area.

## References

- ARMERO, F. [1997a] "Large-Scale Modeling of Localized Dissipative Mechanisms in a Local Continuum: Applications to the Numerical Simulation of Strain Localization in Rate-Dependent Inelastic Solids," SEMM/UCB Report no. 97/12, to appear in *Mech. Cohesive-Frictional Mat.*, in press.
- ARMERO, F. [1997b] "On the Characterization of Localized Solutions in Inelastic Solids: an Analysis of Wave Propagation in a Softening Bar," SEMM/UCB Report no. 97/18, submitted to *Comp. Meth. Appl. Mech. Eng.*.
- ARMERO, F. [1998] "Formulation and Finite Element Implementation of a Multiplicative Model of Poro-Plasticity at Finite Strains under Fully Saturated Conditions," SEMM/UCB Report no. 98/05, to appear in *Comp. Meth. Appl. Mech. Eng.*, in press.
- ARMERO, F. & GARIKIPATI, K. [1995] "Recent Advances in the Analysis and Numerical Simulation of Strain Localization in Inelastic Solids," *Proc. COMPLAS IV*, eds. D.R.J. Owen, E. Onate, and E. Hinton, CIMNE, Barcelona.
- ARMERO, F. & GARIKIPATI, K. [1996] "An Analysis of Strong Discontinuities in Multiplicative Finite Strain Plasticity and their Relation with the Numerical Simulation of Strain Localization in Solids," *Int. J. Solids and Structures*, **33**, 2863-2885.
- BIOT, M.A. [1941] "General Theory of Three-Dimensional Consolidation," *Journal of Applied Physics*, **12**, 155-164.
- COUSSY, O. [1995] *Mechanics of Porous Continua*, Wiley, Chichester.
- LARSSON, R. & RUNESSON, K. [1996] "Element Embedded Localization Band Based on Regularized Displacement Discontinuity," *J. Eng. Mech.*, **122**, 402-411.

- LARSSON, R.; RUNESSON, K. & STURE, S. [1996] "Embedded Localization Band in Undrained Soil Based on Regularized Strong Discontinuity: Theory and FE Analysis," *Int. J. Solids Structures* **33**, 3081-3101.
- LORET, B. & PREVOST, J.H. [1993] "Dynamic Strain Localization in Fluid-Saturated Porous Media," *J. Eng. Mechanics*, **117**, 907-922.
- OLIVER, J. [1996] "Modelling Strong Discontinuities in Solid Mechanics via Strain Softening Constitutive Equations. Part 1: Fundamentals. Part 2: Numerical Simulation," *Int. J. Num. Meth. Eng.*, **39**, 3575-3623.
- PIETRUSZCZAK, S. [1995] "Undrained Response of Granular Soil Involving Localized Deformation," *J. Eng. Mechanics*, **121**, 1292-1297.
- RICE, J.R. [1975] "On the Stability of Dilatant Hardening for Saturated Rock Masses," *J. Geophysical Research*, **80**, 1536-1531.
- RUDNICKI, K. & RICE, J.R. [1975] "Conditions for the Localization of Deformation in Pressure-Sensitve Dilatant Materials," *J. Mech. Phys. Solids*, **23**, 371-394.
- RUNESSON, K.; PERIC, D. & STURE, S. [1996] "Effect of Pore Fluid Compressibility on Localization in Elastic-Plastic Porous Solids under Undrained Conditions," *Int. J. Solids Structures* **33**, 1501-1518.
- SCHREFLER, B.A.; MAJORANA, C.E. & SANAVIA, L. [1995] "Shear Band Localization in Saturated Porous Media" *Arch. Mech.* **47**, 577-599.
- SIMO, J.C; OLIVER, J. & ARMERO, F. [1993] "An Analysis of Strong Discontinuities Induced by Softening Solutions in Rate Independent Solids," *J. Comput. Mech.*, **12**, 277-296.
- STAKGOLD, I. [1979] *Green's Functions and Boundary Value Problems*, Wiley, New York.
- STEINMANN, P.; LARSSON, R. & RUNESSON, K. [1997] "On the Localization Properties of Multiplicative Hyperelasto-plastic Continua with Strong Discontinuities," *Int. Jour. Solids Structures*, **34**, 969-990.
- TRUESDELL & NOLL [1965] "The Nonlinear Field Theories of Mechanics," *Handbuch der Physik Bd. III/3*, ed. by S. Fluegge, Springer Verlag, Berlin.
- VARDOULAKIS, I. [1996] "Deformation of Water-Saturated Sand: I. Uniform Undrained Deformation and Shear Banding; II. Effect of Pore Water Flow and Shear Banding," *Géotechnique*, **46**, 441-472.
- ZHANG, H.W.; SANAVIA, L. & SCHREFLER, B.A. [1998] "An Internal Length Scale in Dynamic Strain Localization of Multiphase Porous Media," preprint submitted to *Mech. Cohesive-Frictional Materials*.

## **APPENDIX IV**

### **An ALE Finite Element Method for Finite Strain Plasticity**

**Based on the paper:**

Armero, F. & Love, E. [2000] "An Arbitrary Eulerian-Lagrangian (ALE) Finite Element Method for Finite Strain Elastoplasticity," to be submitted to *International Journal of Numerical Methods in Engineering*.

## IV.1. Introduction

The Arbitrary Lagrangian-Eulerian(ALE) formulation of continuum mechanics was initially developed to circumvent the limitations of pure Eulerian and pure Lagrangian formulations. In particular, the fundamental idea is to allow the computational mesh to move in an arbitrary manner independent of the physical material motion. By using this approach, the severe mesh distortion of a pure Lagrangian formulation or the complicated boundary tracking of a pure Eulerian formulation can be avoided. Two review papers which discuss the general notion of ALE formulations are BENSON [1989] and BENSON [1992].

Within the context of fluid mechanics, the ALE approach has been used recently by VENKATASUBBAN [1995]. HUERTA & LIU [1988] and CHIPPADA, RAMASWAMY & WHEELER [1994] have considered fluid mechanics problems with free surfaces. Another important area of research is fluid-structure interaction. The reader may consult NOMURA [1994] and NOMURA & HUGHES [1992] for more information. The ALE formulation has obvious appeal in these classes of problems. However, in this work we are primarily interested in non-linear solid mechanics.

A considerable amount of work has been done within the field of non-linear solid mechanics. Authors have considered rolling problems (HU & LIU [1993], HU & LIU [1992]), metal forming and plasticity problems (GHOSH & KIKUCHI [1988], GHOSH & KIKUCHI [1991]) and contact problems (GHOSH [1992]). An important area of research is the numerical simulation of localized failure in solids (GHOSH & RAJU [1996], PIJAUDIERCABOT & HUERTA [1995]). The paper of HUERTA & CASADEI [1994] provides a good general review of ALE formulations in solid mechanics.

Other researchers have considered what is known as adaptive remeshing. In this strategy, an entirely new mesh is generated for the problem once the existing mesh is judged unsuitable. The new mesh is entirely unrelated to the previous mesh, except of course for preservation of the boundary. In a general sense, the adaptive remeshing approach and the ALE approach may be considered related. Much of the work in adaptive remeshing can be found in the papers of CAMACHO & ORTIZ [1997], LEE & BATHE [1994] and ORTIZ & QUIGLEY [1991].

We propose in this work an ALE formulation relevant to solid mechanics. In particular, we consider the numerical simulation of finite strain elasticity and plasticity. Unlike much of the previous ALE performed, the approach here is fully implicit. RODRIGUEZ-FERRAN, CASADEI & HUERTA [1998] have recently discussed both explicit and implicit solution strategies for the ALE problem, but for the so-called hypoelastic models of elastoplasticity in rate form. The interest in this work, however, lies in the consideration of multiplicative models of plasticity, rather than rate models, involving a hyperelastic relation in particular.

The present formulation is based critically on the work of YAMADA & KIKUCHI [1993]. In that paper, the authors consider an implicit ALE finite element method for elasticity

problems. The general basis of the formulation is that the physical particle motion is a composition of two mappings, a mesh motion and a material remap. The authors present only a fully coupled solution strategy; namely, The equilibrium equations couple the mesh motion and material remap. The consideration of purely elastic models in the quasi-static limit, however, simplifies considerably the problem, since the material remap do not imply the advection of any internal variables as it is the case in elastoplasticity, the focus herein.

We develop in this work the complete treatment of multiplicative finite strain elastoplasticity in this context involving a direct solution of the material map. In particular, the direct use and interpolation of this mapping, in contrast with alternative ALE approaches for finite strain elastoplasticity, leads to a considerable simplification of the advection of internal variables. In fact, this advection can be accomplished by an exact simple particle tracking, without the need of complex approximations of the pure advection equation. This particle tracking is efficiently accomplished by the use of the appropriate description of the reference mesh through its connectivity graph. We develop these ideas in the context of a staggered strategy for the solution of the equations. A Lagrangian step is followed by a material remap calculation followed by the aforementioned advection based on this computed material remap. The proposed procedure shows to be, in particular, a very efficient strategy in its computational cost.

An outline of the rest of the paper is as follows. Section IV.2 summarizes the continuum equations of the ALE approach, including a brief description of multiplicative plasticity in Section IV.1.2 as considered in this work. Section IV.3 describes the general approach proposed herein for the solution of the ALE equations. In particular, we describe the algorithms considered for the material remap based on a measure of the mesh distortion. The proposed treatment for the advection of the plastic internal variable is discussed in Section IV.4. We present in Section IV.5 several representative simulations depicting the performance of the proposed approach. Concluding remarks are included in Section IV.6. Finally, we present in a series of appendices several details of the considered implementation. More specifically, Appendix IV.1 summarizes the specific constitutive models considered in the numerical simulations of Section IV.5, Appendix IV.2 presents a summary of the finite element equations.

## IV.2. Continuum Equations of the ALE Formulation

There are many references on the kinematics and dynamics of ALE continuum mechanics. The equations we will discuss can be found in papers such as HUERTA & CASADEI [1994], BENSON [1989], YAMADA & KIKUCHI [1993] and GHOSH & KIKUCHI [1988]. Some other possible references are listed alphabetically in the bibliography of this report.

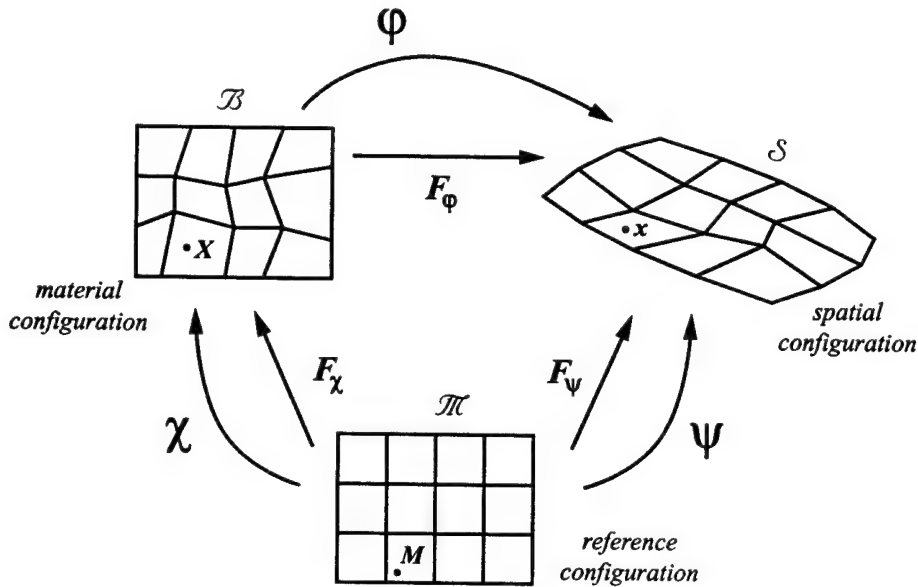


FIGURE IV.2.1 ALE Kinematics

#### IV.2.1. ALE kinematics

Firstly, assume there exists a fixed reference (computational) domain  $\mathcal{M}$  independent of any physical motion of the body. There also exist two additional domains denoted by  $\Omega_0$  and  $\Omega$ , which are the material and spatial configurations of the physical body, respectively. The physical particle motion is given by the one parameter family of diffeomorphisms  $\varphi_t : \Omega_0 \rightarrow \Omega$ . The subscript  $t$  represents time. Assume there exist two additional diffeomorphisms  $\chi_t : \mathcal{M} \rightarrow \Omega_0$  and  $\psi_t : \mathcal{M} \rightarrow \Omega$  which relate the material and spatial configurations to the reference domain. By this construction,  $\varphi_t = \psi_t \circ \chi_t^{-1}$ . Setting  $\chi_t = id$ , so that  $\varphi_t = \psi_t$ , is known as the Lagrangian formulation and is commonly used in solid mechanics. Setting  $\psi_t = id$ , so that  $\varphi_t = \chi_t$ , is known as the Eulerian formulation and is commonly used in fluid mechanics. We, of course, are interested in the case when neither mapping is necessarily the identity. Figure (IV.2.1) is a helpful visual representation of the present discussion.

Define the tangent maps  $F_\psi := D\psi_t$  and  $F_\chi := D\chi_t$ . The physical deformation gradient is defined by  $\mathbf{F} := D\varphi_t$ . By application of the chain rule, we have the important relationship  $\mathbf{F} = F_\psi F_\chi^{-1}$ . If one assumes fixed cartesian coordinate systems for each of the three domains, further developments can be simplified. Let points in  $\mathcal{M}$  be denoted by their position vector  $\mathbf{m}$ . Let points in  $\Omega_0$  be denoted by position vector  $\mathbf{X}$ . Let points in  $\Omega$  be denoted by position vector  $\mathbf{x}$ . Given this, it is possible to then write

$$F_\psi = \frac{\partial \mathbf{x}}{\partial \mathbf{m}} \quad (\text{IV.2.1})$$

$$\mathbf{F}_\chi = \frac{\partial \mathbf{X}}{\partial \mathbf{m}} \quad (\text{IV.2.2})$$

$$\mathbf{F} = \frac{\partial \mathbf{x}}{\partial \mathbf{X}}. \quad (\text{IV.2.3})$$

Define the Jacobians  $J := \det(\mathbf{F})$ ,  $J_\psi := \det(\mathbf{F}_\psi)$  and  $J_\chi := \det(\mathbf{F}_\chi)$ . Next, noting that one may view  $\mathbf{x}$  as a function of  $\mathbf{X}$  and  $t$ , define the physical particle velocity as

$$\mathbf{v} := \frac{\partial \mathbf{x}(\mathbf{X}, t)}{\partial t} =: \left. \frac{\partial \mathbf{x}}{\partial t} \right|_{\mathbf{X}} \quad (\text{IV.2.4})$$

where the introduced notation means the derivative of the position  $\mathbf{x}$  with respect to time  $t$  while holding the position  $\mathbf{X}$  fixed. This notation is often used in the literature and we shall adopt it henceforth here. Of course,  $\mathbf{x}$  may also be viewed as a function of  $\mathbf{m}$  and time  $t$ . Define the mesh velocity as

$$\mathbf{v}_m := \frac{\partial \mathbf{x}(\mathbf{m}, t)}{\partial t} =: \left. \frac{\partial \mathbf{x}}{\partial t} \right|_{\mathbf{m}}. \quad (\text{IV.2.5})$$

where again use is made of the newly introduced notation for the derivative of the position  $\mathbf{x}$  with respect to time  $t$  while holding the position  $\mathbf{m}$  fixed.

#### IV.2.2. Material derivative

It is now possible to develop useful expressions for what is commonly referred to as the material derivative. For notational convenience, define

$$\text{GRAD}_{\mathbf{m}}[\cdot] := \frac{\partial[\cdot]}{\partial \mathbf{m}} \quad (\text{IV.2.6})$$

$$\text{GRAD}_{\mathbf{X}}[\cdot] := \frac{\partial[\cdot]}{\partial \mathbf{X}} \quad (\text{IV.2.7})$$

and

$$\text{grad}_{\mathbf{x}}[\cdot] := \frac{\partial[\cdot]}{\partial \mathbf{x}} \quad (\text{IV.2.8})$$

Let  $f$  be a smooth scalar valued function defined on  $\Omega_0$ . We may write

$$f(\mathbf{X}, t) = f(\mathbf{m}(\mathbf{X}, t), t) = \tilde{f}(\mathbf{m}, t). \quad (\text{IV.2.9})$$

The material derivative of  $f$ ,  $\dot{f}$ , is defined as the derivative

$$\dot{f} := \frac{\partial f(\mathbf{X}, t)}{\partial t} = \left. \frac{\partial f}{\partial t} \right|_{\mathbf{X}}. \quad (\text{IV.2.10})$$

Using the chain rule, write

$$\dot{f} = \frac{\partial \tilde{f}}{\partial t} + \text{GRAD}_{\mathbf{m}}[\tilde{f}] \cdot \frac{\partial \mathbf{m}(\mathbf{X}, t)}{\partial t}. \quad (\text{IV.2.11})$$

For convenience, the tilde notation is dropped and the above simply written, consistent with the new notation,

$$\dot{\mathbf{f}} = \frac{\partial f}{\partial t} \Big|_{\mathbf{m}} + \text{GRAD}_{\mathbf{m}}[f] \cdot \frac{\partial \mathbf{m}}{\partial t} \Big|_{\mathbf{X}} \quad (\text{IV.2.12})$$

Using the above results alternative expressions can be developed for the material velocity  $\mathbf{v}$ . We may write

$$\mathbf{v} = \mathbf{v}_m + \mathbf{F}_{\psi} \frac{\partial \mathbf{m}}{\partial t} \Big|_{\mathbf{X}}. \quad (\text{IV.2.13})$$

which results in

$$\frac{\partial \mathbf{m}}{\partial t} \Big|_{\mathbf{X}} = \mathbf{F}_{\psi}^{-1}(\mathbf{v} - \mathbf{v}_m). \quad (\text{IV.2.14})$$

Making a substitution into (IV.2.12) yields

$$\dot{\mathbf{f}} = \frac{\partial f}{\partial t} \Big|_{\mathbf{m}} + \text{GRAD}_{\mathbf{m}}[f] \cdot \mathbf{F}_{\psi}^{-1}(\mathbf{v} - \mathbf{v}_m). \quad (\text{IV.2.15})$$

Noting that, by simple use of the chain rule,

$$(\text{GRAD}_{\mathbf{m}}[f]) \mathbf{F}_{\psi}^{-1} = \text{grad}_{\mathbf{x}}[f] \quad (\text{IV.2.16})$$

equation (IV.2.15) becomes

$$\dot{\mathbf{f}} = \frac{\partial f}{\partial t} \Big|_{\mathbf{m}} + \text{grad}_{\mathbf{x}}[f] \cdot (\mathbf{v} - \mathbf{v}_m). \quad (\text{IV.2.17})$$

This is the classical relationship between the material time derivative, the referential time derivative and the spatial derivative. It will prove useful in the development of the ALE balance laws.

Finally, consider the material derivative of the material position vector  $\mathbf{X}$ . This produces the equation

$$\dot{\mathbf{X}} = \mathbf{0} = \frac{\partial \mathbf{X}}{\partial t} \Big|_{\mathbf{m}} + \text{GRAD}_{\mathbf{m}}[\mathbf{X}] \frac{\partial \mathbf{m}}{\partial t} \Big|_{\mathbf{X}}. \quad (\text{IV.2.18})$$

Noting Equation (IV.2.2) the above may be rearranged. This produces the desired results

$$\frac{\partial \mathbf{m}}{\partial t} \Big|_{\mathbf{X}} = -\mathbf{F}_{\chi}^{-1} \frac{\partial \mathbf{X}}{\partial t} \Big|_{\mathbf{m}}. \quad (\text{IV.2.19})$$

and

$$\dot{\mathbf{f}} = \frac{\partial f}{\partial t} \Big|_{\mathbf{m}} - \text{GRAD}_{\mathbf{m}}[f] \cdot \mathbf{F}_{\chi}^{-1} \frac{\partial \mathbf{X}}{\partial t} \Big|_{\mathbf{m}}. \quad (\text{IV.2.20})$$

This equation will prove useful in subsequent developments involving implementation of plasticity within an ALE context.

#### IV.2.3. The balance laws

i. *Conservation of mass.* The Eulerian form of conservation of mass may be written

$$\dot{\rho} + \rho \operatorname{div}_x[v] = 0 \quad (\text{IV.2.21})$$

where  $\rho$  is the mass density and  $\operatorname{div}_x[\cdot]$  is the spatial divergence operator. Using the result in (IV.2.17), this equation can be rewritten as

$$\frac{\partial \rho}{\partial t} \Big|_m + \operatorname{grad}_x[\rho] \cdot (v - v_m) = -\rho \operatorname{div}_x[v] , \quad (\text{IV.2.22})$$

showing explicitly the advection of the spatial density.

ii. *Balance of linear momentum.* The Eulerian form of balance of linear momentum may be written

$$\rho \dot{v} = \operatorname{div}_x[\sigma] + \rho b \quad (\text{IV.2.23})$$

where  $\sigma$  is the Cauchy stress tensor and  $b$  is the body force density. Again, using the relationship for material derivatives, we can rewrite the equation (IV.2.23) as

$$\rho \frac{\partial v}{\partial t} \Big|_m + \rho(\operatorname{grad}_x[v])(v - v_m) = \operatorname{div}_x[\sigma] + \rho b . \quad (\text{IV.2.24})$$

Some of the simulations presented in this paper consider the quasi-static approximation defined by the simpler equation

$$\operatorname{div}_x[\sigma] + \rho b = 0 , \quad (\text{IV.2.25})$$

avoiding the need of considering the advection of the velocity  $v$  (or, equivalently, the linear momentum  $\rho v$ ) in (IV.2.24).

**Remark IV.2.1** There exist equivalent alternative equations for the above balance laws. The laws can be written with respect to the reference domain and can also be expressed in what is known as conservation form. It will not be necessary to discuss these alternative representations for the quasi-static problems considered herein. The reader may consult, for example, BENSON [1989] for the conservation forms of the equations. A more detailed derivation of the ALE balance laws can be found in GHOSH & KIKUCHI [1988]  $\square$

#### IV.2.4. Boundary conditions

Along the boundary of the domain, kinematical and dynamical boundary conditions must be defined. Assume the boundary  $\partial\Omega$  admits the decomposition  $\partial\Omega = \overline{\Gamma_v} \cup \overline{\Gamma_t}$  where  $\Gamma_v \cap \Gamma_t = \emptyset$ . Additionally,

$$\mathbf{v} = \bar{\mathbf{v}} \text{ on } \Gamma_v \quad (\text{IV.2.26})$$

$$\boldsymbol{\sigma}\mathbf{n} = \bar{\mathbf{t}} \text{ on } \Gamma_t \quad (\text{IV.2.27})$$

where  $\bar{\mathbf{v}}$  are prescribed velocities,  $\bar{\mathbf{t}}$  are prescribed tractions and  $\mathbf{n}$  is the outward unit normal to the spatial domain. There is an additional boundary condition if some part of the boundary is a material surface. The appropriate boundary condition is

$$(\mathbf{v} - \mathbf{v}_m) \cdot \mathbf{n} = 0. \quad (\text{IV.2.28})$$

It will be of some benefit to derive an alternative equivalent form for this boundary condition. Let  $\mathbf{N}_X$  denote the outward unit normal to the boundary of the material domain  $\Omega_0$ . Let  $\Gamma \subseteq \partial\Omega$  be an open subset of the boundary of the spatial domain and let  $\Gamma_0 = \varphi^{-1}(\Gamma) \subseteq \partial\Omega_0$ . First, we note from equation (IV.2.13) that

$$\mathbf{v} - \mathbf{v}_m = \mathbf{F}_\psi \frac{\partial \mathbf{m}}{\partial t} \Big|_{\mathbf{X}}. \quad (\text{IV.2.29})$$

Using equation (IV.2.19), this may be rewritten as

$$\mathbf{v} - \mathbf{v}_m = -\mathbf{F}_\psi \mathbf{F}_\chi^{-1} \frac{\partial \mathbf{X}}{\partial t} \Big|_{\mathbf{m}} = -\mathbf{F} \frac{\partial \mathbf{X}}{\partial t} \Big|_{\mathbf{m}} \quad (\text{IV.2.30})$$

Now, we may write

$$\begin{aligned} 0 &= \int_{\Gamma} (\mathbf{v} - \mathbf{v}_m) \cdot \mathbf{n} d\Gamma \\ &= - \int_{\Gamma} \mathbf{F} \frac{\partial \mathbf{X}}{\partial t} \Big|_{\mathbf{m}} \cdot \mathbf{n} d\Gamma \\ &= - \int_{\Gamma} \frac{\partial \mathbf{X}}{\partial t} \Big|_{\mathbf{m}} \cdot \mathbf{F}^T \mathbf{n} d\Gamma \\ &= - \int_{\Gamma_0} \frac{\partial \mathbf{X}}{\partial t} \Big|_{\mathbf{m}} \cdot \mathbf{F}^T \mathbf{J} \mathbf{F}^{-T} \mathbf{N}_X d\Gamma_0 \\ &= - \int_{\Gamma_0} \frac{\partial \mathbf{X}}{\partial t} \Big|_{\mathbf{m}} \cdot \mathbf{J} \mathbf{N}_X d\Gamma_0 \end{aligned} \quad (\text{IV.2.31})$$

where the well known transformation (Nansen's Formula) for deforming area elements has been used. Since the above must hold for all open  $\Gamma$  and thus for all open  $\Gamma_0$ , it must be that

$$\frac{\partial \mathbf{X}}{\partial t} \Big|_{\mathbf{m}} \cdot \mathbf{J} \mathbf{N}_X = 0 \quad (\text{IV.2.32})$$

pointwise. Since  $J > 0$  this reduces to

$$\frac{\partial \mathbf{X}}{\partial t} \Big|_{\mathbf{m}} \cdot \mathbf{N}_X = 0 \quad (\text{IV.2.33})$$

This form will prove more useful for future numerical implementation.

#### IV.2.5. Weak formulation

Let  $\boldsymbol{\eta}$  be a kinematically admissible virtual displacement field defined on  $\Omega_0$ . In the present context, every choice of  $\boldsymbol{\eta}$  can be characterized by

$$\boldsymbol{\eta} = \delta\psi \circ \chi^{-1} \quad (\text{IV.2.34})$$

where  $\delta\psi$  is a kinematically admissible virtual displacement field defined on  $\mathcal{M}$ . Let  $\theta$  and  $p$  represent kinematic volume and stress resultant pressure variables, respectively. Additionally, let  $\delta\theta$  and  $\delta p$  be admissible variations of  $\theta$  and  $p$ , respectively. Solving the equilibrium equation, along with compatibility equations for  $\theta$  and constitutive equations for  $p$ , is weakly equivalent to the following set of equations:

$$\int_{\Omega_0} \text{grad}_{\mathbf{x}}[\boldsymbol{\eta}] : [\mathbb{I}_{dev}\tilde{\tau} + pJ\mathbf{1}] d\Omega_0 = P_{ext}(\boldsymbol{\eta}) \quad (\text{IV.2.35})$$

$$\int_{\Omega_0} \delta\theta \left[ \frac{\tilde{\tau} : \mathbf{1}}{3\theta} - p \right] d\Omega_0 = 0 \quad (\text{IV.2.36})$$

$$\int_{\Omega_0} \delta p (J - \theta) d\Omega_0 = 0. \quad (\text{IV.2.37})$$

$\mathbb{I}_{dev}$  is the rank four deviatoric projection tensor defined by  $\mathbb{I}_{dev}\mathbf{t} := \mathbf{t} - \frac{1}{3}\text{trace}(\mathbf{t})\mathbf{1}$  for any rank two tensor  $\mathbf{t}$ , not necessarily symmetric.  $\tilde{\tau}$  is the Kirchhoff stress, computed as a function of

$$\tilde{\mathbf{F}}(\mathbf{u}_\psi, \mathbf{u}_\chi, \theta) := \left( \frac{\theta}{J(\mathbf{u}_\psi, \mathbf{u}_\chi)} \right)^{\frac{1}{3}} \mathbf{F}(\mathbf{u}_\psi, \mathbf{u}_\chi). \quad (\text{IV.2.38})$$

$P_{ext}$  represents external loading.

**Remark IV.2.2** Within the context of finite strain elasticity, the above equations can be viewed as the variation of an energy functional. Assume that the external loading on the body may be characterized by a potential function  $\Pi_{ext}$ . Let  $W(\mathbf{F})$  be the isothermal free energy function defining the elastic response of the material. Proceeding, define the potential energy for the problem as

$$\Pi(\mathbf{u}_\psi, \mathbf{u}_\chi, \theta, p) = \int_{\Omega_0} [W(\tilde{\mathbf{F}}) + p(J - \theta)] d\Omega_0 + \Pi_{ext}. \quad (\text{IV.2.39})$$

This three field expression can be found in SIMO, TAYLOR & PISTER [1985], and has been discussed more recently in SIMO & TAYLOR [1991]. A computation of the first variation of the above generates the system of three equations stated above.  $\square$

#### IV.2.6. Multiplicative plasticity

The goal here is to introduce a formulation for isotropic plasticity at finite strains within a three-dimensional context. The discussion follows very closely the presentations in SIMO & MIEHE [1992] and SIMO [1992]. Also, many of the standard and well known results concerning isotropic tensors and isotropic tensor functions can be found in the appendix of GURTIN [1981].

Let  $\mathcal{E}$  be the isothermal elastic domain, defined in the spatial configuration of the body as

$$\mathcal{E} := \{(\boldsymbol{\tau}, q) \in \mathbb{R}^7 : \phi(\boldsymbol{\tau}, q) \leq 0\} \quad (\text{IV.2.40})$$

where  $\boldsymbol{\tau}$  is the Kirchhoff stress and  $q$  is a scalar stress-like isotropic hardening variable. The scalar valued function  $\phi$ , assumed convex, is commonly referred to as the yield function. The principle of invariance under superposed rigid body motion restricts  $\phi$  to be a isotropic function of  $\boldsymbol{\tau}$ . Invariance requires that

$$\phi(\mathbf{Q}\boldsymbol{\tau}\mathbf{Q}^T, q) = \phi(\boldsymbol{\tau}, q) \quad \forall \mathbf{Q} \in \text{SO}(3). \quad (\text{IV.2.41})$$

We decompose the deformation gradient into elastic and plastic parts via the multiplicative split  $\mathbf{F} = \mathbf{F}^e \mathbf{F}^p$ . For subsequent developments, define two strain measures

$$\mathbf{G}^p := [\mathbf{F}^{p^T} \mathbf{F}^p]^{-1} \quad (\text{IV.2.42})$$

and

$$\mathbf{b}^e := \mathbf{F}^e \mathbf{F}^{e^T}. \quad (\text{IV.2.43})$$

The relationship

$$\mathbf{b}^e = \mathbf{F} \mathbf{G}^p \mathbf{F}^T \quad (\text{IV.2.44})$$

will prove useful for later developments. Set

$$J^p := \det[\mathbf{F}^p] = (\det[\mathbf{G}^p])^{1/2} \quad (\text{IV.2.45})$$

and

$$J^e := \det[\mathbf{F}^e] = (\det[\mathbf{b}^e])^{1/2} \quad (\text{IV.2.46})$$

so that  $J = J^e J^p$ . Finally, time differentiation of (IV.2.44) gives

$$\dot{\mathbf{b}}^e = \mathbf{l}\mathbf{b}^e + \mathbf{b}^e \mathbf{l}^T + \mathbf{f}_v \mathbf{b}^e \quad (\text{IV.2.47})$$

where  $\mathbf{l} := \dot{\mathbf{F}} \mathbf{F}^{-1}$  is the spatial velocity gradient and  $\mathbf{f}_v \mathbf{b}^e := \mathbf{F} \dot{\mathbf{G}}^p \mathbf{F}^T$  is called the Lie Derivative of the elastic left Cauchy-Green tensor  $\mathbf{b}^e$ .

Additionally, and consistent with the assumption of isotropy, we assume the existence of an isothermal free energy function  $W(\mathbf{b}^e, \xi)$ , where  $\xi$  is a scalar strain-like isotropic

hardening variable. The function  $W$  is often referred to as the strain energy density function. This function must also satisfy the invariance requirement

$$W(\mathbf{Q} \mathbf{b}^e \mathbf{Q}^T, \xi) = W(\mathbf{b}^e, \xi) \quad \forall \mathbf{Q} \in \text{SO}(3). \quad (\text{IV.2.48})$$

The equations for this general plasticity model take the form :

1. Hyperelastic response defined by free energy function

$$\boldsymbol{\tau} := 2 \frac{\partial W}{\partial \mathbf{b}^e} \mathbf{b}^e$$

2. Associative Evolution Equations :

$$\begin{aligned} -\frac{1}{2} \mathbf{f}_v \mathbf{b}^e := \gamma \frac{\partial \phi}{\partial \boldsymbol{\tau}} \mathbf{b}^e &\iff \dot{\mathbf{G}}^p = -2\lambda \left( \mathbf{F}^{-1} \left[ \frac{\partial \phi}{\partial \boldsymbol{\tau}} \right] \mathbf{F} \right) \mathbf{G}^p \\ \dot{\xi} := \lambda \frac{\partial \phi}{\partial q} \end{aligned}$$

3. Kuhn-Tucker Conditions

$$\lambda \geq 0 \quad \phi(\boldsymbol{\tau}, q) \leq 0 \quad \lambda \phi(\boldsymbol{\tau}, q) = 0.$$

where  $\lambda$  is the consistency parameter.

The previous flow equations have an alternative form within the ALE context. Using equation (IV.2.20), the flow rule for  $\mathbf{G}^p$  may be rewritten as

$$\left. \frac{\partial \mathbf{G}^p}{\partial t} \right|_{\mathbf{m}} - \text{GRAD}_{\mathbf{m}} [\mathbf{G}^p] \cdot \mathbf{F} \chi^{-1} \left. \frac{\partial \mathbf{X}}{\partial t} \right|_{\mathbf{m}} = -2\lambda \left( \mathbf{F}^{-1} \left[ \frac{\partial \phi}{\partial \boldsymbol{\tau}} \right] \mathbf{F} \right) \mathbf{G}^p \quad (\text{IV.2.49})$$

The hardening law for  $\xi$  has a similar form.

**Remark IV.2.3** An important property to note concerning the flow rule is that for pressure insensitive yield criterion, the plastic volume  $J^p$  is conserved. This is shown simply as follows.

$$\begin{aligned} J^e \dot{J}^p &= \dot{\mathbf{j}} - J^p \dot{\mathbf{j}}^e \\ &= J \text{trace}[\mathbf{d}] - \frac{1}{2} J^p J^e \mathbf{b}^{e-1} : \dot{\mathbf{b}}^e \\ &= J \text{trace}[\mathbf{d}] - \frac{1}{2} J \mathbf{b}^{e-1} : (\mathbf{l} \mathbf{b}^e + \mathbf{b}^e \mathbf{l} + \mathbf{f}_v \mathbf{b}^e) \\ &= J \text{trace}[\mathbf{d}] - J \text{trace}[\mathbf{d}] - J \frac{1}{2} \mathbf{f}_v \mathbf{b}^e : \mathbf{b}^{e-1} \\ &= J \lambda \left[ \frac{\partial \phi}{\partial \boldsymbol{\tau}} \right] \mathbf{b}^e : \mathbf{b}^{e-1} \\ &= J \lambda \text{trace} \left[ \frac{\partial \phi}{\partial \boldsymbol{\tau}} \right] \\ &= 0 \end{aligned} \quad (\text{IV.2.50})$$

assuming that the normal to the yield surface is traceless. This will be the case for the classical von Mises yield criterion based on the deviatoric part of the Kirchhoff stress tensor. This also implies that  $\det[\mathbf{G}^p] = 0$  and thus  $\det[\mathbf{G}^p] = 1$ .

### IV.3. A Staggered Approach to the ALE Problem

We develop in this section a staggered method for the solution of the ALE equations, involving a separate solution of the material and spatial deformation mapping. This strategy is especially convenient for the treatment of the advection of internal variables in the context of elastoplasticity, leading to computationally attractive methods. Section IV.5 includes also purely elastic numerical examples treated with a fully coupled solution of the material  $\chi$  and spatial  $\psi$  deformation mappings. The absence of any advection of internal variables simplifies considerably the problem.

#### IV.3.1. The discrete equations

The continuum equations summarized in the previous section are discretized in space and time using standard techniques in the context of the finite element method. Appendix IV.2 summarizes the mixed finite element implementation considered in this work.

The temporal discretization considered corresponds to the standard Newmark formulas, in terms of the algorithmic parameters  $\gamma$  and  $\beta$ ,

$$\left. \begin{aligned} \mathbf{M}\mathbf{a}(\mathbf{X}, t_{n+1}) + \mathbf{f}_{int}(\mathbf{x}(\mathbf{X}, t_{n+1})) &= \mathbf{f}_{ext_{n+1}} \\ \mathbf{x}(\mathbf{X}, t_{n+1}) &= \mathbf{x}(\mathbf{X}, t_n) + \Delta t \mathbf{v}(\mathbf{X}, t_{n+1}) + \frac{1}{2} \Delta t^2 (2\beta \mathbf{a}(\mathbf{X}, t_{n+1}) + (1 - 2\beta) \mathbf{a}(\mathbf{X}, t_n)) \\ \mathbf{v}(\mathbf{X}, t_{n+1}) &= \mathbf{v}(\mathbf{X}, t_n) + \Delta t (\gamma \mathbf{a}(\mathbf{X}, t_{n+1}) + (1 - \gamma) \mathbf{a}(\mathbf{X}, t_n)) \end{aligned} \right\} \quad (\text{IV.3.1})$$

for the material acceleration  $\mathbf{a}(\mathbf{X}, t)$  and velocity  $\mathbf{v}(\mathbf{X}, t)$  fields, and the spatial position  $\mathbf{x}(\mathbf{X}, t) = \psi(\mathbf{X}, t)$ . The nodal internal and external forces, corresponding to the two terms in the right-hand side of (IV.2.23) have been denoted  $\mathbf{f}_{int}$  and  $\mathbf{f}_{ext}$ , respectively, with  $\mathbf{M}$  referring to the mass matrix of the assumed finite element interpolation. A typical time step  $[t_n, t_{n+1}]$  has been considered. The dependence on the material particle  $\mathbf{X}$  has been indicated in these expressions to emphasize its constancy, reflecting their nature as material time derivatives. Therefore, the different fields at  $t_n$  and  $t_{n+1}$  correspond to different mesh points in the ALE context, requiring then their advection as the following sections.

#### IV.3.2. The global approach

The global approach can be easily outlined as follows. Assume that all variables are known at time step  $n$ . This includes the positions  $\mathbf{X}_n$  and  $\mathbf{x}_n$ , the mixed fields  $p_n$  and

$\theta_n$  and the internal variables  $G_n^p$  and  $\xi_n$ . The solution strategy proceeds in the following steps :

1. Perform a chosen number of pure Lagrangian steps. Hold  $u_\chi$  fixed and solve for  $u_\psi$ ,  $p$  and  $\theta$ . For an associative flow rule model of plasticity, such as the one considered herein, the tangent matrix for this step is *symmetric*.
2. Perform mesh smoothing and advection :
  - 2a. Hold  $u_\psi$  fixed. Choose  $u_\chi$  to minimize mesh distortion. This will define  $X_{n+1}$ . This step is discussed in Section (IV.3.3).
  - 2b. Having defined  $X_{n+1}$ , advect plastic variables to define the new trial state, and the spatial positions, velocities and accelerations appearing in (IV.3.1) for the dynamic case. This step is discussed in Section (IV.4).
  - 2c. Hold  $u_\chi$  fixed. Having determined the new trial state, solve for  $u_\psi$ ,  $p$  and  $\theta$ . This is an equilibrium correction which is necessary since we have changed  $u_\chi$ .
3. Return to Step 1.

A discussion of the strategies for mesh smoothing and plastic variable advection is presented next.

### Remarks IV.3.1.

1. The above approach is also applicable to finite strain elasticity. In such a case, simply omit step 2(b) above for the plastic variables.
2. It may not be necessary to perform step 2c. One may simply skip to step 3 and carry any unbalanced forces on to the next load step.  $\square$

### IV.3.3. Mesh distortion measures

The first objective is to measure the distortion of the spatial mesh. To this purpose, define

$$\bar{\mathbf{F}}_\psi := J_\psi^{-1/3} \mathbf{F}_\psi. \quad (\text{IV.3.2})$$

Let

$$\bar{\mathbf{b}}_\psi := \bar{\mathbf{F}}_\psi \bar{\mathbf{F}}_\psi^T \quad \text{and} \quad \bar{\mathbf{C}}_\psi := \bar{\mathbf{F}}_\psi^T \bar{\mathbf{F}}_\psi. \quad (\text{IV.3.3})$$

Both ODDY, GOLDAK & BIBBY [1988] and SARRATE [1996] have suggested using

$$W_d(\mathbf{F}_\psi) := \|\operatorname{dev} \bar{\mathbf{b}}_\psi\|^2 = \|\operatorname{dev} \bar{\mathbf{C}}_\psi\|^2 = \bar{\mathbf{b}}_\psi : \operatorname{dev} \bar{\mathbf{b}}_\psi \quad (\text{IV.3.4})$$

as a measure of mesh distortion, where  $\text{dev}[\cdot] := [\cdot] - 1/3(\text{trace}[\cdot])\mathbf{1}$ . Note that  $W_d$  as defined is simply an example of a properly invariant stored energy function. In fact, one could use this function to determine the stress response for a finitely elastic material.

With this fact in mind, any properly invariant scalar energy function can be used to measure mesh distortion. The only requirement would be that the function be independent of volumetric distortion. Purely volumetric deformation is not a factor in element distortion. Thus the requirement on the function  $W_d$  is that

$$W_d(\mathbf{A}) = W_d(\lambda \mathbf{A}) \quad \forall \lambda > 0 \quad \forall \mathbf{A} \text{ such that } \det(\mathbf{A}) > 0. \quad (\text{IV.3.5})$$

Any invariant function  $W_d$  which depends only on  $\bar{\mathbf{F}}_\psi$  is an admissible choice.

**Remark IV.3.2** It is possible to choose, for example, a Neo-Hookean or Mooney-Rivlin response function. Another possible choice is a logarithmic stretch model of elasticity such as the one used in our  $J_2$  model of plasticity. In these cases, we would simply set the volumetric energy parameter to zero.  $\square$

#### IV.3.4. Mesh smoothing (determination of $\chi$ )

We discuss in this section the implementation of step 2a above. This involves choosing  $\mathbf{u}_\chi$  so as to minimize spatial mesh distortion as defined by a scalar energy function  $W_d$ . Assume step 1 above has been performed. We now have a spatial mesh distortion  $\bar{\mathbf{F}}_\psi$ , a material remap  $\mathbf{F}_\chi$  and most importantly the physical deformation  $\mathbf{F} := \bar{\mathbf{F}}_\psi \mathbf{F}_\chi^{-1}$ . Note that

$$\bar{\mathbf{F}}_\psi = \mathbf{F} \mathbf{F}_\chi. \quad (\text{IV.3.6})$$

Now, holding  $\mathbf{F}$  fixed, minimize

$$\Pi_d(\mathbf{F}_\chi) := \int_{\mathcal{M}} W_d(\mathbf{F} \mathbf{F}_\chi) d\mathcal{M}. \quad (\text{IV.3.7})$$

The minimization of this functional requires the determination of  $\mathbf{u}_\chi$ .

We define

$$\tau_\psi := \left. \frac{\partial W_d}{\partial \bar{\mathbf{F}}_\psi} \bar{\mathbf{F}}_\psi^T \right|_{\bar{\mathbf{F}}_\psi = \mathbf{F} \mathbf{F}_\chi} \quad (\text{IV.3.8})$$

The first variation ( weak form ) of equation (IV.3.7) is

$$\delta \Pi_d = \int_{\mathcal{M}} \mathbf{F}^T \tau_\psi : \text{grad}_{\mathbf{x}} \boldsymbol{\eta} d\mathcal{M} = 0 \quad (\text{IV.3.9})$$

where  $\boldsymbol{\eta}$  is a kinematically admissible virtual material remap displacement field defined on  $\mathcal{M}$ .

#### IV.4. An Advection Method Based on Particle Tracking

We discuss in this section a procedure for the advection of the internal variables due to the material motion. To this purpose, we first rewrite in Section IV.4.1 the problem in the classical form of the pure advection equation. Section IV.4.2 summarizes some general properties of this equation as well as its numerical treatment through the classical method of characteristics; see PIRONNEAU [1989], page 75, for details. The availability of the actual material mapping in our case of interest identifies a related but much simpler approach to the integration of the advection step. These ideas are developed in Section IV.4.3.

##### IV.4.1. Plastic variable advection

Consider the plastic internal variable  $\mathbf{G}^p$ . Noting equation (IV.2.49), the evolution equation for  $\mathbf{G}^p$  is

$$\frac{\partial \mathbf{G}^p}{\partial t} \Big|_{\mathbf{m}} - \text{GRAD}_{\mathbf{m}} [\mathbf{G}^p] \cdot \mathbf{F}_\chi^{-1} \frac{\partial \mathbf{X}}{\partial t} \Big|_{\mathbf{m}} = -2\lambda \left( \mathbf{F}^{-1} \left[ \frac{\partial \phi}{\partial \tau} \right] \mathbf{F} \right) \mathbf{G}^p \quad (\text{IV.4.1})$$

During the advection step, one must transport  $\mathbf{G}^p$  by solving the above with zero right hand side ( $\lambda = 0$ ). More precisely, the advection equation to be solved is

$$\frac{\partial \mathbf{G}^p}{\partial t} \Big|_{\mathbf{m}} - \text{GRAD}_{\mathbf{m}} [\mathbf{G}^p] \cdot \mathbf{F}_\chi^{-1} \frac{\partial \mathbf{X}}{\partial t} \Big|_{\mathbf{m}} = 0. \quad (\text{IV.4.2})$$

The same equation is used to determine advected values of  $\xi$  and any other internal variables. Define

$$\mathbf{a} := -\mathbf{F}_\chi^{-1} \frac{\partial \mathbf{X}}{\partial t} \Big|_{\mathbf{m}}. \quad (\text{IV.4.3})$$

With this notation, equation (IV.4.2) reads

$$\frac{\partial \mathbf{G}^p}{\partial t} \Big|_{\mathbf{m}} + \mathbf{a} \cdot \text{GRAD}_{\mathbf{m}} [\mathbf{G}^p] = 0, \quad (\text{IV.4.4})$$

corresponding to the pure advection equation. We discuss next a general treatment of this equation.

##### IV.4.2. The pure advection equation

The considerations in the previous section led to the consideration of the equation

$$\frac{d}{dt} \phi(\mathbf{m}, t) + \mathbf{a}(\mathbf{m}, t) \cdot \text{GRAD}_{\mathbf{m}} \phi(\mathbf{m}, t) = 0 \quad (\text{IV.4.5})$$

on the fixed domain  $\mathcal{M}$  during the plastic variable advection step. The variable  $\phi$  may represent the components of the plastic strain  $\mathbf{G}^p$ , for example. In the above,  $t$  is time,  $\mathbf{a}$  is the advection velocity and  $\text{GRAD}_{\mathbf{m}}$  is the standard gradient operator. Let  $\mathbf{X}(\tau)$ , with  $\tau$  a scalar time-like variable, be the solution of

$$\frac{d}{d\tau} \mathbf{X}(\tau) = \mathbf{a}(\mathbf{X}(\tau), \tau) \quad (\text{IV.4.6})$$

subject to the condition  $\mathbf{X}(t) = \mathbf{m}$ . Given that  $\mathbf{a}$  is the velocity of the material particles,  $\mathbf{X}$  is the trajectory of the material particle that passes  $\mathbf{m}$  at time  $t$ . Since  $\mathbf{X}$  depends on the parameters  $\mathbf{m}$  and  $t$ , we denote the solution by  $\mathbf{X}(\mathbf{m}, t; \tau)$ . This solution is often referred to as the “characteristic” of the hyperbolic equation (IV.4.5).

The important result of the above can be obtained by application of the chain rule :

$$\left. \frac{d}{d\tau} \phi(\mathbf{X}(\mathbf{m}, t; \tau), \tau) \right|_{t=\tau} = \frac{d}{dt} \phi(\mathbf{m}, t) + \mathbf{a} \cdot \text{GRAD}_{\mathbf{m}} \phi(\mathbf{m}, t). \quad (\text{IV.4.7})$$

Then equation (IV.4.5) can be written

$$\frac{d}{d\tau} \phi = 0 \quad (\text{IV.4.8})$$

when defined on the domain  $\Omega_0$  of material particles  $\mathbf{X}$  as defined by the mapping of equation (IV.4.6). The physical interpretation of this is simple :  $\phi$  is temporally constant along the path of a given material particle  $\mathbf{X}$ . In other words,  $\phi$  is transported along the “characteristics”  $\mathbf{X}$  of the advection equation. If it is possible to track the material particles  $\mathbf{X}$ , this will lead easily to determining advected values of  $\phi$ .

#### Remarks IV.4.1.

1. As indicated in Section IV.3.1, the velocity and acceleration fields require also to be advected in the dynamic case. The above development apply to these cases with  $\phi(\cdot)$  denoting each component of these fields. To this purpose, the nodal values are considered, that is,  $\mathbf{m}$  refers to a node in this case, with the corresponding nodal values of these fields defining their conforming interpolations.
2. Recall that  $\mathbf{X}$  is actually given by the material remap  $\chi$ , and that the velocity  $\mathbf{a}$  is actually computed from  $\mathbf{X}$ , rather than converse which equation (IV.4.6) implies. In our case,  $\mathbf{a}$  is defined by (IV.4.3). Nevertheless, the previous arguments are still valid.  
□

#### IV.4.3. Numerical particle tracking

One approach to solving equation (IV.4.5) numerically is the Euler scheme

$$\phi(\mathbf{m}, t + \Delta t) = \phi(\tilde{\mathbf{m}}, t) \quad (\text{IV.4.9})$$

where

$$\tilde{\mathbf{m}} := \mathbf{m} - \mathbf{a}(\mathbf{m}, t + \Delta t) \Delta t. \quad (\text{IV.4.10})$$

In the above,  $t$  denotes time as before and  $\Delta t$  is the numerical time step. This is a *backward* particle tracking technique. Higher order accurate approaches are also available. The above technique is reviewed on pp.84-90 of PIRONNEAU [1989]. This method is obviously not exact. The backward tracked particle locations  $\tilde{\mathbf{m}}$  are only approximate unless  $\mathbf{a}$  is spatially and temporarily constant. In our case, this approach can be written as

$$\tilde{\mathbf{m}} = \mathbf{m} + \mathbf{F}_{\chi}^{-1}(\mathbf{m}, t) \Delta \mathbf{u}_{\chi} \quad (\text{IV.4.11})$$

where  $\Delta \mathbf{u}_{\chi}$  is the displacement increment to the material position  $\mathbf{X}$  (see Appendix IV.2.1).

We shall not use the Euler scheme just presented. We are already *tracking particles exactly*. The finite element displacement field  $\mathbf{u}_{\chi}$  is exactly the motion of the material particles  $\mathbf{X}$  relative to the fixed mesh coordinates  $\mathbf{m}$ . Thus the chosen advection technique is to solve for  $\tilde{\mathbf{m}}$  by solving the material particle tracking equation

$$\mathbf{X}(\tilde{\mathbf{m}}, t) = \mathbf{X}(\mathbf{m}, t + \Delta t) \quad (\text{IV.4.12})$$

where  $\mathbf{X}$  is the material particle locations in  $\Omega_0$ . This equation can be rewritten (see Appendix IV.2.1)

$$\boxed{\tilde{\mathbf{m}} + \mathbf{u}_{\chi}(\tilde{\mathbf{m}}, t + \Delta t) = \mathbf{m} + \mathbf{u}_{\chi}(\mathbf{m}, t).} \quad (\text{IV.4.13})$$

Having determined  $\tilde{\mathbf{m}}$ , the advected scalar field may be computed by

$$\phi_{\text{advected}}(\tilde{\mathbf{m}}) = \phi_{\text{unadvected}}(\mathbf{m}). \quad (\text{IV.4.14})$$

This must be done at each quadrature point  $\mathbf{m}$  of the mesh after the smoothing step has determined new values of  $\Delta \mathbf{u}_{\chi}$ .

Equation (IV.4.13) is non-linear. There exist at least two possible ways to solve it. The first is a simple fixed point iteration. To this purpose, equation (IV.4.13) can be rearranged as

$$\tilde{\mathbf{m}} = \mathbf{m} + \mathbf{u}_{\chi}(\mathbf{m}, t) - \mathbf{u}_{\chi}(\tilde{\mathbf{m}}, t + \Delta t). \quad (\text{IV.4.15})$$

The above equation is now in the form of a fixed point iteration for  $\tilde{\mathbf{m}}$ . Alternatively, one can use Newton's method to solve the residual equation

$$\mathbf{r}(\tilde{\mathbf{m}}) := [\tilde{\mathbf{m}} + \mathbf{u}_{\chi}(\tilde{\mathbf{m}}, t + \Delta t)] - [\mathbf{m} + \mathbf{u}_{\chi}(\mathbf{m}, t)] = 0, \quad (\text{IV.4.16})$$

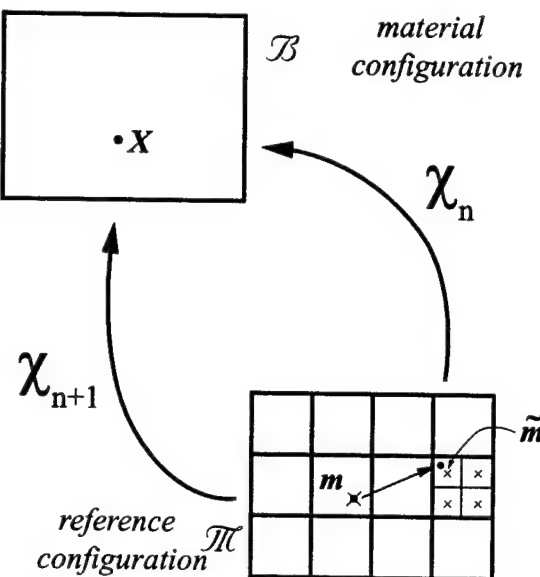


**FIGURE IV.4.1** Particle tracking. Computation of  $\tilde{m}$

a rearrangement again of (IV.4.13). In this case, the tangent at each Newton step is given by

$$\frac{\partial r}{\partial \tilde{m}} = \mathbf{I} + \left. \frac{\partial u_\chi(m, t + \Delta t)}{\partial m} \right|_{m=\tilde{m}} = F_\chi(\tilde{m}, t + \Delta t). \quad (\text{IV.4.17})$$

In principle, the convergence of the fixed point iteration is only linear. The convergence of Newton's method is quadratic. In all of the numerical simulations, Newton's method is used. No problems have been noticed in the convergence of this approach.

#### IV.4.4. Additional practical considerations

One issue is how to determine which element contains the new point  $\tilde{m}$ . This determination must be performed at every Newton step until convergence is achieved. Given that each element is a convex set (otherwise negative Jacobians are detected), the inside/outside check is not difficult. Simply check the components of the new point with respect to a tangent/normal coordinate system originating at the midpoint of each element side. The normal component must be negative for the point to be inside the element. See Figure IV.4.2.

The issue of the order in which to check the elements is more important. One could simply loop over all the elements starting from element one, performing the inside/outside check for each element. This “bucket search” is clearly inefficient. The most probable situation is one in which the new point  $\tilde{m}$  is inside an element which is geometrically close

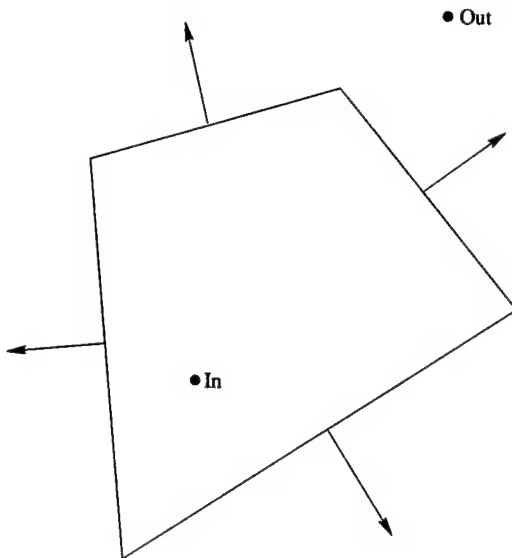


**FIGURE IV.4.2** Quadrilateral finite element as a convex set

to the original element containing the quadrature point at position  $\mathbf{m}$ . With this in mind, we have chosen to determine the order for checking by using a *breadth first search of the element connectivity graph*.

A third issue is that of local interpolation for the plastic internal variables. In all probability, the new point  $\tilde{\mathbf{m}}$  will not be a quadrature point. Thus it is necessary to interpolate for the internal variables locally at the element level. We could of course project the quadrature point values onto a continuous interpolation defined by the natural coordinate basis functions  $\{1, L_1, L_2, L_1L_2\}$  defined on the parent domain  $[-1, 1] \times [-1, 1]$ . A discontinuous interpolation is also possible. Note that in each of the subdomains  $[-1, 0] \times [-1, 0]$ ,  $[0, 1] \times [-1, 0]$ ,  $[0, 1] \times [0, 1]$  and  $[-1, 0] \times [0, 1]$  there is one quadrature point. See figure (IV.4.3). Define the interpolation as constant over each of these subdomains, equal to the value at the quadrature point which the domain contains. Since the interpolation is locally constant the constraint  $\det \mathbf{G}^p = 1$  will be preserved.

Having defined an interpolation in terms on the natural coordinates of the element, we need to determine the natural coordinates of the point whose mesh coordinates are  $\tilde{\mathbf{m}}$ . Let  $\hat{\mathbf{m}}(L_1, L_2)$  represent the mapping from the domain  $[-1, 1] \times [-1, 1]$  to the physical domain of the element in question. The following problem needs to be solved : find  $(L_1, L_2)$  such that  $\hat{\mathbf{m}}(L_1, L_2) = \tilde{\mathbf{m}}$ . If the element is a parallelogram, this problem will be linear. In general it is non-linear. It can be solved using Newton's Method, a standard approach for non-linear problems. A reasonable initial guess for  $(L_1, L_2)$  is  $(0, 0)$ . LEE & BATHE [1994] have used Newton's method to solve this same problem, referring to it as the inverse isoparametric mapping technique.

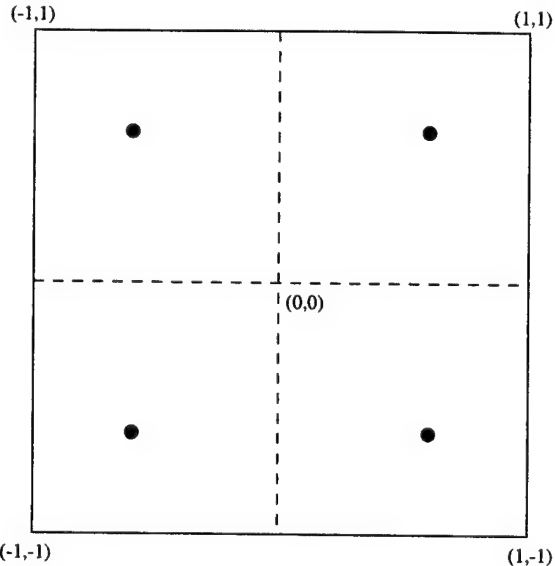


**FIGURE IV.4.3** Local Interpolation on Quadrilateral Element

**Remark IV.4.2** In the *absence of advection*, i.e.  $\Delta u_\chi = 0$ , this approach is *exact at the quadrature points*.  $\square$

## IV.5. Representative Numerical Simulations

In the following, the finite elasticity problems are performed using a fully coupled ALE solution strategy. Please see Appendix (IV.2) for more details. The plasticity calculations are performed using the staggered ALE approach just discussed. All simulations use the well known Q1/P0 four node quadrilateral element. ( bilinear displacements and constant mixed variables; see BREZZI & FORTIN [1990]).

### IV.5.1. Patch test

We perform a pure tension patch test in an axisymmetric setting. We consider a 3x3 square patch discretized with 4 finite elements. The material parameters chosen are  $c_1 = 1.5$ ,  $c_2 = 0.5$  and  $\kappa = 10^3$ . We perform five augmentations (see Appendix IV.2) per load step to enforce the incompressibility constraint. A total of 5 load steps is used to reach the final deformation shown in the figures. For a given node, there are four degrees of freedom. We have two displacements for  $\psi$  and two displacements for  $\chi$ . Let us order these  $(u_\psi)_1$ ,  $(u_\psi)_2$ ,  $(u_\chi)_1$  and  $(u_\chi)_2$ . At a given node, we can have no more than two active degrees of freedom.

**TABLE IV.5.1** Patch Test. Nodal constraints

| Node Number | $\Delta(u_\psi)_1$ | $\Delta(u_\psi)_2$ | $\Delta(u_\chi)_1$ | $\Delta(u_\chi)_2$ |
|-------------|--------------------|--------------------|--------------------|--------------------|
| 1           | fixed              | free               | fixed              | fixed              |
| 2           | free               | free               | fixed              | fixed              |
| 3           | fixed              | free               | fixed              | fixed              |
| 4           | fixed              | fixed              | fixed              | fixed              |
| 5           | fixed              | free               | free               | fixed              |
| 6           | fixed              | free               | fixed              | fixed              |
| 7           | fixed              | free               | fixed              | fixed              |
| 8           | free               | free               | fixed              | fixed              |
| 9           | fixed              | free               | fixed              | fixed              |

**TABLE IV.5.2** Patch Test. Nodal displacements

| Node Number | $\Delta(u_\psi)_1$ | $\Delta(u_\psi)_2$ | $\Delta(u_\chi)_1$ | $\Delta(u_\chi)_2$ |
|-------------|--------------------|--------------------|--------------------|--------------------|
| 1           | 0                  | -                  | 0                  | 0                  |
| 2           | -                  | -                  | -3/10              | 0                  |
| 3           | 3/10               | -                  | 0                  | 0                  |
| 4           | 0                  | 0                  | 0                  | 0                  |
| 5           | -3/20              | -                  | -                  | 3/20               |
| 6           | 3/10               | -                  | 0                  | -3/10              |
| 7           | 0                  | -                  | 0                  | 0                  |
| 8           | -                  | -                  | -3/10              | 0                  |
| 9           | 3/10               | -                  | 0                  | 0                  |

The nodal constraints for this problem are summarized in Table IV.5.1. Table IV.5.2 includes the imposed displacement increments proportionally per load step. All of these constraints are consistent with the boundary conditions discussed in the chapter on ALE continuum mechanics. In particular, by our choices we satisfy

$$\mathbf{u}_\chi \cdot \mathbf{N}_X = 0 \quad (\text{IV.5.1})$$

pointwise, which in this quasi-static setting is equivalent to the boundary condition

$$\left. \frac{\partial \mathbf{X}}{\partial t} \right|_m \cdot \mathbf{N}_X = 0 \quad (\text{IV.5.2})$$

discussed in a previous chapter.

Figure IV.5.1 shows the mesh motion relative to the reference domain. Figure IV.5.2 shows the material remap relative to the reference domain. We note that the stresses,

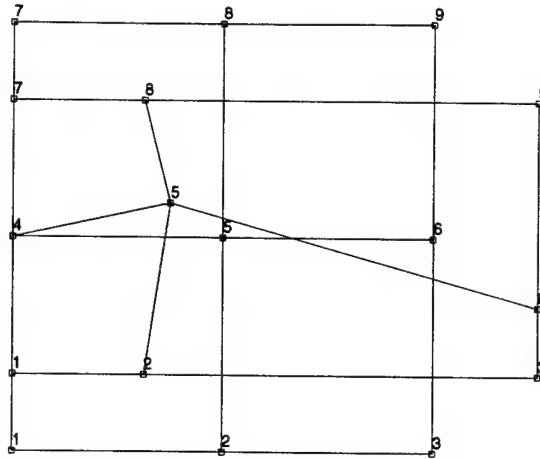


**FIGURE IV.5.1** Mesh motion  $u_\psi$  and reference domain

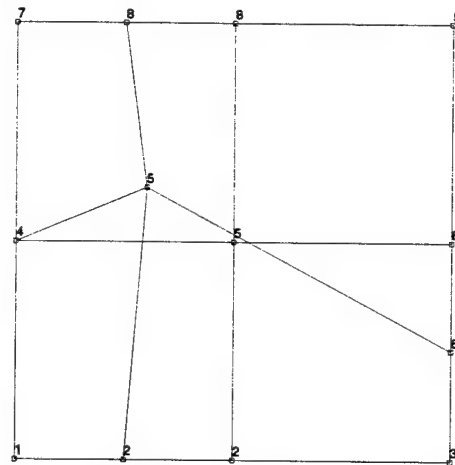


**FIGURE IV.5.2** Material remap  $u_\chi$  and reference domain

although not shown here, are constant and match pure Lagrangian calculations. Thus the formulation passes this patch test.

#### IV.5.2. Indentation of an elastic block

Now consider the indentation of an elastic block in an axisymmetric setting. YAMADA & KIKUCHI [1993] consider a very similar problem in a plane strain setting. Consider a  $2 \times 1$  block discretized with  $32 \times 16$  Q1/P0 finite elements. Our material parameters are  $c_1 = 1.5$ ,  $c_2 = 0.5$  and  $\kappa = 10^4$ . We shall prescribe negative nodal displacements on the left half of

**TABLE IV.5.3** Indentation of an elastic block. Interior nodal conditions

| $(u_\psi)_1$ | $(u_\psi)_2$ | $(u_\chi)_1$ | $(u_\chi)_2$ |
|--------------|--------------|--------------|--------------|
| fixed        | free         | free         | fixed        |

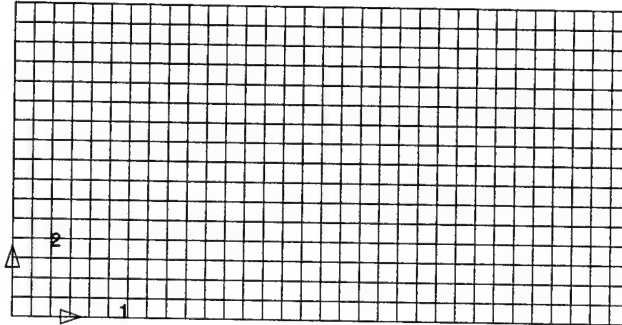


**FIGURE IV.5.3** Indentation of an elastic block. Reference domain

the upper face of the block. The nodal displacement increment per load step is  $-0.005$ . A total of 75 load steps are performed. For nodes in the interior of the domain, we prescribe

On the bottom boundary we prescribe  $(u_\psi)_1 = 0$ ,  $(u_\psi)_2$  free,  $(u_\chi)_1 = 0$  and  $(u_\chi)_2 = 0$ . On the left side boundary, we prescribe  $(u_\psi)_1 = 0$ ,  $(u_\psi)_2$  free,  $(u_\chi)_1 = 0$  and  $(u_\chi)_2 = 0$ . On the right side boundary, we prescribe  $(u_\psi)_1 = 0$ ,  $(u_\psi)_2$  free,  $(u_\chi)_1 = 0$  and  $(u_\chi)_2 = 0$ . On the left half of the upper face, we prescribe  $(u_\psi)_1 = 0$ ,  $(u_\psi)_2$  to be the negative nodal displacements discussed above,  $(u_\chi)_1 = 0$  and  $(u_\chi)_2 = 0$ . Finally, on the right half of the upper face, we prescribe  $(u_\psi)_1$  free,  $(u_\psi)_2$  free,  $(u_\chi)_1 = 0$  and  $(u_\chi)_2 = 0$ . All of these constraints are consistent with the boundary conditions discussed in the section on ALE continuum mechanics.

Figure IV.5.3 depicts the reference mesh. Figure IV.5.4 shows the mesh motion at final deformation. Figure IV.5.5 shows the material remap at final deformation. Included for reference purposes is a pure Lagrangian calculation of the same problem. However, the pure Lagrangian calculation did not converge at load step 63. The deformed mesh for the Lagrangian calculation after convergence at load step 62 is shown in Figure IV.5.6. We see, at least visually, that the results of the ALE calculation are similar to that of the pure Lagrangian calculation. In fact, in this case the element distortion of the ALE formulation appears to be less severe than that of the Lagrangian formulation, particularly in the neighborhood of the obvious singularity.

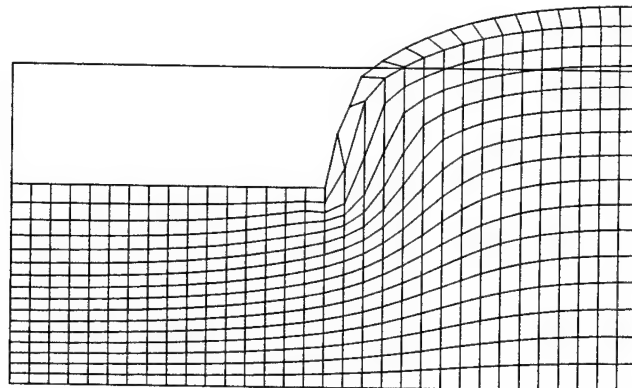


**FIGURE IV.5.4** Indentation of an elastic block. Mesh motion  $\mathbf{u}_\psi$

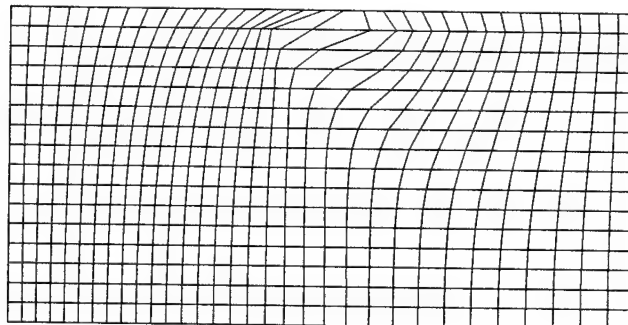


**FIGURE IV.5.5** Indentation of an elastic block. Material remap  $\mathbf{u}_x$

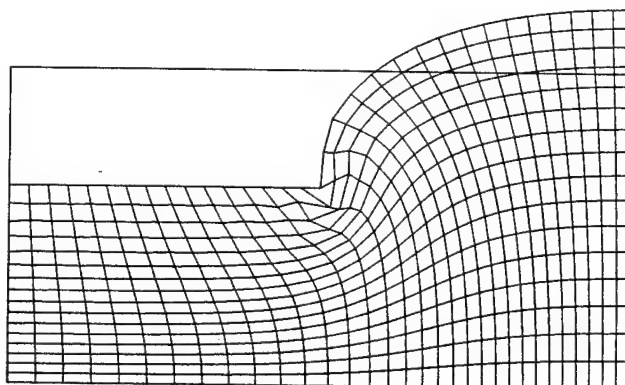


**FIGURE IV.5.6** Indentation of an elastic block. Pure Lagrangian approximation to indentation problem



**FIGURE IV.5.7** Necking problem. Deformed Lagrangian mesh.

#### IV.5.3. Necking of a circular bar

Consider the necking of a circular bar. This is the same problem as considered by SIMO [1988b]. Only 1/4 of the domain is discretized. The bar 53.334 in length. Thus the computational domain is 53.334/2 is length. The radius of the bar is 6.413. The material properties are as follows :  $K = 164.206$ ,  $\mu = 80.1938$ ,  $\sigma_0 = 0.450$ ,  $\sigma_\infty = 0.715$ ,  $\delta = 16.93$  and  $H = 0.12924$ . The radius of the bar is reduced to 0.995 of the original radius to introduce a defect and induce a necking response.

The bar (a quarter domain) is extended to a total elongation of 7. This is performed using fifty(50) proportional displacement increments. The final deformed mesh for the pure Lagrangian calculation is shown in Figure IV.5.7. For ease of visual interpretation, the entire domain is shown in the figure.

For the ALE calculation, smoothing has been performed during the first 45 time steps. The last 5 are pure Lagrangian. The material remap  $\chi$  is determined using a Mooney-Rivlin energy function with  $c_1/c_2 = 3$ . In this case, unlike those that follow,



**FIGURE IV.5.8** Necking problem. Deformed ALE mesh necking problem at elongation 7.0.

the determination of  $\chi$  is based only on  $F_{22}$ . In other words, the smoother performs calculations based the assumption that  $\mathbf{F}$  is of the form  $\mathbf{F} := \mathbf{I} + F_{22}\mathbf{e}_2 \otimes \mathbf{E}_2$ . Other components are not considered. The final deformed mesh for the ALE simulation is shown in Figure IV.5.8. The final material remap  $\chi$  is shown in Figure IV.5.9. Finally, the neck radius vs. elongation curve for both calculations is shown in figure IV.5.10).

#### IV.5.4. Plane strain tension test

Consider now the softening behavior of a tension strip in plane strain. The height/width ratio of the strip is three(3). The material properties are  $K = 164.206$ ,  $\mu = 80.1938$  and  $\sigma_0 = 0.450$  along with linear isotropic softening behavior. Forty-eight(48) proportional load steps are performed. For the ALE calculation, the material remap  $\chi$  is determined using a Mooney-Rivlin energy function with  $c_1/c_2 = 3$ . Smoothing is performed at every time step.

The final deformed meshes for the pure Lagrangian and the ALE simulations are shown in Figure IV.5.11. The final material remap  $\chi$  is shown in Figure IV.5.12. The distribution of the equivalent plastic strain is shown in Figure IV.5.13. Finally, the neck load vs. displacement curve for both calculations is shown in figure IV.5.14. The softer

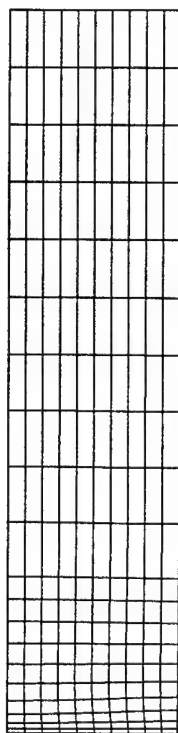


**FIGURE IV.5.9** Material Remap Necking Problem (1/4 domain)

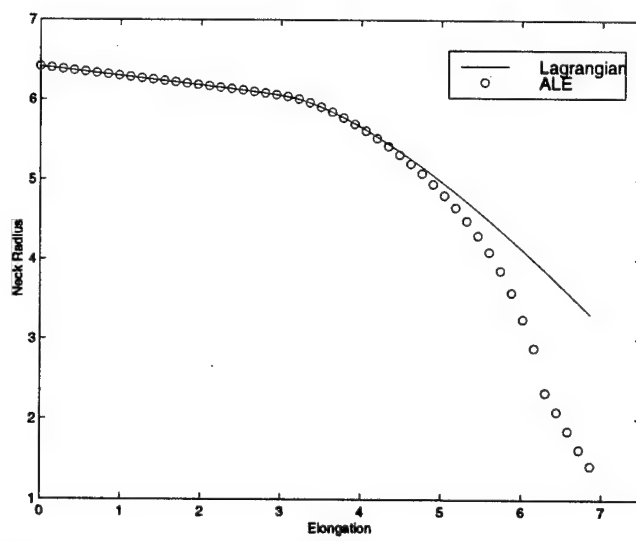


**FIGURE IV.5.10** Necking problem. Neck Radius vs. Elongation

response of the ALE solution is to be noted. We observe also the sharper localization of the plastic strain in the ALE solution, as it can be observed in the deformed boundary of the strip.

#### IV.5.5. Indentation of an elastoplastic block

Consider now the softening behavior of a compressed region in plane strain. The length/height ratio of the strip is two(2). The material properties are  $K = 164.206$ ,  $\mu = 80.1938$  and  $\sigma_0 = 0.450$  along with linear isotropic softening behavior. Twenty(20) proportional load steps are performed. For the ALE calculation, the material remap  $\chi$  is determined using a Mooney-Rivlin energy function with  $c_1/c_2 = 3$ . Smoothing is performed at every time step.

The final deformed mesh for the pure Lagrangian calculation is shown in Figure IV.5.15. The final deformed mesh for the ALE simulation is shown in Figure IV.5.16. The final material remap  $\chi$  is shown in Figure IV.5.17. Figure IV.5.18 depicts the distribution of the equivalent plastic strain for both solutions. Finally, the neck load vs. displacement curve for both calculations is shown in Figure IV.5.19. The softer response of the ALE solution is to be noted again, improving on the resolution of the shear band.

#### IV.5.6. Impact of a circular bar

We consider in this section the dynamic impact of a circular bar on a rigid frictionless wall. This is a commonly simulated test problem in the finite element literature and a standard benchmark problem for transient dynamic computer codes. The problem was originally studied both theoretically and experimentally by TAYLOR [1948], where a correlation was obtained between the initial velocity of the bar and its final length. This relationship depends critically upon the yield stress of the bar, leading to a useful method to determine experimentally the yield limit of the material under high strain-rate conditions. WILKINS & GUINAN [1973] extended this original work with further experiments and numerical simulations. In particular, they developed the improved relation

$$\frac{\rho_0 v_0^2}{2\sigma_{wg}} = \log \frac{l_0 - h}{l_f - h}, \quad (\text{IV.5.3})$$

where  $v_0$  is the initial velocity,  $l_0$  is the initial length and  $l_f$  is the final length. The parameter  $h$  is the mean position of the plastic front, which is assumed to be approximately  $h \approx 0.12l_0$ , independent of the material properties. Finally,  $\sigma_{wg}$  is the yield limit of the material under high strain-rate conditions. This stress parameter is correlated to fit the experimental and numerical work in WILKINS & GUINAN [1973].

Based on the experimental results reported in WILKINS & GUINAN [1973], we consider a bar of length  $l_0 = 32.4$  mm and a circular cross section of radius  $r_0 = 3.2$  mm. Two

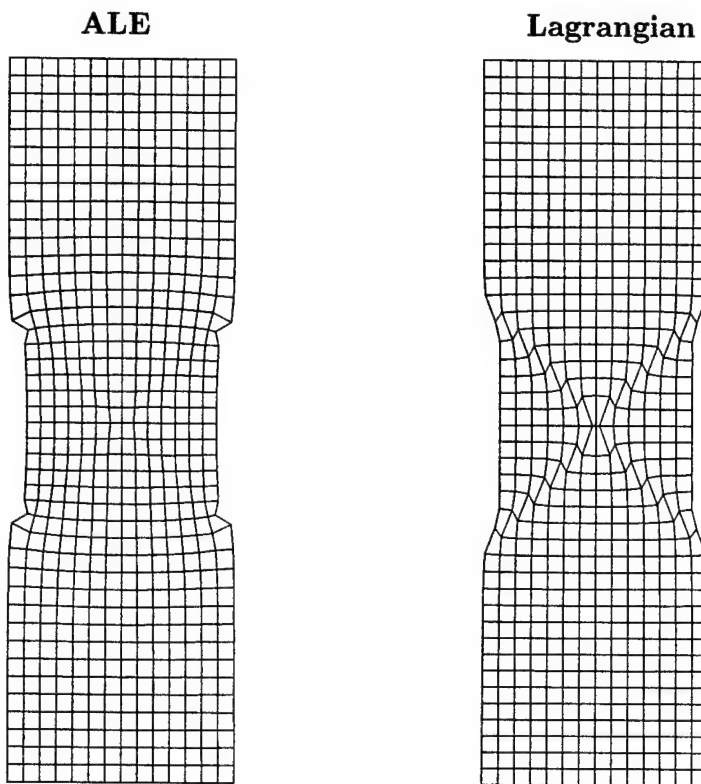


**FIGURE IV.5.11** Plane strain tension test. Deformations for the ALE and Lagrangian solutions.

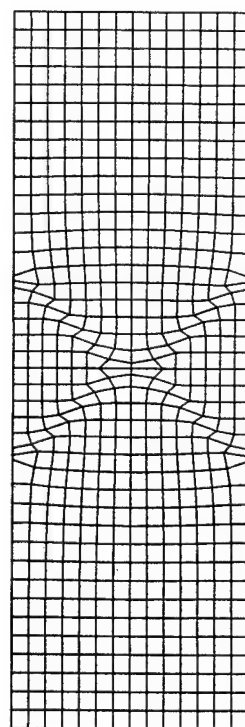


**FIGURE IV.5.12** Plane strain tension test. Material remap in the ALE solution.

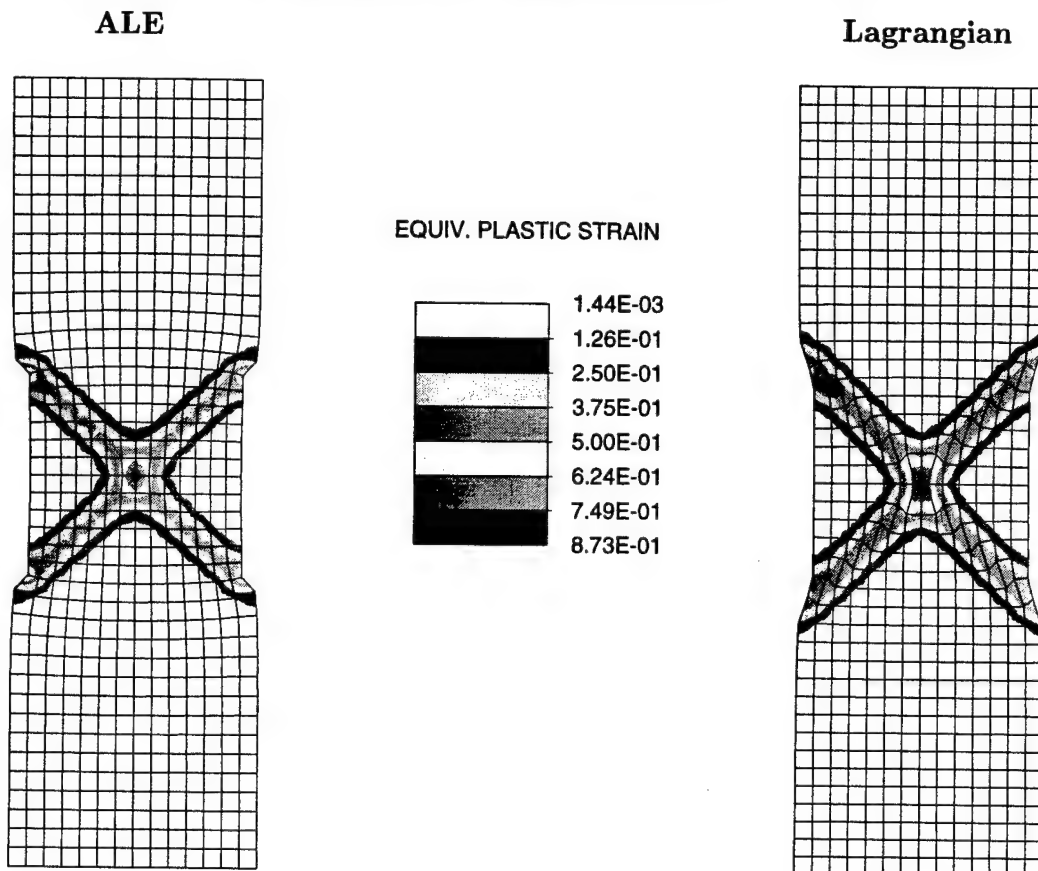


**FIGURE IV.5.13** Plane strain tension test. Distribution of the equivalent plastic strain for the Lagrangian and ALE solutions

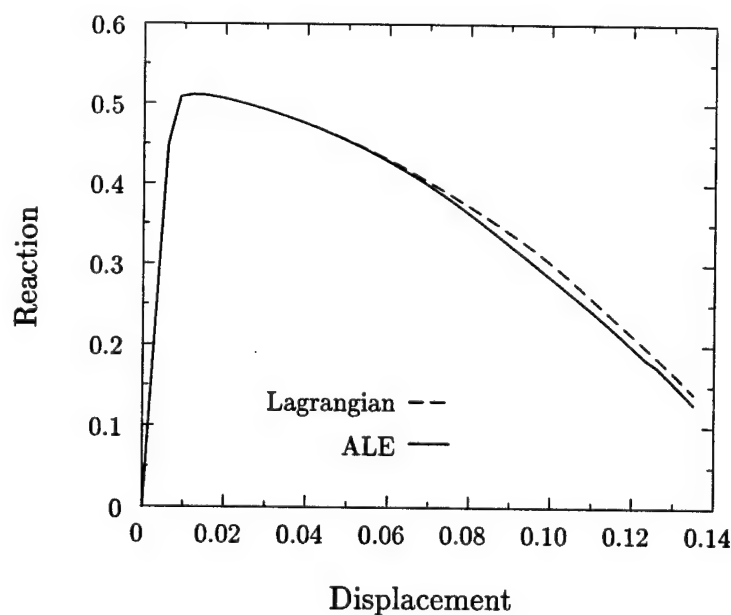


**FIGURE IV.5.14** Plane strain tension test. Load-displacement curve.

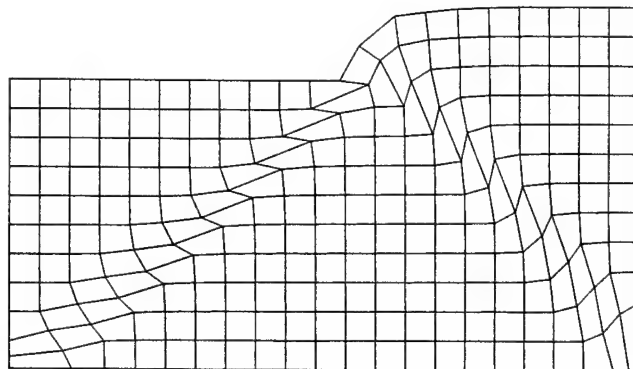


**FIGURE IV.5.15** Indentation of an elastoplastic block. Deformed Lagrangian mesh compression localization problem

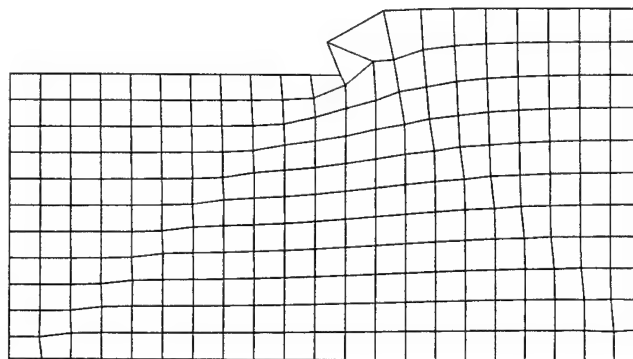


**FIGURE IV.5.16** Indentation of an elastoplastic block. Deformed ALE mesh compression localization problem

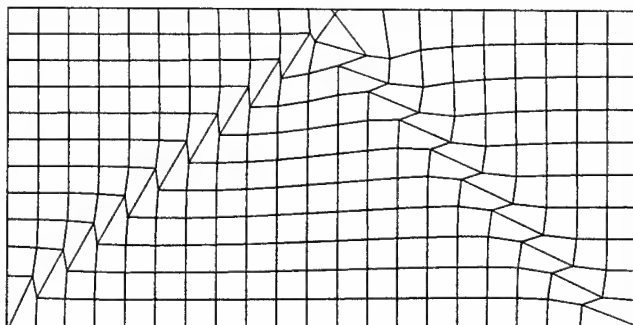
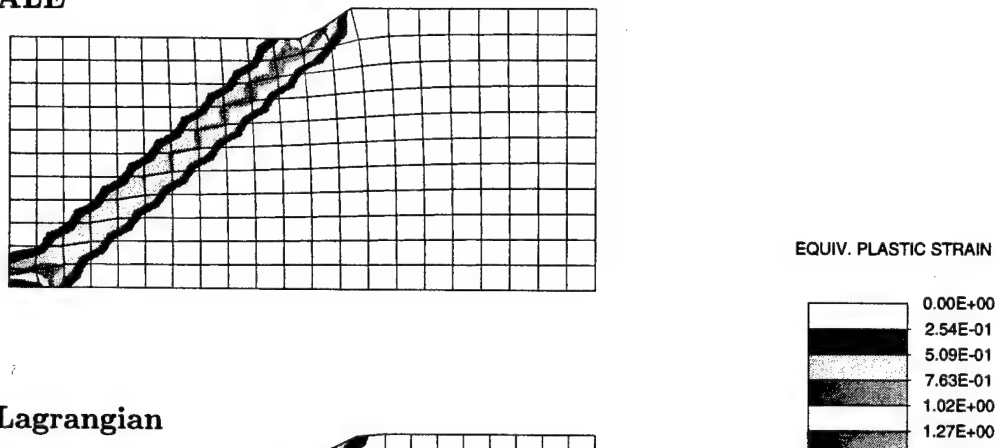


**FIGURE IV.5.17** Indentation of an elastoplastic block. Material remap compression localization problem

ALE



Lagrangian

**FIGURE IV.5.18** Indentation of an elastoplastic block. Distribution of the equivalent plastic strain for the Lagrangian and ALE solutions.

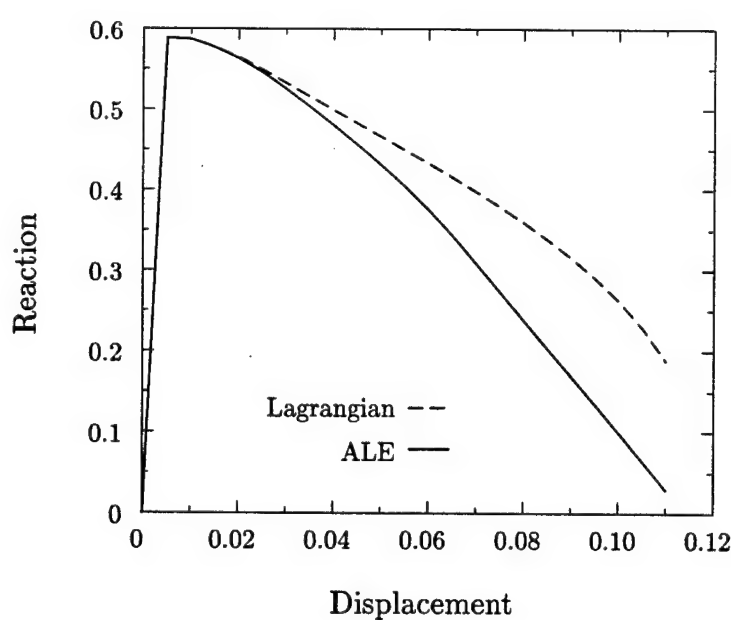


**FIGURE IV.5.19** Indentation of an elastoplastic block. Load-displacement curve.

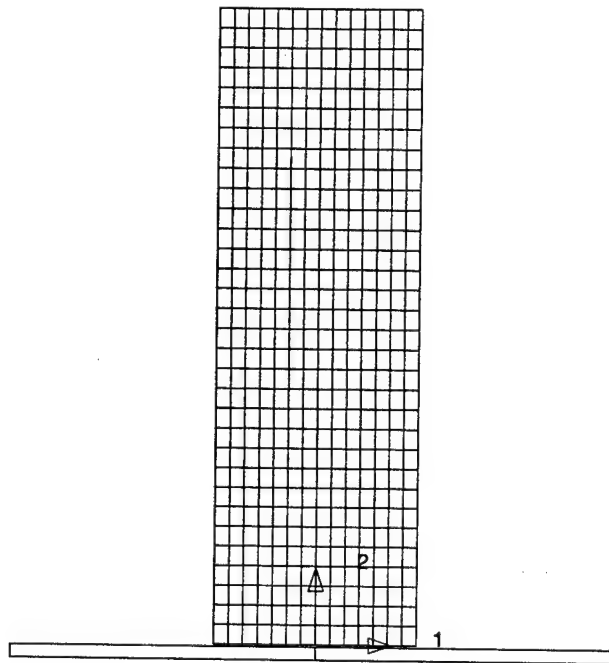


**FIGURE IV.5.20** Impact of a circular bar. Reference mesh. Only half of the specimen is discretized with  $7 \times 32$  Q1/P0 mixed finite elements, with axisymmetric conditions.

**TABLE IV.5.4** Impact of a circular bar. Assumed material properties for Copper OFHC.

|                      |            |         |                   |
|----------------------|------------|---------|-------------------|
| Bulk Modulus         | $\kappa$   | 130.000 | GPa               |
| Shear Modulus        | $\mu$      | 43.333  | GPa               |
| Flow Stress          | $y_o$      | 0.12    | GPa               |
| Saturation Hardening | $y_\infty$ | 0.62    | GPa               |
| Hardening Exponent   | $\delta$   | 3.01    |                   |
| Density              | $\rho_o$   | 8930.   | kg/m <sup>3</sup> |

**TABLE IV.5.5** Impact of a circular bar. Assumed material properties for Aluminum 6061-T6.

|                      |            |          |                   |
|----------------------|------------|----------|-------------------|
| Bulk Modulus         | $\kappa$   | 58.33333 | GPa               |
| Shear Modulus        | $\mu$      | 26.92308 | GPa               |
| Flow Stress          | $y_o$      | 0.30     | GPa               |
| Saturation Hardening | $y_\infty$ | 0.42     | GPa               |
| Hardening Exponent   | $\delta$   | 28.60    |                   |
| Density              | $\rho_o$   | 2700.    | kg/m <sup>3</sup> |

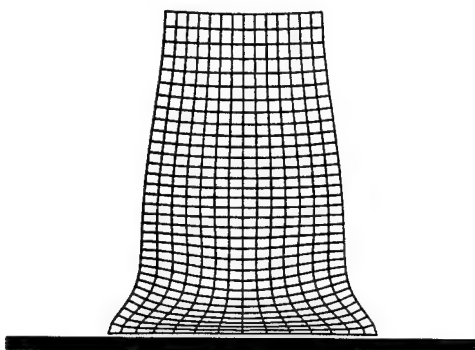
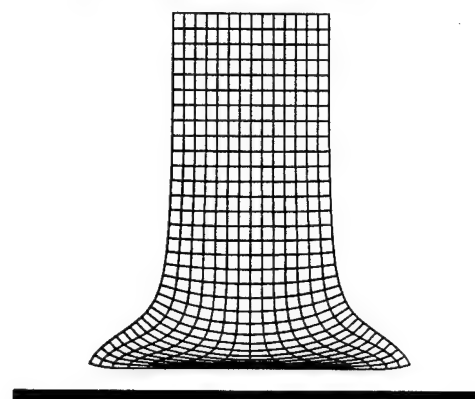
materials are considered: pure copper (Copper OFHC) and a structural aluminum alloy (Aluminum 6061-T6). The assumed material parameters are summarized in Tables IV.5.4 and IV.5.5, respectively. The contact with the rigid wall is assumed frictionless and non-sticky, that is, with the bar free to rebound from the wall. The reference mesh for all the simulations is shown in Figure IV.5.20.

The time step used in the numerical calculations is  $\Delta t = 1.0 \mu s$ . The Newmark parameters are chosen as  $\beta = 0.5$  and  $\gamma = 1.0$ . For the ALE calculation, the material remap  $\chi$  is determined using a Mooney-Rivlin energy function with  $c_1/c_2 = 3$  and  $\kappa = 0$ . The determination of  $\chi$  is based only on  $F_{22}$ . In other words, the smoother performs calculations based on the assumption that  $\mathbf{F}$  is of the form  $\mathbf{F} := \mathbf{I} + F_{22}\mathbf{e}_2 \otimes \mathbf{E}_2$ . Other components are not considered. This is the same methodology used for the necking problem of the previous section.

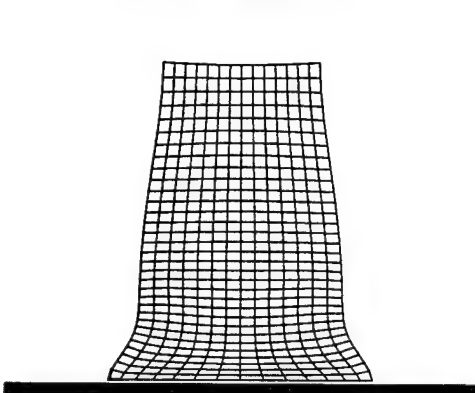
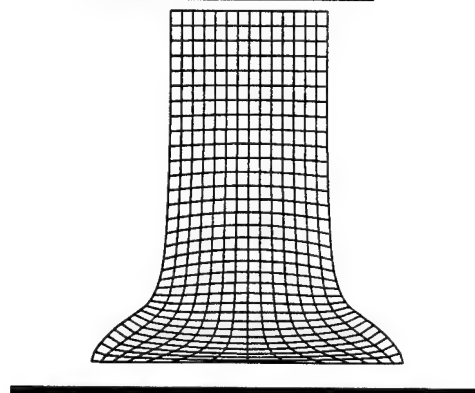
The initial velocities considered in the numerical simulations are  $v_0 = 0.210 \text{ mm}/\mu s$  for the Copper OFHC, and  $v_0 = 0.373 \text{ mm}/\mu s$  for the Aluminum 6061-T6. The final deformed meshes obtained in fully Lagrangian simulations are shown in Figure IV.5.21 for both the Copper OFHC and Aluminum 6061-T6 specimens. Figure IV.5.22 depicts the spatial meshes obtained in the ALE simulations. We note that these deformed meshes do not reflect directly the deformation of the material. They correspond to the deformations from the material mesh, which is depicted in Figure IV.5.23 for both cases. The distortion of the mesh in the original Lagrangian simulation is avoided by rezoning the material domain. The smaller distortion of the meshes in Figure IV.5.22 is to be noted when compared with the Lagrangian solutions in Figure IV.5.21.

Figure IV.5.24 includes a picture of some of the deformed specimens reported by WILKINS & GUINAN [1973], together with the solutions computed in this work depicting the distribution of the equivalent plastic strain confirming the preceding observations. A good agreement is observed on the final deformation of the specimens. It is interesting to note the differences in the results between the aluminum and the copper. Note that the contours of equivalent plastic strain for the copper bar are less concentrated in the impact region than in the aluminum bar. The copper strain hardens much more than the aluminum, and thus the deformation in the copper bar is less concentrated and more diffuse. The characteristic bulging of the specimen is to be noted. The aluminum hardens less and over a smaller range of strain than the copper. Under these impact conditions, the aluminum behaves essentially as a elastic-perfectly plastic with no hardening at an initial yield stress of  $\sigma_\infty$ . Upon impact, the aluminum hardens and reaches this limiting value quickly. On the other hand, the copper does not reach the limiting value of  $\sigma_\infty$  so quickly, and thus assuming the copper to be elastic-perfectly plastic is not reasonable. The value of  $\sigma_{wg}$  is chosen less than  $\sigma_\infty$  to account for the extensive ductility and wide range of strain-hardening the copper undergoes.

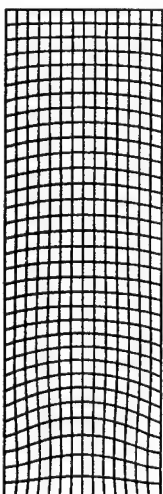
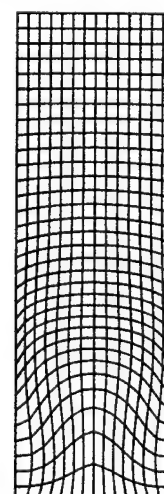
Finally, Figure IV.5.25 depicts a plot of the scaling law, equation (IV.5.3), the com-

Copper OFHCAluminum 6061-T6

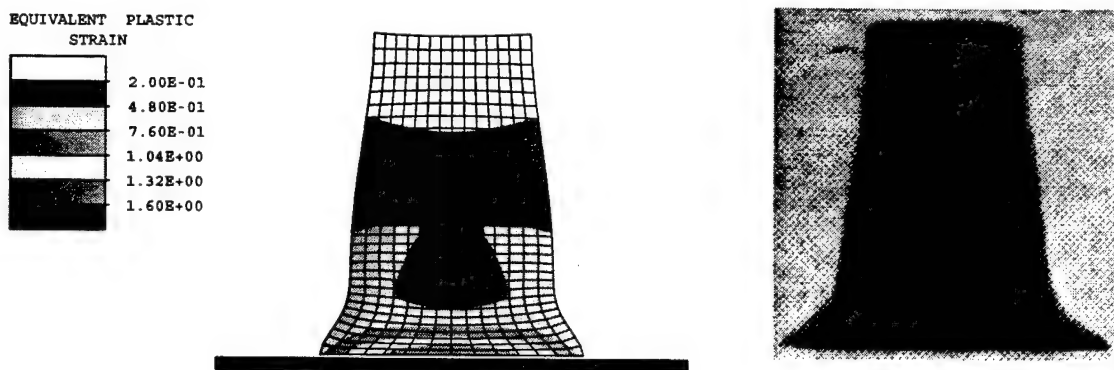
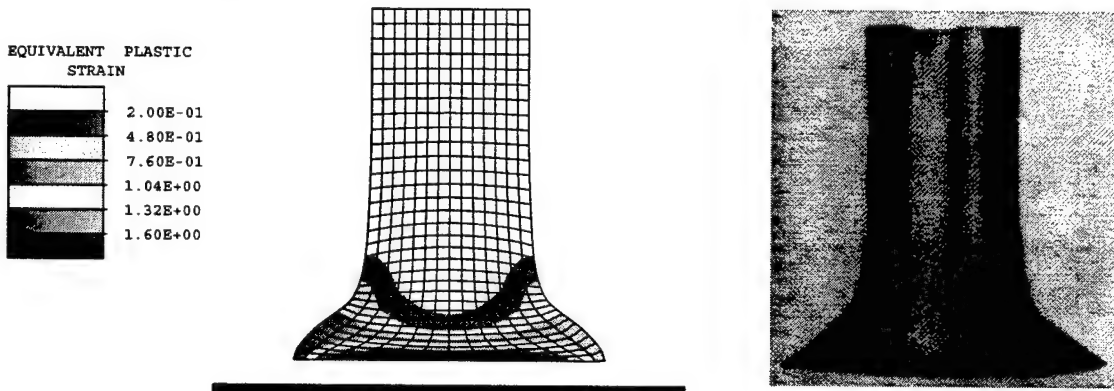
**FIGURE IV.5.21** Impact of a circular bar. Lagrangian solutions for the Copper OFHC and Aluminum 6061-T6 bars.

Copper OFHCAluminum 6061-T6

**FIGURE IV.5.22** Impact of a circular bar. ALE solutions for the Copper OFHC and Aluminum 6061-T6 bars. The spatial mesh is shown.

Copper OFHCAluminum 6061-T6

**FIGURE IV.5.23** Impact of a circular bar. ALE solutions for the Copper OFHC and Aluminum 6061-T6 bars. The material remap is shown.

**Copper OFHC****Aluminum 6061-T6**

**FIGURE IV.5.24** Impact of a circular bar. ALE numerical solutions for the Copper OFHC and Aluminum 6061-T6 bars showing the equivalent plastic strain, and the experimental results reported by WILKINS & GUINAN [1973].

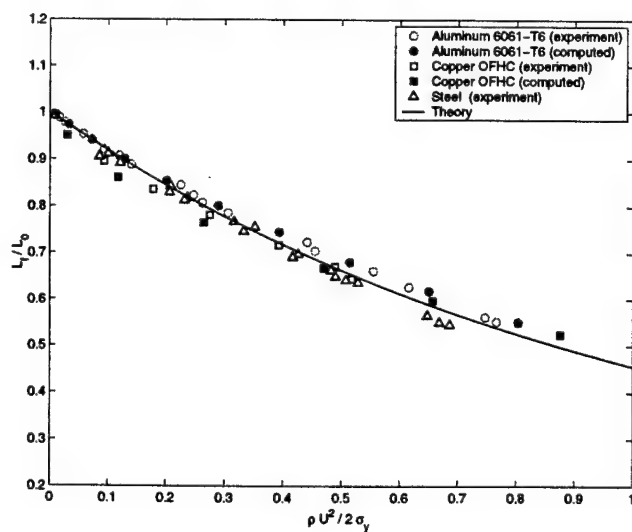


**FIGURE IV.5.25** Impact of a circular bar. Comparison between computed results, experiments and scaling law.

puted ALE solutions for the copper and the aluminum bars, and the reported experimental results. A good correlation is found, validating the proposed ALE finite element methods.

## IV.6. Concluding Remarks

We have presented an Arbitrary Lagrangian-Eulerian (ALE) formulation for solid mechanics which may be used for the finite element simulation of elasticity and plasticity problems. The proposed method involves a fully implicit formulation, with a staggered treatment of the advection of the internal variables. In particular, the direct use and interpolation of the material map  $\chi$  has been shown to lead to a simplified treatment of the advection part, in contrast with existing procedures. Numerical simulations have verified the validity of the approach. Current work includes the consideration of the fully dynamic problem

## Appendix IV.1. Constitutive Models

We summarize in this appendix the specific constitutive models used in the numerical simulations presented in Section IV.5. For all the elasticity numerical simulations, we consider the classical Mooney-Rivlin model for rubber elasticity, modified to allow for non-isochoric response. Given a deformation gradient  $\mathbf{F}$ , define  $\bar{\mathbf{F}} := \det(\mathbf{F})^{-\frac{1}{3}}\mathbf{F}$ . Let  $\bar{\mathbf{C}} := \bar{\mathbf{F}}^T\bar{\mathbf{F}}$ . In the actual numerical implementations, we evaluate the constitutive response using  $\tilde{\mathbf{F}}$  defined in equation (IV.2.38). Then, the free energy function  $W$  is given by

$$W(\mathbf{F}) := c_1 [I_1(\bar{\mathbf{C}}) - 3] + c_2 [I_2(\bar{\mathbf{C}}) - 3] + \kappa U(J), \quad (\text{IV.1.1})$$

where  $I_1$  and  $I_2$  are the first and second invariants of a symmetric rank two tensor, respectively, and  $J = \det(\mathbf{F})$ . Also,  $U(\cdot)$  is the volumetric response function and  $c_1 > 0$ ,  $c_2 > 0$  and  $\kappa > 0$  are fixed material parameters. We use  $U(J) := \frac{1}{2}(J^2 - 1) - \log(J)$ . This is a convex function of the argument  $J$ .

For all the plasticity numerical simulations, we use a finite strain  $J_2$  flow theory designed to mimic the classical model of infinitesimal elasto-plasticity. It is the same model as discussed in section 5 of SIMO [1992]. Define  $\{\epsilon_1^e, \epsilon_2^e, \epsilon_3^e\}$  as the principal values of  $\frac{1}{2}\log\mathbf{b}^e$ . These are the principal logarithmic elastic stretches. Next, define

$$\boldsymbol{\epsilon}^e := \left\{ \begin{array}{c} \epsilon_1^e \\ \epsilon_2^e \\ \epsilon_3^e \end{array} \right\}. \quad (\text{IV.1.2})$$

Let

$$\mathbf{a} := \begin{bmatrix} K + \frac{4}{3}\mu & K - \frac{2}{3}\mu & K - \frac{2}{3}\mu \\ K - \frac{2}{3}\mu & K + \frac{4}{3}\mu & K - \frac{2}{3}\mu \\ K - \frac{2}{3}\mu & K - \frac{2}{3}\mu & K + \frac{4}{3}\mu \end{bmatrix} \quad (\text{IV.1.3})$$

where  $K > 0$  and  $\mu > 0$  are two material constants. Let

$$\beta := \alpha \epsilon^e \quad (\text{IV.1.4})$$

be the principal Kirchhoff stresses ( the principal values of  $\tau$  ).

The model of plasticity is given by

1. Hyperelastic response defined by free energy function :

$$W(\epsilon) := \frac{1}{2} \epsilon^e \cdot \alpha \epsilon^e$$

2. von Mises yield criterion :

$$\phi(\tau, q) := \|\text{dev}\beta\| - \sqrt{\frac{2}{3}}q \leq 0$$

3. Saturation Isotropic Hardening :

$$q(\xi) := \sigma_\infty + (\sigma_0 - \sigma_\infty)\exp(-\delta\xi) + H\xi$$

where  $\sigma_0$ ,  $\sigma_\infty$ ,  $\delta$  and  $H$  are prescribed material parameters.

4. Associative Evolution Equations :

$$-\frac{1}{2} \mathbf{f} \cdot \mathbf{v} \mathbf{b}^e := \gamma \frac{\partial \phi}{\partial \tau} \mathbf{b}^e \quad \equiv \quad \dot{\mathbf{G}}^p = -2\lambda \left( \mathbf{F}^{-1} \left[ \frac{\partial \phi}{\partial \tau} \right] \mathbf{F} \right) \mathbf{G}^p$$

$$\dot{\xi} := \lambda \sqrt{\frac{2}{3}}$$

with  $\partial\phi/\partial\tau = \text{dev}\beta/\|\beta\|$  in the principal directions.

The model is implemented numerically using an exponential return mapping approach. The reader may consult CUITINO & ORTIZ [1992] and SIMO [1992] for more detailed information.

## Appendix IV.2. Numerical Implementation of Three Dimensional Elasticity

The discussion in this section focuses on the finite element implementation of finite strain elasticity within an ALE context. The discussion is very similar to that of YAMADA & KIKUCHI [1993]. In this paper, the authors discuss the equations within a two field variational context. Here, we shall discuss a three field approach to the problem. The discussion here assumes a fully coupled solution strategy to the elasticity problem.

#### IV.2.1. Preliminaries

Assume there exists a fixed Cartesian coordinate system for our problem which all three domains (reference, material, spatial) share. In such a case, introduce displacement fields  $\mathbf{u}_\chi$  and  $\mathbf{u}_\psi$  such that

$$\mathbf{X} = \mathbf{m} + \mathbf{u}_\chi \quad (\text{IV.2.1})$$

and

$$\mathbf{x} = \mathbf{m} + \mathbf{u}_\psi \quad (\text{IV.2.2})$$

where  $\mathbf{m}$  is the reference coordinate,  $\mathbf{X}$  is the material coordinate and  $\mathbf{x}$  is the spatial coordinate. This then gives

$$\mathbf{F}_\chi = \text{GRAD}\mathbf{m}[\mathbf{X}] = \mathbf{1} + \text{GRAD}\mathbf{m}[\mathbf{u}_\chi] \quad (\text{IV.2.3})$$

and

$$\mathbf{F}_\psi = \text{GRAD}\mathbf{m}[\mathbf{x}] = \mathbf{1} + \text{GRAD}\mathbf{m}[\mathbf{u}_\psi]. \quad (\text{IV.2.4})$$

The fields  $\mathbf{u}_\chi$  and  $\mathbf{u}_\psi$  shall be discretized using standard finite element interpolations.

Let  $\Delta\mathbf{u}_\chi$  be an arbitrary increment to  $\mathbf{u}_\chi$  and let  $\Delta\mathbf{u}_\psi$  be an arbitrary increment to  $\mathbf{u}_\psi$ . For future use, define

$$\Delta\mathbf{F} := \left[ \frac{d}{d\alpha} \mathbf{F}(\mathbf{u}_\psi + \alpha\Delta\mathbf{u}_\psi, \mathbf{u}_\chi + \alpha\Delta\mathbf{u}_\chi) \right]_{\alpha=0} \quad (\text{IV.2.5})$$

and

$$\mathbf{l}_{\Delta u} := (\Delta\mathbf{F}) \mathbf{F}^{-1}. \quad (\text{IV.2.6})$$

After some manipulations, one may produce the result

$$\mathbf{l}_{\Delta u} = \text{grad}_{\mathbf{x}}[\Delta\mathbf{u}_\psi] - \mathbf{F} \text{grad}_{\mathbf{x}}[\Delta\mathbf{u}_\chi] \quad (\text{IV.2.7})$$

Assume there exists an isothermal free energy function  $W(\mathbf{F})$  describing the constitutive response of the elastic material. Defining  $\boldsymbol{\tau}$  as the Kirchhoff stress tensor, one has the well known result

$$\boldsymbol{\tau} = \frac{\partial W}{\partial \mathbf{F}} \mathbf{F}^T \quad (\text{IV.2.8})$$

This constitutive response will produce, upon time differentiation, a rank four tensor  $\mathbb{D}(\mathbf{F})$  such that  $\dot{\boldsymbol{\tau}} = \mathbb{D}\mathbf{l}$  where  $\mathbf{l} := \dot{\mathbf{F}}\mathbf{F}^{-1}$  is the spatial velocity gradient.

#### IV.2.2. Linearizations

In this section we give the consistent linearizations of the three weak equations (IV.2.35) - (IV.2.37). We have previously defined  $\Delta\mathbf{u}_\psi$  and  $\Delta\mathbf{u}_\chi$ . Let  $\Delta\theta$  and  $\Delta p$  be arbitrary increments to  $\theta$  and  $p$ , respectively. Note that the volume element  $d\Omega_0$  is not

constant in this case, but can be related to the constant reference volume element by  $d\Omega_0 = J_\chi d\mathcal{M}$ .

#### IV.2.2.1. Linear Momentum

The linearization of the linear momentum equation yields the terms

$$\begin{aligned} \text{TANGENT} = & - \int_{\Omega_0} \text{grad}_x[\eta] \text{grad}_x[\Delta u_\psi] : [\mathbb{I}_{dev} \tilde{\tau} + pJ \mathbf{1}] d\Omega_0 \\ & + \int_{\Omega_0} \text{grad}_x[\eta] : [\mathbb{I}_{dev} \tilde{\mathbb{D}} \mathbb{I}_{dev} + pJ \mathbf{1} \otimes \mathbf{1}] \mathbf{l}_{\Delta u} d\Omega_0 \\ & + \int_{\Omega_0} \text{grad}_x[\eta] : \left( \frac{1}{3\theta} \mathbb{I}_{dev} \tilde{\mathbb{D}} \mathbf{1} \right) \Delta \theta d\Omega_0 \\ & + \int_{\Omega_0} \text{grad}_x[\eta] : J \mathbf{1} \Delta p d\Omega_0 \\ & + \int_{\Omega_0} \text{grad}_x[\eta] : [(\mathbb{I}_{dev} \tilde{\tau} + pJ \mathbf{1}) \otimes \mathbf{F}^T] \text{grad}_x[\Delta u_\chi] d\Omega_0. \end{aligned} \quad (\text{IV.2.9})$$

#### IV.2.2.2. Constitutive Equation for Pressure

The linearization of the constitutive equation for  $p$  yields the terms

$$\begin{aligned} \text{TANGENT} = & \int_{\Omega_0} \delta \theta \left[ -\frac{1}{3\theta^2} (\tilde{\tau} : \mathbf{1}) + \frac{1}{9\theta^2} (\tilde{\mathbb{D}} \mathbf{1} : \mathbf{1}) \right] \Delta \theta d\Omega_0 \\ & + \int_{\Omega_0} \delta \theta \left[ \frac{1}{3\theta} \mathbb{I}_{dev} \tilde{\mathbb{D}}^T \mathbf{1} \right] : \mathbf{l}_{\Delta u} d\Omega_0 \\ & + \int_{\Omega_0} \delta \theta \left[ \frac{\tilde{\tau} : \mathbf{1}}{3\theta} - p \right] \mathbf{F}^T : \text{grad}_x[\Delta u_\chi] d\Omega_0 \\ & + \int_{\Omega_0} \delta \theta \Delta p d\Omega_0. \end{aligned} \quad (\text{IV.2.10})$$

#### IV.2.2.3. Compatibility Equation for Theta

The linearization of the compatibility equation for  $\theta$  generates the terms

$$\begin{aligned} \text{TANGENT} = & \int_{\Omega_0} \delta p J \mathbf{1} : \text{grad}_x[\Delta u_\psi] d\Omega_0 \\ & - \int_{\Omega_0} \delta p \theta \mathbf{F}^T : \text{grad}_x[\Delta u_\chi] d\Omega_0 \\ & - \int_{\Omega_0} \delta p \Delta \theta d\Omega_0. \end{aligned} \quad (\text{IV.2.11})$$

### Remarks IV.2.1.

1. In general, the system tangent matrix is *unsymmetric*.
2. The pure Lagrangian formulation is easily recovered by setting  $\mathbf{u}_\chi := 0$ , so that  $\chi := \text{id}$ . In this case,  $\mathbf{F} = \mathbf{F}_\psi$ . Additionally, all terms involving  $\text{grad}_{\mathbf{x}}[\Delta \mathbf{u}_\chi]$  in the tangent terms are to be neglected. In particular, we get the simplification  $\mathbf{l}_{\Delta u} = \text{grad}_{\mathbf{x}}[\Delta \mathbf{u}_\psi]$ .  $\square$

### IV.2.3. Augmented Lagrangian modifications

The augmented Lagrangian technique to be presented here is reviewed within the purely Lagrangian finite element setting in SIMO & TAYLOR [1991]. We wish to enforce the constraint of incompressibility upon this formulation of finite strain elasticity. To that end, assume that the free energy function may be additively decomposed such that

$$W(\mathbf{F}) = \hat{W}\left(\det[\mathbf{F}]^{-\frac{1}{3}}\mathbf{F}\right) + \kappa U(\det[\mathbf{F}]) \quad (\text{IV.2.12})$$

where  $\kappa > 0$  is a penalty parameter,  $\hat{W}$  is a free energy function based on the isochoric component of  $\mathbf{F}$  and  $U$  is a scalar convex function of the determinant of  $\mathbf{F}$ . If  $W(\tilde{\mathbf{F}})$  is evaluated, the result is

$$W(\tilde{\mathbf{F}}) = \hat{W}\left(J^{-\frac{1}{3}}\mathbf{F}\right) + \kappa U(\theta). \quad (\text{IV.2.13})$$

The constraint chosen is  $h(\theta) := \theta - 1 = 0$ . Other equivalent forms for the function  $h$  may be chosen. For example,  $h(\theta) = \log(\theta)$  is also a suitable choice. The requirements for  $h$  are simply that  $h(1) = 0$  and that  $h'(1) \neq 0$ .

Towards enforcement of said constraint, add the following term to the potential energy expression  $\Pi$ :

$$\int_{\Omega_0} \lambda_A h(\theta) d\Omega_0, \quad (\text{IV.2.14})$$

where  $\lambda_A$  is the augmented Lagrangian parameter. Thus, the constitutive equation for pressure becomes

$$\int_{\Omega_0} \delta\theta \left[ \frac{\tilde{\tau} : \mathbf{1}}{3\theta} - p + \lambda_A h'(\theta) \right] d\Omega_0 = 0 \quad (\text{IV.2.15})$$

This produces two extra tangent terms, which are

$$\begin{aligned} \text{TANGENT} = & \int_{\Omega_0} \delta\theta \lambda_A \mathbf{F}^T : \text{grad}_{\mathbf{x}}[\Delta \mathbf{u}_\chi] d\Omega_0 \\ & + \int_{\Omega_0} \delta\theta h''(\theta) \Delta\theta d\Omega_0. \end{aligned} \quad (\text{IV.2.16})$$

The actual implementation of the augmented Lagrangian technique involves a nested iteration process. First, for a given time step, an initial value of  $\lambda_A$  is chosen. One usually

chooses the converged value from the previous global time step. Next, the above equations are solved with this fixed value of  $\lambda_A$ . After convergence is achieved, the parameter is updated using the equation

$$\lambda_A^{(i+1)} := \lambda_A^{(i)} + \kappa h(\theta^{(i)}) \quad (\text{IV.2.17})$$

where the equations have been solved at augmented Lagrangian iteration  $(i)$  and the analysis is to advance to iteration  $(i+1)$ . This process continues until the constraint is satisfied to some chosen numerical tolerance. The convergence rate towards the constraint is expected to be linear. Then, we may advance to the next global time step.

## References

- BENSON, D.J. [1989] "An Efficient, Accurate, Simple ALE Method for Nonlinear Finite Element Programs", *Computer Methods in Applied Mechanics and Engineering*, **72**, 305-350.
- BENSON, D.J. [1992] "Computational Methods in Lagrangian and Eulerian Hydrocodes", *Computer Methods in Applied Mechanics and Engineering*, **99**, 235-394.
- BREZZI, F. & M. FORTIN [1990] *Mixed and Hybrid Finite Element Methods*, Springer-Verlag, Berlin, Germany.
- CAMACHO, G. T. & M. ORTIZ [1997] "Adaptive Lagrangian Modelling of Ballistic Penetration of Metallic Targets", *Computer Methods in Applied Mechanics and Engineering*, **142**, 269-301.
- CHIPPADA, S., B. RAMASWAMY & M. F. WHEELER [1994] "Numerical Simulation of Hydraulic Jump", *International Journal for Numerical Methods in Engineering*, **37**, 1381-1397.
- CUITINO, A. & M. ORTIZ [1992] Cuitino, A. & M. Ortiz, "A Material-Independent Method for Extending Stress Update Algorithms from Small-Strain Plasticity to Finite Plasticity with Multiplicative Kinematics", *Engineering Computations*, **9**, 437-451.
- CORMEN, T.H., CH.E. LEISERSON & R.L. RIVEST [1989] *Introduction to Algorithms*, McGraw-Hill Book Company, San Francisco, California.
- GHOSH, S. [1992] "Arbitrary Lagrangian-Eulerian Finite Element Analysis of Large Deformation in Contacting Bodies", *International Journal for Numerical Methods in Engineering*, **33**, 1891-1925.
- GHOSH, S. & N. KIKUCHI [1991] "An Arbitrary Lagrangian-Eulerian Finite Element Method for Large Deformation Analysis of Elastic-Viscoplastic Solids", *Computer Methods in Applied Mechanics and Engineering*, **86**, 127-188.

- GHOSH, S. & N. KIKUCHI [1988] "Finite Element Formulation for the Simulation of Hot Steel Metal Forming Processes", *International Journal of Engineering Science*, **26**, 143-161.
- GHOSH, S. & S.RAJU [1996] "R-S Adapted Arbitrary Lagrangian- Eulerian Finite Element Method for Metal-forming Problems with Strain Localization", *International Journal for Numerical Methods in Engineering*, **39**, 3247-3272.
- GURTIN, M.E. [1981] *An Introduction to Continuum Mechanics*, Academic Press, New York.
- HU, Y. K. & W. K. LIU [1993] "An ALE Hydrodynamic Lubrication Finite Element Method with Application to Strip Rolling", *International Journal for Numerical Methods in Engineering*, **36**, 855-880.
- HU, Y. K. & W. K. LIU [1992] "ALE Finite Element Formulation for Ring Rolling Analysis", *International Journal for Numerical Methods in Engineering*, **33**, 1217-1236.
- HUERTA, A. & F. CASADEI [1994] "New ALE Applications in Non-Linear Fast-Transient Solid Dynamics", *Engineering Computations*, **11**, 317-345.
- HUERTA, A. & WING KAM LIU [1988] "Viscous Flow with Large Free Surface Motion", *Computer Methods in Applied Mechanics and Engineering*, **69**, 277-324.
- KARYPIS, G. & V. KUMAR [1997] *METIS : A Software Package for Partitioning Unstructured Graphs, Partitioning Meshes, and Computing Fill-Reducing Orderings of Sparse Matrices*, version 3.0.3, University of Minnesota, Department of Computer Science/Army HPC Research Center, Minneapolis, Minnesota (November 5, 1997).
- KNUTH, D.L. [1997] *The Art of Computer Programming, Vol 1 : Fundamental Algorithms*, 3rd ed., Addison-Wesley, Berkeley, California.
- LEE, N.S.& K.J. BATHE [1994] "Error Indicators and Adaptive Remeshing in Large Deformation Finite Element Analysis", *Finite Elements in Analysis and Design*, **16**, 99-139.
- NOMURA, T. [1994] "ALE Finite Element Computations of Fluid-Structure Interaction Problems", *Computer Methods in Applied Mechanics and Engineering*, **112**, 291-308.
- NOMURA, T. & T. J. R. HUGHES [1992] "An Arbitrary Lagrangian-Eulerian Finite Element Method for Interaction of Fluid and a Rigid Body", *Computer Methods in Applied Mechanics and Engineering*, **95**, 115-138.
- ODDY, A., J. GOLDAK, M. McDILL & M. BIBBY [1988] "A Distortion Metric for Isoparametric Finite Elements", *Transactions of the Canadian Society for Mechanical Engineering*, **12**, 213-217.
- ORTIZ, M. & J. J. QUIGLEY IV [1991] "Adaptive Mesh Refinement in Strain Localization

- Problems", *Computer Methods in Applied Mechanics and Engineering*, **90**, 781-804.
- PIJAUDIERCABOT, G., L. BODE & A. HUERTA [1995] "Arbitrary Lagrangian-Eulerian Finite Element Analysis of Strain Localization in Transient Problems", *International Journal for Numerical Methods in Engineering*, **38**, 4171-4191.
- PIRONNEAU [1989] *Finite Element Methods for Fluids*, John Wiley & Sons, New York.
- REDWINE, C. [1995] *Upgrading to Fortran90*, Springer, New York.
- RODRIGUEZ-FERRAN, A., F. CASADEI & A. HUERTA [1998] "ALE Stress Update for Transient and Quasi-Static Processes", *International Journal for Numerical Methods in Engineering*, **43**, 241-262.
- RODRIGUEZ-FERRAN, A. & A. HUERTA [1995] "Comparison of Two Arbitrary Lagrangian-Eulerian Formulations", in *Simulation of Materials Processing : Theory, Methods and Applications (NUMIFORM 95)*, eds. Shan-Fu Shen and Paul Dawson, A. A. Balkema Publishers, Brookfield, VT.
- SARRATE, J. [1996] *Modelizacion Nuerica de la Interaccion Fluido-Solido Rígido : Desarrollo de Algoritmos, Generacion de Malla y Adaptabilidad* (translation *Numerical Modelling of the Interaction of Fluids and Rigid Solids : Development of Algorithms, Mesh Generation and Adaptability*) Ph.D. Dissertation, Universitat Politecnica de Catalunya, Barcelona, Catalonia, Spain (1996) (in Spanish).
- SIMO, J. C. [1992] "Algorithms for Static and Dynamic Multiplicative Plasticity that Preserve the Classical Return Mapping Schemes of the Infinitesimal Theory", *Computer Methods in Applied Mechanics and Engineering*, **99**, 61-112.
- SIMO, J. C. [1988a] "A Framework for Finite Strain Elastoplasticity Based on Maximum Plastic Dissipation and the Multiplicative Decomposition : Part I. Continuum Formulation", *Computer Methods in Applied Mechanics and Engineering*, **66**, 199-219.
- SIMO, J. C. [1988b] "A Framework for Finite Strain Elastoplasticity Based on Maximum Plastic Dissipation and the Multiplicative Decomposition : Part II. Computational Aspects", *Computer Methods in Applied Mechanics and Engineering*, **68**, 1-31.
- SIMO, J. C. & C. MIEHE [1992] "Associative Coupled Thermoplasticity at Finite Strains : Formulation, Numerical Analysis and Implementation", *Computer Methods in Applied Mechanics and Engineering*, **98**, 41-104.
- SIMO, J. C. & R. L. TAYLOR [1991] "Quasi-Incompressible Finite Elasticity in Principal Stretches. Continuum Basis and Numerical Algorithms", *Computer Methods in Applied Mechanics and Engineering*, **85**, 273-310.
- SIMO, J. C., R. L. TAYLOR & K. S. PISTER [1985] "Variational and Projection Methods for the Volume Constraint in Finite Deformation Plasticity", *Computer Methods in*

*Applied Mechanics and Engineering*, **51**, 177-208.

TAYLOR, R.L. [1998] *FEAP : A Finite Element Analysis Program Version 6.3 User Manual*, Department of Civil and Environmental Engineering, University of California, Berkeley, California (March 1998).

TAYLOR, G. [1948] "The Use of Flat-Ended Projectiles for Determining Dynamic Yield Stress I. Theoretical Considerations", *Proceedings of the Royal Society, Series A*, **194**, 289-299.

VENKATASUBBAN, C. S. [1995] "A New Finite Element Formulation for ALE (Arbitrary Lagrangian Eulerian) Fluid Mechanics, *International Journal of Engineering Science*, **33**, 1743-1762.

WILKINS, M.L. & GUINAN, M.W. [1973] "Impact of Cylinders on a Rigid Boundary", *Journal of Applied Physics*, **44**, 1200-1206.

YAMADA, T. & F. KIKUCHI [1993] "An Arbitrary Lagrangian-Eulerian Finite Element Method for Incompressible Hyperelasticity", *Computer Methods in Applied Mechanics and Engineering*, **102**, 149-177.

# REPORT DOCUMENTATION PAGE

*Form Approved  
OMB No. 0704-0188*

Public reporting burden for this collection of information is estimated to average 1 hour per response, including the time for reviewing instructions, searching data sources, gathering and maintaining the data needed, and completing and reviewing the collection of information. Send comments regarding this burden estimate or any other aspect of this collection of information, including suggestions for reducing this burden to Washington Headquarters Service, Directorate for Information Operations and Reports, 1215 Jefferson Davis Highway, Suite 1204, Arlington, VA 22202-4302, and to the Office of Management and Budget, Paperwork Reduction Project (0704-0188) Washington, DC 20503.

**PLEASE DO NOT RETURN YOUR FORM TO THE ABOVE ADDRESS.**

|  |  |  |   |   |  |  |
|--|--|--|---|---|--|--|
| <b>1. REPORT DATE (DD-MM-YYYY)</b><br>15-08-2000   |  |  | <b>2. REPORT DATE</b><br>Final  |   | <b>3. DATES COVERED (From - To)</b><br>June 1, 1996 – May 31, 2000   |  |
| <b>4. TITLE AND SUBTITLE</b><br><br>Analysis and Numerical Simulation of Strain Localization in Inelastic Solids under Fully Coupled Thermomechanical and Poroplastic Conditions   |  |  | <b>5a. CONTRACT NUMBER</b><br><br><b>5b. GRANT NUMBER</b><br>N00014-96-1-0818   |   |  |  |
| <b>6. AUTHOR(S)</b><br><br>Armero, Francisco   |  |  | <b>5c. PROGRAM ELEMENT NUMBER</b><br><br><b>5d. PROJECT NUMBER</b><br><br><b>5e. TASK NUMBER</b><br><br><b>5f. WORK UNIT NUMBER</b> |   |  |  |
| <b>7. PERFORMING ORGANIZATION NAME(S) AND ADDRESS(ES)</b><br><br>The Regents of the University of California<br>University of California, Berkeley<br>Sponsored Projects Office<br>336 Sproul Hall, Berkeley, CA 94720   |  |  |   | <b>8. PERFORMING ORGANIZATION REPORT NUMBER</b>       |  |  |
| <b>9. SPONSORING/MONITORING AGENCY NAME(S) AND ADDRESS(ES)</b><br><br>Office of Naval Research<br>Computational Mechanics Program, ONR 334<br>Ballston Center Tower One<br>800 North Quincy Street, Arlington, VA 22217-5660   |  |  |   | <b>10. SPONSOR/MONITOR'S ACRONYM(S)</b><br>ONR        |  |  |
| <b>12. DISTRIBUTION AVAILABILITY STATEMENT</b><br>Approved for public release; Distribution is unlimited   |  |  |   | <b>11. SPONSORING/MONITORING AGENCY REPORT NUMBER</b> |  |  |
| <b>13. SUPPLEMENTARY NOTES</b>   |  |  |   |   |  |  |
| <b>14. ABSTRACT</b><br><p>We present in this report a summary of the research supported by the ONR during the period June 1 1996 to May 31 2000 on the analysis and numerical simulation of strain localization in inelastic solids. Special attention is given to the analysis of failure under coupled thermo- and poro- plastic conditions, as well as the consideration of coupled plastic damage in solids. The highly non-smooth solutions of interest involve discontinuous displacement fields, the so-called strong discontinuities, requiring the formulation of a new framework for their inclusion in the local continuum and the development of enhanced finite element techniques that incorporate the associated singular strain fields to capture the localized dissipative mechanisms characteristic of the failure of solids in a physically correct and efficient manner. Both Lagrangian and arbitrary Lagrangian-Eulerian finite element techniques have been developed. The resulting models and numerical methods have been studied and evaluated in detail through rigorous mathematical analyses and a number of numerical simulations.</p> |  |  |   |   |  |  |
| <b>15. SUBJECT TERMS</b><br><br>Strong discontinuities, strain localization, failure, elastoplasticity and damage, coupled thermoplasticity and propoplasticity, enhanced finite elements, ALE methods, closest-point projection schemes.  |  |  |   |   |  |  |
| <b>16. SECURITY CLASSIFICATION OF:</b><br>a. REPORT    b. ABSTRACT    c. THIS PAGE<br>U              U              U  |  |  | <b>17. LIMITATION OF ABSTRACT</b><br>UU   | <b>18. NUMBER OF PAGES</b><br>194                     | <b>19a. NAME OF RESPONSIBLE PERSON</b><br>Francisco Armero<br><b>19b. TELEPHONE NUMBER (Include area code)</b><br>510-643-0813 |  |